RT DOCUMENTATION PAGE

AD-A232 717

	1b RESTRICTIVE MARKINGS
2b DECLASSIFICATION / DOWNGRADING SCHEDULE	3 DISTRIBUTION / AVAILABILITY OF REPORT Approved for public release, distribution unlimited

4 PERFORMING ORGANIZATION REPORT NUMBER(S) MIT-CE-R-90-23	5 MONITORING ORGANIZATION REPORT NUMBER(S) AFOSR-TR. 91 0132

6a. NAME OF PERFORMING ORGANIZATION Massachusetts Institute of Tech. Dept. of Civil Engineering	6b OFFICE SYMBOL *(If applicable)*	7a NAME OF MONITORING ORGANIZATION U.S. Air Force Office of Scientific Research

6c. ADDRESS *(City, State, and ZIP Code)* 77 Massachusetts Avenue Cambridge, Massachusetts 02139	7b ADDRESS *(City, State, and ZIP Code)* BK 410 Bolling Air Force Base Washington D.C. 20332-6445

8a. NAME OF FUNDING / SPONSORING ORGANIZATION AFOSR and AFESC	8b. OFFICE SYMBOL *(If applicable)* NK	9 PROCUREMENT INSTRUMENT IDENTIFICATION NUMBER AFOSR-87-0260

8c. ADDRESS *(City, State, and ZIP Code)* AFOSR - Bolling AFB, Washington D.C. 20332-6448 BK 410 AFESC - Tyndall AFB, Florida 32404-6061	10 SOURCE OF FUNDING NUMBERS			
	PROGRAM ELEMENT NO. 61102F	PROJECT NO. 2302	TASK NO. C2	WORK UNIT ACCESSION NO

11. TITLE *(Include Security Classification)*
Stochastic and Centrifuge Modelling of Jointed Rock Vol. 1 - Fracturing of Fractured Rock

12. PERSONAL AUTHOR(S) Olivia Reyes, Herbert H. Einstein

13a. TYPE OF REPORT Final	13b. TIME COVERED FROM 6/87 TO 5/90	14. DATE OF REPORT *(Year, Month, Day)* 1990, August, 31	15 PAGE COUNT 211

16. SUPPLEMENTARY NOTATION

17.	COSATI CODES		18. SUBJECT TERMS *(Continue on reverse if necessary and identify by block number)*
FIELD	GROUP	SUB-GROUP	Jointed (Fractured) Rock, Stochastic Modelling, Fracture Geometry

19. ABSTRACT *(Continue on reverse if necessary and identify by block number)*

Rock mass failure can occur through the propagation of cracks emanating from and causing coalescence of pre-existing fractures. The objective of this research was to develop a mechanical model for fracture coalescence which can be used in conjunction with numerical methods to simulate rock mass failure.

(Continued on next page.)

20. DISTRIBUTION / AVAILABILITY OF ABSTRACT ☐ UNCLASSIFIED/UNLIMITED ☐ SAME AS RPT ☐ DTIC USERS	21. ABSTRACT SECURITY CLASSIFICATION UNCLASSIFIED
22a. NAME OF RESPONSIBLE INDIVIDUAL DR S WU	22b. TELEPHONE *(Include Area Code)* 202-767-6963	22c. OFFICE SYMBOL NA

DD FORM 1473, 94 MAR   83 APR edition may be used until exhausted.
All other editions are obsolete.

SECURITY CLASSIFICATION OF THIS PAGE

Block 19 - continued

Fractures in a rock mass can be considered as pre-existing flaws in an otherwise continuous medium. It was initially thought that crack propagation criteria from fracture mechanics, which were experimentally verified on polymers, could be applied to this conceptual model of fractured rock. However, a systematic experimental study of coalescence between pre-existing flaws in gypsum blocks showed fracture patterns that were very different from what was expected on the basis of fracture mechanics theory and what had been shown in experiments on polymers. The most significant observation was the coalescence of pre-existing flaws through secondary crack growth that occurred after the usual appearance of wing cracks.

Linear elastic analyses of the experimental flaw geometries indicated that a smeared crack/damage approach would be a better framework for a fracture coalescence model when compared to the more commonly used discrete crack approach. Furthermore, the observed coalescence cracks appeared to be located in regions of high tensile strains rather than high tensile stresses. Thus, a tensile strain-based damage model was formulated and implemented as a material subroutine for ABAQUS. Material parameters were determined by fitting the simulated coalescence load to the observed value for one of the test flaw geometries. These same parameter values were then used to predict coalescence loads for the other flaw arrangements. Very satisfactory agreement was obtained between experimental and computed coalescence load values.

This report volume contains the results of the text series conducted during the last year of research and the development of the analytical model. Extensive test series and numerical studies were conducted in the preceding years. The reader is referred to the annual reports 1987/88 and 1988/89 as well as to the MS thesis "Experimental Study and Analytical Modelling of Fracture Coalescence in Brittle Materials", by O. M. Reyes for details on this initial research effort.

MIT CE R-90-23

STOCHASTIC AND CENTRIFUGE MODELLING OF JOINTED ROCK

Part I - Fracturing of Fractured Rock

Grant No. AFOSR-87-0260

Final Report 1990

Prepared by

Olivia Reyes
Herbert H. Einstein

December 1990

Acknowledgements

(This page intentionally left blank)

Table of Contents

Chapter 1
Introduction

Rock mass failure has been viewed as occuring in either one of two ways: (1) failure along continuous pre-existing fractures, or (2) fracturing of the intact rock. In frequent cases where the fractures are not continuous (Fig. 1.1a), failure occurs through fracturing of the intact rock bridges that leads to coalescence of the pre-existing fractures (Fig. 1.1b). Present models for rock mass failure prediction typically assume that the fractures are continuous, thus neglecting the significant contribution of the intact rock bridges to the overall strength of the rock mass. The objective of this study is *to develop a mechanical model for fracture coalescence* that can be used to improve failure prediction of rock masses with discontinuous fractures.

Fractures in a rock mass can be considered as pre-existing cracks in an otherwise continuous medium. It was initially thought that crack propagation criteria from fracture mechanics, which have been verified using polymeric materials, could be applied to this conceptual model of fractured rock (Chan, 1986). However, published results of experiments exhibited crack growth in rock that was very different from what was seen in polymers (see Chapter 2). Preliminary tests using gypsum as a model material for rock showed coalescence between pre-existing fractures that had never occured in similar tests on polymers. More importantly, the observed coalescence could not be predicted by existing crack propagation criteria. Since gypsum more closely modelled rock behavior, the fracture patterns in the preliminary tests were more likely to occur in a fractured rock mass. Thus, these initial findings led to a systematic experimental and analytical investigation of crack growth and coalescence mechanisms in rock, using gypsum as a model material. The study consisted of:

(1) Monitoring crack growth in uniaxially compressed gypsum specimens with pre-existing fractures with various arrangements. Consistent coalescence behavior as a function of pre-existing fracture geometry was noted and is documented in Chapter 3.

(2) Development of an analytical coalescence model based on correlations between computed stress/strain fields and observed fracturing in the experiments. Using this analytical model, satisfactory agreement was achieved between simulated and experimental coalescence behavior as a function of pre-existing fracture geometry. The development, application and validation of this coalescence model are described in Chapter 4.

Conclusions and recommendations for future study are then given in Chapter 5.

Note: In the following chapters of this report, the term "flaw" will be used to refer to pre-existing fractures. Also, the standard mechanics sign convention is used, i.e., positive and negative values refer to tensile and compressive stress/strain components, respectively.
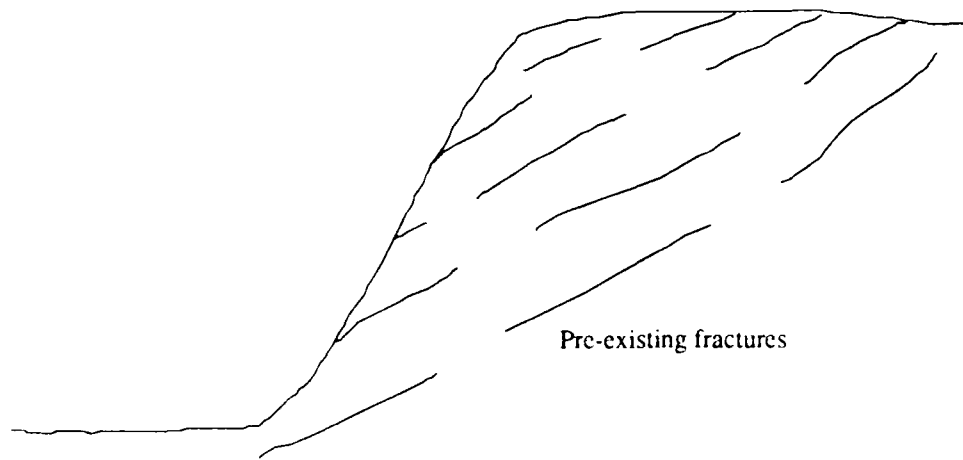
Figure 1.1(a)   Rock slope with discontinuous fractures
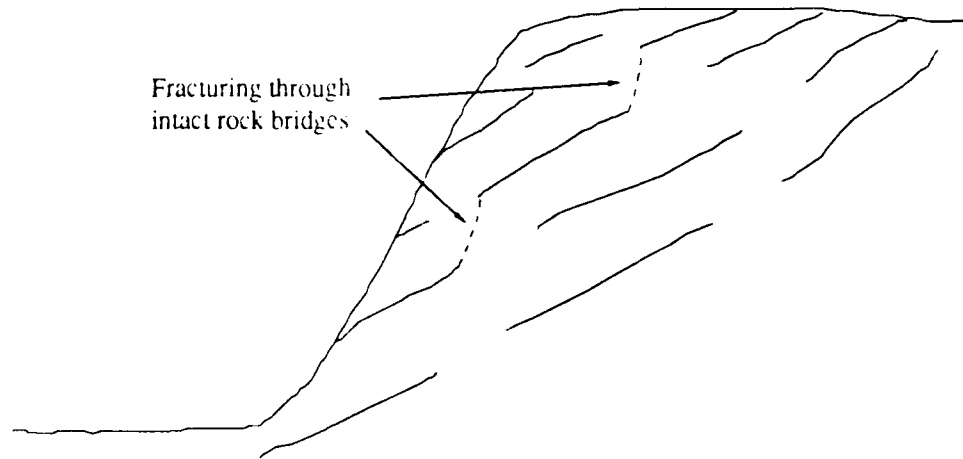
Figure 1.1(b) Failure in a rock slope due to coalescence of pre-existing fractures

20

Chapter 2
Previous Work: Crack Growth from Inclined Flaws in Compression

2.1 Introductory Remarks

Starting with the pioneering work of Erdogan and Sih (1963), numerous papers have been written on the problem of predicting crack growth from inclined pre-existing flaws, also referred to as mixed-mode crack propagation. Comprehensive reviews of the various crack propagation criteria and supporting experimental studies have already been presented by Maiti and Smith (1984) and by Yarema and Ivanitskaya (1986). There has also been an entire conference devoted to mixed-mode crack propagation (Sih and Theocaris, 1981) as well as a book written by Gdoutous (1984) on the same subject. Since such comprehensive reviews already exist, this chapter will focus on work reported in the literature that is most relevant to this study, i.e., crack propagation from inclined flaws subjected to far-field compression and, most importantly, coalescence between multiple pre-existing flaws.

The first section of this chapter presents experimental work performed by others on (1) crack growth from single flaws, and (2) crack coalescence between multiple flaws. Two general types of materials were used in these experiments: polymers such as glass, PMMA and CR39, and rocks. Polymers are favored model materials for studying rock structures due to their photoelastic properties and easy machinability. However, this review will show that conclusions drawn from fracture experiments in polymers may not be applicable to fracturing of rock. Specifically, differences between crack propagation from single flaws in polymers and in rocks can be clearly established by comparing

published results between several experiments using these materials. On the other hand, as far as crack coalescence is concerned, only one such experiment is known to have been performed in rocks and its results differed significantly from similar tests on polymers. The observations in this single experiment corroborate the findings presented in Chapter 3 of this report.

The second section of this chapter describes analyses using existing crack propagation criteria that successfully modelled the observed crack growth from flaws in polymer specimens. However, the observed crack growth from flaws in rock was not explicitly simulated by these analyses, thus highlighting the inadequacy of existing crack propagation criteria for modelling rock fracture.

2.2 Observed Crack Growth from Single and Multiple Flaws

2.2.1 Specimens with Single Inclined Flaws

It has been been well documented in the literature that when a single, inclined flaw is subjected to uniaxial compression, cracks initiate from the flaw tips approximately perpendicular to the plane of the flaw, curve and propagate parallel to the applied uniaxial compressive load (see Fig. 2.1). These cracks, referred to as wing cracks in this study, grow stably, i.e., an increase in load is required for them to lengthen. Wing cracks were seen growing from inclined flaws in polymer materials such as *polymethymethacrylate* or *PMMA* (McClintock,1963; Adams and Sines, 1978; Ingraffea and Heuze, 1980), *glass* (Brace and Bombolakis, 1963; Hoek and Bieniawski, 1965) and*Columbia Resin 39* or *CR39*(Horii and Nemat-Nasser, 1986). Specimens with open and closed pre-existing flaws both exhibited wing crack growth.

Wing cracks were also seen in uniaxial compression tests on rock specimens with pre-existing. open flaws. However, secondary fractures, which were not observed in any of the experiments on polymers, propagated and eventually caused the failure of the rock specimens. For example, Fig. 2.2 shows the crack growth sequence that Lajtai (1974) observed in *plaster of paris*. What he labelled as "tensile" fractures appeared first and probably correspond to the wing cracks described above. Upon further loading, other fractures were observed and were labelled as "normal" and "inclined shear" fractures. These labels reflect the author's hypotheses regarding the stresses which produced these cracks.

Ingraffea and Heuze (1980) performed uniaxial compression tests on *limestone* and *granodiorite* specimens with single inclined flaws. They reported the following sequence of crack growth (see Fig. 2.3 for schematic diagram of observed cracks):

1) Cracks initiated from tensile stress concentration points near the flaw tips. These cracks were labelled "primary" and correspond to wing cracks in this study.

2) These "primary" cracks propagated stably along a curvilinear path.

3) Another set of cracks, labelled "secondary", *apparently* initiated at compressive stress concentration points near flaw tips. It was claimed that these secondary cracks actually initiated from tensile stress concentrations remote from the flaw tip (see Section 2.2.2).

4) The secondary cracks propagated unstably and led to specimen failure at loads that were 3 to 5 times higher than the load at which primary cracks were first observed.

Wang et al. (1987) also reported secondary fracturing in a uniaxial compression test of a *marble* specimen with a single inclined flaw. The crack growth sequence is the same as that observed by Lajtai (1974), and by Ingraffea and Heuze (1980). Tensile cracks initiated near the tips of the flaws and propagated curvilinearly to align with the applied uniaxial compressive load. This was followed by the appearance of what they called "X-type shear fractures" which also intiated from the flaw tips (see Fig. 2.4e, f). These new fractures caused the final rupture of the specimens.

Petit and Barquins (1988) looked into crack propagation from single inclined flaws in uniaxially compressed specimens made of low and high porosity *sandstones*. Fig. 2.5 shows a schematic diagram of the observed fracture process. They labelled the fractures as "bf" for branch fractures, and "sz" for shear zones. As in all the previous crack growth sequences, the first cracks to grow were the "branch fractures" which are equivalent to the wing cracks in this study, to Lajtai's and Wang et al.'s tensile cracks, and

24

to Ingraffea's primary cracks. This was followed by the appearance of the "shear zones" which could be the same as the secondary fracturing that was observed in the experiments described previously.

2.2.2 Specimens with Multiple Inclined Flaws

In the early 60's, several researchers were proposing a model for the formation of shear faults in rocks through the coalescence of pre-existing flaws. In order to explore the validity of this shear fault model, experiments on arrays of interacting flaws in *glass* and other photoelastic (*polymer*) materials were performed by, among others, Hoek and Bieniawski (1965), Bombolakis (1964) and Paulding (1965). However, coalescence was never observed in these experiments, as summarized by Brace and Byerlee (1967) in the following statement:

"...for each individual [flaw] in the array, crack growth followed approximately the same directions as for an isolated crack, namely, along a curving path which approached the direction of maximum compression. Clearly, for an en-echelon array, this would not lead to a through-going fracture. [see Fig. 2.6]"[2.1]

These conclusions regarding non-coalescence between interacting flaws was reinforced by experiments reported by Ingraffea and Heuze (1980) and by Horii and Nemat-Nasser (1986) using *PMMA* and *CR39*, both of which are polymers. Fig. 2.7 shows a schematic diagram of a final fracture pattern given by Ingraffea and Heuze (1980).

[2.1] Quoted from W. Brace and J. Byerlee, "Recent experimental studies of brittle fracture of rocks," in Failure and Breakage of Rock, AIME, pp. 57-81, 1967.

The figure shows that wing cracks grew as in the single flaw case but did not cause the coalescence of the pre-existing flaws.

The multiple-flaw tests reported by Horii and Nemat-Nasser (1986) were performed to establish physical evidence for a mechanism of faulting which the authors were proposing. Their model for shear failure is very similar to that being proposed by Hoek, Brace and others and is also based on the idea that a shear fault is formed from the interaction of many pre-existing flaws. Note that the original "shear fault" model stipulated that the pre-existing flaws would literally link-up to form a through-going discontinuity. However, such coalescence was never observed in the previous tests, nor was it seen in the tests reported by Horii and Nemat-Nasser (1986). This is shown in Fig. 2.8 which is a schematic diagram of a plate with multiple, parallel flaws after it had been biaxially compressed. Wing cracks grew out of the tips of all the flaws and resulted in coalescence between only one pair of pre-existing flaws (see Fig. 2.8). In order to make their model for a shear fault more plausible, the authors had to claim that the shear fault would form due to the unstable propagation of wing cracks caused by interaction. The original concept of "linking flaws" had to be discarded in view of the results of their model tests.

The only experiments involving interacting flaws in compressed rock specimens were performed by Wang et al. (1987). They tested a marble specimen with flaws very similar to those shown in Fig. 2.7. However, unlike the flaws in PMMA, coalescence did occur betwen these flaws in marble through the growth of a crack between the internal flaw tips (Fig. 2.9). It was not stated whether the coalescing crack was actually the intersection of the wing cracks growing from the internal flaw tips, or whether a different crack initiated and propagated between the two flaws. The second possibility seems more likely in light of the secondary cracking observed for single flaws in rock specimens (see Sec. 2.2.1) as well as experiments presented in this report (see Section 3.3).

26

A dependence of crack growth behavior on material type was also noted in double-edge notch bend specimens such as that shown in Fig. 2.10 (Melin, 1989). This geometry was being proposed as a suitable "shear fracture" specimen for concrete[2.2] since tests reported by Bazant and Pffeifer (1986) had shown fracturing in the region of high shear stresses between the two notches (see Fig. 2.11). On the other hand, tests on a similar specimen geometry but using PMMA show cracks that initiate at the edge of the notches and propagate in a curvilinear path (see Fig. 2.12). The difference between the fracture behavior in Figs. 2.11 and 2.12 is similar to the observed coalescence and non-coalescence between flaws in rock and polymers.

[2.2] Concrete and rock are both classified as cohesive, frictional materials. Thus, the behavior of these materials is expected to be similar.
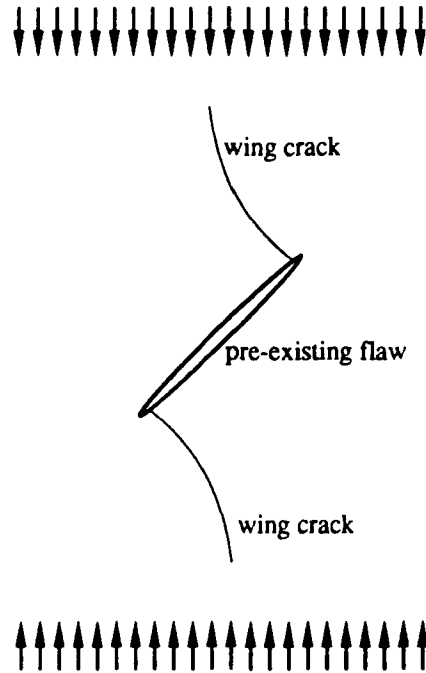
Figure 2.1   Typical crack growth from a pre-existing flaw in *polymer* specimens subjected to uniaxial compression.
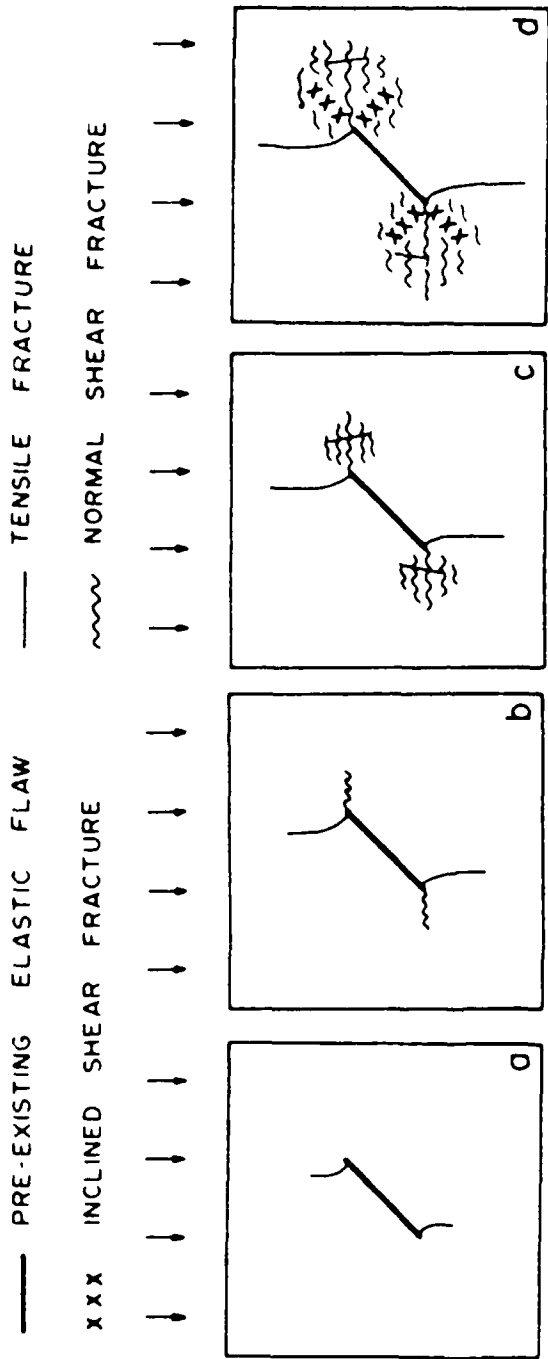
Figure 2.2   Crack growth from a single inclined flaw in a *plaster-of-paris* specimen under uniaxial compression [from Lajtai, 1974].

29
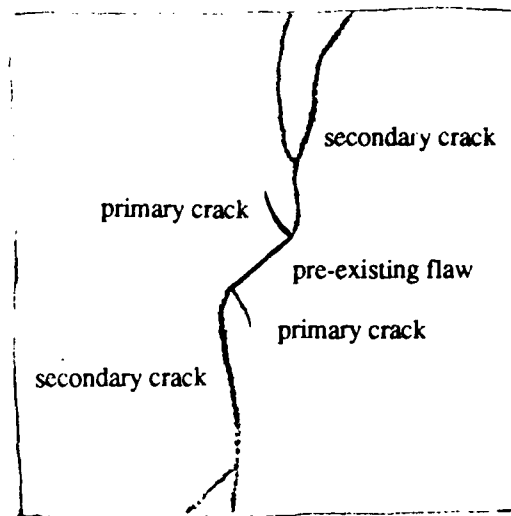
Figure 2.3   Crack growth from a single inclined flaw in a *limestone* specimen under uniaxial compression [from Ingraffea and Heuze, 1980].

30
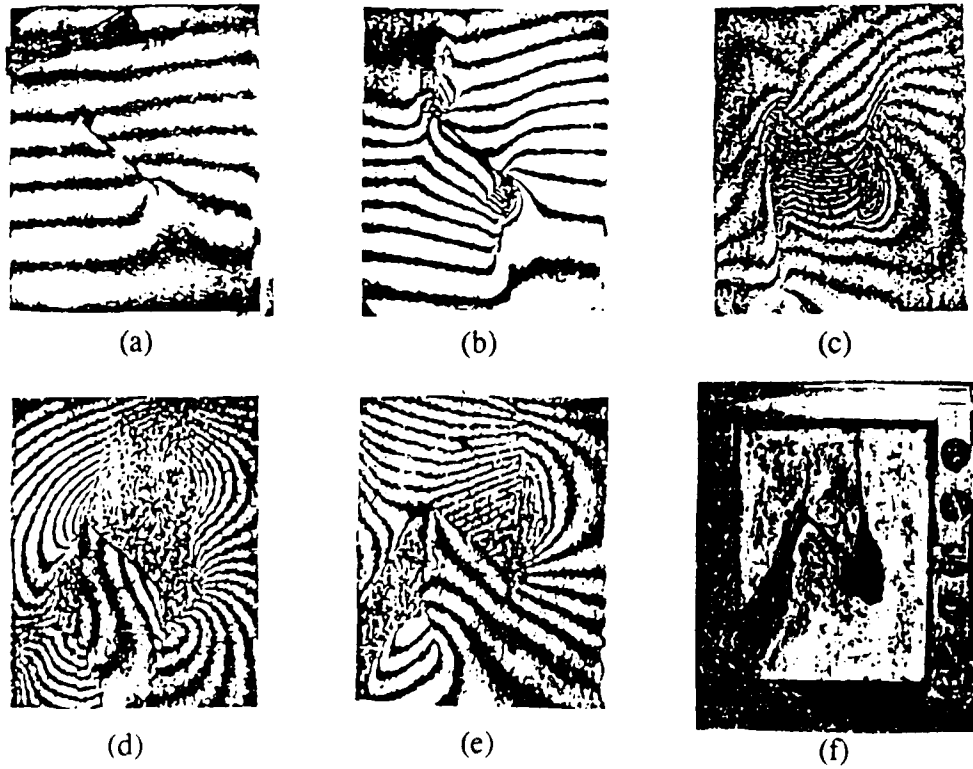
Figure 2.4   (a) - (e) Holograms taken during uniaxial compression of a *marble* specimen with a single flaw, (f) fractured *marble* specimen with a single pre-existing flaw, [from Wang et al., 1987].
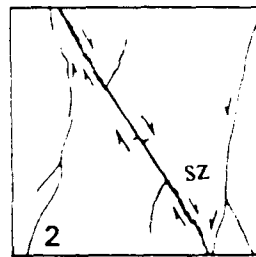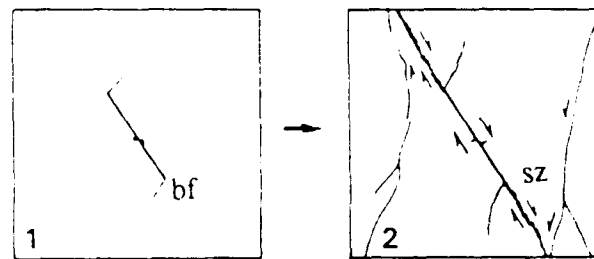
high porosity sandstone
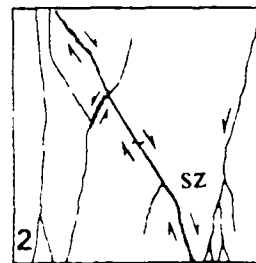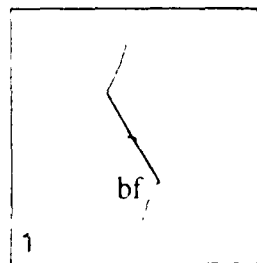
low porosity sandstone

Figure 2.5   Crack growth from a single-inclined flaw in low and high porosity
             sandstone specimens under uniaxial compression [from Petit and Barquins,
             1988].
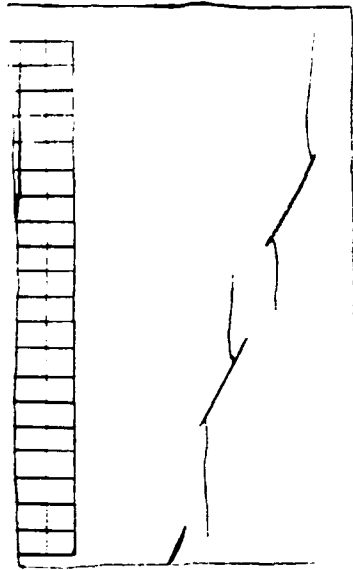
Figure 2.6   Crack growth from multiple, en-echelon flaws in a *glass* specimen under
uniaxial compression [from Brace and Byerlee, 1967].
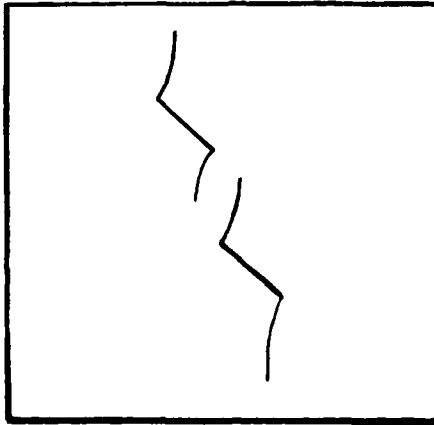
Figure 2.7   Crack growth from multiple flaws in a *PMMA* specimen under uniaxial compression [from Ingraffea and Heuze, 1980].
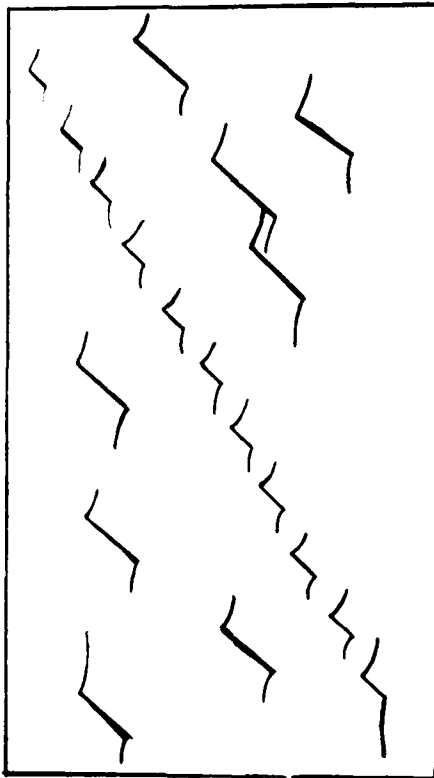
Figure 2.8   Crack growth from multiple flaws in a *CR39* specimen under uniaxial compression [from Horii and Nemat-Nasser, 1986].

34
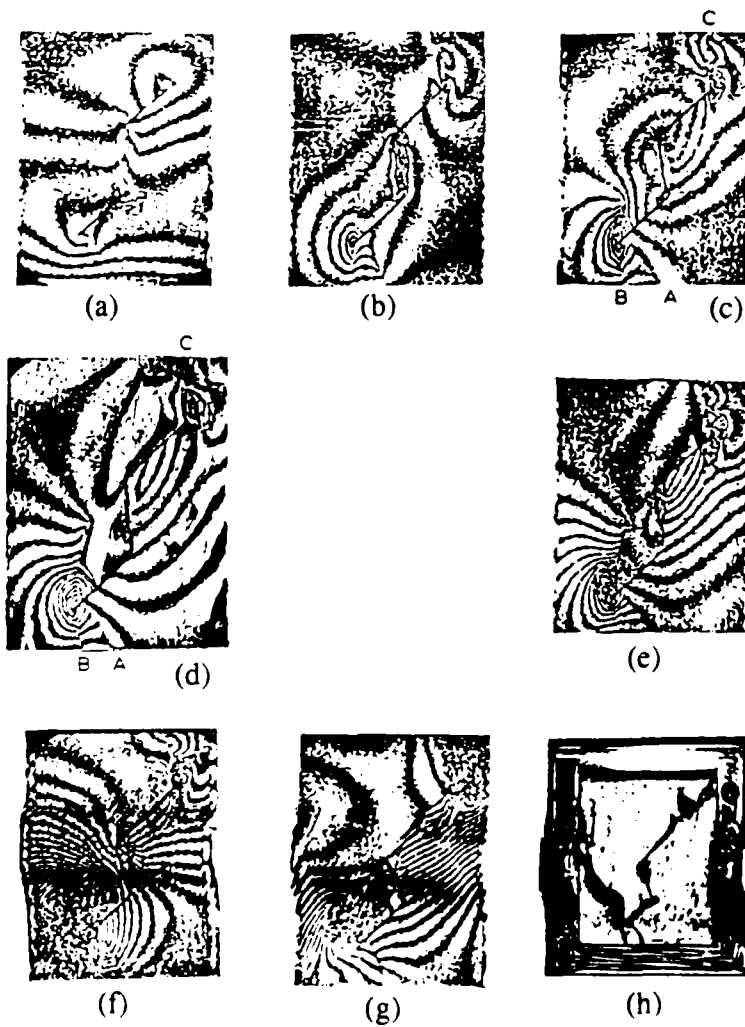
Figure 2.9   (a)-(g) Holograms taken during uniaxial compression of a *marble* specimen
with two pre-existing flaws, (h) fractured *marble* specimen with two pre-
existing flaws [from Wang et al., 1987].
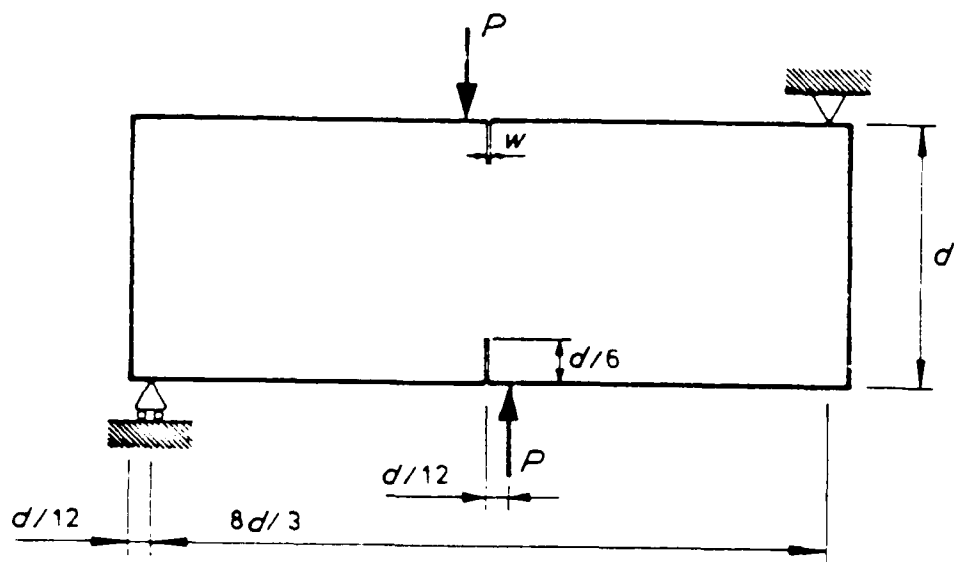
Figure 2.10   Geometry of a double-edge notched specimen, also shows support and load
application during testing [from Melin, 1989].
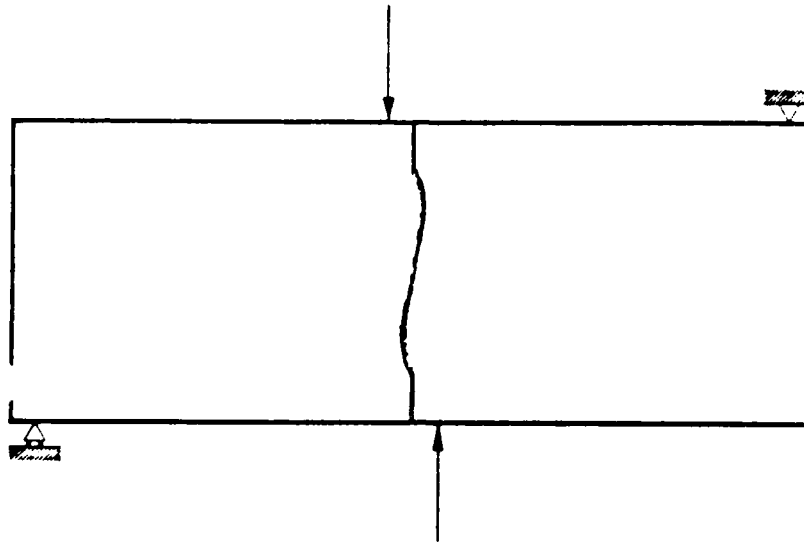
Figure 2.11   Crack growth in a double-edge notched *concrete* specimen [from Bazant and Pffeifer, 1986].
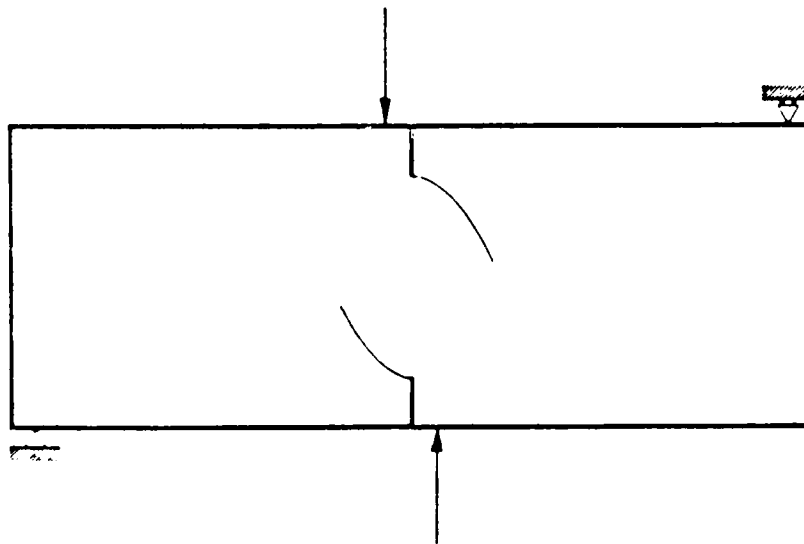
Figure 2.12   Crack growth in a double-edge notched *PMMA* specimen [from Melin, 1989].

37

2.3 Modelling of Crack Growth from Inclined Flaws

There are two general approaches to modelling crack growth: (1) the discrete crack approach and (2) the smeared crack approach. In the discrete crack approach (e.g. Ingraffea and Heuze, 1980; Chan, 1986; Annigeri, 1984), certain rules are applied to determine the <u>direction</u> and <u>load</u> at which crack extension occurs. These rules are called crack propagation criteria, examples of which are given in Table 2.1.

| *Table 2.1 Summary of Crack Propagation Criteria*		
Erdogan and Sih (1963)	Maximum Circumferential Stress Criterion	Crack propagates perpendicular to the direction of maximum tensile hoop stress.
Kipp and Sih (1974)	Minimum Strain Energy Density Criterion	Crack propagates along the direction of minimum strain energy density
Chang (1974)	Maximum Circumferential Strain Criterion	Crack propagates perpendicular to the direction of maximum tensile hoop strain.

Once the direction has been established using any one of these criteria, an actual discontinuity is attached to the existing crack. Subsequent crack extension is determined from the stress/strain energy/strain field at the tip of this added discontinuity.

In the smeared crack approach (e.g. Bazant and Oh, 1983; Rots et al., 1985), fracturing is modelled through a constitutive law that simulates the effects of material degradation (e.g. loss of stiffness and strain softening). Thus, if the constitutive law assumes that material degradation is dependent on tensile principal stresses, then the "fractured" zone would be expected to lie along the most highly stressed regions but would not necessarily be perpendicular to the tensile principal stresses as in the discrete crack approach.

Both the discrete crack and the smeared crack approaches have been applied to modelling mixed-mode crack growth in notched three-point and four-point bend specimens (Ingraffea and Panthaki, 1985; Swartz and Taha, 1990; Rots, 1986). However, only the discrete crack approach has been used to simulate crack growth from an inclined flaw in uniaxial compression (Ingraffea and Heuze, 1980).

Ingraffea and Heuze (1980) employed the finite element method and applied existing crack propagation criteria to successfully simulate the "primary" (wing) crack growth which they had observed in their experiments. The criteria which they used were: the maximum circumferential stress criterion (Erdogan and Sih, 1963) and the minimum strain energy density criterion (Kipp and Sih, 1975), see Table 2.1. A comparison of the wing crack paths are shown in Fig. 2.13. Note that the simulated paths follow the general shape of the observed primary (wing) crack, i.e., the simulated paths are curvilinear and eventually align with the applied compressive load. In explaining the growth of the secondary cracks, Ingraffea and Heuze looked at the stress field after the growth of the wing crack and found a region of tensile principal stresses around the location of the secondary crack (see Fig. 2.14). Since rock is weak in tension, they claimed that the secondary crack initiated within this tensile region, specifically at point A (Fig. 2.14) which is at a distance from the notch tip. Once initiated, secondary crack growth was driven by

the tensile principal stresses. The possibility of the secondary crack initiating from the point of compressive stress concentration at the notch tip was dismissed on the basis of photographic proof which, however, was not explicitly described.

Only Horii and Nemat-Nasser (1986) have attempted to analytically model crack propagation from multiple flaws in compression. Wing cracks were represented by a superposition of dislocations such that when boundary conditions were enforced, dislocation densities could be determined from a system of integral equations (for more details, refer to Horii and Nemat-Nasser, 1986). Interaction between adjacent flaws was approximated by the "method of pseudotractions" which Horii and Nemat-Nasser (1985) had also developed. This method, however, can only be used for an infinite line of parallel and equidistant flaws (see Fig. 2.15). Furthermore, since their experiments in CR39 only showed this kind of fracturing, wing crack growth alone was modelled and coalescence was not observed in their simulations.
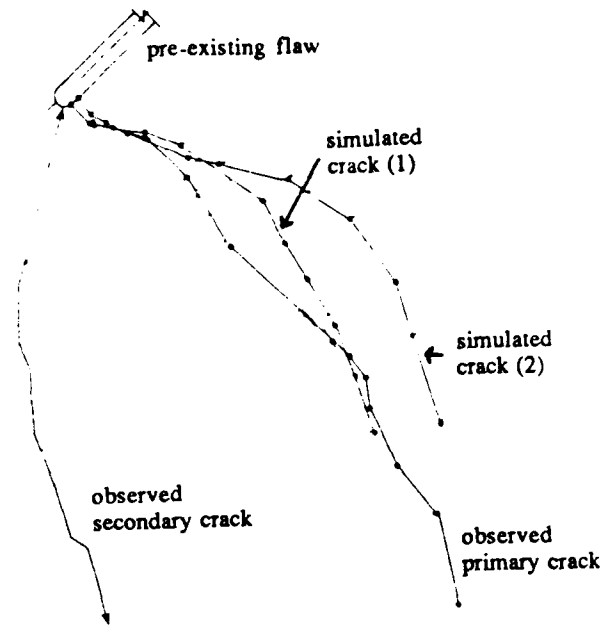
Figure 2.13   Comparison of observed and simulated primary cracks, simulated crack (1)
generated using Maximum Circumferential Stress Criterion, simulated crack
(2) generated by Minimum Strain Energy Density Criterion [from Ingraffea
and Heuze, 1980].
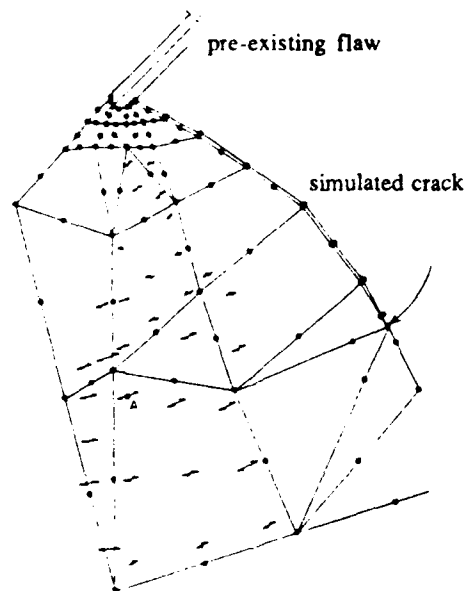
Figure 2.14   Tensile stress region (marked by arrows) near tips of a pre-existing flaw
with a primary crack. Secondary crack (see Fig. 2.13) thought to have
initiated at pt. A [from Ingraffea and Heuze, 1980].

41
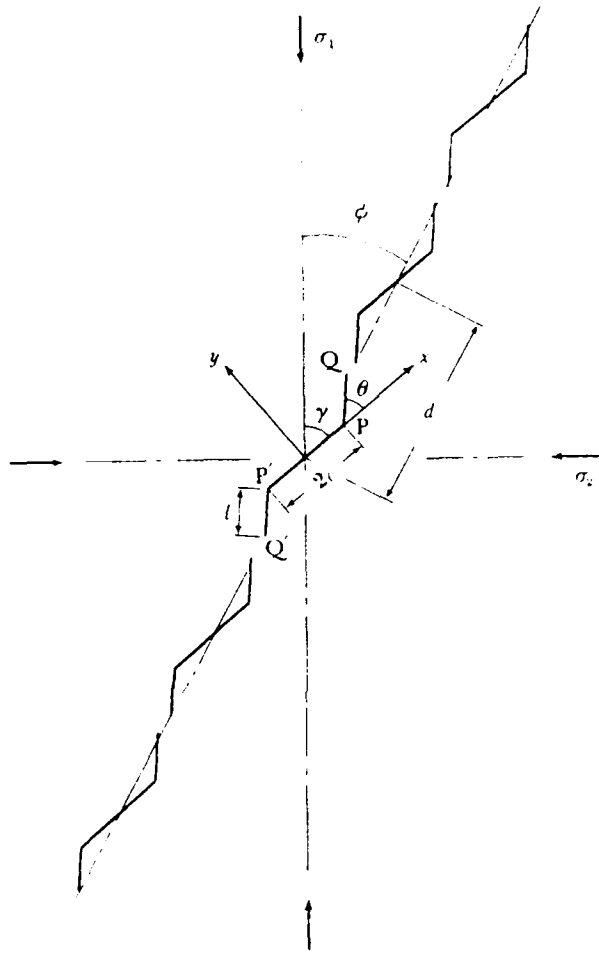
Figure 2.15   Shear fault formation through crack propagation from multiple pre-existing
flaws. P-P' and similar segments are pre-existing flaws. P'-Q' and P-Q
are wing cracks [from Horii and Nemat-Nasser, 1980].

Chapter 3
Experimental Procedures and Results

3.1 Introductory Remarks

As pointed out in Chapter 2, crack propagation criteria from fracture mechanics have been successfully used to simulate wing crack growth observed in compressed polymer blocks with pre-existing flaws (Horii and Nemat-Nasser, 1985; Ingraffea and Heuze, 1980). On the other hand, initial experiments on flawed gypsum blocks exhibited fracture behavior that was quite different from what was observed in polymer materials and predicted by fracture mechanics theory. In particular, coalescence occured through the growth of secondary cracks that were distinct from the wing cracks.

There was thus a discrepancy between different experimental and analytical studies, and a systematic investigation was necessary to determine coalescence mechanisms of flaws in rock-like materials. This chapter presents the experimental aspect of this investigation. It is subdivided into two main sections: Section 3.2 contains the procedures for specimen fabrication, loading and crack monitoring while Section 3.3 concentrates on the results of the experiments in form of photographs and loads corresponding to the various stages of the crack growth process. Some observations relating to the surface characteristics of the wing and secondary cracks are also included in Section 3.3.

3.2 Experimental Procedures

3.2.1 Model Material

The material chosen for this study is hydrated gypsum made from a mixture of Hydrocal B-11 (manufactured by US Gypsum Company), celite and water. The following mass proportions were used:

$$\frac{water}{gypsum} = 0.40 \qquad \frac{water}{celite} = 35.$$

Approximate tensile and compressive strengths were obtained from data collected by Nelson (1968) on a mix that is similar to what was used in this study:

$$\frac{water}{gypsum} = 0.45 \qquad \frac{water}{celite} = 32: \quad \text{Uniaxial Compressive Strength} = 23 \text{ MPa}$$

$$\text{Uniaxial Tensile Strength} = 2.3 \text{ MPa}.$$

Thus, this mix exhibits a compressive strength/tensile strength ratio of about 10.0, which is in the lower range of ratios for naturally occuring rocks.

Gypsum was selected as a model material primarily due to the ease with which flaws can be introduced into the specimens by pre-moulding them in. Other natural rocks were considered, but the costs for cutting harder rocks to simulate flaws would have restricted the number of flaw arrangements tested.

3.2.2 Specimen Geometry

The dimensions of the gypsum blocks are shown in Figure 3.1. The thickness of the blocks varied between 28 to 30 mm. The specimen length was set at twice the width in order to reduce end effects. Parallel flaws that were 12.7 mm (0.5") long and approximately 0.254 mm (0.01") wide were molded into the blocks such that the planes of the flaws were perpendicular to the 76.2 mm x 152.4 mm face of the the block. The model tests were thus limited to the investigation of the two-dimensional fracture patterns associated with these flaws. It was also assumed that the out-of-plane-stress had a minimal effect on the fracturing.

The geometric parameters which characterize the flaw arrangements, namely the flaw inclination angle and the ligament inclination angle, are shown in Fig. 3.2. The "external" and "internal" flaw tips are also identified in this figure since these terms will be used in the subsequent descriptions of crack growth (Section 3.3). The flaw arrangements could be classified according to non-overlapping and overlapping flaws (Fig. 3.3), where the non-overlapping flaws are characterized by a ligament inclination angle which is less than or equal to 90°, while the overlapping flaws have ligament inclination angles that are greater than 90°. The overlap is determined with respect to the direction of the applied uniaxial compression which coincides with the longer axis of the block (Fig. 3.3). Three inclination angles were used in the experiments: 30°, 45° and 60°. The non-overlapping geometries for each inclination angle are shown in Figs. 3.4 through 3.6 while the overlapping geometries for all three inclination angles are shown in Fig. 3.7. In the following discussion, the following convention for labelling flaw arrangments will be used: "X°-Y°" where X is the flaw inclination angle and Y is the ligament inclination angle. For example, "30°-45°" will refer to flaws inclined at 30° having a ligament that is inclined at 45° with respect to the horizontal.

All flaw arrangements had ligament lengt:.s of 12.7 mm which is equal to the length of the flaws.

3.2.3 Specimen Fabrication

The mold consisted of 4 stainless steel plates that were bolted together to form a 76.2mm x 152.4 mm block. These four plates were fastened onto a stainless steel base plate that was then clamped to a vibrating table. The inside surfaces of the four steel plates were wrapped in vinyl sheets to prevent bubbling at the steel shims which was observed when the mold was left unlined.[3.1]

The flaws were pre-molded by steel shims which were arranged in the mold to produce the desired flaw geometries. The shims were pulled out after the gypsum had hardened sufficiently. The step-by-step procedure for mold preparation was as follows (see Figure 3.8):

(1) A stiff piece of cardboard was cut to the dimensions of the block (76.2mm x 152.4 mm). This cardboard was wrapped in a vinyl sheet to prevent it from absorbing water from the pre-hardened gypsum. Two slits were cut into the cardboard, corresponding to the desired flaw arrangements.

[3.1] The bubbling could be related to an "electrolytic" current between the stainless steel plates and the non-stainless steel shims. It was oberved that the bubbling was significantly reduced when the steel plates where wrapped in self-adhesive vinyl shelf paper.

(2)   Filler gage steel stock with a width of 12.7 mm (0.5") and thickness of 0.10 mm (0.004") was cut into 50.8 mm (2") long pieces. Two of these steel shims were inserted into one of the slits in the cardboard. Two 0.004" shims were used rather than one 0.008" shim because it was more difficult to pull out one 0.008" shim than it was to pull out one 0.004" shim at a time. The shims were also greased to prevent the gypsum from adhering to the steel.

(3)   Two slits were cut into a shorter piece of 76.2 mm wide cardboard. This smaller piece was used to ensure that the shims were more or less perfectly vertical while the gypsum was being poured into the mold. (See Figure 3.8.)

(4)   The entire cardboard-steel shim assembly was then set into the stainless steel mold.

In order to have blocks with uniform properties, the mixing and curing process was strictly controlled. The mixing/curing/polishing procedure was as follows:

(1)   The water and celite were combined and mixed for 30 seconds.

(2)   The gypsum was gradually added to the water-celite mixture and blended for four minutes.

(3)   The mixture was immediately poured into the mold after blending. The mold was vibrated during and a few minutes after the mixture was poured into it in order to remove entrained bubbles.

(4)   When the mixture had sufficiently hardened, the blocks were taken out of the mold. The shims were pulled out prior to polishing and curing.

(5)   The blocks were allowed to air dry for about a day, after which the 76.2 x 152.4 mm surfaces were ground and polished. This made it easier for fractures to be observed during testing.

(6)   The mass of the blocks was measured before they were cured in an oven at 40°C. The blocks were occasionally weighed during the curing process. When the mass had stabilized indicating that all free water had been removed, the blocks were ready for testing.

3.2.4 Loading and Crack Monitoring Procedure

Specimens were uniaxially compressed in a computer-controlled INSTRON Model 1331 servohydraulic machine. The compression loading fixture had a ball and socket joint that compensated for specimen ends that were not perfectly parallel. Step loading was done under displacement control with ~0.05 - 0.15 mm per step[3.2] applied at a rate of 0.005 mm/sec. After each load step was applied and without unloading the specimen, the specimen surfaces were scanned for newly formed fractures through a low powered microscope (20x). The stereomicroscope had to be equipped with a stand that allowed one to view the specimen surface while translating along a vertical plane.

Early tests were performed with continuous loading and a video camera to record crack growth [Reyes et al. 1989]; however, the video equipment used did not have enough resolution to pick up some of the hair-line cracks. The crack growth at failure was also very rapid when the specimens were continuously loaded. It was found that some cracks, which were unobservable with the naked eye, were clearly visible with the microscope. Furthermore, step loading was adopted since compression crack growth is usually stable prior to final specimen failure and this allowed more time to scan the critical regions on the specimen surface. Step loading and crack growth monitoring through a microscope resulted in a better documentation of the crack growth sequence during uniaxial compression.

[3.2] Lower range is used when block is close to failure point.
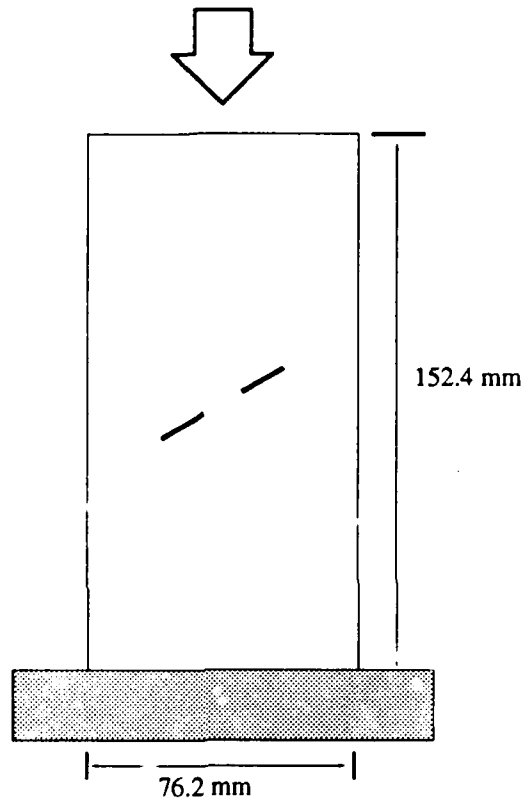
Figure 3.1   Geometry of prismatic specimens with pre-existing flaws.
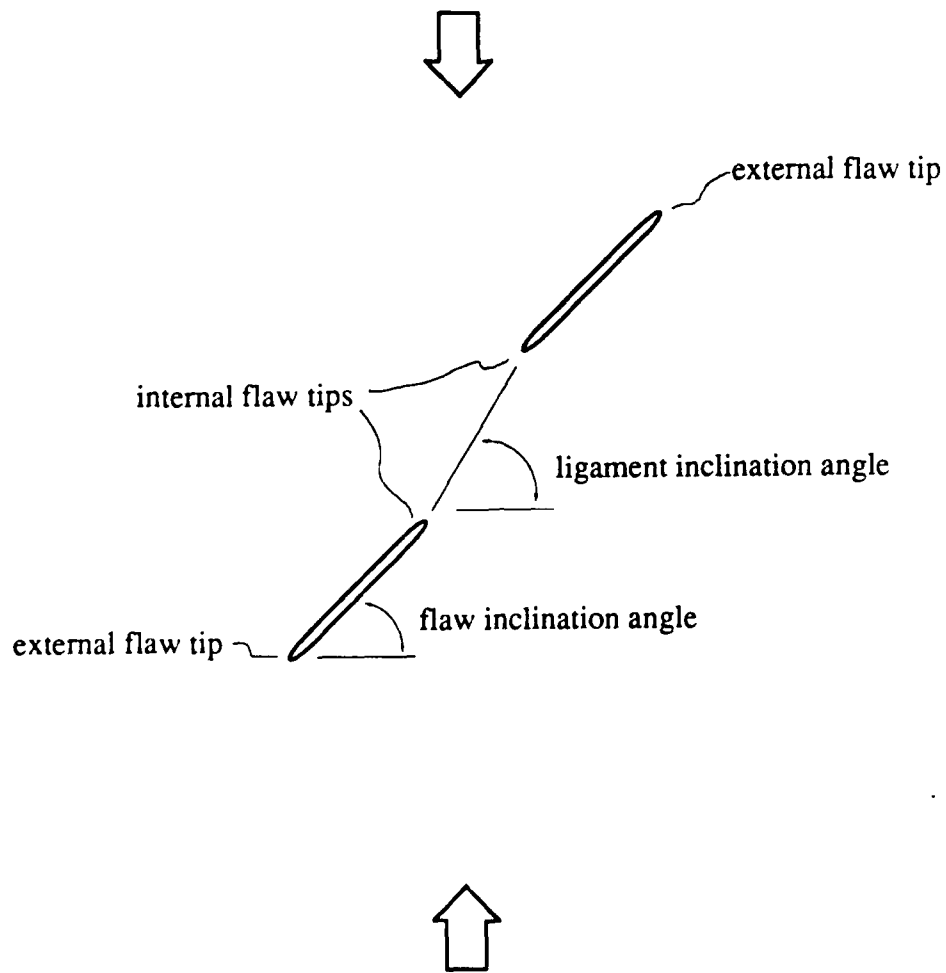
Figure 3.2   Parameters defining flaw geometry.
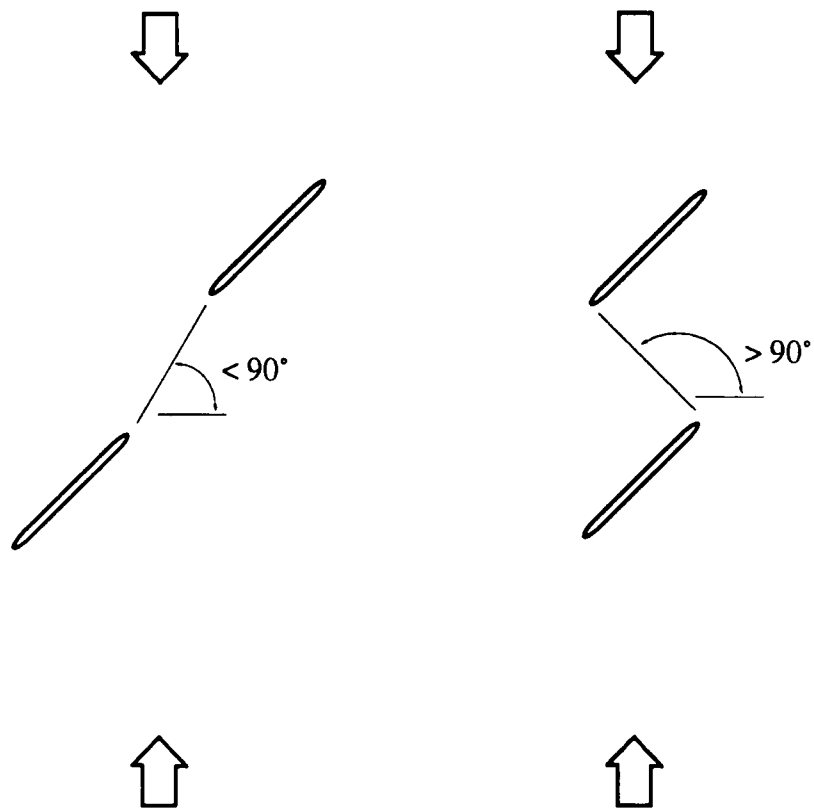
Figure 3.3   Non-overlapping (left) and overlapping (right) flaws.

L.I.A. = 90°

L.I.A. = 75°

L.I.A. = 60°

L.I.A. = 45°

L.I.A. = 30°
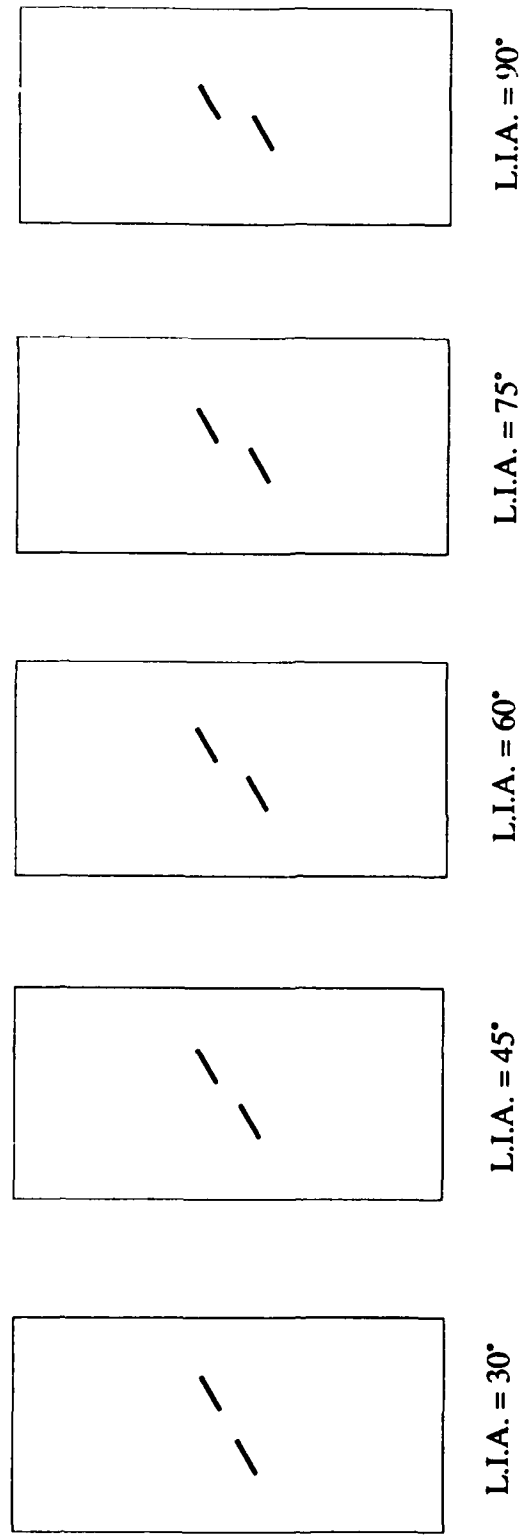
Figure 3.4   Non-overlapping flaw geometries, flaw inclination angle = 30°.
(L.I.A. = Ligament Inclination Angle)
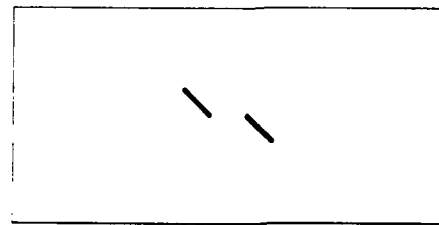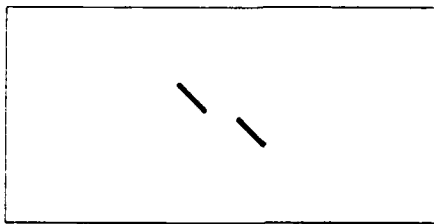
L.I.A. = 45°   L.I.A. = 60°   L.I.A. = 75°   L.I.A. = 90°
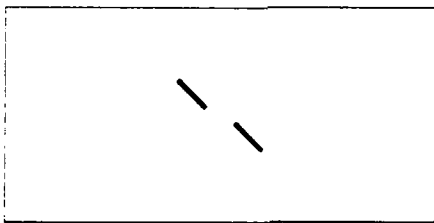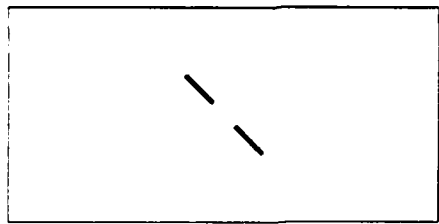
Figure 3.5   Non-overlapping flaw geometries, Flaw Inclination Angle = 45°.
(L.I.A. ≡ Ligament Inclination Angle)

54

L.I.A. = 45°   L.I.A. = 60°   L.I.A. = 75°   L.I.A. = 90°
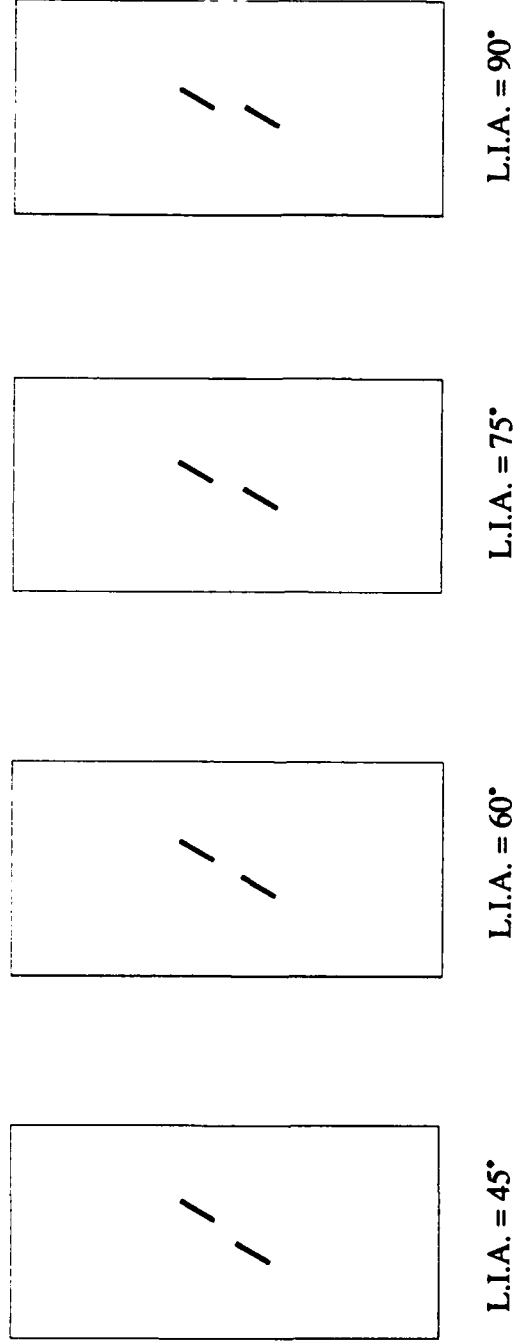
Figure 3.6   Non-overlapping flaw geometries, Flaw Inclination Angle = 60°.
(L.I.A. = Ligament Inclination Angle).

55

F.I.A. = 45°
L.I.A. = 135°

F.I.A. = 30°
L.I.A. = 135°

F.I.A. = 30
L.I.A. = 120°

F.I.A. = 60°
L.I.A. = 150°

F.I.A. = 60°
L.I.A. = 135°

F.I.A. = 60°
L.I.A. = 105°
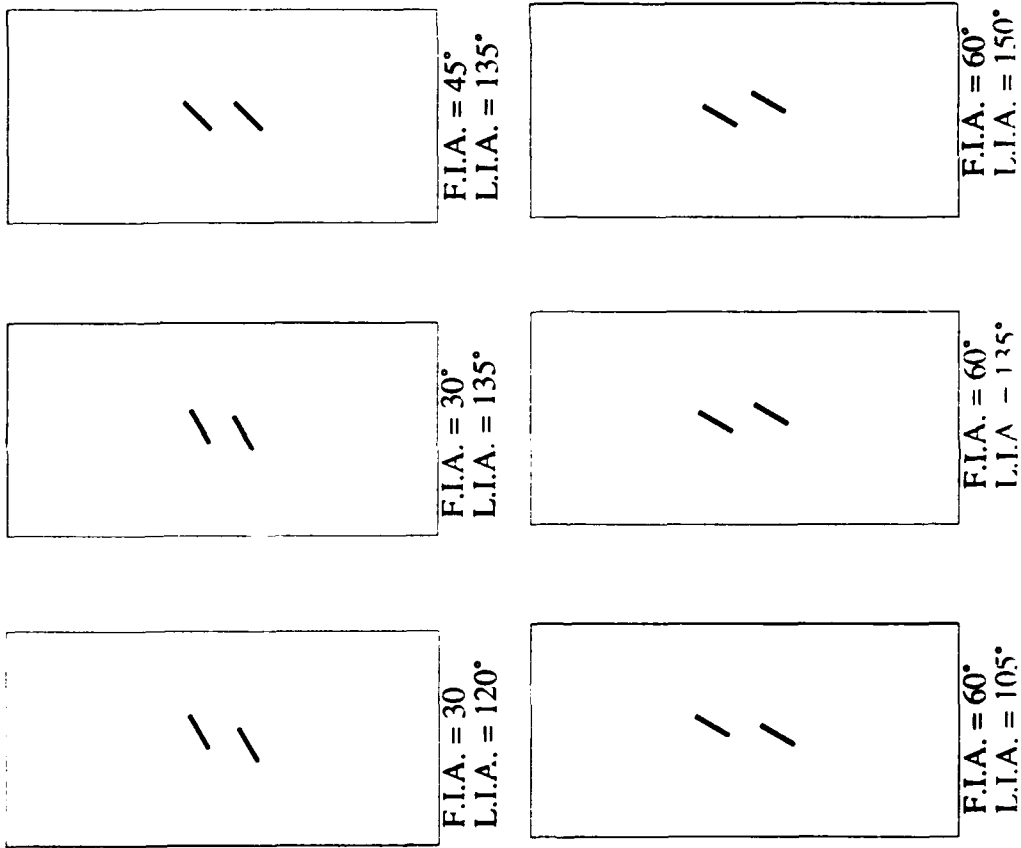
Figure 3.7   Overlapping flaw geometries.
(F.I.A. = Flaw Inclination Angle; L.I.A. = Ligament Inclination Angle)

56
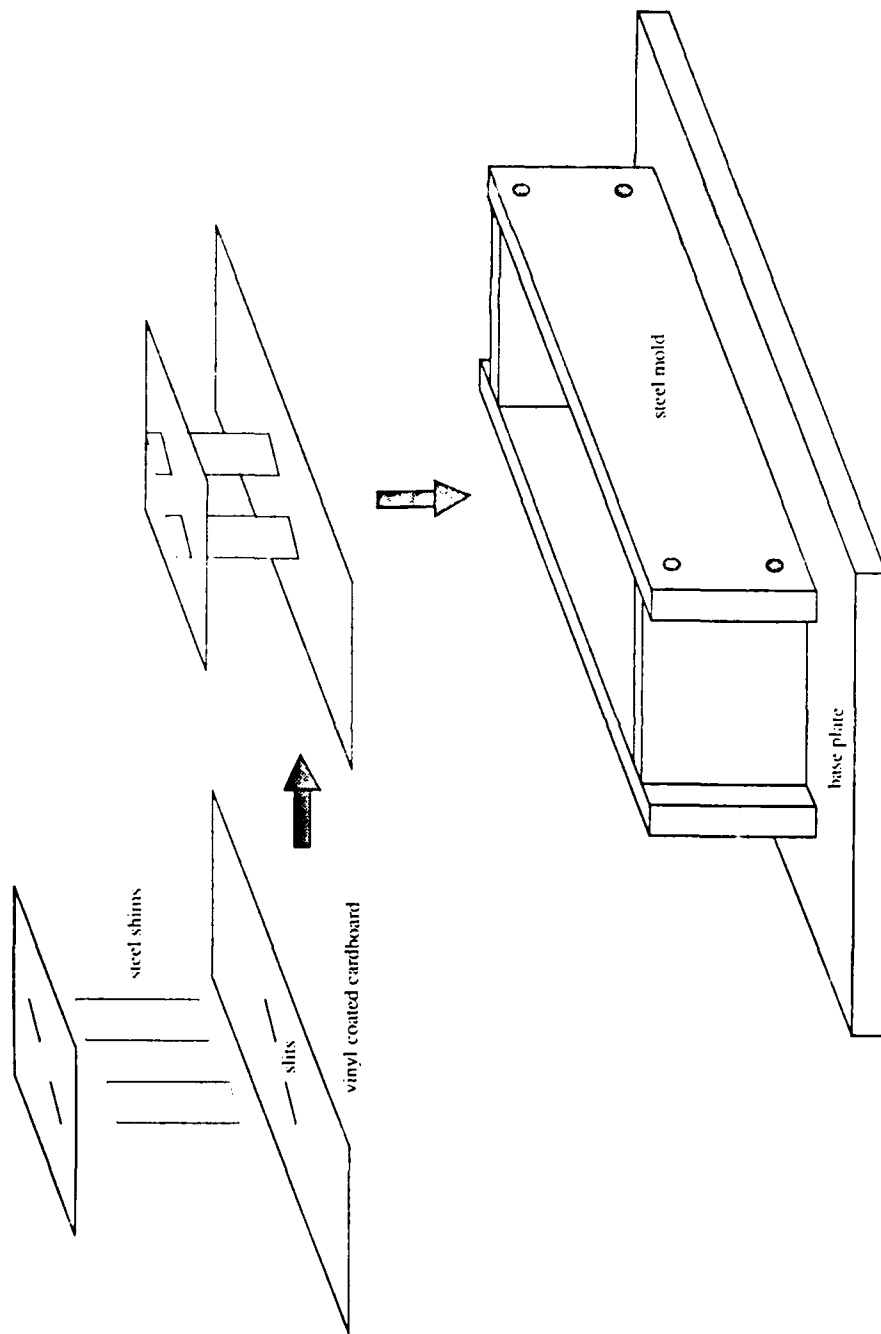
Figure 3.8   Mold preparation procedure.

57

3.3   Experimental Results

3.3.1   Sequence and Patterns of Fracture Growth

For all flaw geometries, wing cracks at the external and internal flaw tips appeared first. Subsequent fracture behavior was more dependent on the flaw geometry, particularly on whether the flaws were overlapping or not:

(1)   For all non-overlapping flaw geometries, the internal wing crack growth was arrested (i.e., wing cracks did not propagate through the entire specimen) and, with an increase in load, was followed by the appearance of secondary cracks. These secondary cracks caused coalescence between flaws in all non-overlapping arrangements except between 45°-45° and 30°-30° flaws (note that both are coplanar geometries).

(2)   For the overlapping flaw geometries, coalescence occured through wing crack growth for most cases. There was one case where it occured through secondary fracturing and two cases where coalescence did not take place at all prior to complete disintegration of the specimen.

Coalescence between Non-overlapping Flaws

Fracturing between non-overlapping flaws was very consistent in specimens with identical flaw geometries, i.e., tests were reproducible. Furthermore, except for two coplanar cases which will be described later, secondary crack growth resulted in the coalescence of the internal flaw tips.   Differences among coalescence mechanisms for various non-overlapping flaw geometries were found in: (1) measured loads at which coalescence occured (Section 3.3.2) and (2) surface characteristics of coalescence cracks (Section 3.3.3). However, since the sequence of crack propagation was generally the same

for all the non-overlapping geometries, only the crack growth processes for three representative flaw arrangements will be described, namely 30°-45°, 45°-90° and 60°-60° flaws.

Crack growth from 30°-45° flaws

Fig. 3.9 is a load-displacement curve obtained from uniaxial compression of a block with 30°-45° flaws. The loads at which the photographs in Figs. 3.10 through 3.12 were taken are also indicated on this graph. Figure 3.10(a) and (b), taken at an applied load of 47 kN (21 MPa) [3.3], show wing cracks propagating out of the flaw tips. The wing cracks were first observed at a load of 25 kN (11.2 MPa). Slight spalling or crushing is also evident in both Figs. 3.10(a) and (b) as marked by the arrows. At an applied load of 54 kN (24.1 kN), coalescence suddenly occured through the growth of a secondary crack that connected the internal flaw tips (see Fig. 3.11). Note that the previously observed crushing/spalling became a part of this coalescence crack; however, the coalescence crack propagated so rapidly that it was impossible to establish whether it propagated from the center of the ligament or from the flaw tips. Fig. 3.12 is an expanded view of the flaws after coalescence. The external wing cracks had opened and extended at this point. Whether the external wing cracks extended before or after coalescence could not be established due to the rapidity of crack growth. However, it seems likely that the coalescence crack preceded the opening and extension of the external wing cracks. What

_____

[3.3] In the subsequent discussion, the applied force will be given followed by the equivalent applied traction enclosed in parentheses. The applied traction is equal to the applied force divided by the specimen's loading surface.

could have happened was the following: (1) the linkage of the flaws resulted in a longer "effective flaw", (2) the increase in "effective flaw" length increased the relative sliding displacements of the flaw surfaces, (3) the increase in relative sliding displacements caused the external wing cracks to open, (4) the opening of the wing cracks then increased the singularity at the wing crack tips and drove the wing cracks to lengthen.
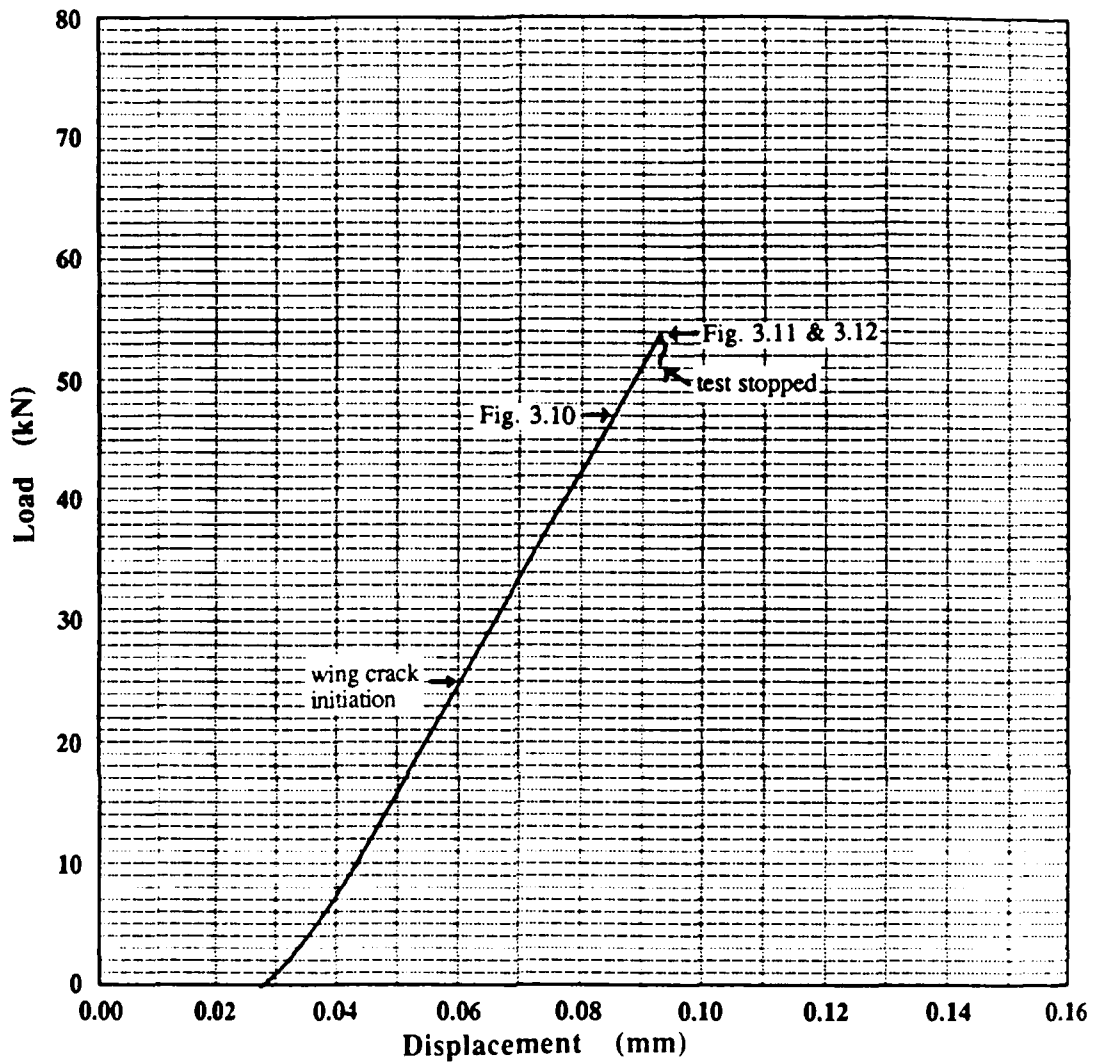
Figure 3.9   Load-displacement curve taken from uniaxial compression of a gypsum block with 30°-45° flaws. Loads at which subsequent photos were taken are marked on the graph.
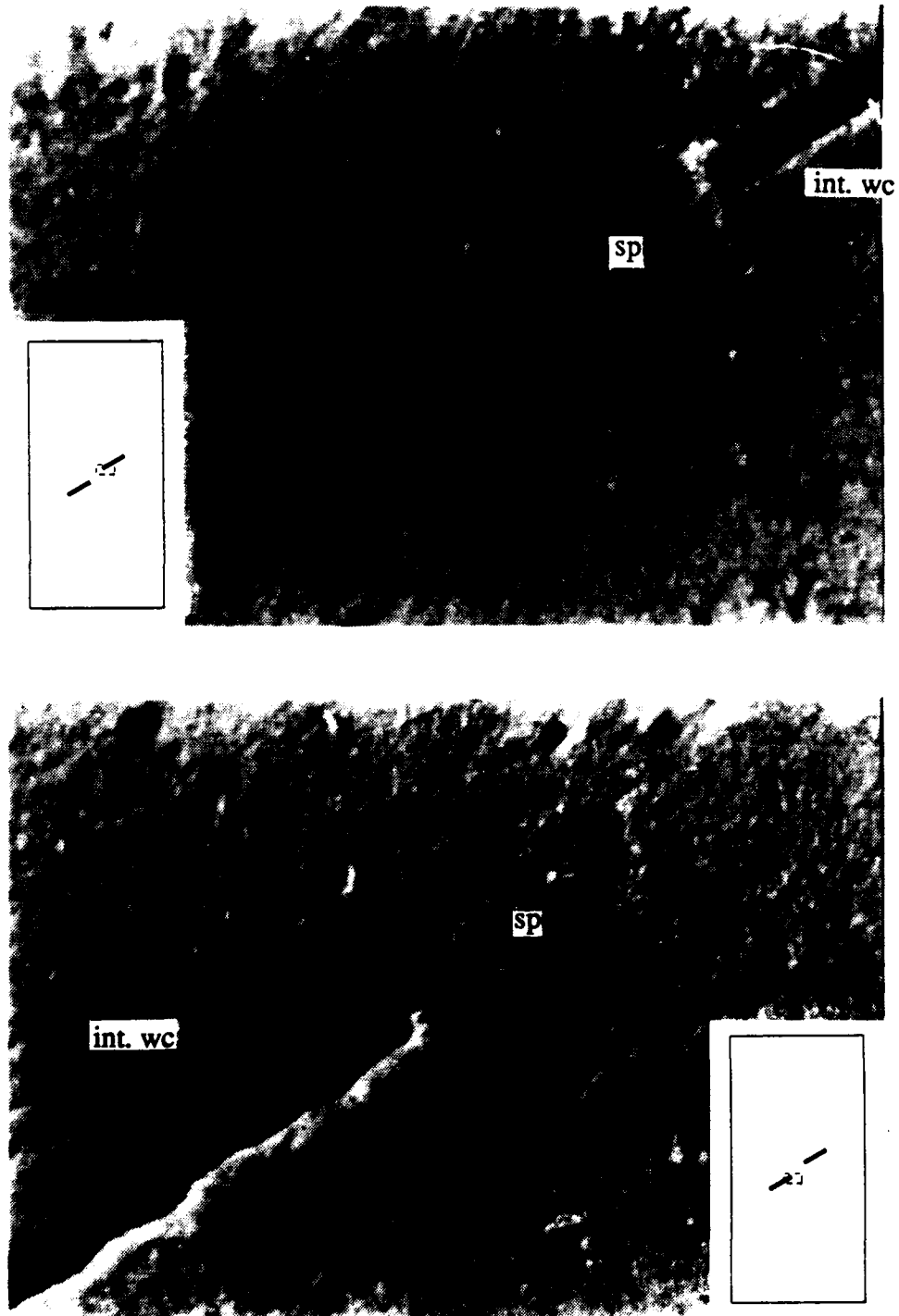
Figure 3.10   (a) and (b) Wing crack growth and spalling from internal 30°-45° flaw tips
[applied load = 47kN].
sp = spalling; int. wc = internal wing crack.
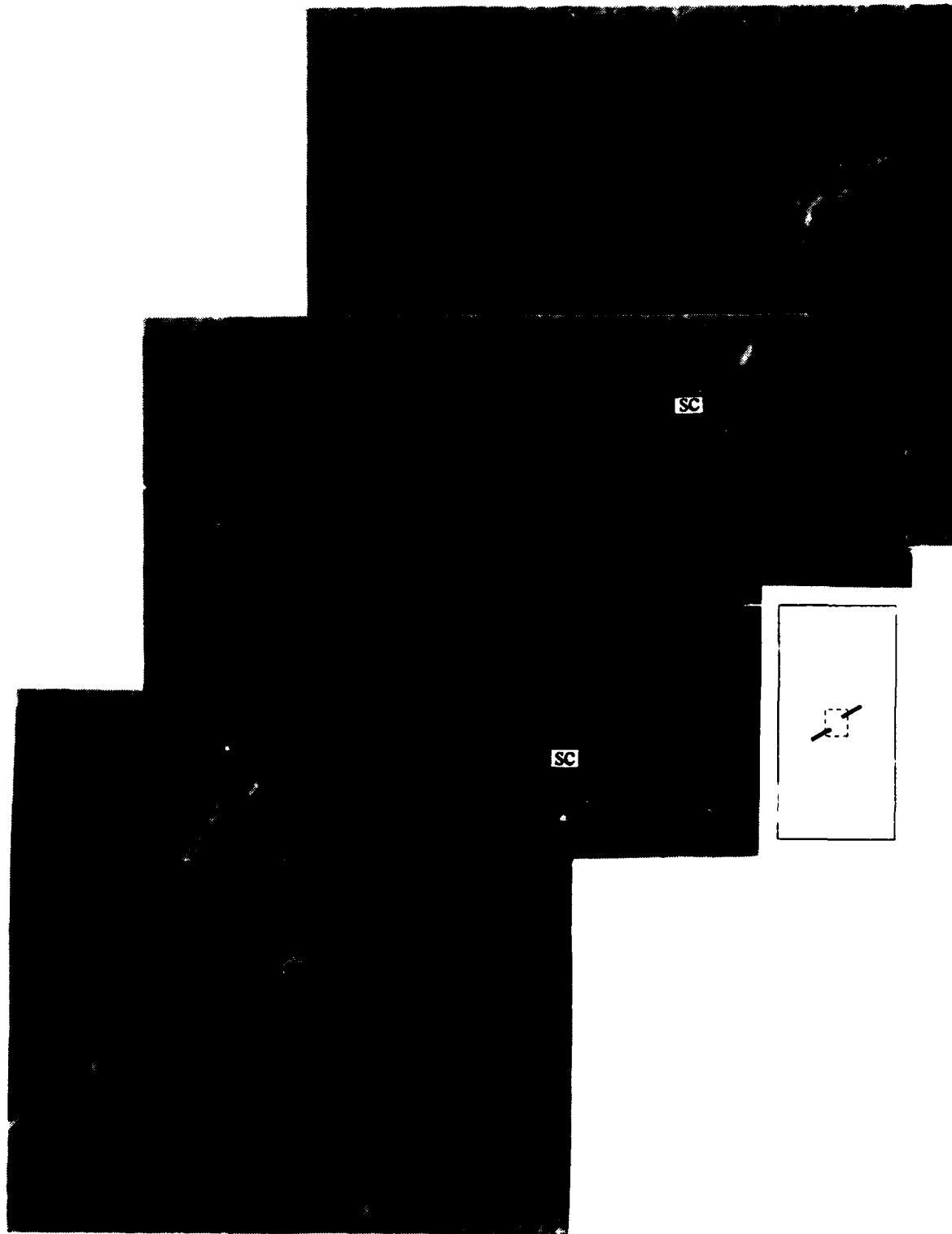
Figure 3.11   Secondary crack growth resulting in coalescence between internal 30°-45° flaw tips [applied load = 54kN].
sc = secondary crack.
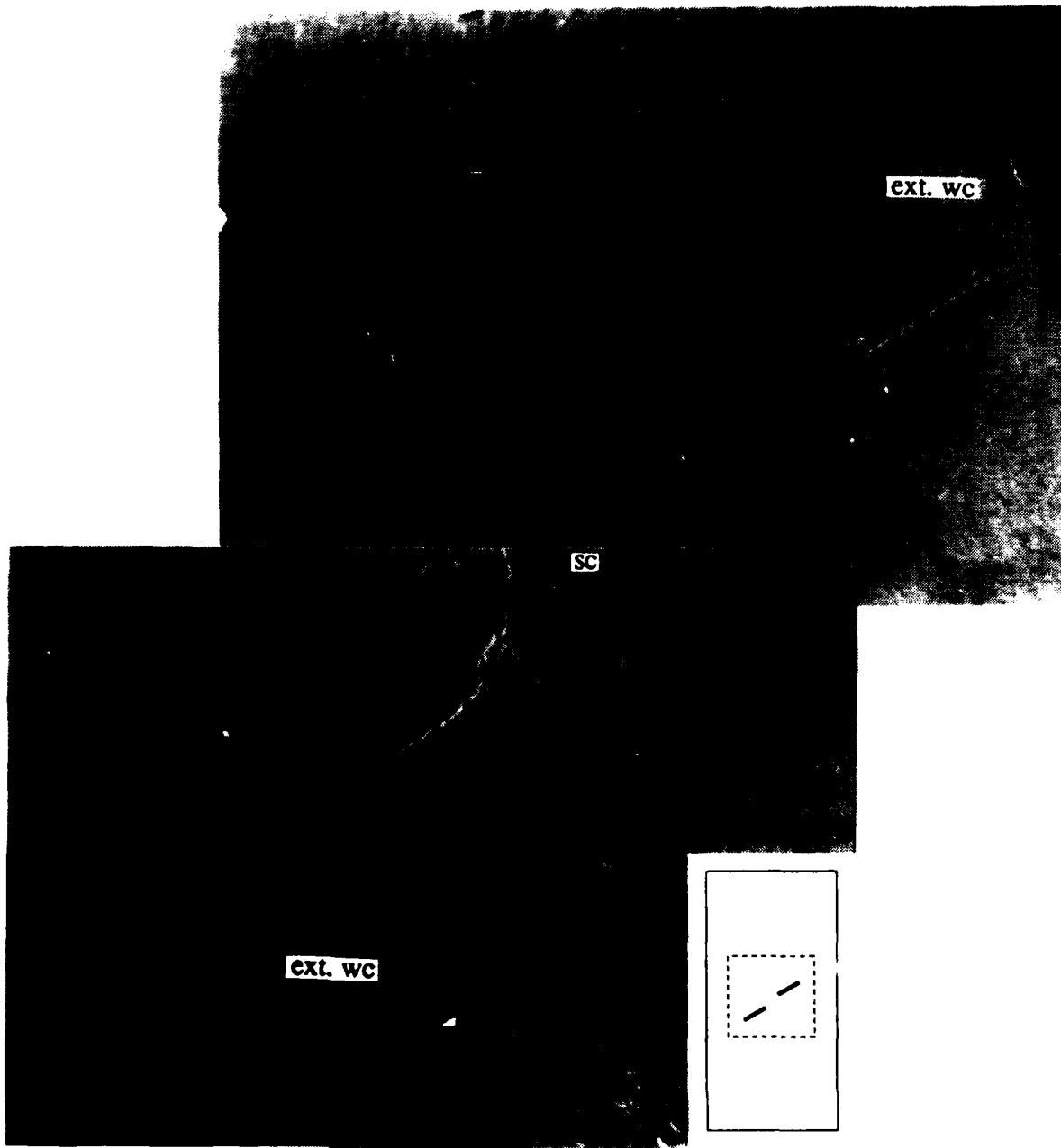
Figure 3.12   Expanded view of 30°-45° flaws after coalescence. Note open and extended
external wing cracks [applied load = 54kN].
sc = secondary cracks; ext. wc = external wing crack.

Crack growth from 45°-90° flaws

Figure 3.13 is a load-displacement curve obtained from uniaxial compression of a block with 45°-90° flaws. The loads at which the photographs in Figures 3.14 through 3.18 were taken are also indicated on this graph. In this test, the wing cracks were first observed at an applied load of 27 kN (12.5 MPa). Wing crack growth with slight spalling at the internal flaw tips are shown in Figs. 3.14 taken at applied loads of 37 kN (17.1 MPa). At a load of 50 kN (23.2 MPa), the external wing cracks [Figs. 3.15(a) and (c)] were longer than the internal wing cracks [Figs. 3.15(b)], i.e., the internal wing cracks were arrested upon reaching the level of the adjacent flaw tip. At a load of 51 kN (26.4 MPa), spalling increased at the internal flaw tips (see Fig. 3.16) and finally, at a load of 61 kN (28.3 MPa), coalescence occured through the sudden growth of a crack in the zone between the internal wing cracks (see Fig. 3.17). An expanded view of the final fracture pattern after coalescence is shown in Fig. 3.18. As in the 30°-45° case, the external wing cracks opened and extended while the internal wing cracks closed after coalescence.
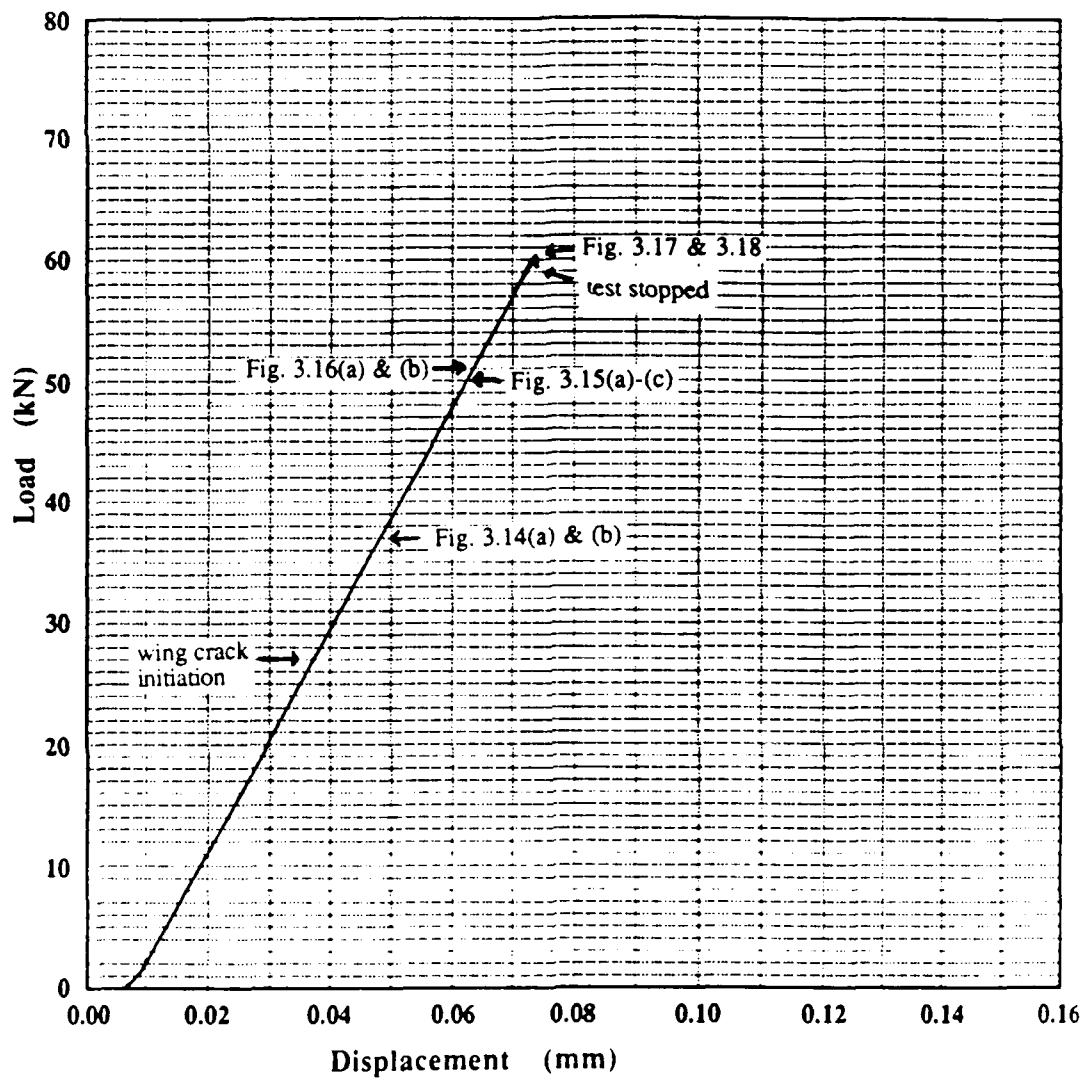
Figure 3.13   Load-displacement curve taken from uniaxial compression of a gypsum block with 45°-90° flaws. Loads at which subsequent photos were taken are marked on the graph.

66
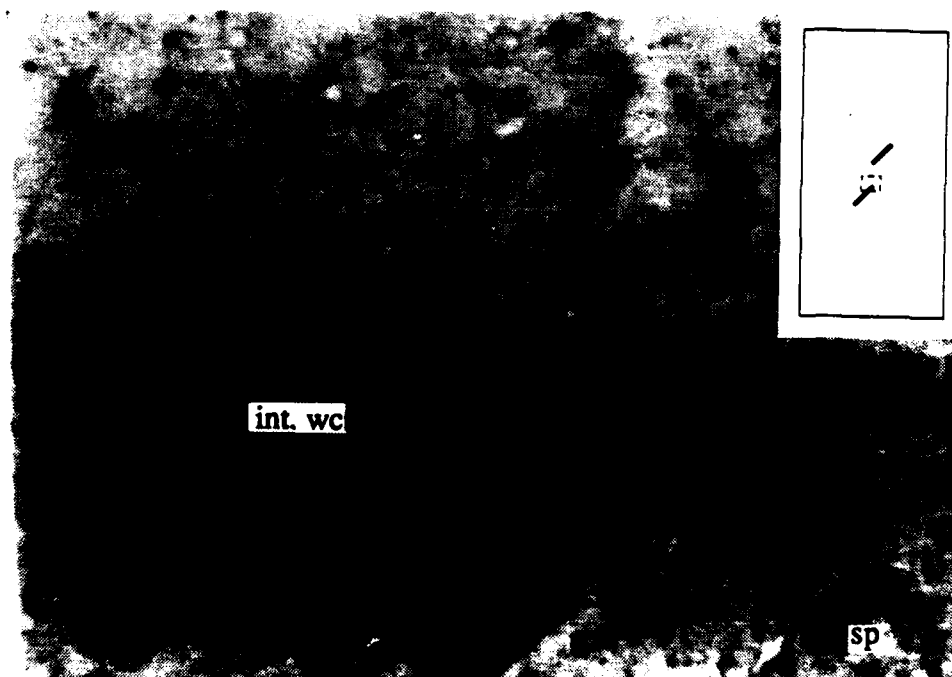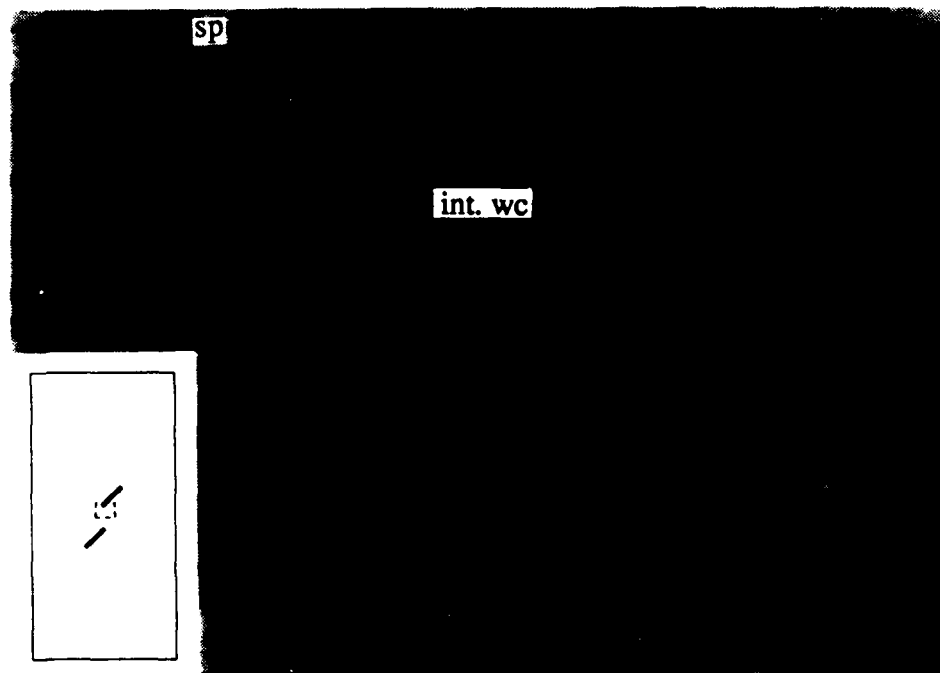
Figure 3.14   Wing crack and spalling from internal 45°-90° flaw tips [applied load = 37kN]
sp = spalling; int. wc = internal wing cracks.
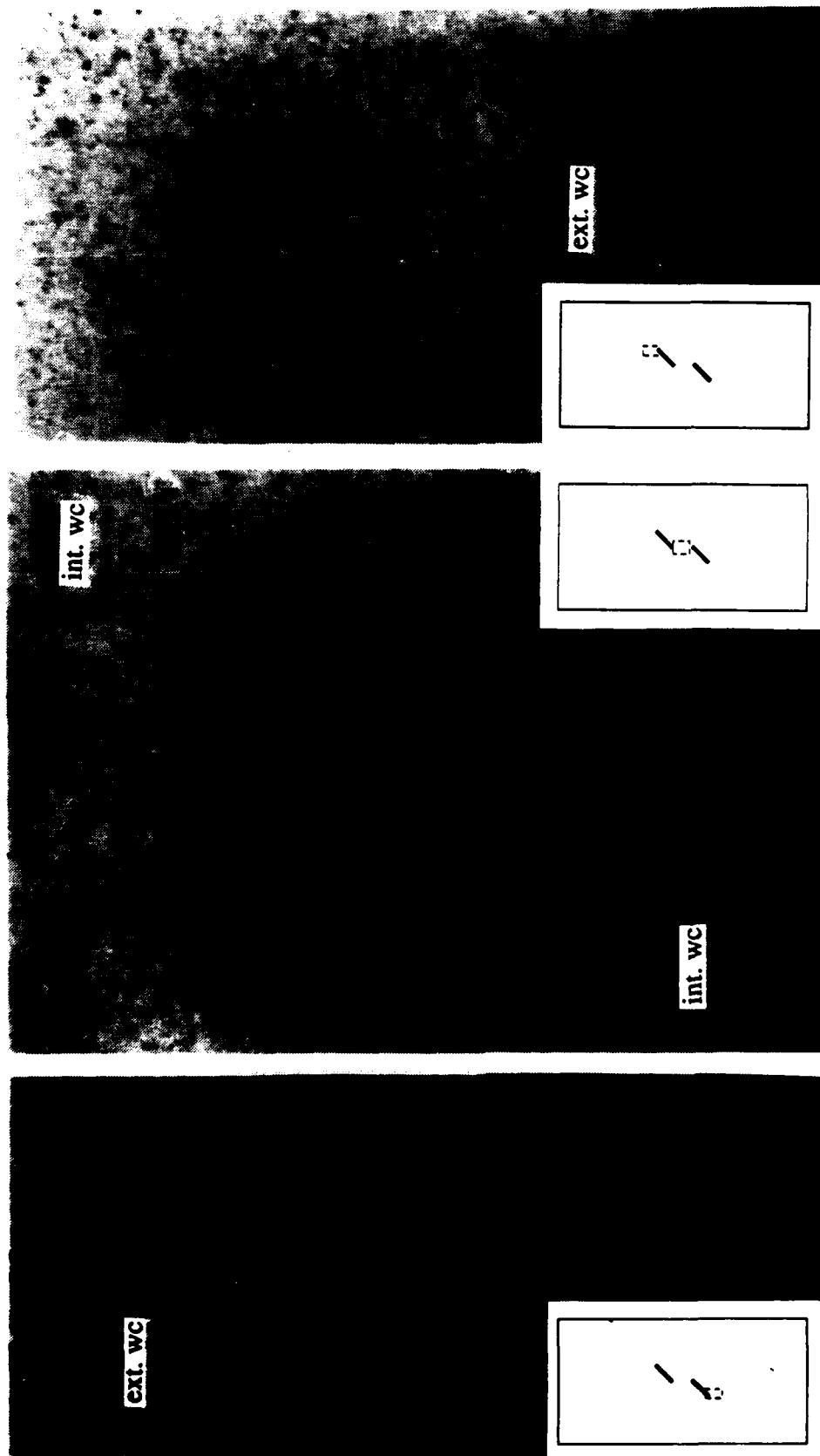
Figure 3.15 Extended external wing cracks (a,c) and arrested internal wing cracks (b) growing from 45°-90° flaws [applied load = 50kN]. int. wc = internal wing crack; ext. wc = external wing crack
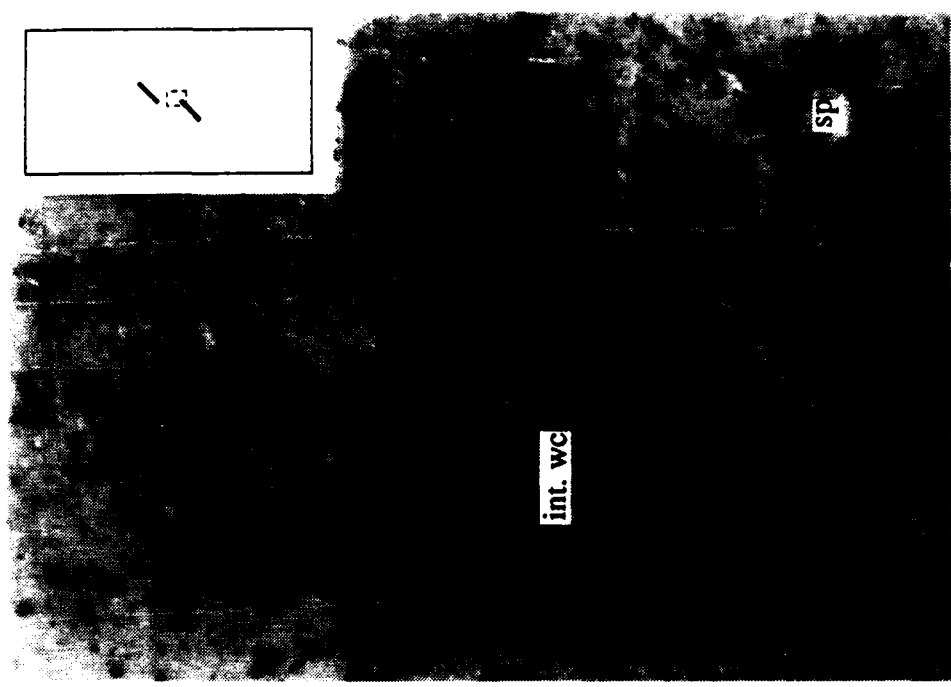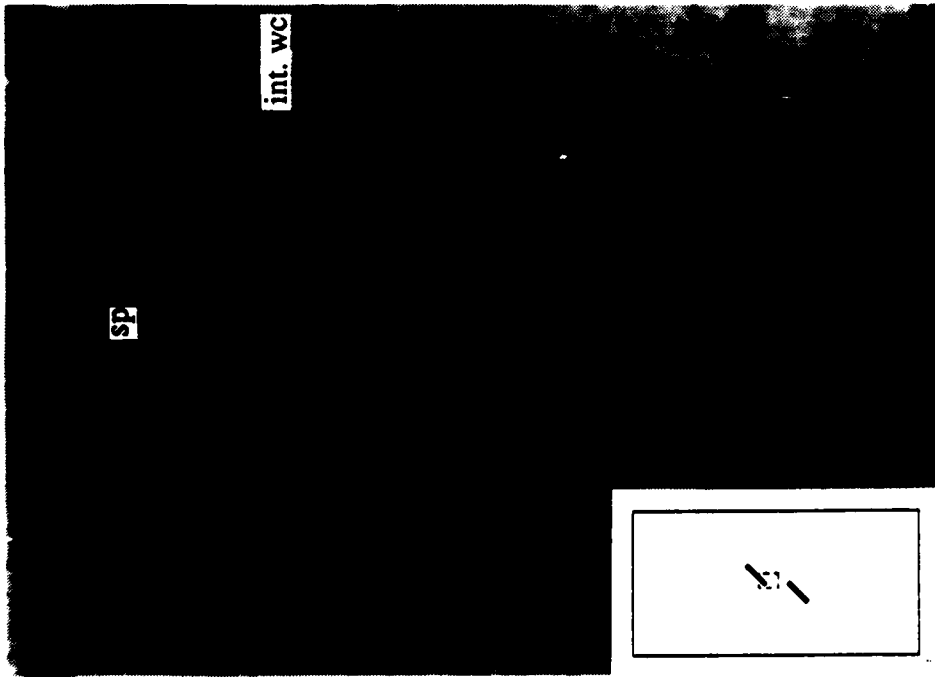
Figure 3.16   Wing crack growth and spalling from internal 45°-90° flaw tips, compare
with Fig. 3.14 [applied load = 51kN]
int. wc = internal wing crack; sp = spalling
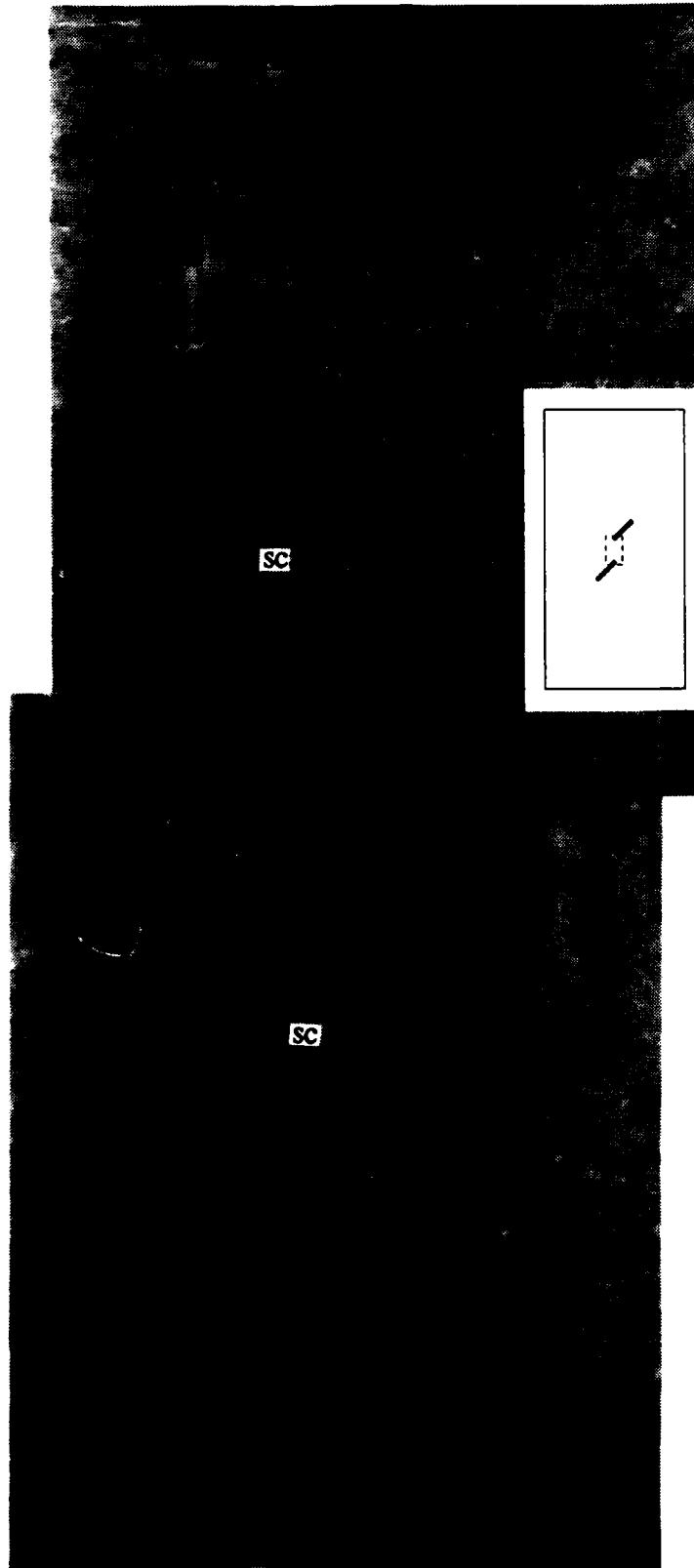
Figure 3.17   Secondary crack growth resulting in coalescence between internal 45°-90° flaw tips [applied load = 61kN].
sc = secondary crack

Figure 3.18   Expanded view of 45°-90° flaws after coalescence. Note open and extended external wing cracks [applied load = 61kN].
sc = secondary crack, ext. wc = external wing crack

Crack growth from 60°-60° flaws

Figure 3.19 is a load-displacement curve obtained from uniaxial compression of a block with 60°-60° flaws. The loads at which the photographs in Figure 3.20 through 3.22[3.4] were taken are also indicated on this graph. Wing cracks were first visible at an applied load of 56 kN (25.3 MPa). At 70 kN (31.7 MPa), spalling or possibly secondary cracking initiated from the internal tips (Fig. 3.20) but did not "connect" until the applied load was increased to 73 kN (33 MPa), see Fig. 3.21. This test was one of the few cases where coalescence clearly intiated from the flaw tips. An expanded view of the flaws is shown in Fig. 3.22. Though not visible in the photograph, the external wing cracks had opened and extended after coalescence.

[3.4] In this test, red ink was used to mark the observed cracks.
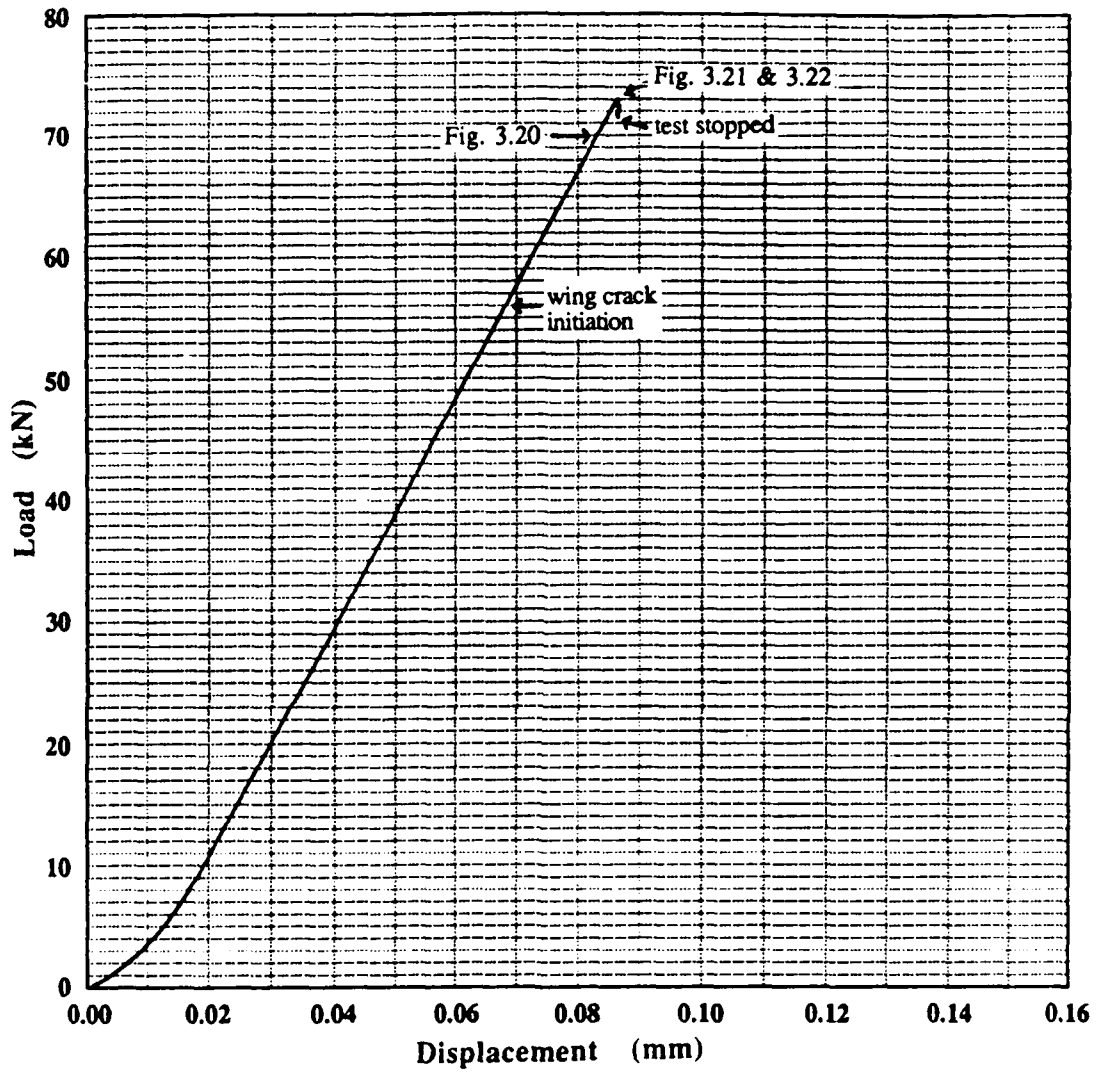
Figure 3.19   Load-displacement curve taken from uniaxial compression of a gypsum block with 60°-60° flaws. Loads at which subsequent photos were taken are marked on the graph.

73

Figure 3.20   Spalling or secondary crack growth from internal 60°-60° flaw tips [applied load = 70kN].
sp = spalling

Figure 3.21   Coalescence between internal 60°-60° flaw tips [applied load = 73kN].
sc = secondary crack
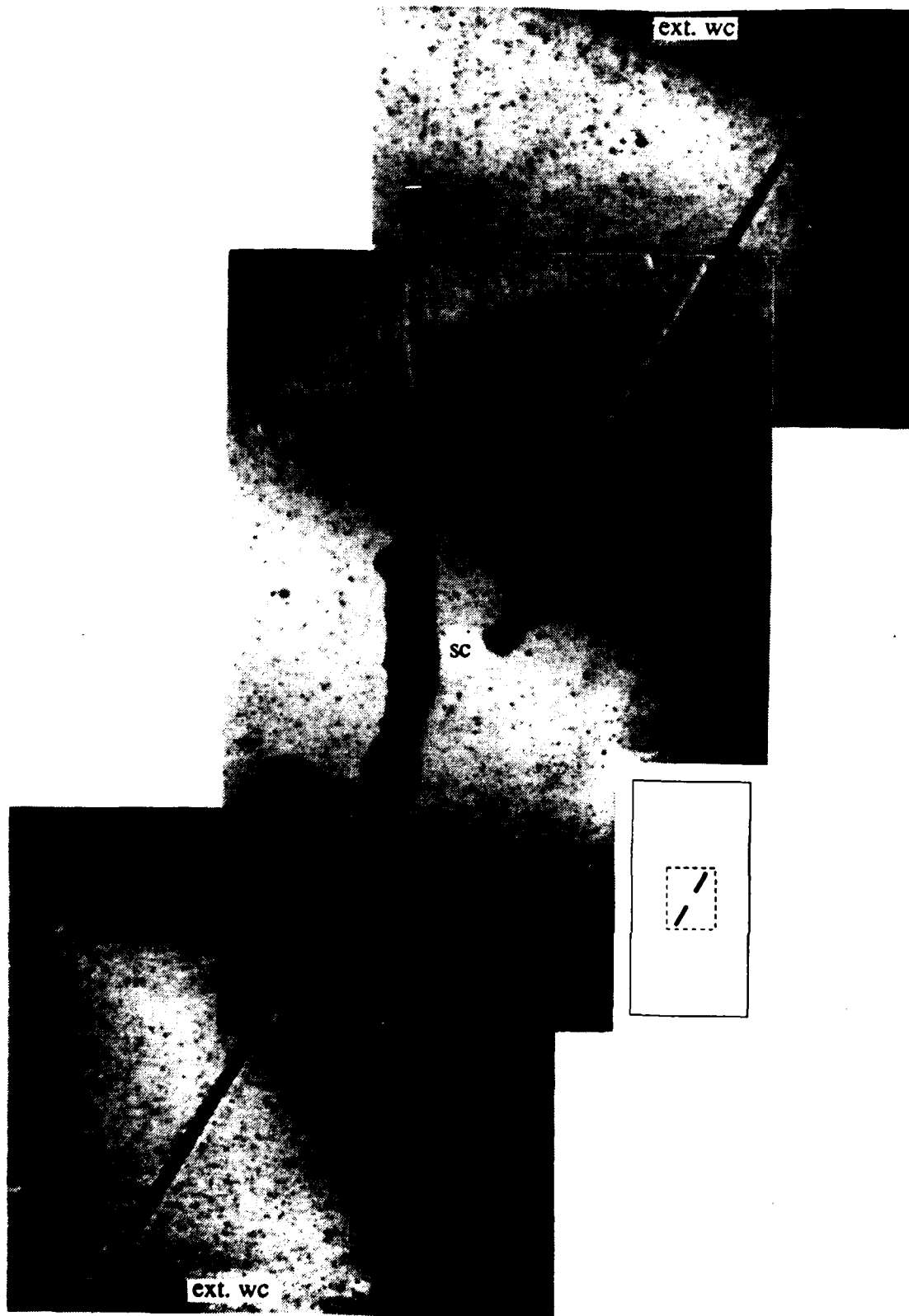
Figure 3.22   Expanded view of 60°-60° flaws after coalescence, external wing cracks
opened and extended at this load [applied load = 73kN].
sc = secondary crack, ext. wc = external wing crack

Crack growth from flaws with other non-overlapping geometries

Coalescence crack patterns for other non-overlapping flaw geometries are shown in Figs. 3.23 through 3.28. Fig. 3.23 shows the coalescence crack for a specimen with 30°-45° flaws, identical to the one shown in Fig. 3.11 (also shows 30°-45° flaws). Figs. 3.24 and 3.25 are photographs of coalescence cracks for two identical specimens with 30°-75° cracks. The similarity between the coalescence cracks in Figs. 3.24 and 3.25 is rather striking; both are oriented parallel to the applied vertical compressive load. Figs. 3.26 and 3.27 show coalescence cracks for identical specimens with 45°-60° flaws. One can observe that the coalescence cracks between 45°-60° flaws consist of "shearing" and "tensile" segments, as indicated in the figures. Fig. 3.28 shows the coalescence crack between 60°-45° flaws. It is interesting to see that coalescence took place for this geometry even though the flaws were left-stepping (see schematic drawing on figure) rather than right stepping like the other geometries.

In most of the specimens tested, the external wing cracks did not propagate all the way to the top and bottom edges of the specimens. These specimens remained intact after they were unloaded, and in order to inspect the surface of the coalescence cracks (see Sec. 3.3.3 for a discussion of surface characteristics), they had to be cut as shown in Fig. 3.29.

This process of cutting was useful for verifying or refuting observed coalescence between pre-existing flaws. For example, Fig. 3.30 shows an "apparent" coalescence crack that connected the internal tips of two 45°-45° flaws at an applied load of 64.4 kN (29 MPa). When this crack appeared, the specimen was unloaded because it was thought that linkage had already taken place. However, upon cutting this specimen, it could not be pulled apart along the ligament. This clearly indicated that coalescence had not occured and that the "apparent" coalescence crack was actually an initial stage of spalling within the ligament area.

Fig. 3.30 also shows that the external wing cracks remained closed even after the appearance of the "apparent" coalescence crack. Recalling the earlier explanation regarding the opening of external wing cracks as an effect of coalescence, this observation is not at all surprising since the 45°-45° flaws were not connected at the time the photo was taken. It was also observed from the load-displacement curves in Fig. 3.9, 3.13 and 3.19 that, under displacement control, coalescence was always accompanied by a drop in the load. Such a load drop was not present in the load-displacement curve of the specimen with 45°-45° flaws. This is also consistent with the fact that coalescence did not take place between the flaws in this specimen.

The "real" coalescence behavior of 45°-45° flaws could not be obtained from the specimen shown in Fig. 3.30. Unfortunately, the second specimen with 45°-45° flaws disintegrated completely when the testing machine malfunctioned and overloaded the block. Hence, the fracture coalescence behavior for 45°-45° flaws could not be established by the test series performed in this study.

The fracture behavior of 30°-30° flaws was also different from the rest of the non-overlapping flaw geometries. A specimen with 30°-30° flaws is shown in Fig. 3.31 at an applied load of 64 kN (29 MPa). Substantial spalling can be seen at the flaw tips, and when failure occured at 67 kN (30 MPa), the secondary cracks did not connect the flaw tips (see Fig. 3.32) as they did in the other flaw geometries. The second specimen with 30°-30° flaws was loaded until spalling similar to that shown in Fig. 3.31 occured. The specimen was then unloaded, and an attempt to section the ligament area was made. It was thought that sections taken immediately prior to failure would show some microstructural evidence of progressive fracturing. However, gypsum has a strong tendency to pulverize and suffered too much disturbance after the sectioning process. Thus, no evidence of pre-fracturing could be observed.

78

Figure 3.23   Secondary crack growth resulting in coalescence between 30°-45° flaws,
               compare with Fig. 3.11.
               sc = secondary crack
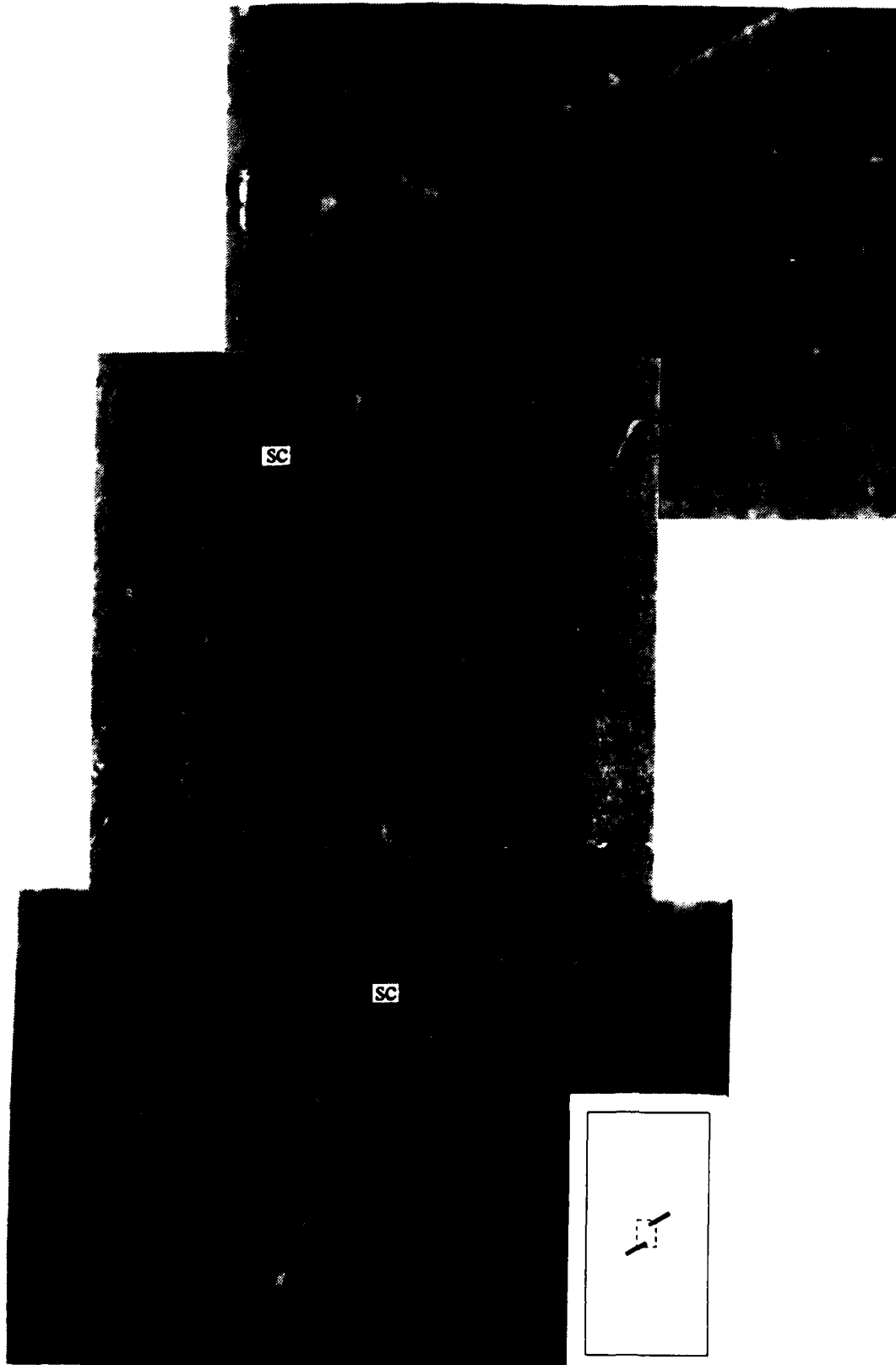
Figure 3.24   Secondary crack growth resulting in coalescence between 30°-75° flaws,
              compare with Fig. 3.25.
              sc = secondary crack
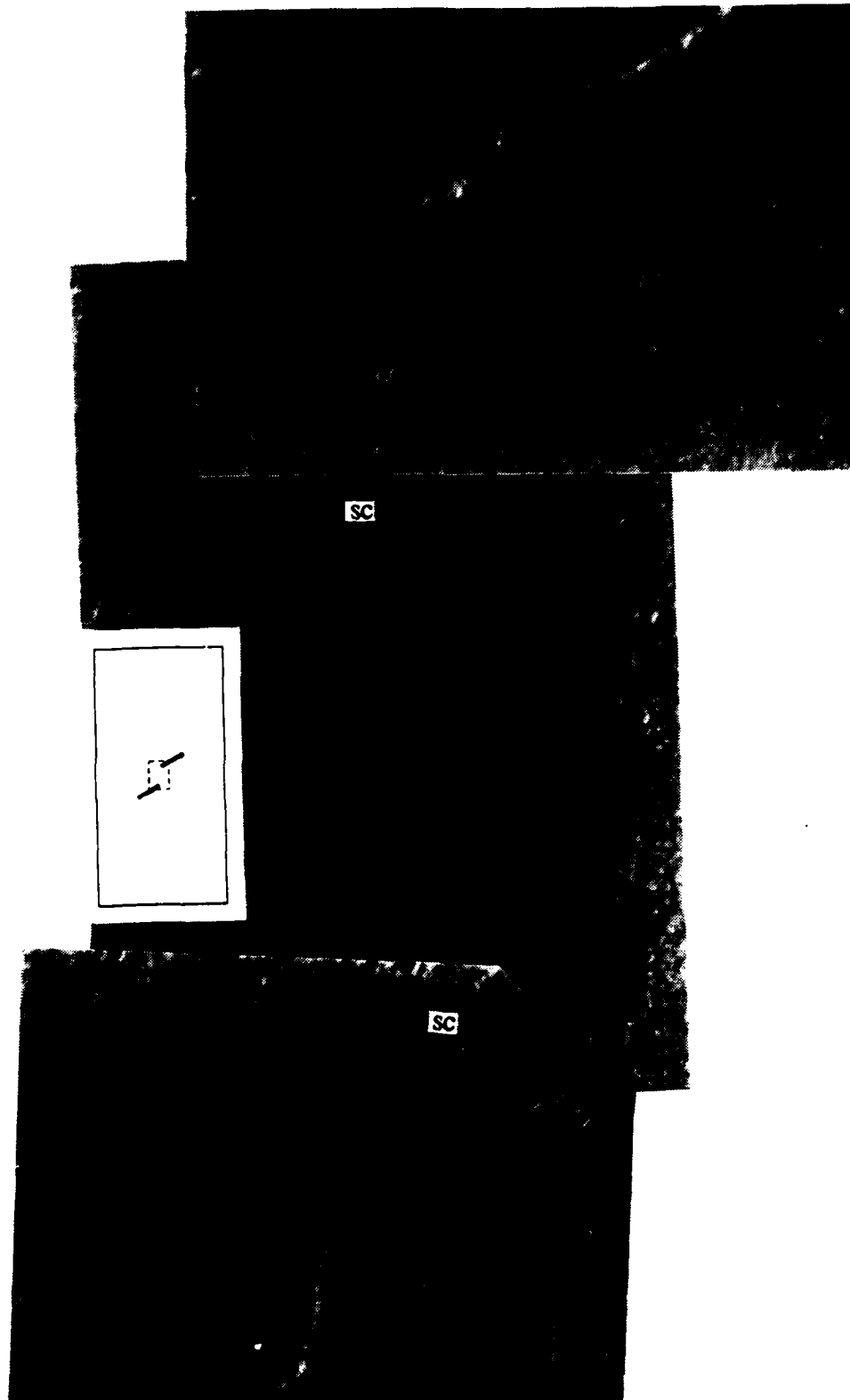
Figure 3.25   Secondary crack growth resulting in coalescence between.30°-75° flaws,
               compare with Fig. 3.24.
               sc = secondary crack
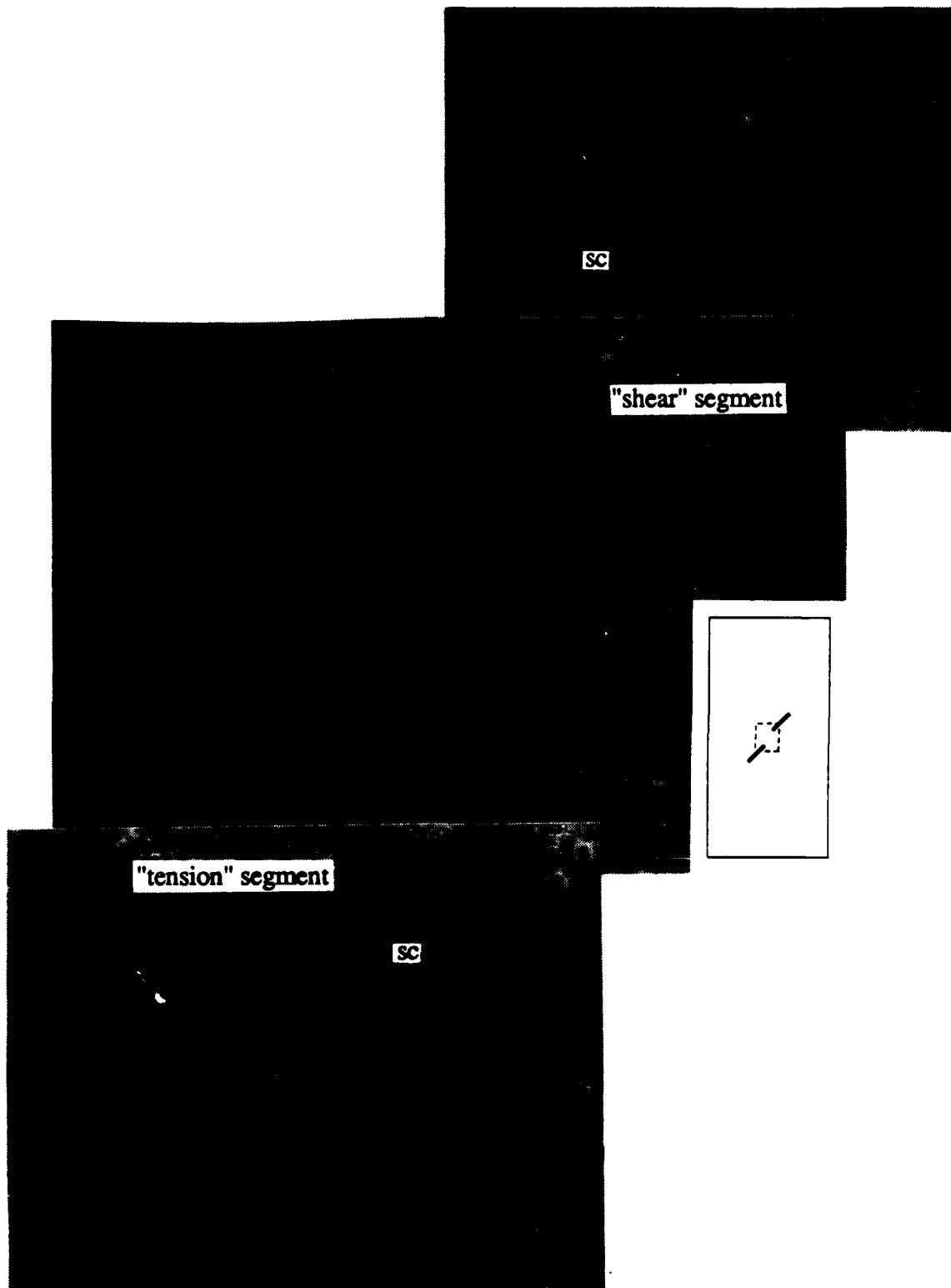
Figure 3.26   Secondary crack growth resulting in coalescence between 45°-60° flaws, specimen #1 (compare with Fig. 3.27).
sc = secondary crack
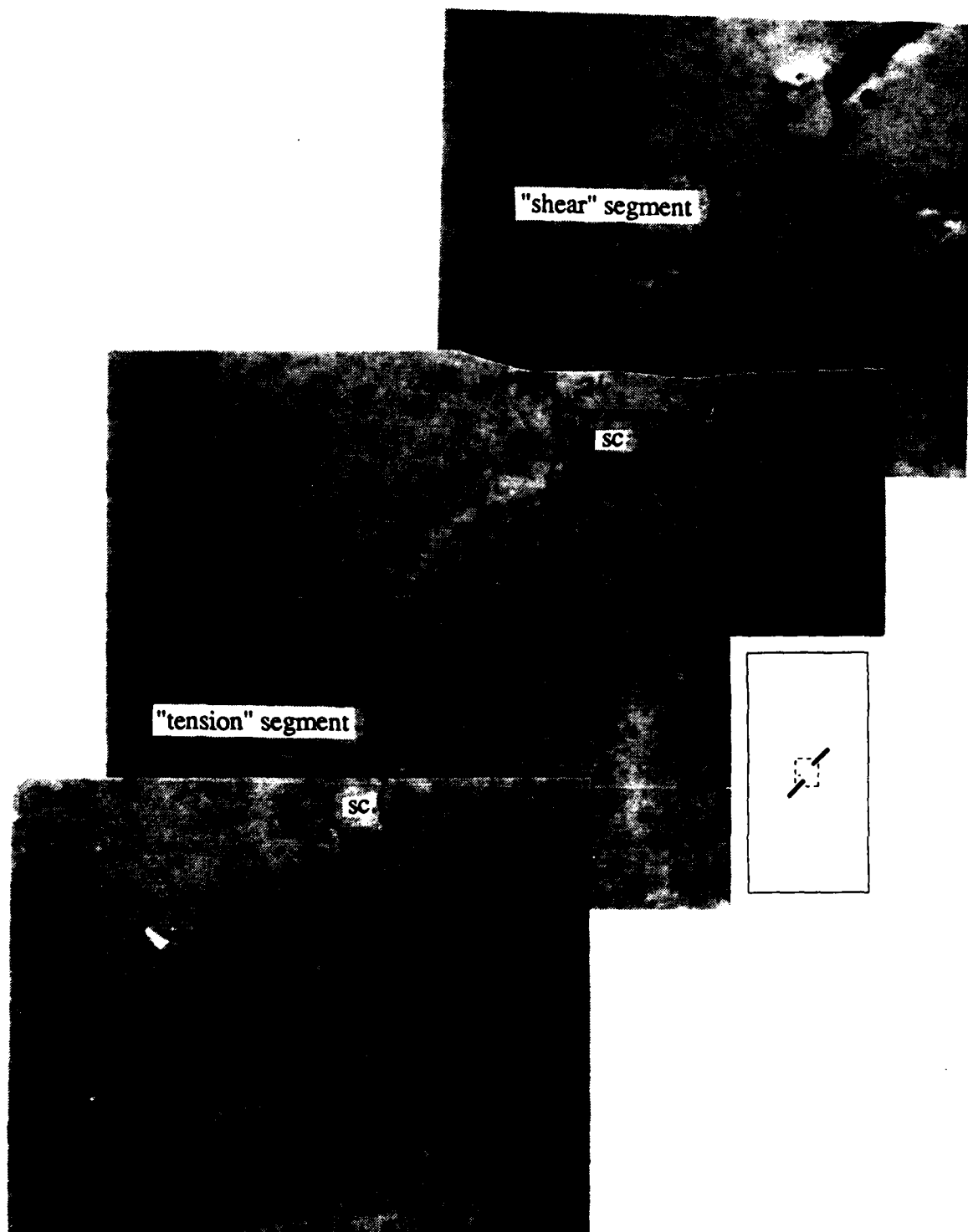
Figure 3.27   Secondary crack growth resulting in coalescence between 45°-60° flaws, specimen #2 (compare with Figure 3.26).
sc = secondary crack

Figure 3.28   Secondary crack growth resulting in coalescence between 60°-45° flaws.
sc = secondary crack
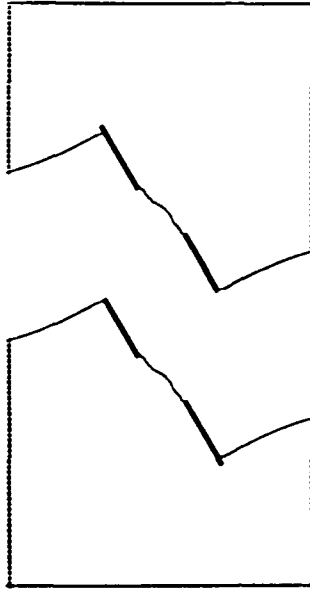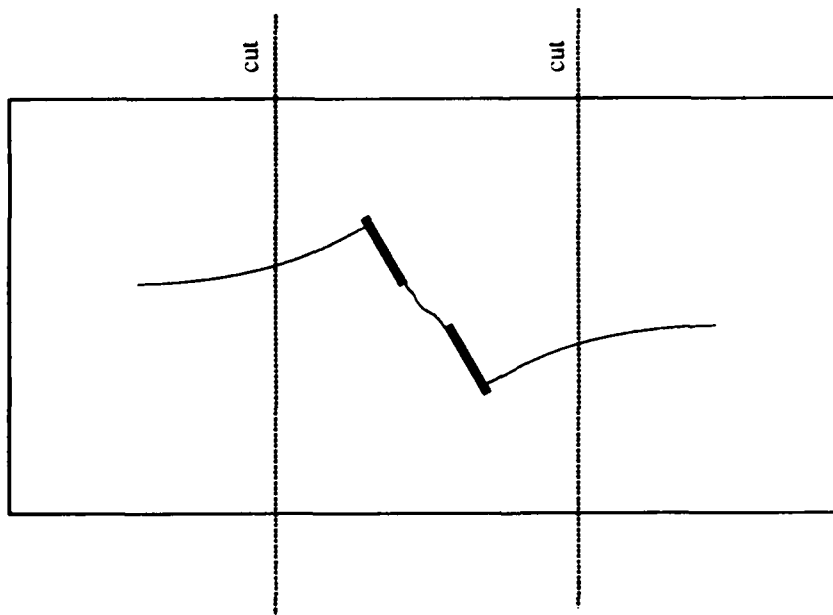
coalescence and wing crack surfaces exposed

Figure 3.29   Specimen cutting procedure to expose crack surfaces.

85
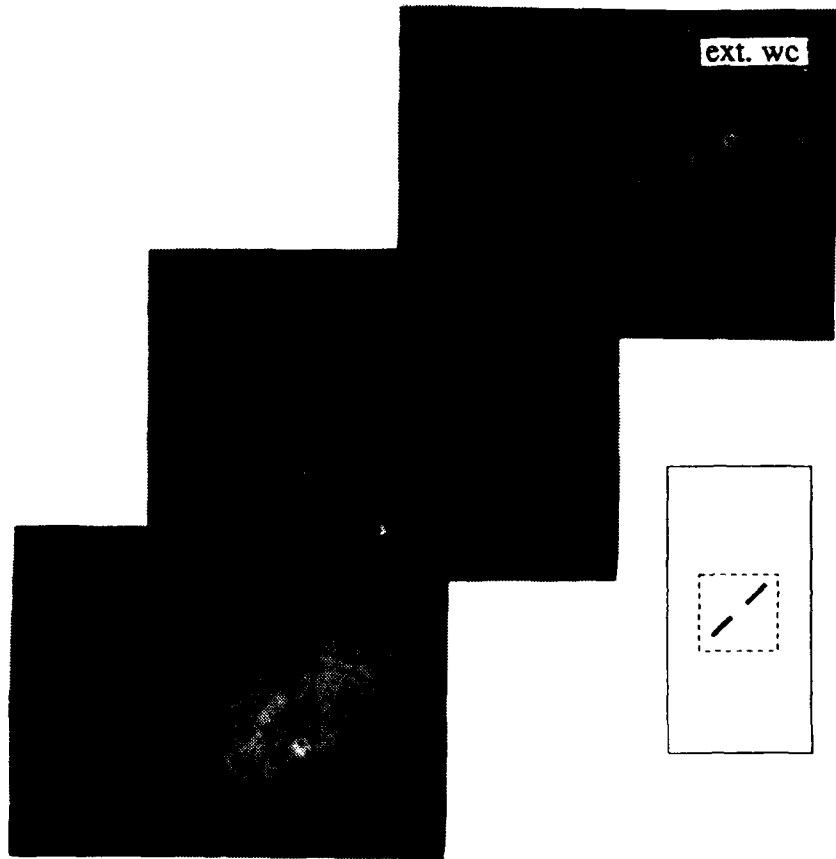
Figure 3.30   "Apparent" coalescence crack (marked by arrows) between 45°-45° flaws. Closed external wing cracks hardly visible in photo.
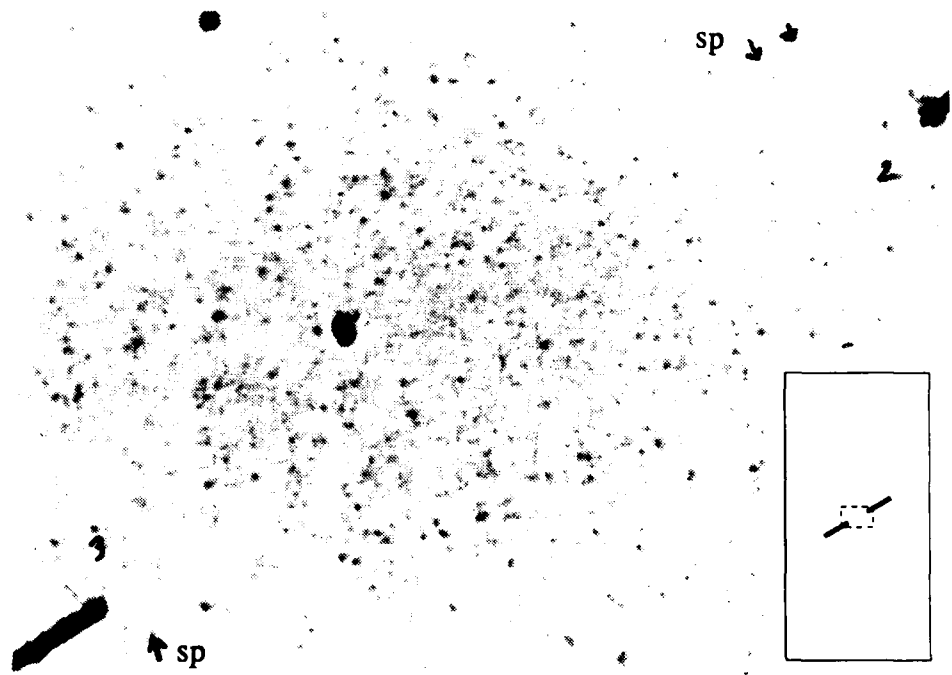
Figure 3.31   Spalling around internal 30°-30° flaw tips [applied load = 64kN].
sp = spalling
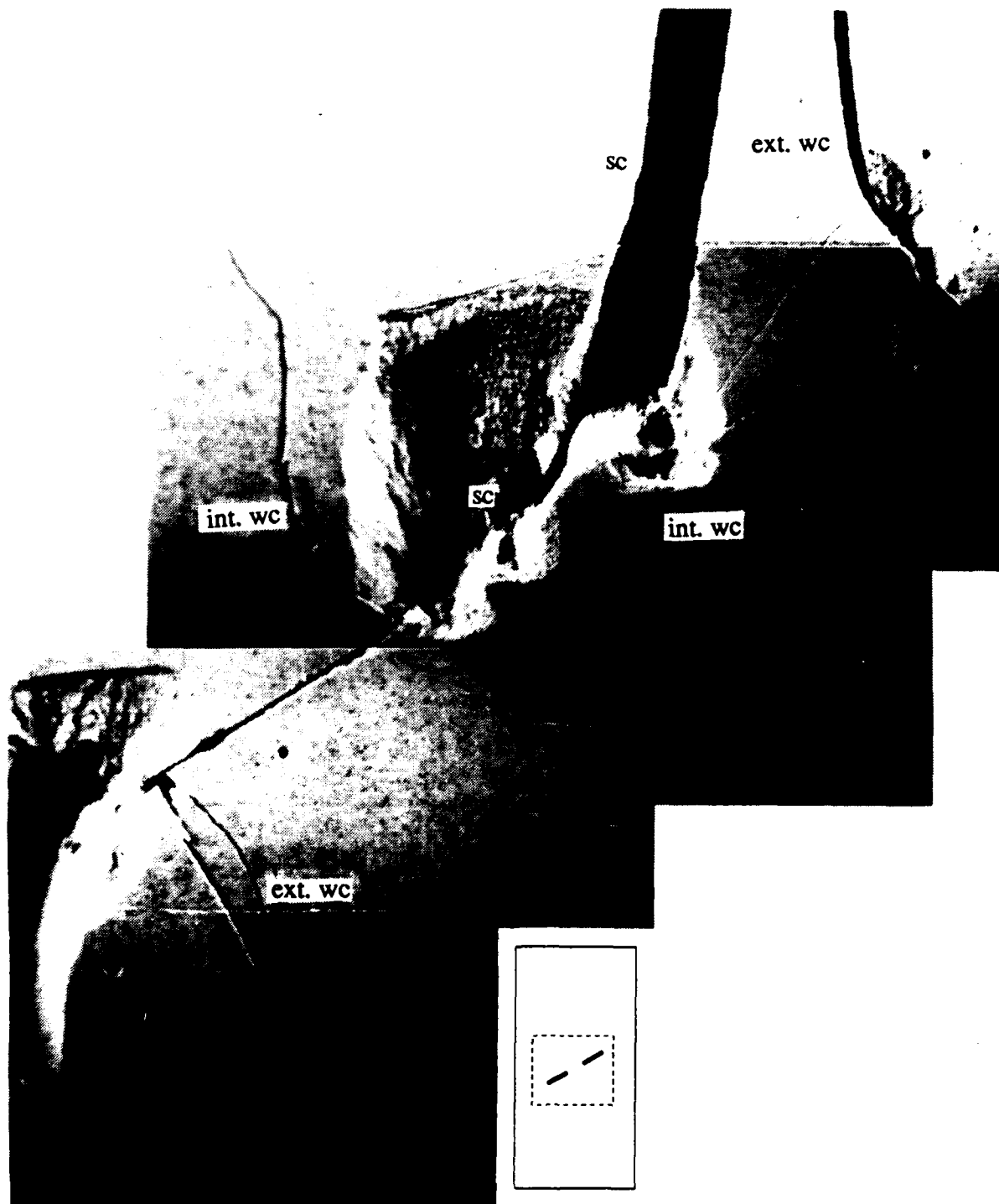
Figure 3.32   Secondary crack growth without coalescence between 30°-30° flaws
[applied load = 67kN].
int. wc = internal wing crack, ext. wc = external wing crack, sc =
secondary crack.

Coalescence between Overlapping Flaws

Fig. 3.33(a) and (b) are photographs from separate tests on specimens with 30°-120° flaws under applied loads of 62.4 kN (27.5 MPa) and 61 kN (27.4 MPa), respectively. Linkage of the flaws is not evident in the photographs, but cutting both specimens showed that in each case the internal wing cracks were connected to the adjacent internal flaw tips, i.e., coalescence occured through wing crack growth. Coalescence was also indicated by drops in load under displacement control and by the open external wing cracks (see discussion on coalescence in non-overlapping flaws). The fracture behavior was also remarkably consistent between the two identical specimens.

For one of the specimens with 30°-135° flaws (Fig. 3.34), coalescence occured through the growth of the lower internal wing crack towards the upper internal flaw tip at an applied load of 67.5 kN (29.2 MPa). Coalescence is rather obvious from the photograph, and is also indicated by the open external wing cracks. Significant spalling and other cracks (marked by "A" in Fig. 3.34) occured simultaneously with coalescence. The other specimen with 30°-135° flaws is shown in Fig. 3.35 under an applied load of 53.5 kN (24.7 MPa). The wing cracks from both internal flaw tips appear to have interesected to form a coalescence crack. However, this "apparent" coalescence crack as well as the external wing cracks were closed under the applied load of 53.5 kN. Loading of this specimen was discontinued shortly after the photograph in Fig. 3.35 was taken because of splitting along the external edge of the block. Upon cutting (as in Fig. 3.29), the block had to be pulled apart with some force along the "apparent" coalescence crack, thus establishing that the crack shown in Fig. 3.35 did not actually connect the internal flaw tips.

In one of the specimens with 45°-135° flaws (see Fig. 3.36) under an applied load of 72 kN (33 MPa), secondary crack growth connected each external flaw tip with the

89

internal tip of the adjacent flaw. This was accompanied by the opening of the external wing cracks and by a load drop under displacement control. In the other specimen, the lower internal wing crack suddenly extended toward the upper flaw at an applied load of 66 kN (30 MPa) as schematically illustrated in Fig. 3.37. There was no load drop when this happened, and the external wing cracks remained closed.

A schematic illustration of the fracturing observed between 60°-105° flaws (true for both specimens) at an applied load of 74 kN (33 MPa) is shown in Fig. 3.38. The upper internal wing crack propagated towards the lower internal flaw tip but it was not apparent whether this wing crack had actually connected with the flaw tip. No load drop occured and the external wing cracks stayed closed. One specimen was unloaded after the fracture pattern in Fig. 3.38 was observed. Cutting this specimen revealed that the wing crack had not connected with the lower internal flaw tip, i.e., coalescence had not taken place. The other specimen was loaded until it failed explosively under an applied load of 84 kN (37 MPa).

The fracture coalescence between 60°-135° flaws is shown in Figs. 3.39(a) and (b). For one specimen schematically drawn in Fig. 3.39(a), the lower internal wing crack propagated towards the upper external flaw tip at an applied load of 72.5 kN (32 MPa). For the other specimen shown in Fig. 3.39(b), the upper internal wing crack propagated towards the lower external flaw tip at an applied load of 75 kN (34 MPa). The fracturing just described was accompanied by a load drop in both specimens. Thus, although these specimens were not cut, it is likely that the flaws were connected by wing cracks because of the observed correlation between coalescence and load drops in the other flaw geometries.

Finally, for the 60°-150° flaws, no coalescence was observed for both specimens which were loaded up to about 75 kN (33 MPa). At this load, the upper internal wing

90

crack had propagated towards the lower internal flaw tip as schematically drawn in Fig. 3.40. It was not apparent whether this wing crack had actually connected with the flaw tip. Loading was discontinued at 75 kN because it was thought that any additional increase in load would have resulted in complete disintegration of the specimens such as what occured for one of the specimens with 60°-105° flaws. This latter case showed that no additional information about fracture patterns could be obtained from specimens which failed explosively.
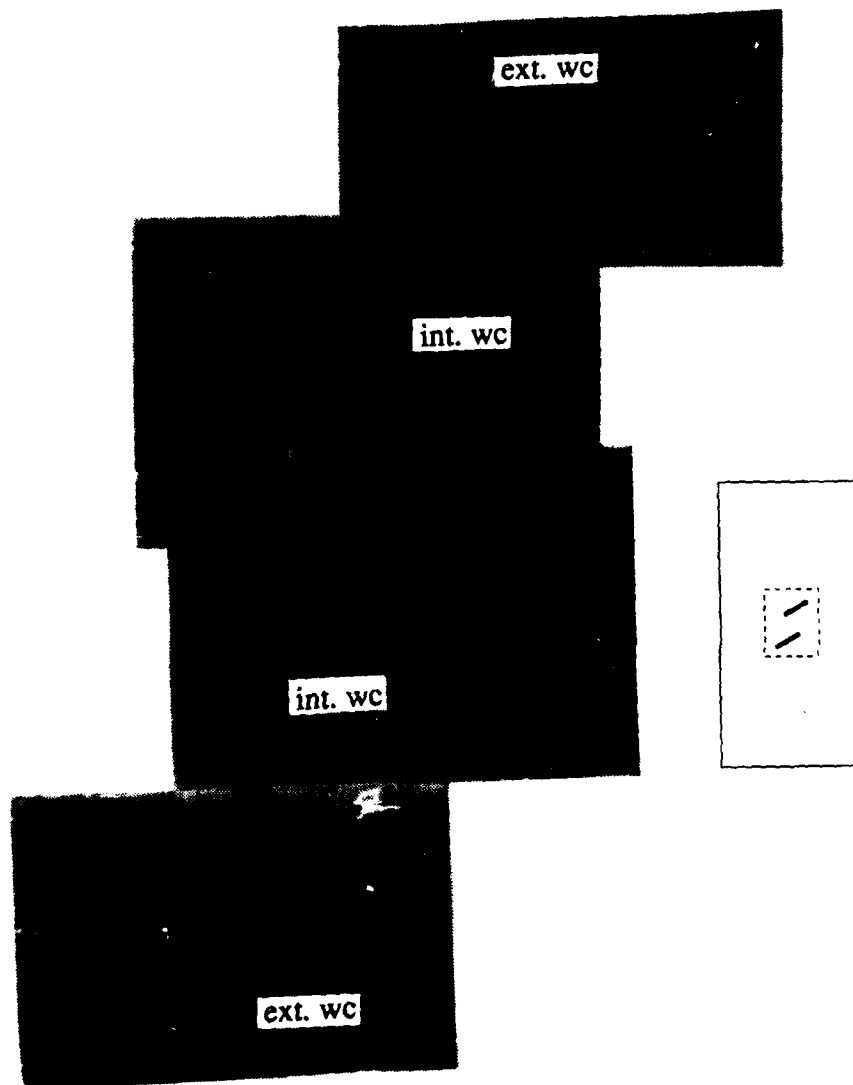
Figure 3.33(a) Internal wing crack growth resulting in coalescence between 30°-120°
flaws, specimen #1 [applied load = 62.4kN].
int. wc = internal wing crack, ext. wc = external wing crack
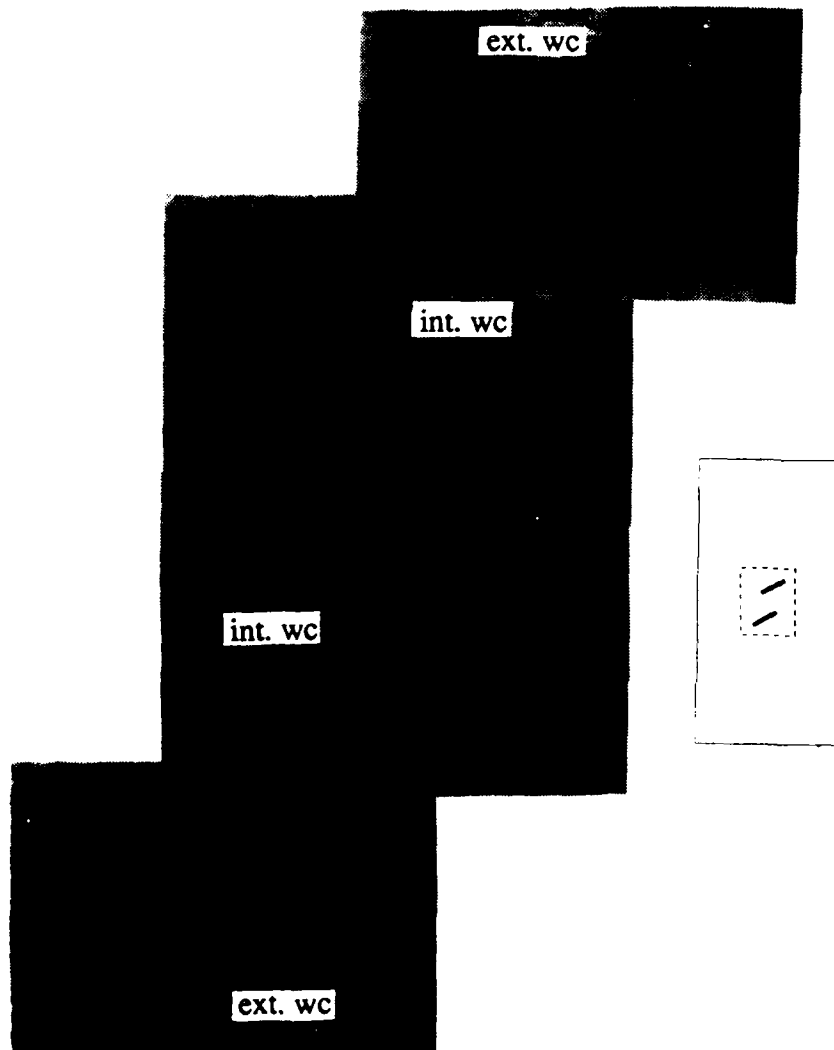
Figure 3.33(b) Internal wing crack growth resulting in coalescence between 30°-120°
flaws, specimen #2 [applied loads = 61kN].
int. wc = internal wing crack, ext. wc = external wing crack.
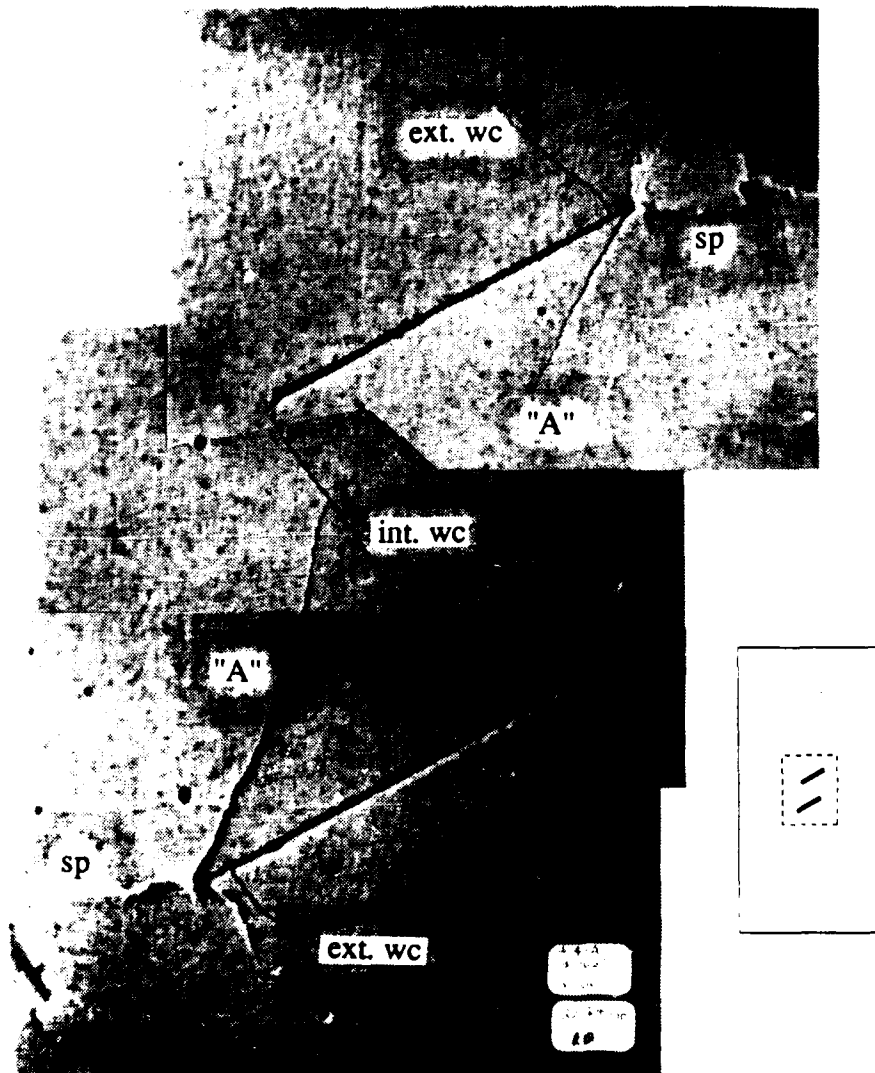
Figure 3.34   Internal wing crack growth resulting in coalescence between 30°-135° flaws specimen #1, accompanied by spalling and cracking marked by "A" [applied load = 67.5kN].
int. wc = internal wing crack, ext. wc = external wing crack, sp = spalling.
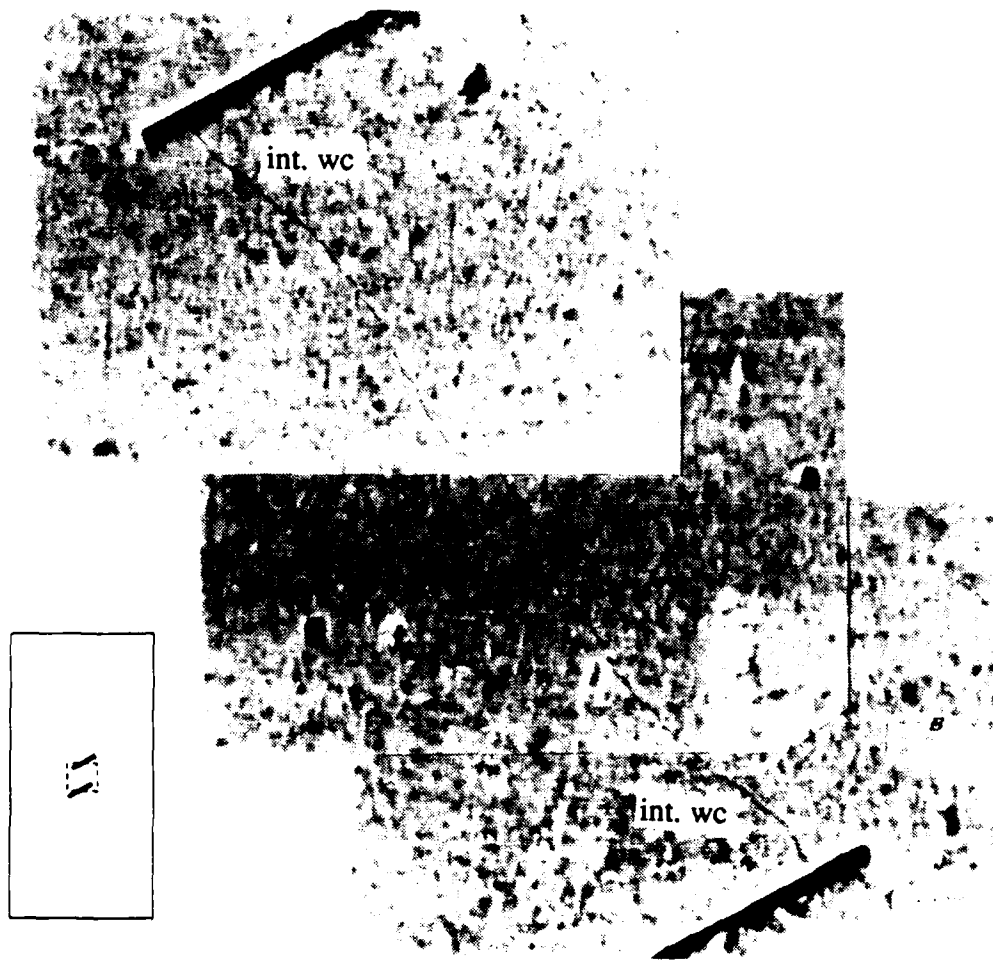
Figure 3.35   "Apparent" coalescence due to internal wing crack growth between 30°-135°
flaws, specimen #2 [applied load = 53.5kN].
int. wc = internal wing crack.
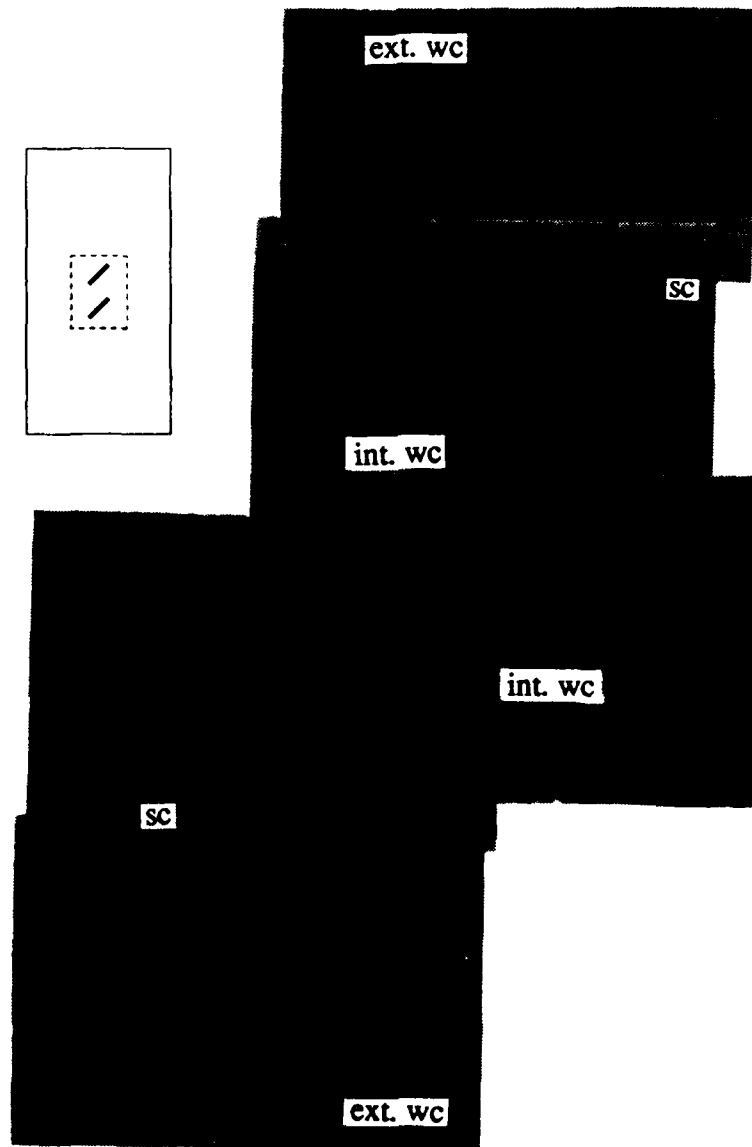
Figure 3.36   Secondary crack growth resulting in coalescence between 45°-135° flaws,
specimen #1 [applied load = 72kN]. Note: secondary cracks grow between
internal and external flaw tips.
int. wc = internal wing crack, ext. wc = external wing crack,
sc = secondary crack.
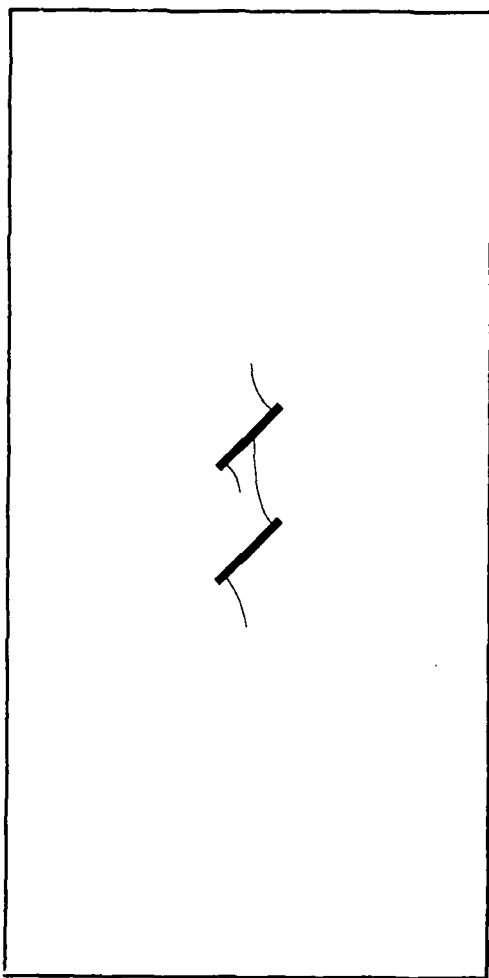
Figure 3.37   Wing crack growth from 45°-135° flaws, specimen #2. Note: lower
internal wing crack propagated towards upper flaw [applied load = 66 kN].
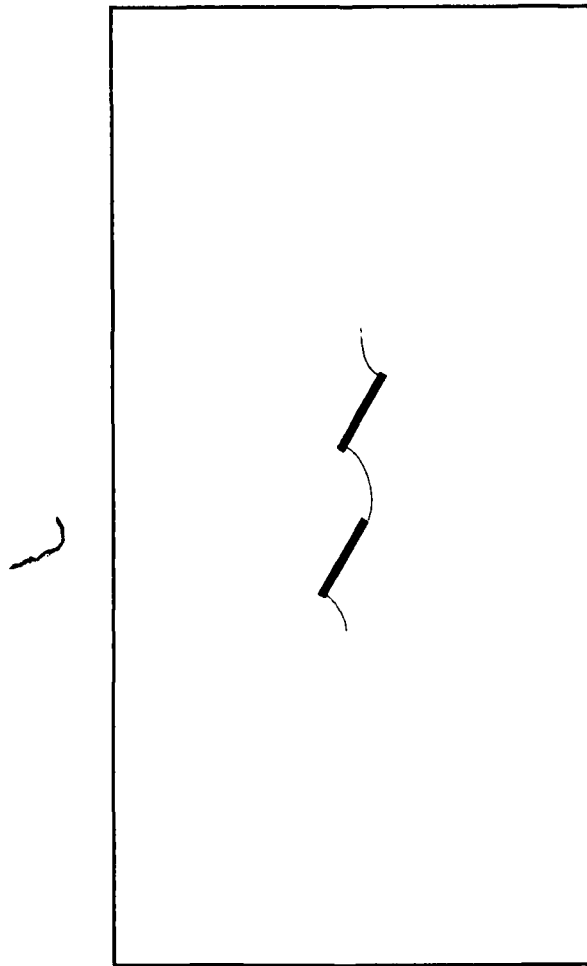
Figure 3.38   Wing crack growth from 60°-105° flaws [applied load = 74kN].
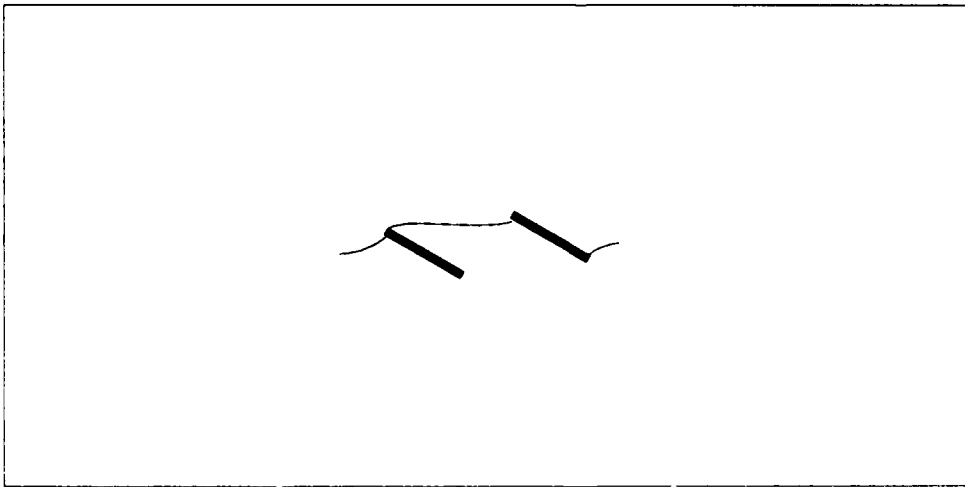
(a) Specimen 1, applied load = 72.5 kN (32 MPa)
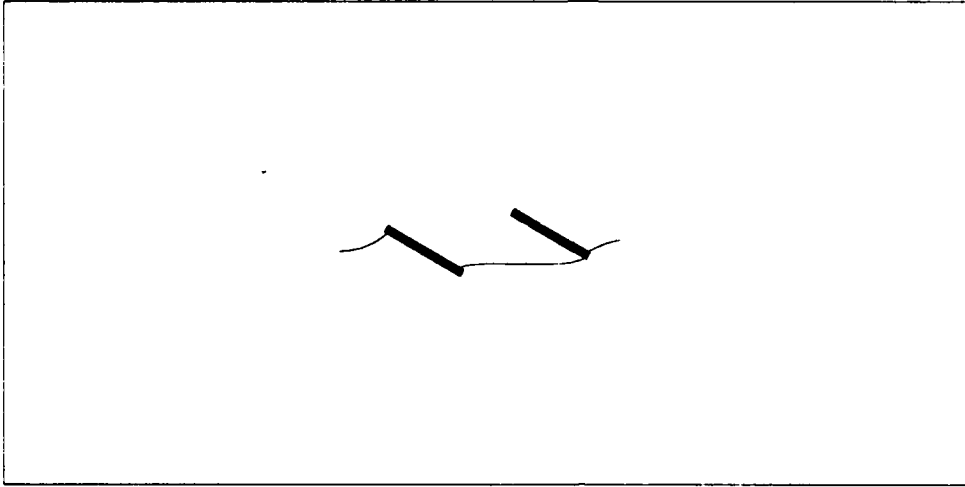
(a) Specimen 2, applied load = 75 kN (34 MPa)

Figure 3.39   (a) and (b) Wing crack growth from 60°-135° flaws.
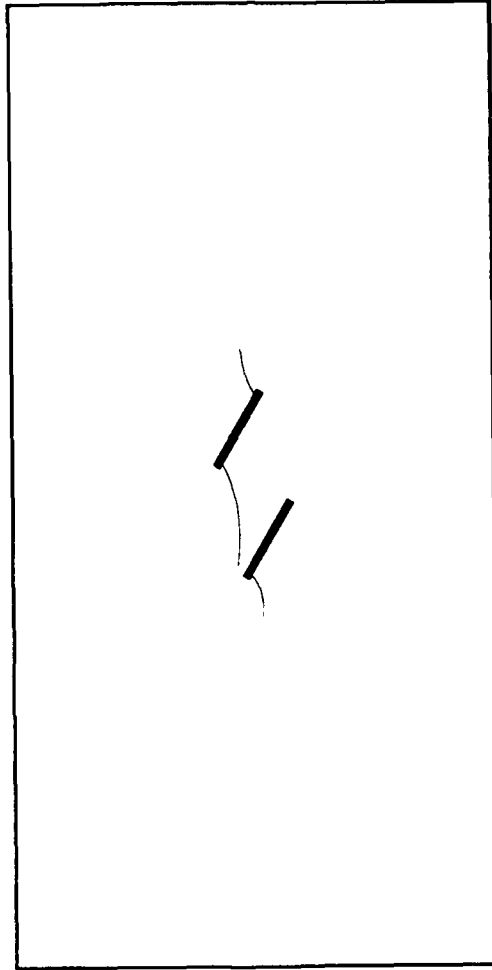
Figure 3.40   Wing crack growth from 60°-150° flaws [applied load = 75kN].

3.2.2 Wing Crack Initiation and Coalescence Loads

The applied loads at which wing cracks became visible is plotted versus the ligament inclination angle in Fig. 3.41. Triangular, square and circular symbols were used for 30°, 45° and 60° inclined flaws respectively. For the same ligament inclination angle, the wing crack initiation loads were always lowest for the 30° inclined flaws and highest for the 60° inclined flaws. An explanation for this observation, given in more detail in Section 4.2, can be found from the variation of stress fields around flaws with different inclination angles. Furthermore, for the same flaw inclination, there appears to be some dependence of the wing crack initiation loads on the ligament inclination angle. For all three inclination angles, the wing crack initiation loads were lowest for ligament inclination angles between 50° and 100°.

Figs. 3.42, 3.43 and 3.44 are plots of maximum test loads[3.5] versus ligament inclination angles for 30°, 45° and 60° inclined flaws, respectively. Dotted lines divide the graphs into "non-overlapping" (ligament inclination angle ≤ 90°) and "overlapping" (ligament inclination angle > 90°) regions. Hollow symbols are used to plot maximum loads at which coalescence actually took place. As noted in the previous section, coalescence always took place through secondary crack growth for non-overlapping flaws, and through either wing or secondary crack growth for the overlapping flaws. Solid

---

[3.5] The maximum test load is the largest load applied during each test. In cases where loading was stopped after coalescence (see Figs. 3.9, 3.13 and 3.19), the maximum est load corresponds to the coalescence load. Otherwise, the maximum test load is the load at which a specimen failed (i.e., severely cracked) or at which testing was stopped before coalescence or failure occured.

symbols are used to plot maximum loads that correspond either to loads at failure without coalescence, or loads at which testing was discontinued before failure.

In general, for the same flaw inclination angles, the coalescence loads were lower for non-overlapping when compared to overlapping flaw geometries. The rest of this report will focus on modelling coalescence mechanisms between non-overlapping flaws since these cases are usually more critical and exhibit secondary crack growth that cannot be explained by existing fracture mechanics theories (see Section 2.3). Fig. 3.45 is a plot of the observed coalescence loads versus ligament inclination angle for only non-overlapping flaws with 30°, 45° and 60° inclinations. One can see that the measured coalescence loads are consistent between specimens with identical flaw geometries (two were tested for each geometry). This established the reproducibility of the observed coalescence phenomenon. Furthermore, for the same ligament inclination angle, coalescence loads increased with increasing flaw inclination angle. Finally, for a given flaw inclination angle, coalescence loads were lowest for a ligament orientation angle of 75°. It was the goal of the modelling effort described in Chapter 4 to reproduce these trends.
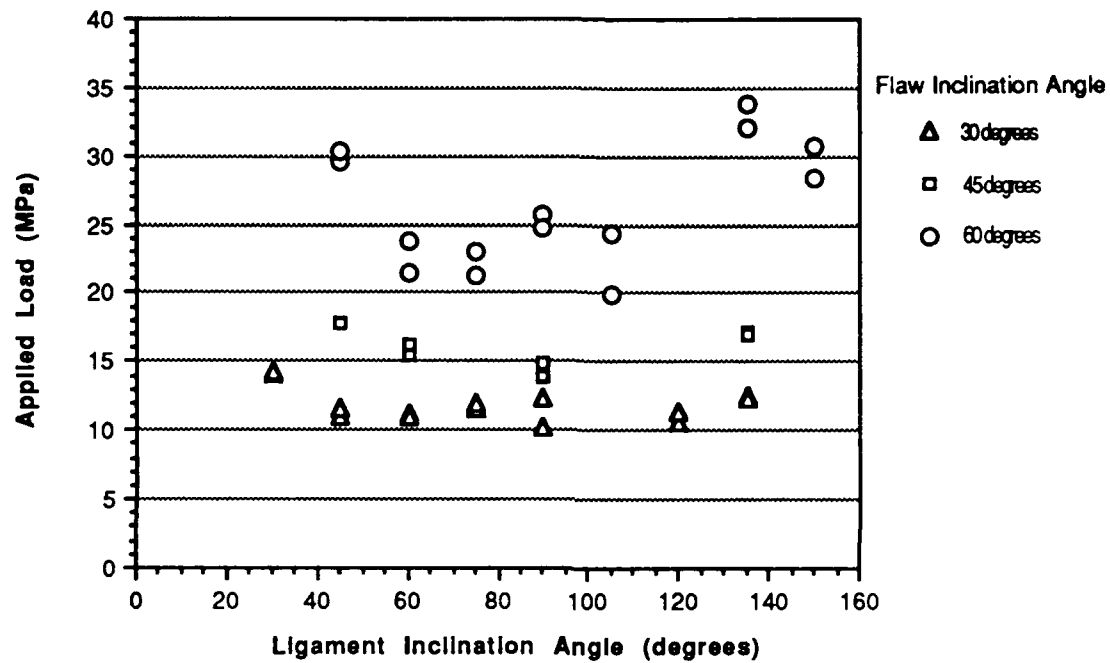
Figure 3.41   Wing crack initiation loads.
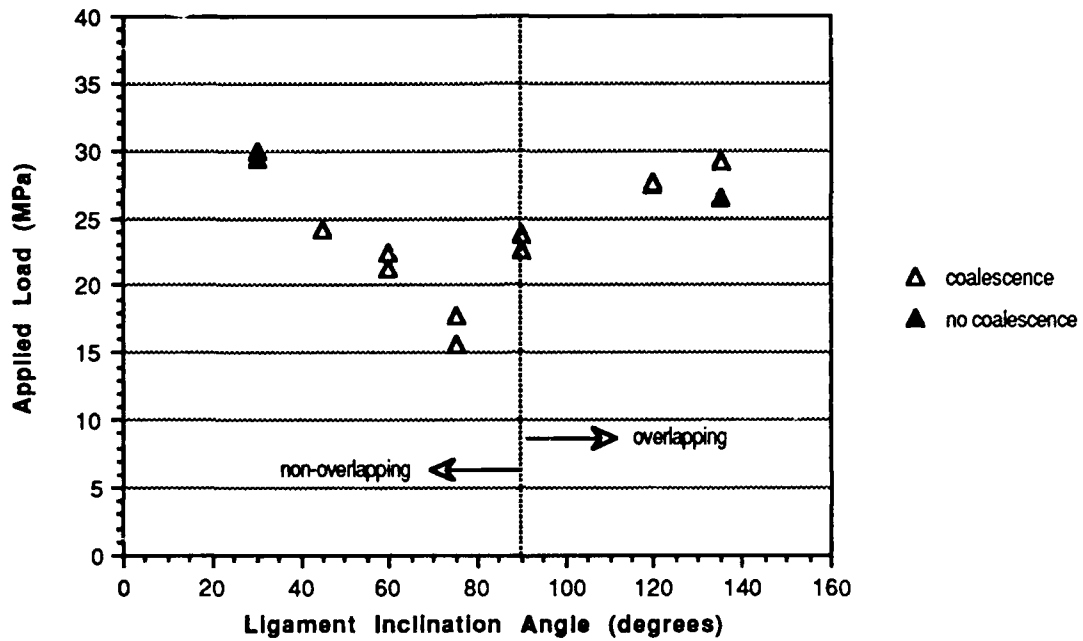
Figure 3.42   Maximum test load vs. ligament inclination angle for 30° flaws.
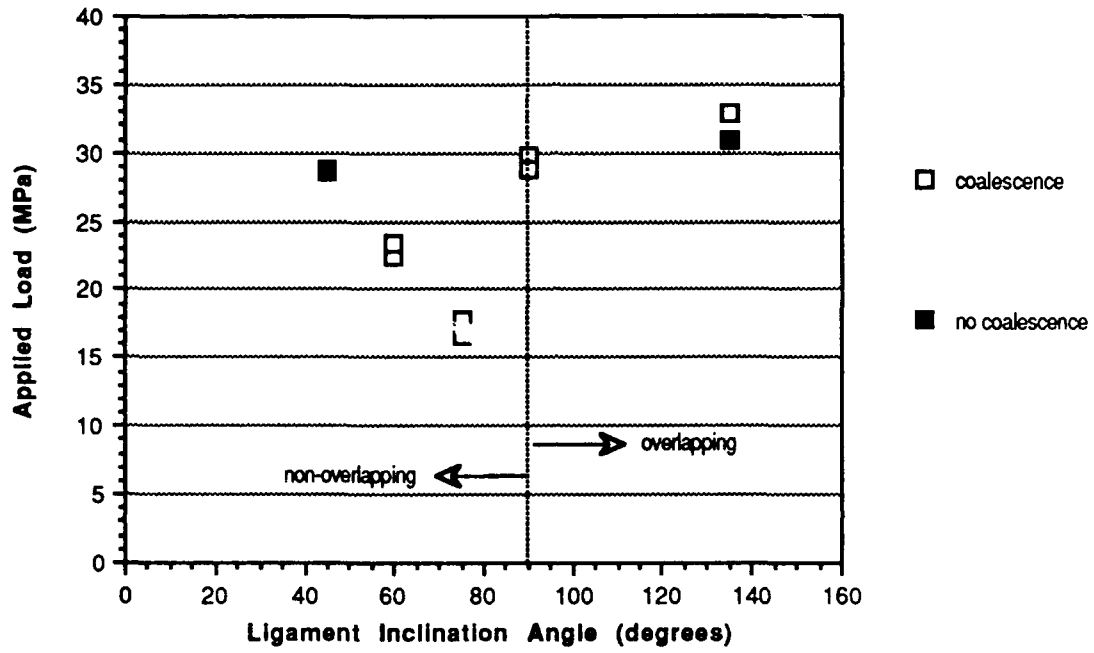
Figure 3.43   Maximum test load vs. ligament inclination angle for 45° flaws.
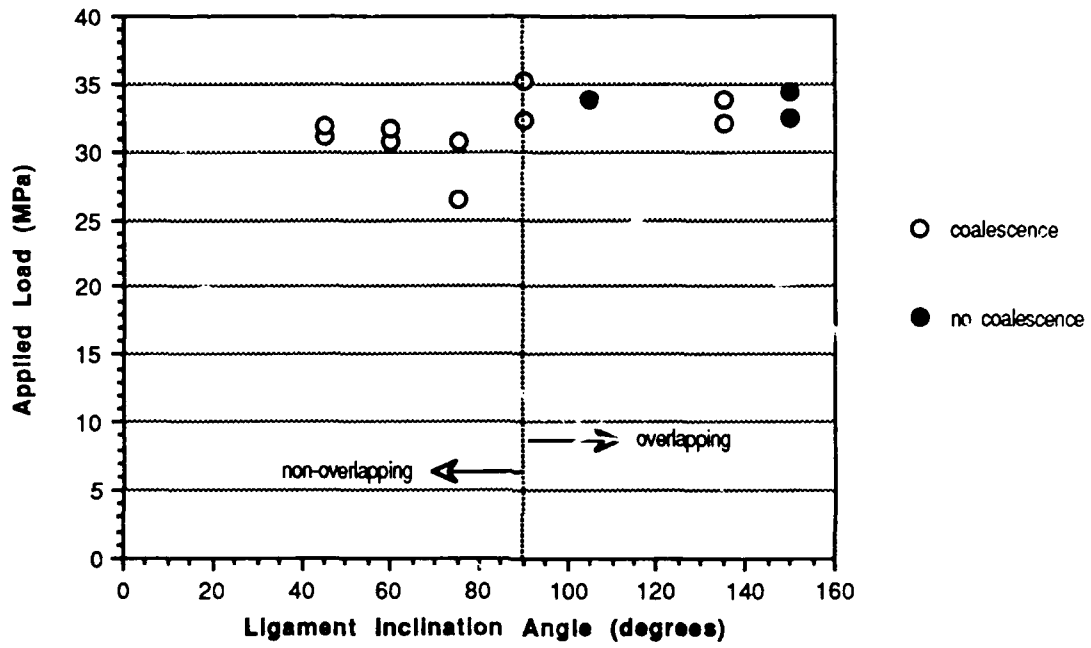
Figure 3.44   Maximum test load vs. ligament inclination angle for 60° flaws.
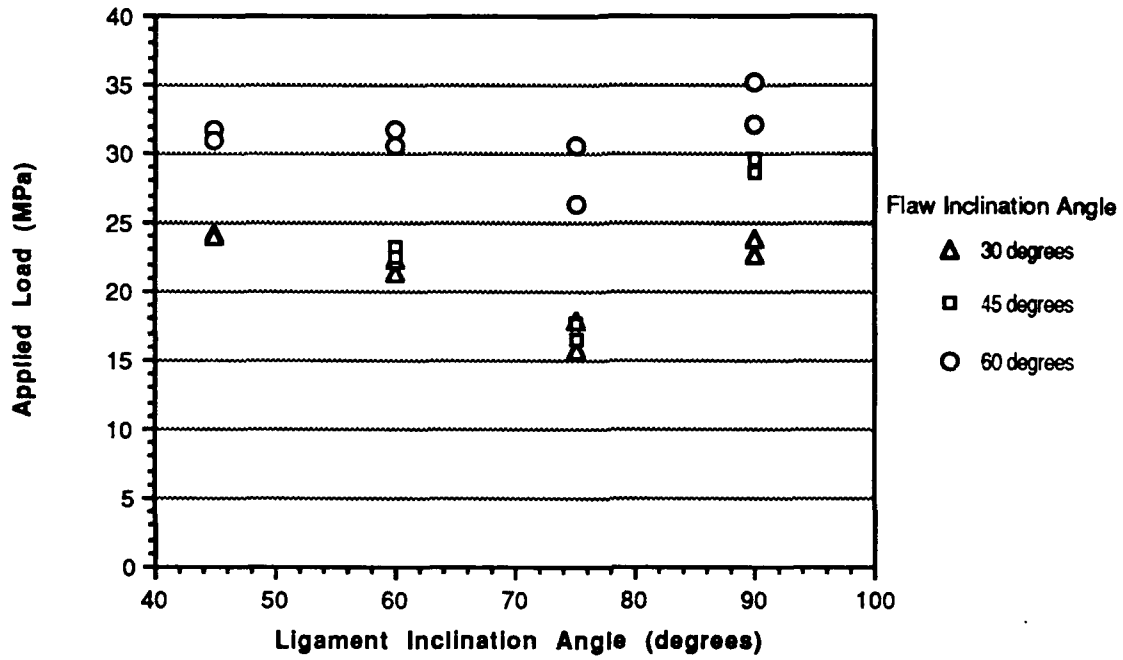
Figure 3.45 Coalescence load vs. ligament inclination angle for non-overlapping flaw geometries.

3.3.3 Fracture Surface Morphologies

Fig. 3.46 contains schematic drawings of the specimens with 30°-45° flaws[3.6] after they had been cut to expose the wing and coalescence crack surfaces. The three types of areas, distinguished by the markings on the figures, may be described as follows:

Type I (dotted region) : This is characterized by the complete absence of pulverized gypsum and a smooth appearance. A magnified view of this surface type (Fig. 3.47) shows that the surface is not glassy smooth; however, the uniformity of the roughness makes it appear smooth when the surface is observed without any magnification.

Type II (dashed region) : This is characterized by traces of pulverized gypsum. A magnified view (see Fig. 3.48) shows that the surface is not uniformly rough like the Type I surface. Instead, small patches of roughness are interspersed in a surface area that is actually smoother than the Type I surface. However, the patchy roughness seen under magnification causes this type of fracture surface to appear rougher, when viewed without magnification, than the Type I surface.

Type III (shaded region) : This is characterized by significant amounts of pulverized gypsum. A magnified view of this surface is shown in Fig. 3.49. The roughness is interspersed as in the Type II surface; however, the ridges are higher in the Type III surface which causes it too look rougher than the Type II surface when viewed without magnification.

The Type I and Type II surfaces were also observed under a scanning electron microscope at a ~1000x magnification (Figs. 3.50 and 3.51 respectively). Fig. 3.50

[3.6] Thes are the same specimens shown in Figs. 3.11 and 3.23.

shows the porous microstructure of gypsum which consists of interlocking needle-like grains. When Figs. 3.50 and 3.51 are compared, the Type II surface shows more compacted grains with less pore-space than the Type I surface. This is probably why the area between the patchy roughness of the Type II surface seen in Fig. 3.48 appears to be smoother than the Type I surface in Fig. 3.47.

A photograph at ~1000x magnification, shown in Fig. 3.52, was taken very close to one of the internal flaw tips where there was a very small region of pulverized gypsum. The micrograph shows severely crushed and compacted grains, especially when compared to the micrographs in Figs. 3.50 and 3.51.

Fig. 3.53 and 3.54 show the surface features of cracks growing from 30°-75° and 45°-60° flaws. It is evident from these figures that coalescence crack surfaces are consistent in blocks with identical flaw geometries, as in the case of 30°-45° flaws shown in Fig. 3.46. Furthermore, in comparing coalescence crack surfaces among the different flaw arrangements, one sees that coalescence crack surface features vary with the flaw arrangement.

All the external wing cracks, regardless of the flaw inclination or the flaw geometry, only had Type I surfaces[3.7]. Hackle marks, which are usually associated with dynamic crack propagation, were seen on the external wing cracks but at some distance from the flaw tips. It is not surprising that these marks were not present near the flaw tips since the wing cracks grew quasi-statically initially and only extended rapidly at

---

[3.7] It is likely that the internal wing cracks had the same surface type. However, the surfaces of these cracks were not exposed by the cutting process shown in Fig. 3.29 for cases where coalescence was through secondary cracking.

coalescence. In contrast to the wing cracks, the coalescence cracks consisted of regions with different surface types, as can be seen in Fig. 3.46. 3.53 and 3.54.

The Type I surface is characteristic of surfaces that run parallel or subparallel to the applied uniaxial compressive load. Examples of these are the dotted regions in the 30°-75° flaws. Thus, the Type I surface is typically found in coalescence cracks in specimens with large ligament inclination angles (i.e., close to 90°). The Type II surfaces are inclined at intermediate angles with respect to the horizontal while the Type III surfaces are sub-horizontal or are inclined at very low angles with respect to the horizontal. Both these latter types are present in all coalescence cracks but with varying areal extents among the flaw geometries. They are usually found in coalescence cracks in flaw geometries with smaller ligament orientation angles (e.g., 30°-45° and 45°-60° flaws).

The complete absence of pulverized gypsum in the Type I crack surface could be considered as evidence that this portion of the crack was created in tension since the surfaces must have immediately pulled apart after the crack was formed. On the other hand, the presence of pulverized gypsum in the Type II and Type III crack surfaces does not necessarily mean that these portions of the coalescence cracks were created in shear: it is also possible that they were created in tension but that the surfaces slid past each other causing the gypsum to be pulverized.
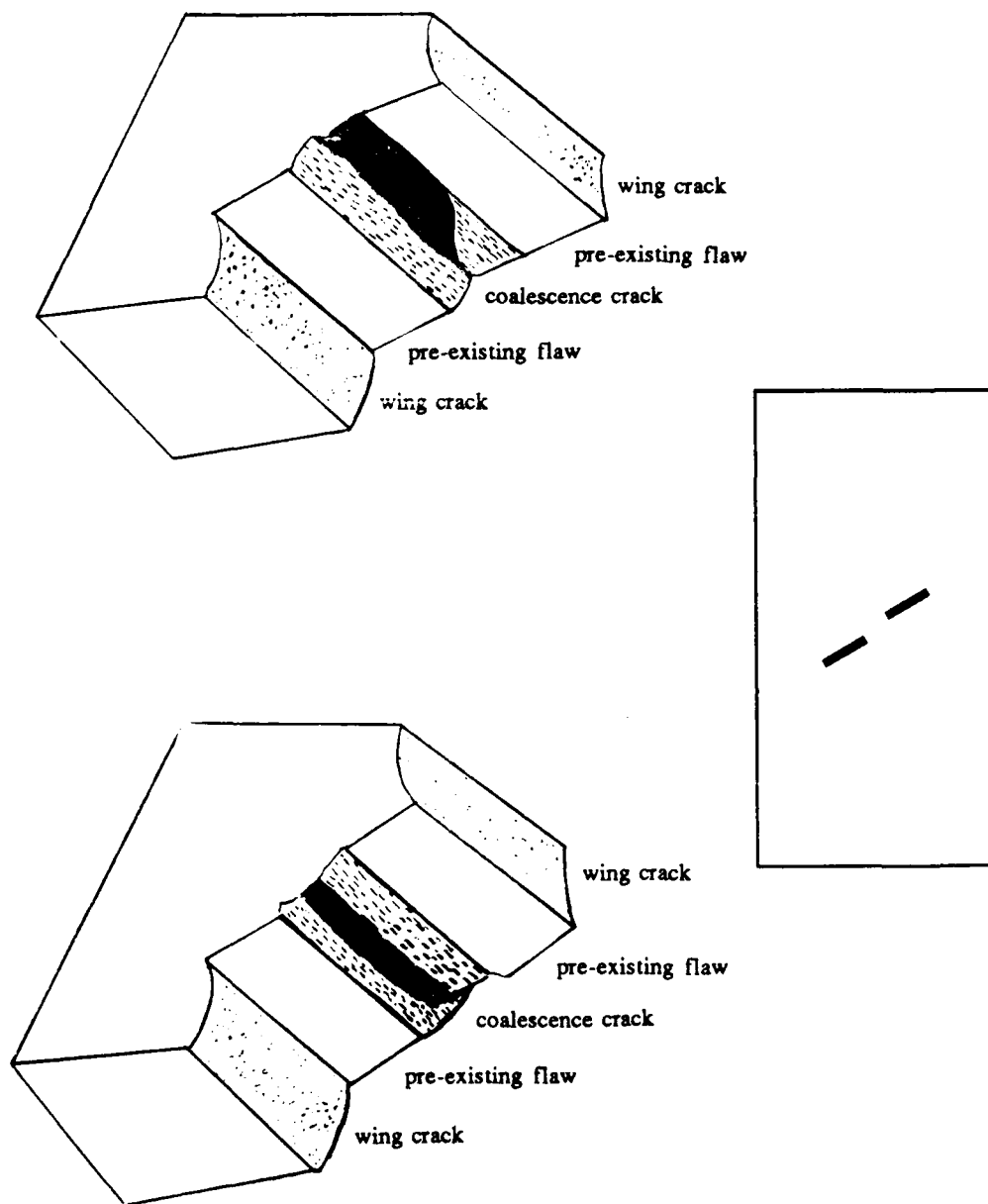
Figure 3.46   Surface morphologies of cracks in cut specimens with 30°-45° flaws.
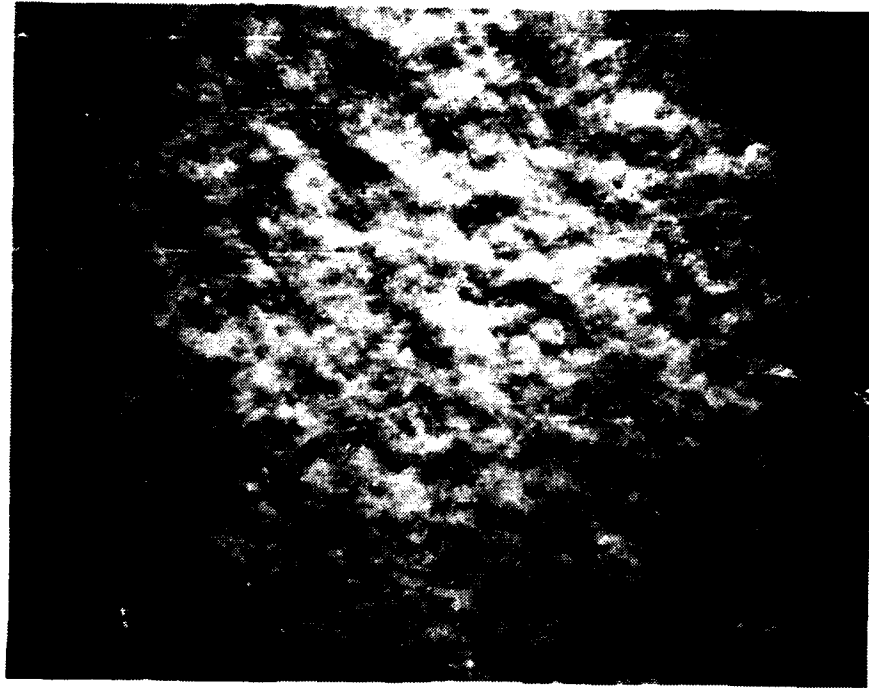
Figure 3.47   Micrograph (~15 x) of Type I surface.
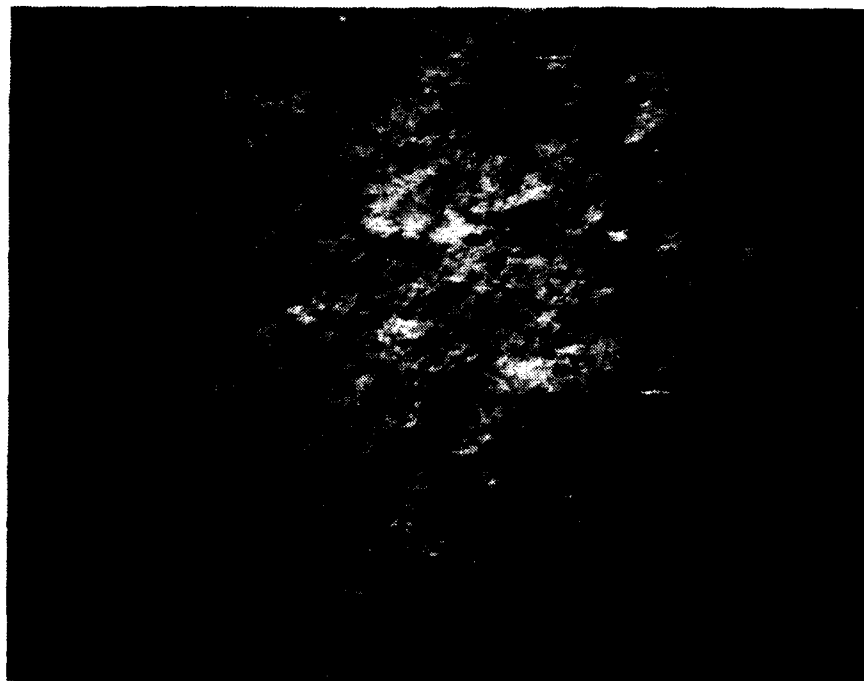
Figure 3.48   Micrograph (~15 x) of Type II surface.

Figure 3.49   Micrograph (~15 x) of Type III surface.
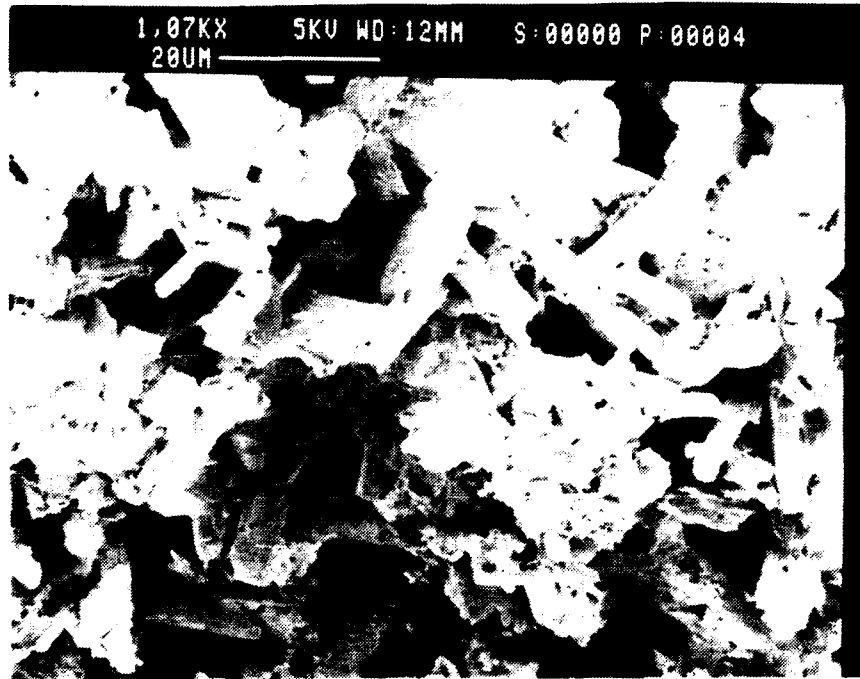
Figure 3.50   Micrograph (1000 x) of Type I surface.
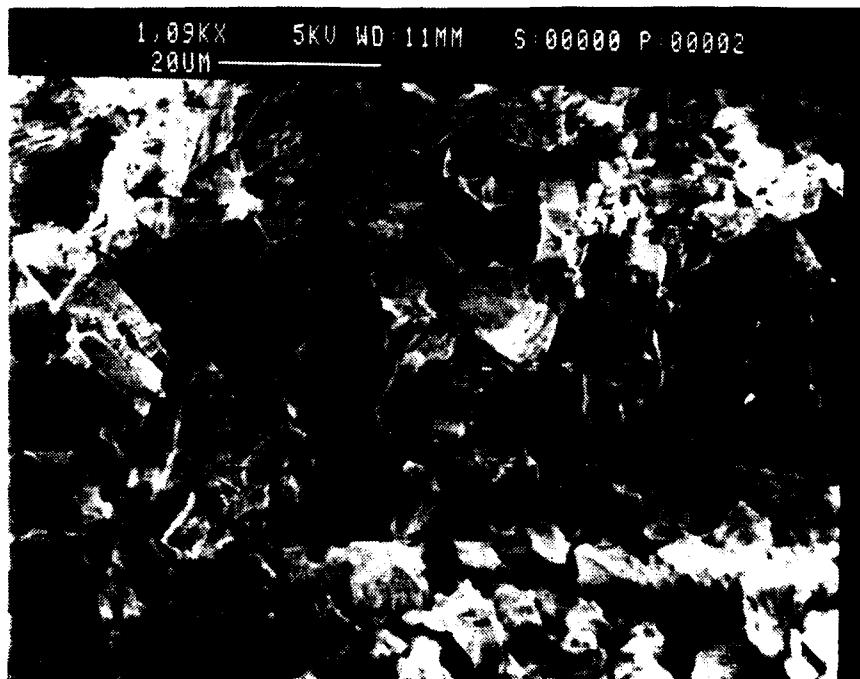
Figure 3.51   Micrograph (1000 x) of Type II surface.

114
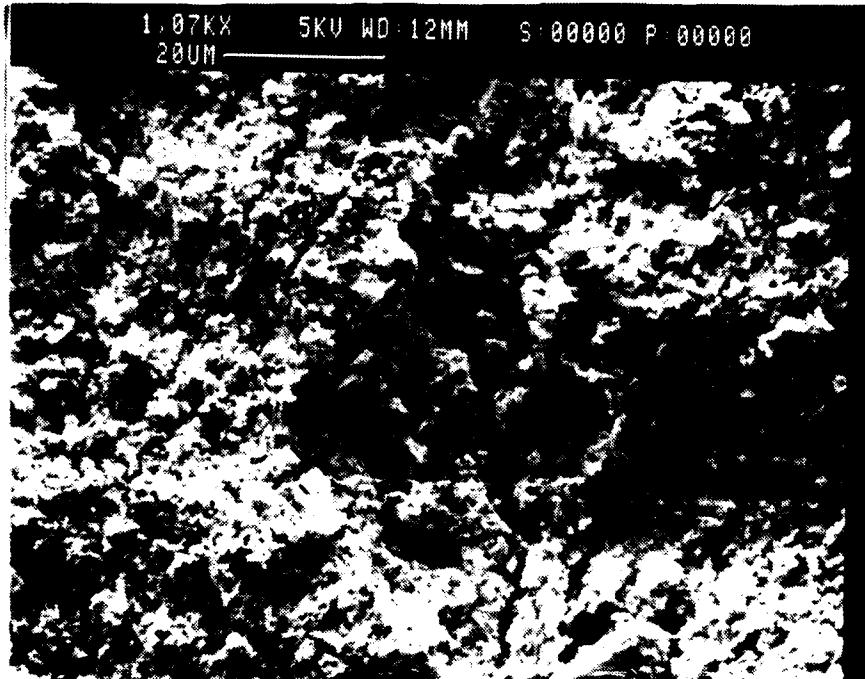
Figure 3.52   Micrograph taken near tip of flaw.
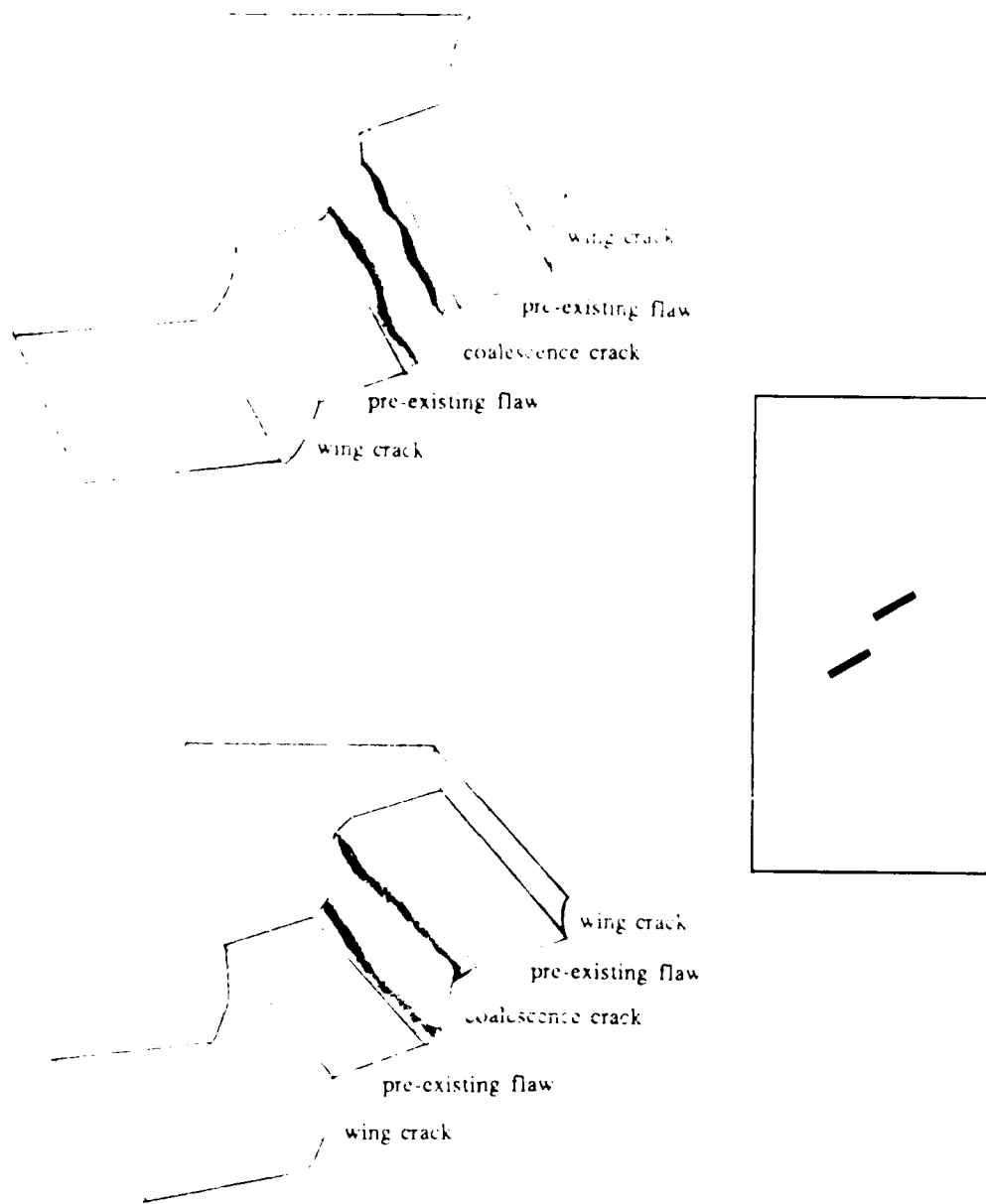
Figure 3.53   Surface morphologies of cracks in cut specimens with 30°-75° flaws.
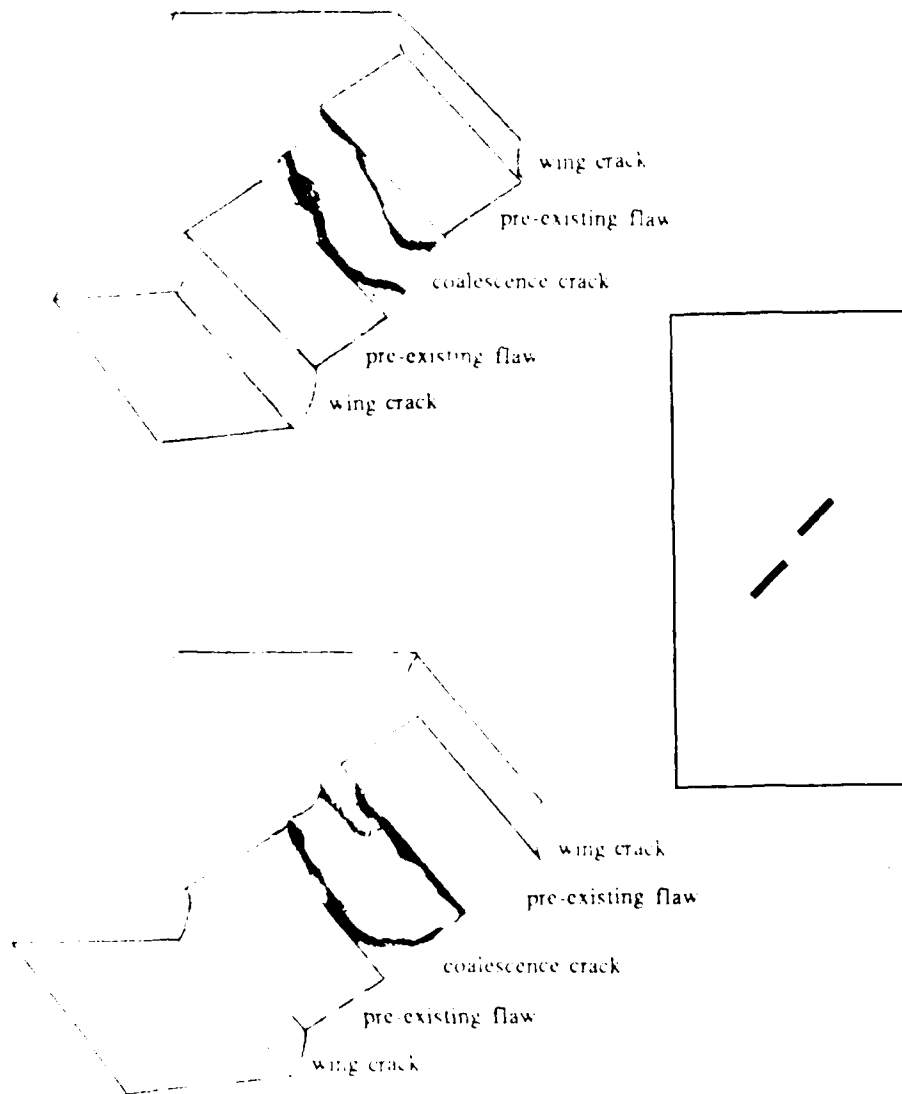
Figure 3.54   Surface morphologies of cracks in cut specimens with 45°-60° flaws.

Chapter 4
Analysis and Coalescence Model Development

4.1 Introductory Remarks

The modelling process described in this chapter consisted of three stages. In the first stage, stress fields around interacting flaws were established using analytical elastic solutions for plates with elliptical holes under far-field uniform loading (Section 4.2). Correlations were made between these stress fields and the observed loads at which wing cracks initiated. However, it was noted in the previous chapter that coalescence always came *after* wing cracks had propagated. Thus, in the second stage of the modelling process, the stress/strain fields around flaws *with* wing cracks were determined (Section 4.3). The finite element method was used in the stress analyses since analytical solutions do not exist for open flaws with wing cracks. By correlating the observed coalescence mechanisms in the experiments with the calculated stress/strain fields around interacting flaws with wing cracks, the suitability of some fracture modelling approaches was evaluated. A smeared-crack damage model coupled with a strain-based failure criterion was found to be most appropriate for modelling coalescence. Therefore, in the final stage of the modelling process, a strain-based damage model was formulated, implemented and used to simulate the experiments described in Chapter 3 (Section 4.4). Very satisfactory agreement between the observed and simulated fracture behavior was achieved.

4.2 Interacting Elliptical Flaws in an Infinite Medium under Far-field Compression

4.2.1 Solution for a single flaw

The stress field around an elliptical flaw under far-field uniaxial stress has been derived by Inglis (1913) and is given in elliptical coordinates by the following expressions (K. Chang, 1981):

$$\sigma_{\xi\xi} + \sigma_{\eta\eta} = p\,e^{2\xi_o}\cos 2\beta$$
$$+ \alpha p\left[\sinh 2\xi\left(1 - e^{2\xi_o}\cos 2\beta\right) - e^{2\xi_o}\sin 2\beta\sin 2\eta\right] \tag{4.1a}$$

$$\sigma_{\xi\xi} - \sigma_{\eta\eta} = \alpha^2 p\left[-\sinh 2\xi\left(\cosh 2\xi_o - \cos 2\beta\right) + \sinh 2\xi\cos 2\eta\left(1 - e^{2\xi_o}\cos 2\beta\right)\right.$$
$$- e^{2\xi_o}\sin 2\beta\sin 2\eta\cosh 2\xi - e^{2\xi_o}\sinh 2\xi\sinh 2(\xi - \xi_o)\cos 2(\eta - \beta)$$
$$\left. - e^{2\xi_o}\sin 2\eta\cosh 2(\xi - \xi_o)\sin 2(\eta - \beta)\right] \tag{4.1b}$$
$$+ 2\alpha p\,e^{2\xi_o}\cosh 2(\xi - \xi_o)\cos 2(\eta - \beta)$$

$$\tau_{\xi\eta} = \frac{1}{2}\alpha^2 p\left[\left(1 - e^{2\xi_o}\cos 2\beta\right)\sin 2\eta\cosh 2\xi - \sin 2\eta\left(\cosh 2\xi_o - \cos 2\beta\right)\right.$$
$$+ e^{2\xi_o}\sin 2\beta\cos 2\eta\sinh 2\xi + e^{2\xi_o}\sinh 2\xi\cosh 2(\xi - \xi_o)\sin 2(\eta - \beta)$$
$$\left. - e^{2\xi_o}\sin 2\eta\sinh 2(\xi - \xi_o)\cos 2(\eta - \beta)\right] \tag{4.1c}$$
$$- \alpha p\,e^{2\xi_o}\sin 2(\eta - \beta)\sinh 2(\xi - \xi_o)$$

where $\alpha = (\cosh 2\xi - \cos 2\eta)^{-1}$, ξ and η are elliptical coordinates as illustrated in Fig. 4.1, ξ_o is the elliptical coordinate corresponding to the boundary of the elliptical flaw, p is the far-field stress (see Fig. 4.1, positive for tension, negative for compression) and β is the angle between the applied stress and the major axis of the elliptical flaw (i.e. it is equal to 90° minus the flaw inclination angle; the latter as defined in Chapter 3).

119

The observed trends in wing crack initiation loads (Section 3.3.2) can be compared to predictions using the single flaw solutions. At the edge of the flaw, $\sigma_{\xi\xi} = 0$ so that $\sigma_{\eta\eta}(\xi=\xi_0)$ can be obtained by substituting $\xi=\xi_0$ into Eqn. (4.1a):

$$\sigma_{\eta\eta}(\xi = \xi_0) = \alpha p \left[\cos 2\beta + \sinh 2\xi_0 - e^{2\xi_0} \cos(\beta - \eta) \right]. \qquad (4.2)$$

This stress has a maximum value at some η as shown in Fig. 4.2 where it is plotted against η for flaw inclination angles $30°$, $45°$ and $60°$ (corresponding to $\beta = 60°$, $45°$ and $30°$, respectively). Assuming that fracturing initiates when the maximum tensile hoop stress reaches a critical value (the maximum tensile principal stress criterion or MTPS) and using Fig. 4.2, one would predict that crack initiation will occur at a lower load for the $60°$ inclined flaw when compared to the $45°$ and $30°$ inclined flaws. However, quite the opposite was observed in the experiments described in the previous chapter. The wing cracks for the $30°$ inclined flaws were visible at lower loads when compared to wing cracks growing from $60°$ inclined flaws (see Fig. 3.41 for wing crack inititiation loads from experiments). A possible explanation for this apparent disagreement between the theoretical prediction and the experimental observation will be given below.

Figs. 4.3(a), (b) and (c) are tensile principal stress vector plots for the three flaw inclinations $30°$, $45°$ and $60°$. All three cases were computed for the same compressive load, the magnitude of which is shown at the bottom of the figures. These figures show that high tensile stresses exist around the flaw tips but eventually decrease away from the flaw tips. Furthermore, even though the hoop stresses are higher for the $60°$ flaw, the tensile stresses decrease more rapidly with distance from the flaw tip for the $60°$ flaw when compared to the $45°$ and $30°$ flaws. The wing cracks growing from the $60°$ flaws may initiate at lower loads but need only propagate a short distance to reach an area with lower tensile stresses. On the other hand, wing cracks growing from the $45°$ and $30°$ flaws would have to propagate a longer distance before reaching an area with lower tensile

120

stresses. Thus, it is no longer surprising that wing cracks were _visible_ at lower loads for the 45° and 30° flaws even though Eqn. (4.2) predict lower wing crack _initiation_ loads for 60° flaws. This highlights the fact that the determination of the "critical flaw inclination" in compressive fields must be based on studies of _crack growth_ rather than _crack initiation_ alone, as Hoek and Bieniawski (1965) and others have pointed out. This is the primary difference between fracture studies in compression and tension: "failure" in tension generally coincides with crack initiation due to unstable crack propagation that is frequently associated with predominantly tensile stress fields. On the other hand, propagation in compressive fields is usually stable, i.e., a load increase is required for cracks to lengthen.

4.2.2 Superposition of Stress Fields from Two Elliptical Flaws

A first-order approximation of the stress field around two interacting elliptical flaws can be obtained by superposing the fields given by Eqns. (4.1a-c). This superposition procedure is applied to various flaw geometries and the results for 30°-75° and 30°-45° arrangements are shown in Figs. 4.4 and 4.5, respectively. These are major principal stress vector plots and only the tensile stresses are plotted. Note that tensile stresses exist within the ligament area between the flaws and, if a fracture criterion based on maximum tensile principal stresses is adopted, crack initiation and growth in that region may be expected. However, tensile stresses of about the same magnitude exist in areas outside of the ligament (encircled areas in Figs. 4.4 and 4.5) although no such cracking was observed in these regions for 30°-45° (see photograph in Fig. 3.12) and 30°-75° flaws. It is possible that these latter tensile stresses were relieved by wing crack growth which always preceded coalescence (see Section 3.2.1). However, the relief of tensile stresses _within_ the ligament by wing crack growth is just as likely. Thus, there is obviously a need to determine stress fields around interacting flaws _after_ wing crack growth before any definite conclusions can

121

be drawn regarding the mechanism underlying the experimentally observed fracture coalescence. In recognition of this need, a series of finite element studies were performed to determine the stress fields around pre-existing flaws <u>with</u> wing cracks. The results of these analyses are described in the following section.
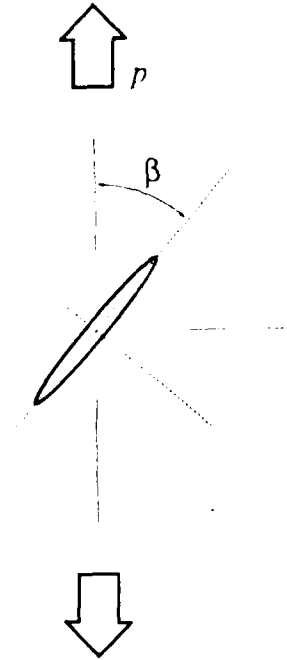
Figure 4.1(a)   Inclined elliptical flaw subjected to uniaxial compression
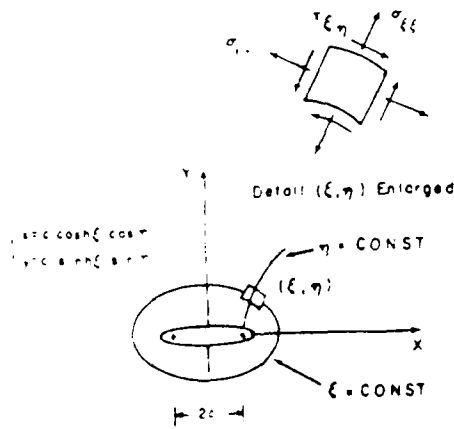
Figure 4.1(b)   Definition of elliptical coordinates
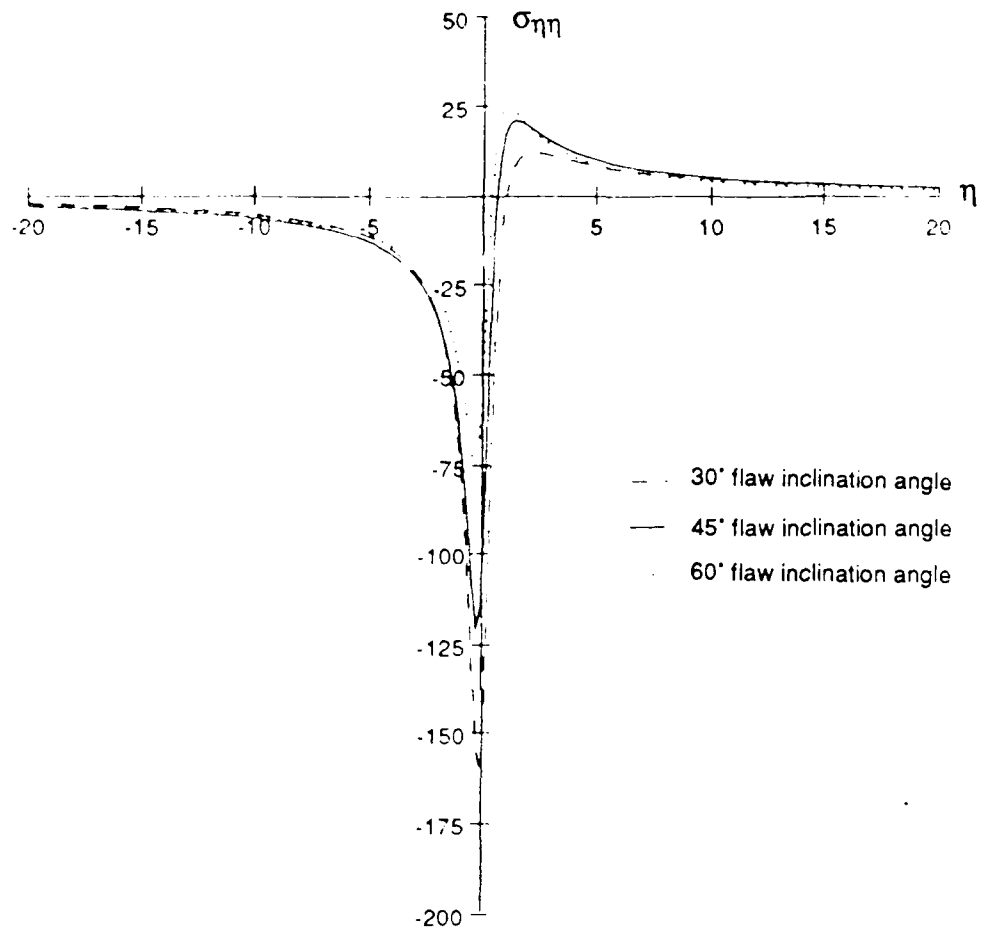
Figure 4.2   Hoop stress ($\sigma_{\eta\eta}$) as a function of η, plotted for 30°, 45° and 60° flaw inclination angles.

124
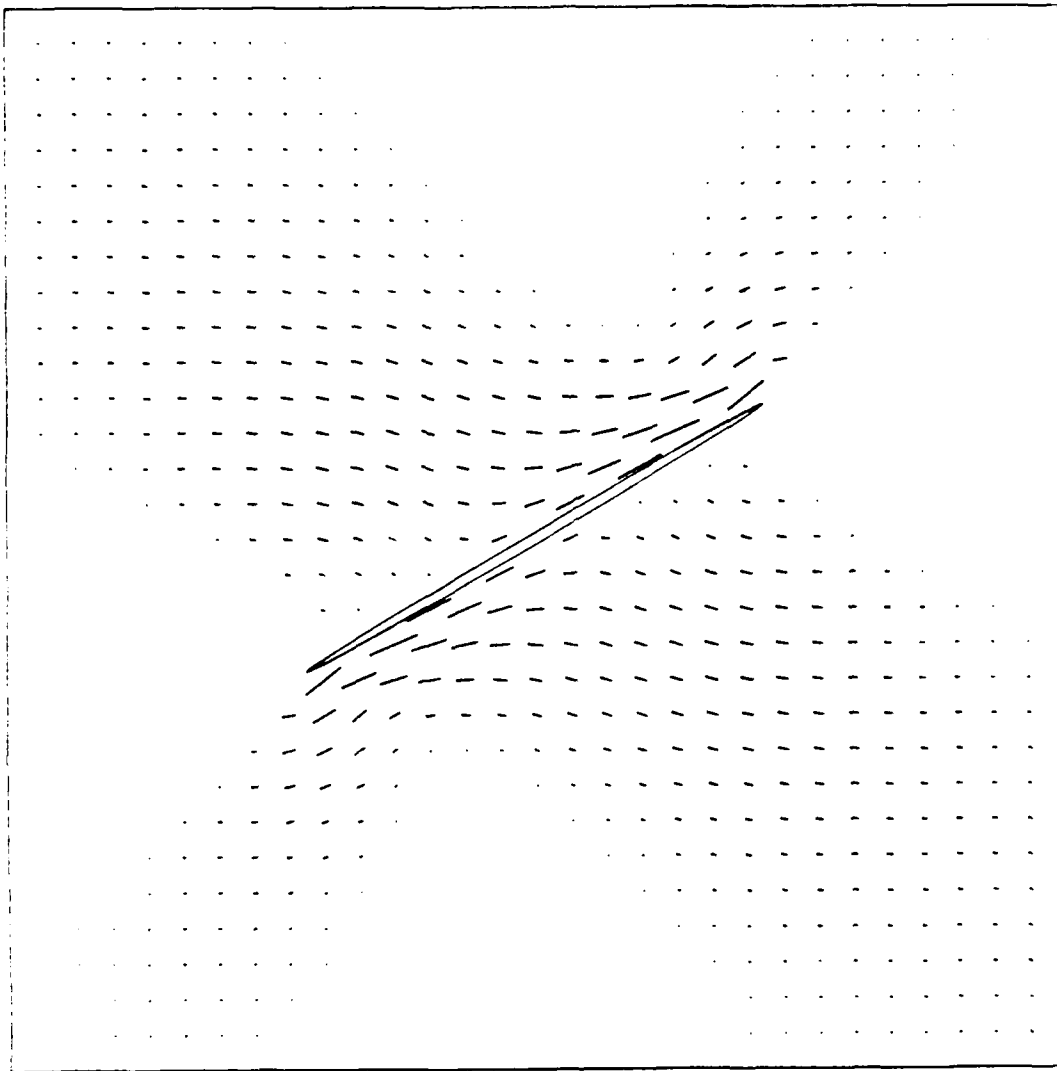
Scale: Applied Vertical Compressive Stress

Figure 4.3(a)   Vector plot of the maximum principal stresses around a 30° flaw under far-field uniaxial compression (only tensile stresses are plotted).

125
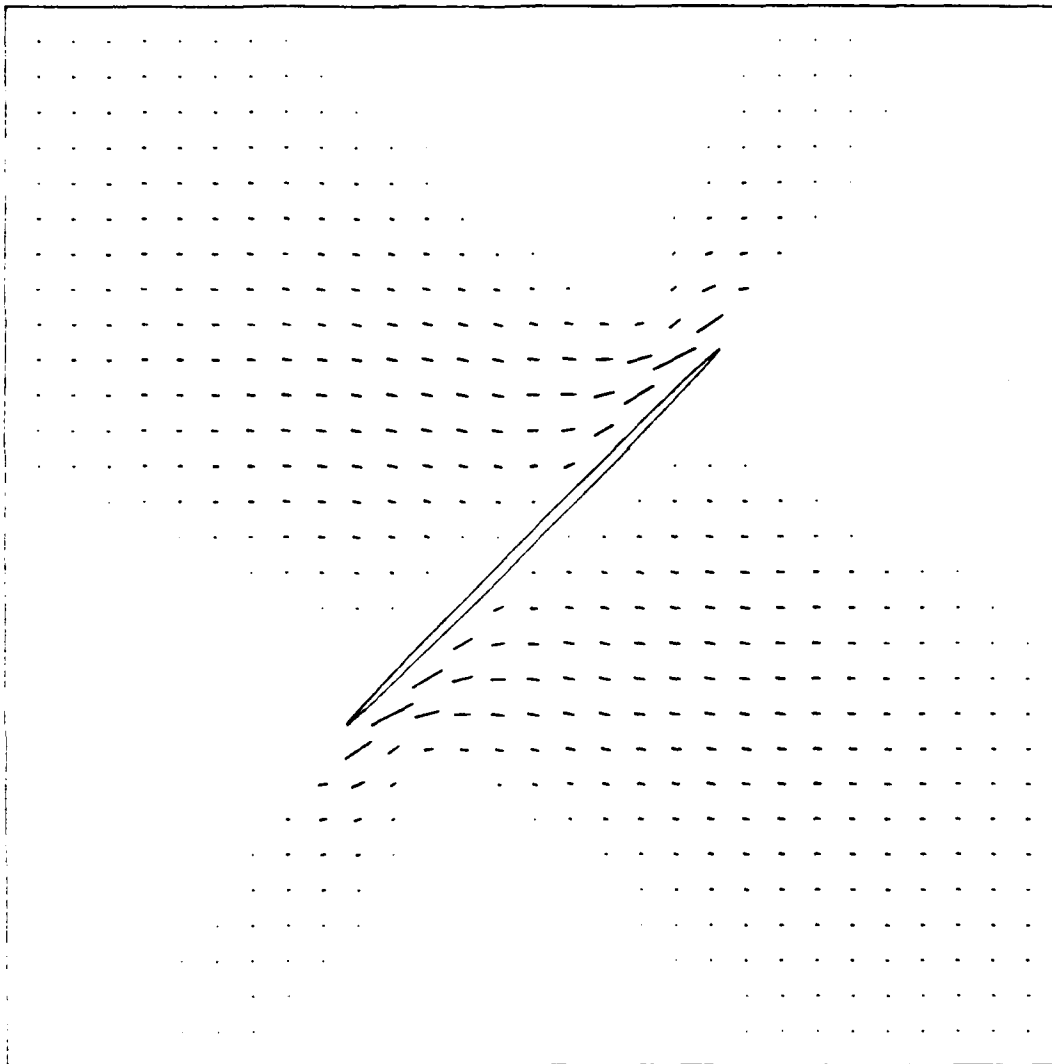
Scale: Applied Vertical Compressive Stress

Figure 4.3(b)   Vector plot of the maximum principal stresses around a 45° flaw under far-field uniaxial compression (only tensile stresses are plotted).
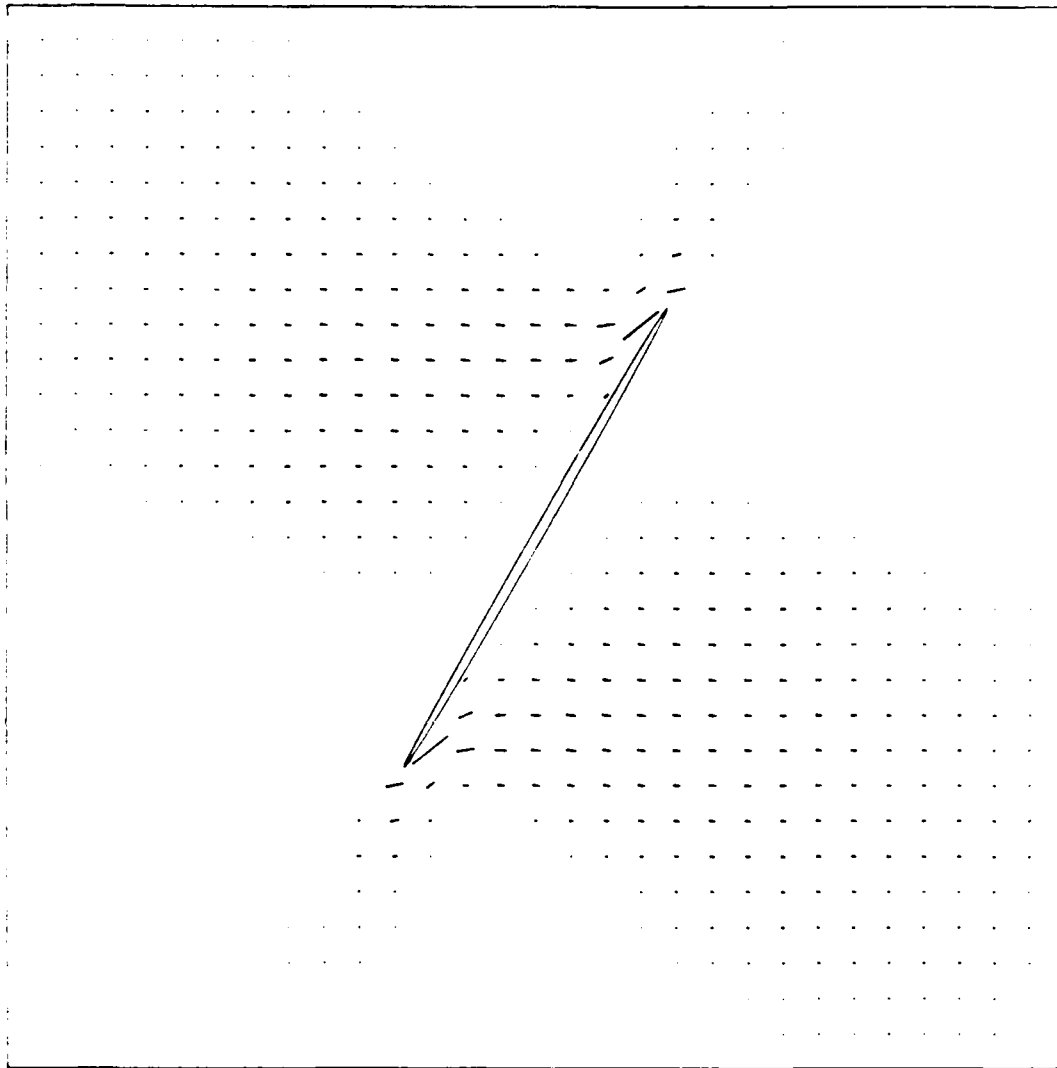
—— Scale: Applied Vertical Compressive Stress

Figure 4.3(c)   Vector plot of the maximum principal stresses around a 60° flaw under far-field uniaxial compression (only tensile stresses are plotted).

127
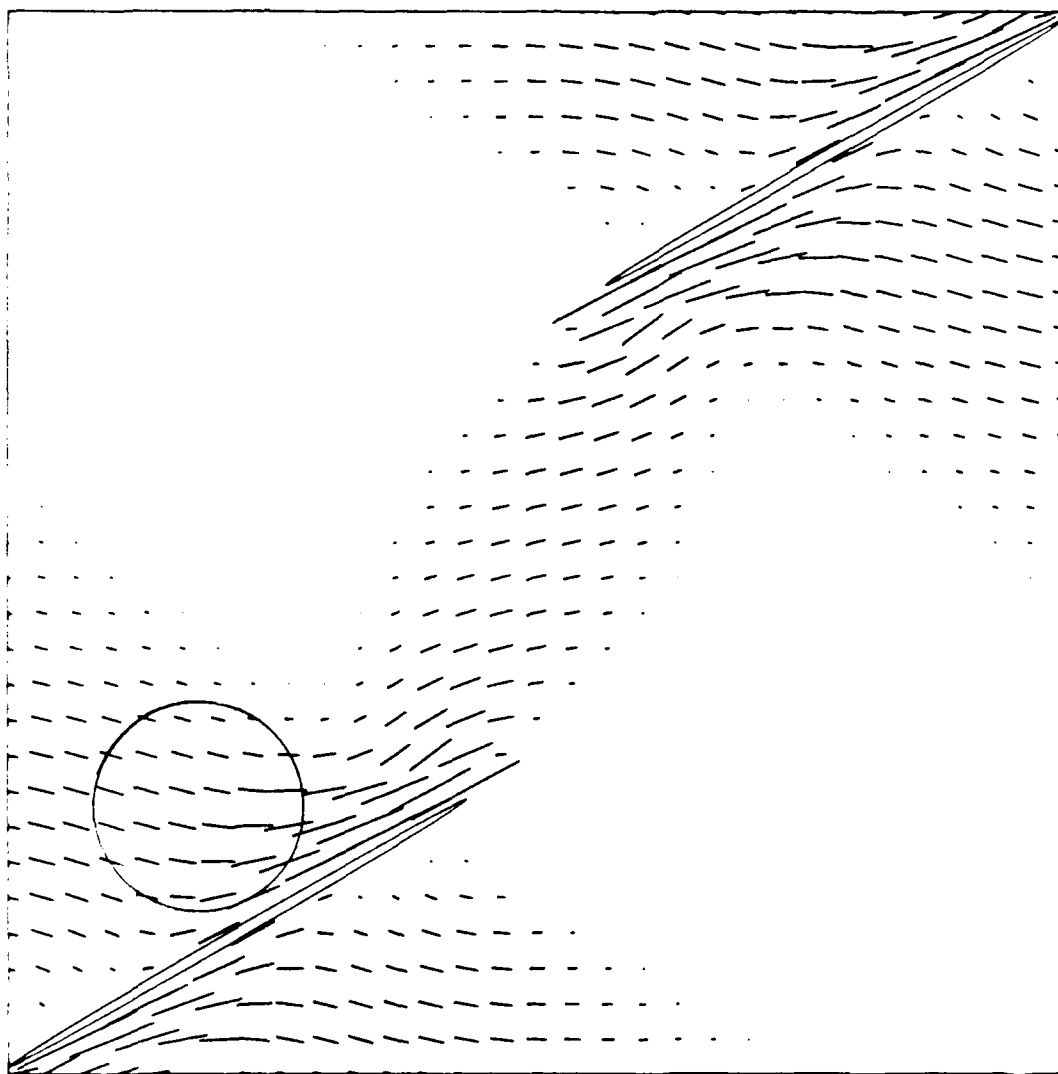
Scale: Applied Vertical Compressive Stress

Figure 4.4   Vector plot of maximum principal stresses around 30°-75° flaws under far-field uniaxial compression (obtained from superposing single flaw solution; only tensile stresses are plotted). High tensile stresses away from ligament area exist within encircled region.

128
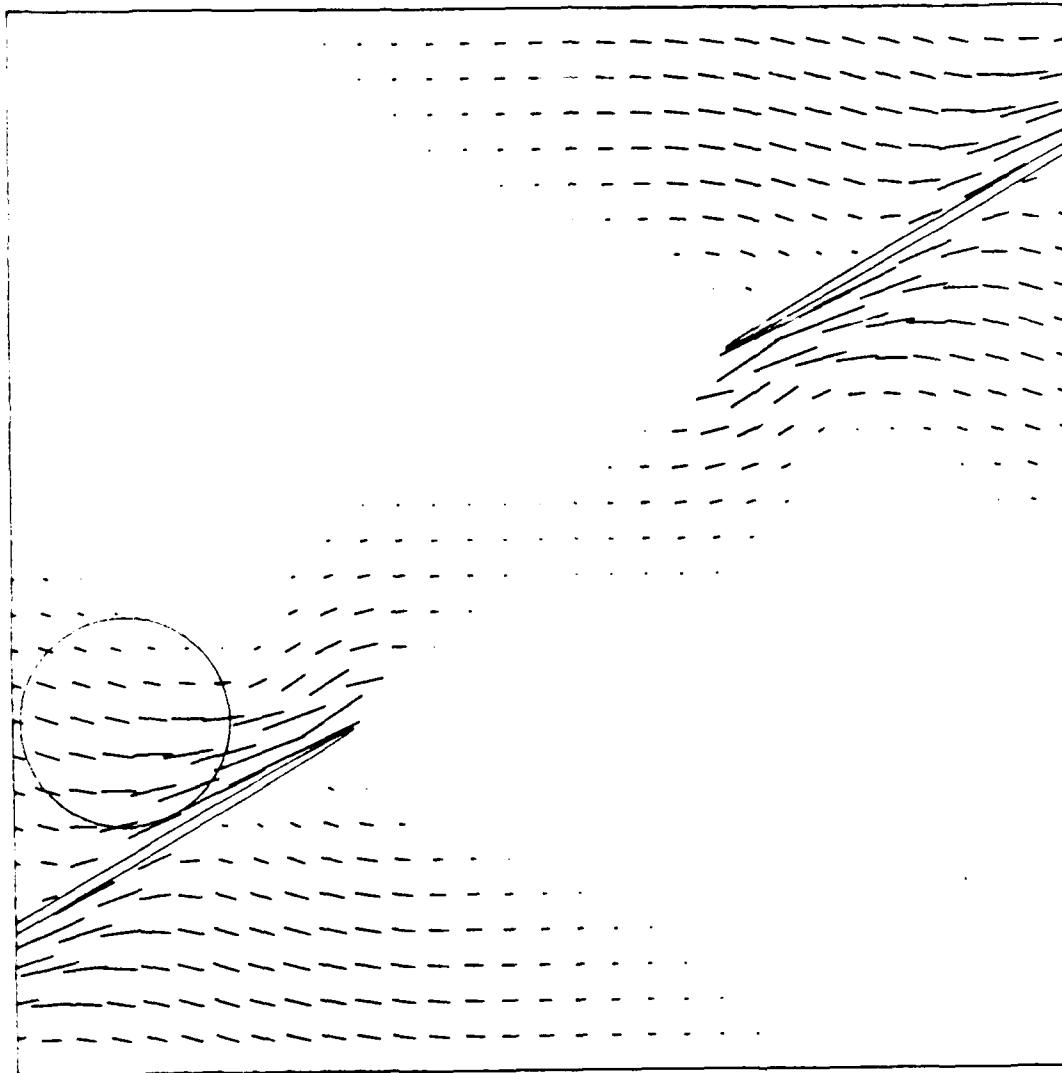
Scale: Applied Vertical Compressive Stress

Figure 4.5   Vector plot of maximum principal stresses around 30°-45° flaws under far-field uniaxial compression (obtained from superposing single flaw solution; only tensile stresses are plotted). High tensile stresses away from ligament area exist within encircled region.

4.3 Stress Analysis of Interacting Flaws with Wing Cracks

4.3.1 Description of Finite Element Models

In order to establish the stress conditions after wing crack growth and prior to crack coalescence, finite element analyses were performed on a number of the flaw arrangements that were studied experimentally. A linear elastic material was assumed for these analyses, primarily because there were no signs of gross material plasticity or damage prior to coalescence in the experiments. A Young's modulus of approximately 6200 MPa was obtained from the experimental load-displacement curves and used in the analyses. A Poisson's ratio of 0.28 was assumed.

Fig. 4.6 shows an example of a finite element model for determining the stress field around pre-existing flaws (in this case, 30°-75° flaws) with wing cracks. It must noted that no attempt was made to simulate the actual growth of the wing cracks. Successful simulations of wing crack growth have already been reported by Ingraffea and Heuze (1980). Furthermore, the experiments in Chapter 3 have shown that the growth of wing cracks did not directly result in coalescence although it may have indirectly affected the crack growth by altering the stress field around the pre-existing flaws. The elements on each side of the thickened lines in the finite element model shown in Fig. 4.6 are not "connected" by common nodes, thus forming a discontinuity corresponding to the wing cracks along these lines. The shape of the wing cracks in the analyses were obtained from photographs of wing cracks taken during the experiments.

All elements in the model are plane strain, 8-noded quadrilaterals. Special singular elements were not used around the wing cracks tips because the stress intensity factors at the wing crack tips were only of secondary importance in this study.

130

The following boundary conditions were applied on the finite element model: zero vertical displacements along the bottom edge, and a uniform distributed load on the top surface, the magnitude of which was approximately the measured coalescence load (in MPa) for the flaw geometry being analyzed (see Section 3.3.2). It was assumed that the flaws were sufficiently far from the top and bottom edges of the block such that the exact distribution of loads on these edges did not significantly affect the stresses around the flaws. Because the model is two-dimensional, three-dimensional effects in the experiments were neglected.

4.3.2   Linear Elastic Analysis Results and Discussion

The analyses showed that tensile stresses in the ligament areas were not relieved by wing crack growth, a possibility that was raised in Section 4.2.2. This can be seen in Figs. 4.7 and 4.8 which are major principal stress vector plots generated from the analysis results for $30°-75°$ and $30°-45°$ flaws (compare with Fig. 4.4 and 4.5).

The stress fields after wing crack growth were combined with experimental observations to look into possible models that would reproduce the observed coalescence process. Two possible approaches to modelling the coalescence fracture are: (1) a discrete crack approach coupled with the maximum tensile principal stress fracture criterion (MTPS), and (2) a smeared crack approach coupled with MTPS. The appropriateness of each approach will now be discussed.

In a discrete crack approach coupled with MTPS, cracks are assumed to propagate perpendicular to the direction of maximum tensile principal stress. The coalescence cracks shown in the photographs of $30°-75°$ flaws (see Figs. 3.24 and 3.25) do lie perpendicular to the stress vectors plotted in Fig. 4.7. Thus, in the case of the $30°-75°$ flaws, the discrete

131

crack approach coupled with MTPS may succesfully simulate coalescence. However, the path of the coalescence cracks shown in the photographs of 30°-45° flaws (see Figs. 3.23 and 3.27) do not run perpendicular to the tensile stress vectors in Fig. 4.8. This is contrary to what is assumed when applying the discrete crack approach.

In a smeared crack approach coupled with MTPS, cracks initiate and propagate along regions where the highest tensile principal stresses exist. However, in contrast to the discrete crack approach, these cracks do not necessarily grow perpendicular to the direction of the tensile stresses. If the magnitude of the maximum tensile principal stress is used as a criterion for smeared cracking, this approach would predict cracks initiating within the shaded regions on the stress contour plots for the 30°-75° and 30°-45° flaws (see Figs. 4.9 and 4.10). The approximate path of the observed coalescence crack between the 30°-75° flaws, superposed on the stress contour plot in Fig. 4.9, does intersect this shaded region. On the other hand, this is not true for coalescence crack between the 30°-45° flaws which is schematically shown in Fig. 4.10. Further evidence against the use of the smeared crack approach coupled with MTPS is shown in Fig. 4.11(a). This is an expanded view of the stress field around the 30°-45° flaws in Fig. 4.10. Regions of high tensile stresses exist outside of the ligament between the flaws (refer to dotted areas in Fig. 4.11(a)). Thus, a smeared crack approach coupled with MTPS would predict cracking in these areas whereas no such cracking was observed in the experiments (see photograph in Fig. 3.12). Unless the actual stress field is different from the computed stress field in the case of the 30°-45° flaws, it appears that the smeared crack approach using MTPS will not successfully simulate the coalescence crack for this geometry.

A third possibility for modelling fracture coalescence is a smeared crack approach coupled with a maximum tensile principal strain fracture criterion (MTPSN). The suitability of this approach can also be tested against the observed fracture patterns and the results of the stress analyses described above. Fig. 4.11(b) is a contour plot of the major

principal strains from the same analysis that was used to generate the principal stress contour plot in Fig. 4.11(a)[1]. Aside from areas around the wing crack tip where a singularity was introduced by the sharpness of the crack tip, regions of highest tensile strains exist only at the tips of the pre-existing flaws and within the ligament zone. Thus, a smeared crack approach based on MTPSN will predict cracking to initiate at all the flaw tips and, from the internal flaw tips, to propagate through the ligament zone forming a coalescence crack (see dotted regions in Fig. 4.11(b)). In the experiments, it was impossible to verify that the coalescence cracks initiated at the flaw tips due to the rapidity with which these appeared in most flaw geometries, unless the observed spalling is taken as an indicator of smeared cracking at the flaw tips. However, the observed coalescence crack does approximately fall within the highly strained (dotted) region marked in Fig. 4.11(b).

It is also interesting to compare the spreading of cracked regions predicted by tensile stress-based and tensile strain-based smeared crack models. Without running a non-linear analysis, one could obtain an idea of this spreading from the linear elastic stress and strain contour plots as shown in Figs. 4.12 through 4.17. In these plots, regions between stress/strain contour lines that would "connect" the internal flaw tips have been shaded. These shaded regions would then approximate the extent of smeared cracking prior to coalescence. In all the flaw geometries, the estimated smeared crack regions in the principal strain contour plots (Figs. 4.12(a) through 4.17(a)) are more localized than those in the principal stress contour plots (Figs. 4.12(b) through 4.17(b)). Thus, the strain-

---

[1] It must be emphasized that the maximum principal strain is not simply proportional to the maximum principal stress in the same direction, e.g., $\varepsilon_1 = \frac{\sigma_1}{E} - \frac{\nu}{E}(\sigma_2 + \sigma_3)$. This implies that tensile principal strains are higher for regions where there is a combination of large tensile and compressive stresses.

133

based smeared crack approach would simulate a more localized damaged region that is closer to what was observed in the experiments. A similar observation regarding more localized predictions of damage for a strain-based criterion was made by Tvergaard (1982) in his study of void coalescence in ductile materials.
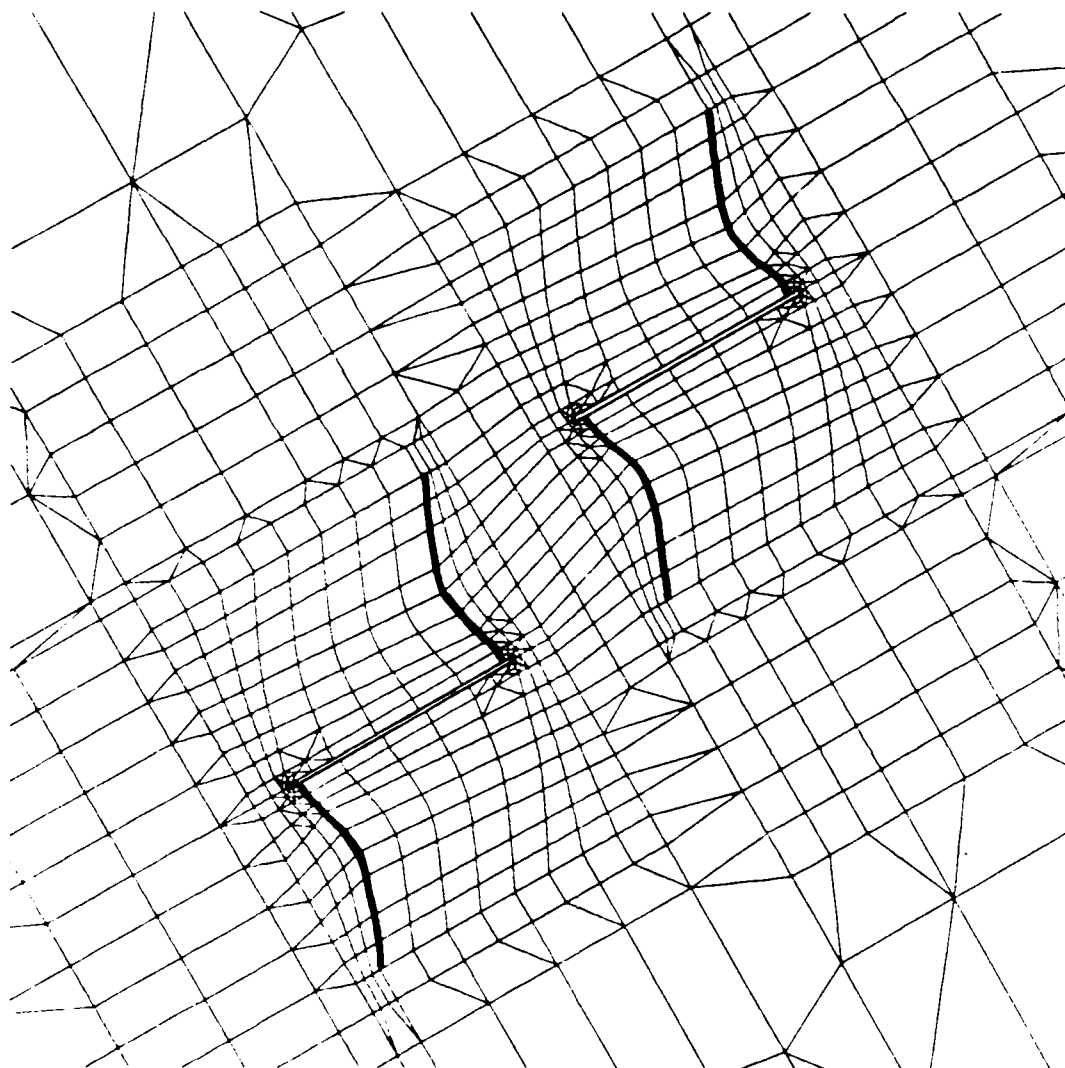
Figure 4.6   Finite element model for determining stress field around 30°-75° flaws with wing cracks.

135
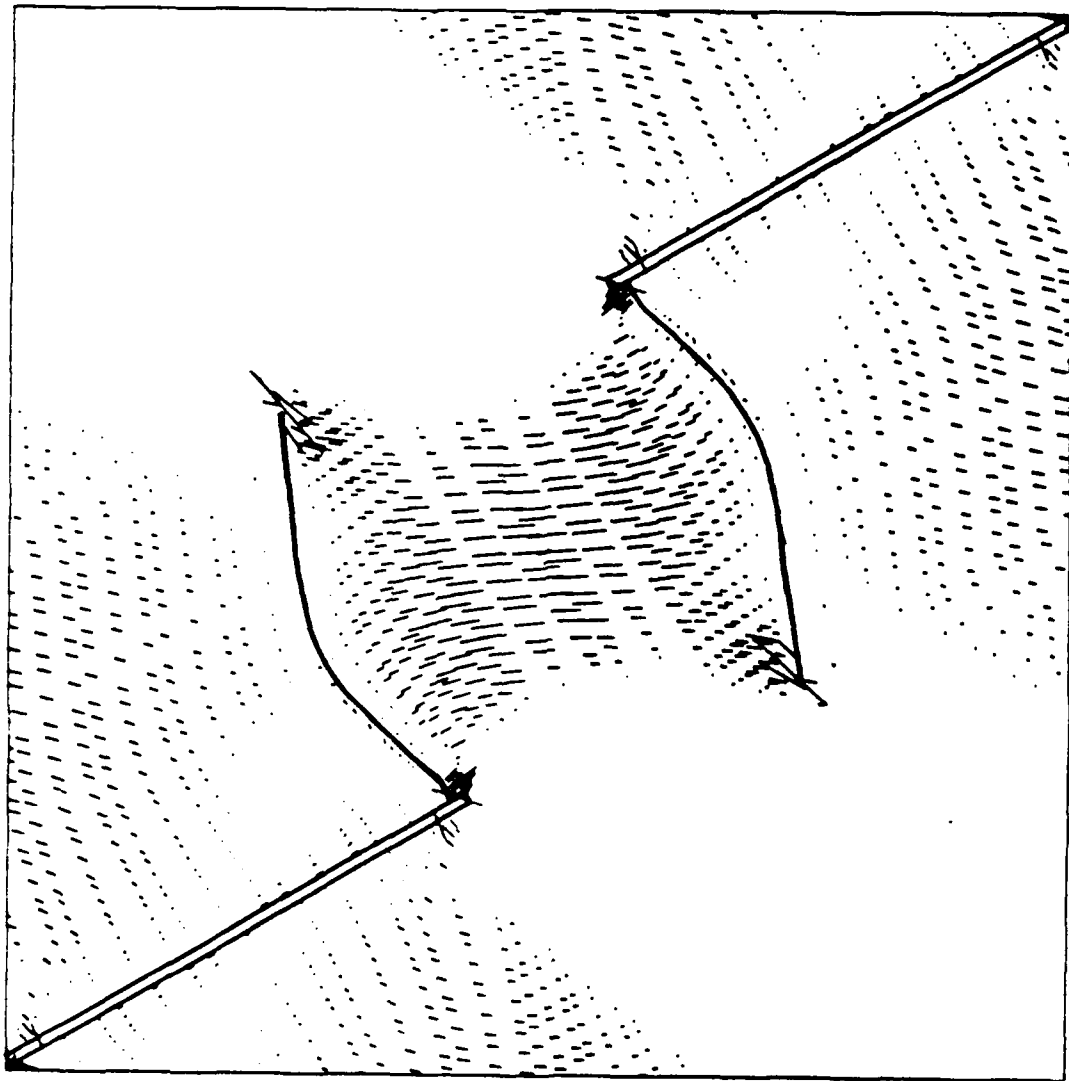
Scale: Applied Vertical Compressive Stress

Figure 4.7   Vector plot of maximum principal stresses around 30°-75° flaws with wing cracks under far-field uniaxial compression (obtained from finite element analysis results; only tensile stresses are plotted).
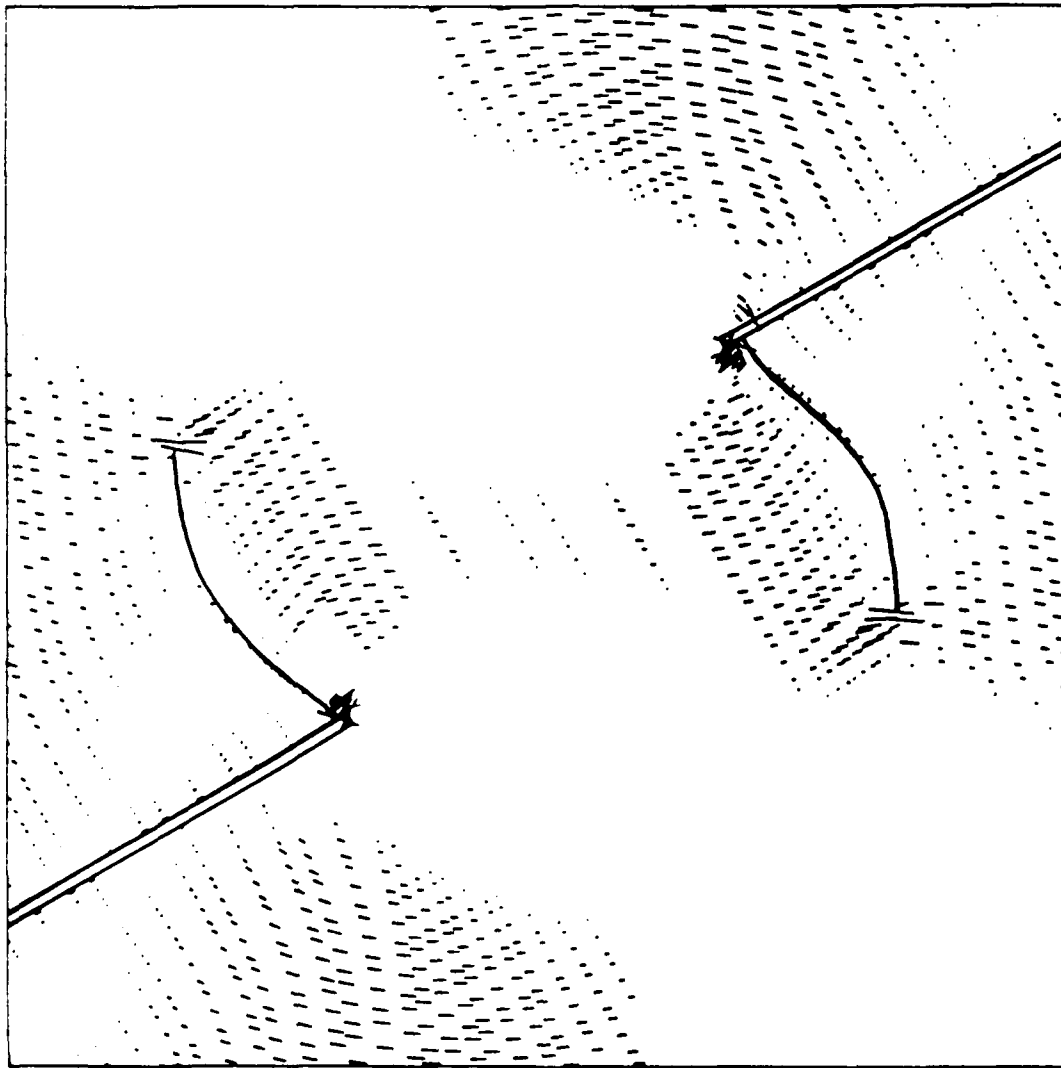
Scale: Applied Vertical Compressive Stress

Figure 4.8   Vector plot of maximum principal stresses around 30°-45° flaws with wing cracks under far-field uniaxial compression (obtained from finite element analysis results; only tensile stresses are plotted).

137
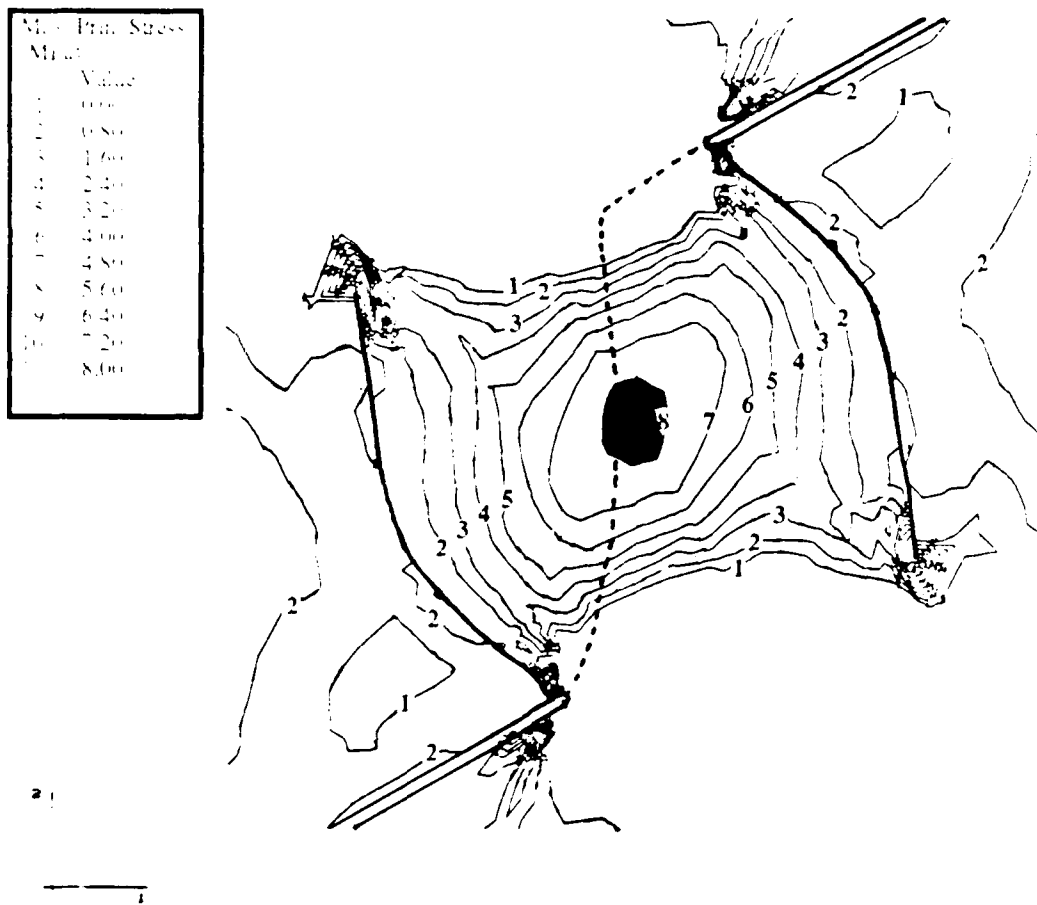
Figure 4.9   Contour plot of maximum principal stresses around 30°-75° flaws with wing cracks under far-field compression. Dotted line marks approximate path of coalescence crack observed in experiments. Region with highest maximum principal stresses has been shaded.

138
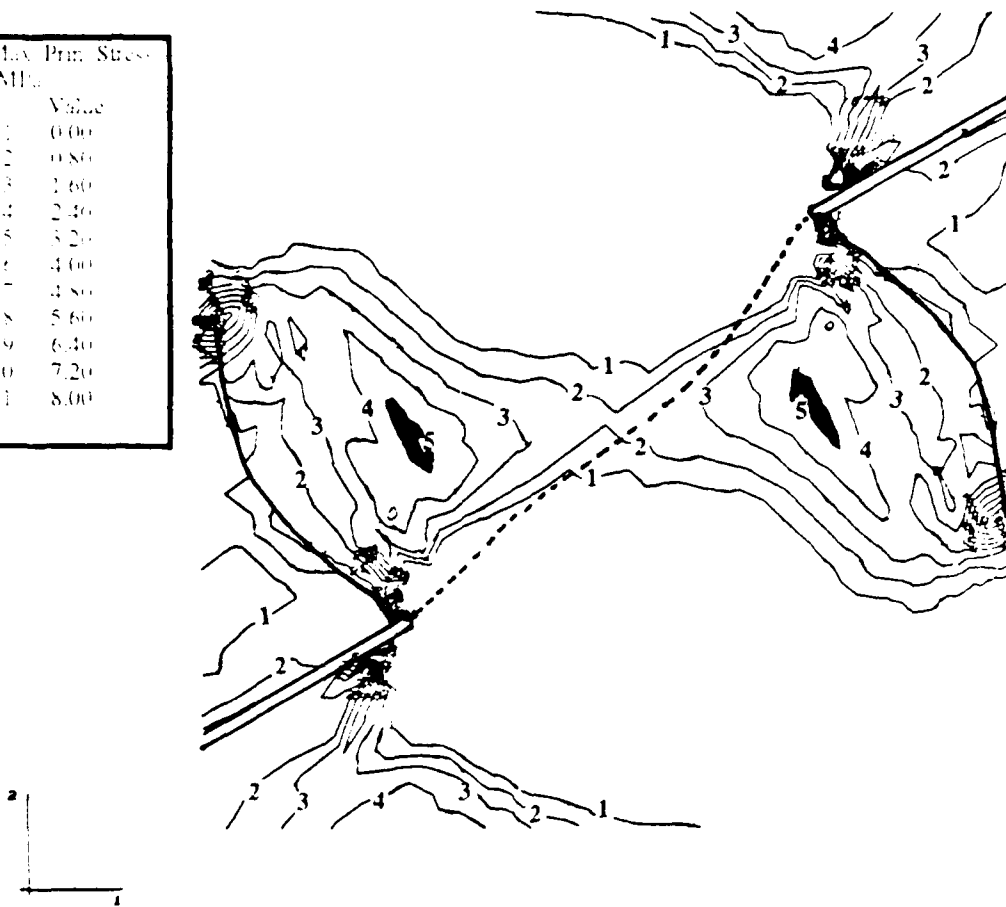
Figure 4.10 Contour plot of maximum principal stresses around 30°-45° flaws with wing cracks under far-field compression. Dotted line marks approximate path of coalescence crack observed experiments. Regions with highest maximum principal stresses have been shaded.

139
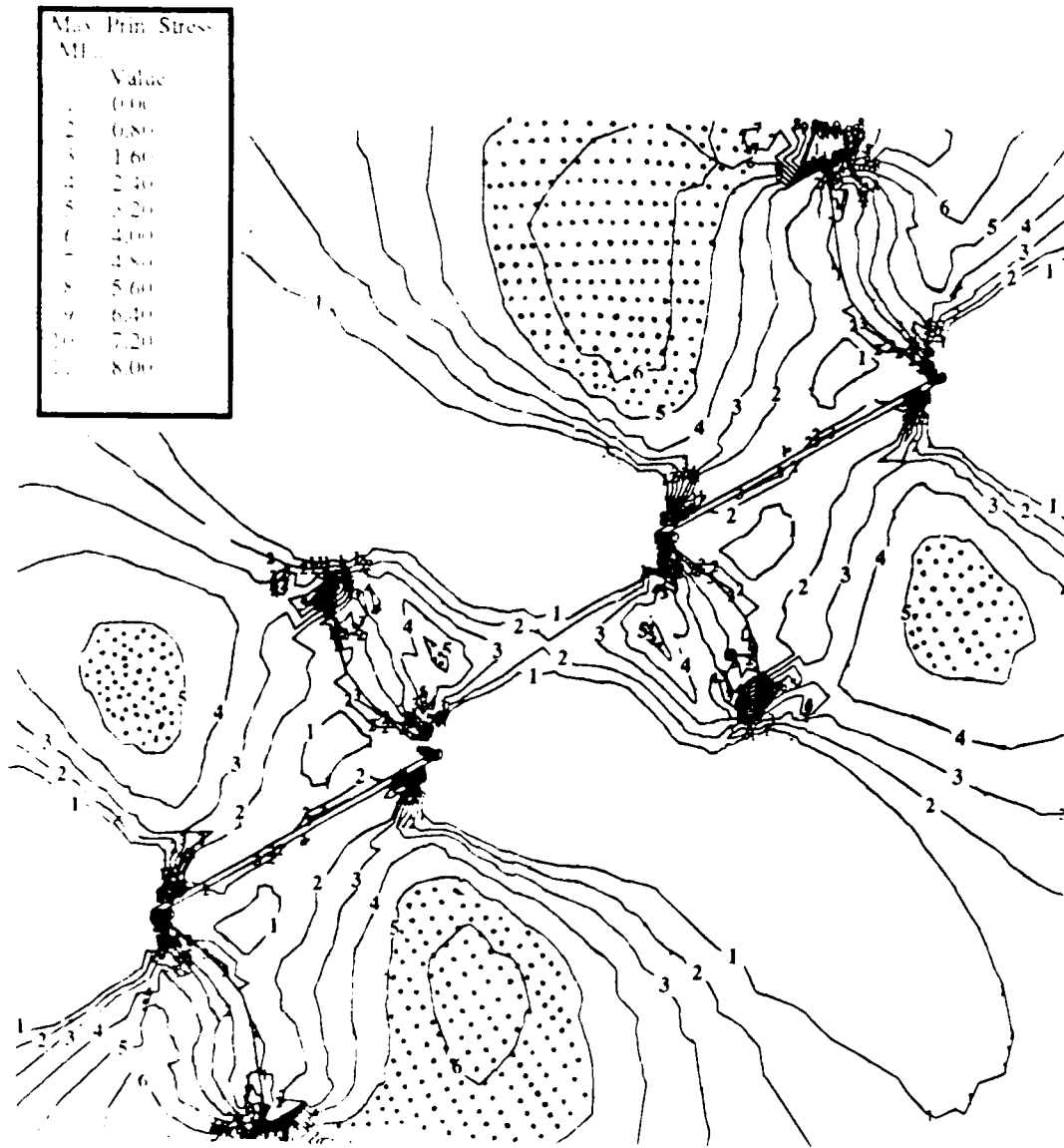
Figure 4.11(a) Expanded contour plot of maximum principal stresses around 30°-45° flaws with wing cracks under far-field compression. Highest maximum principal stresses exist within dotted regions.
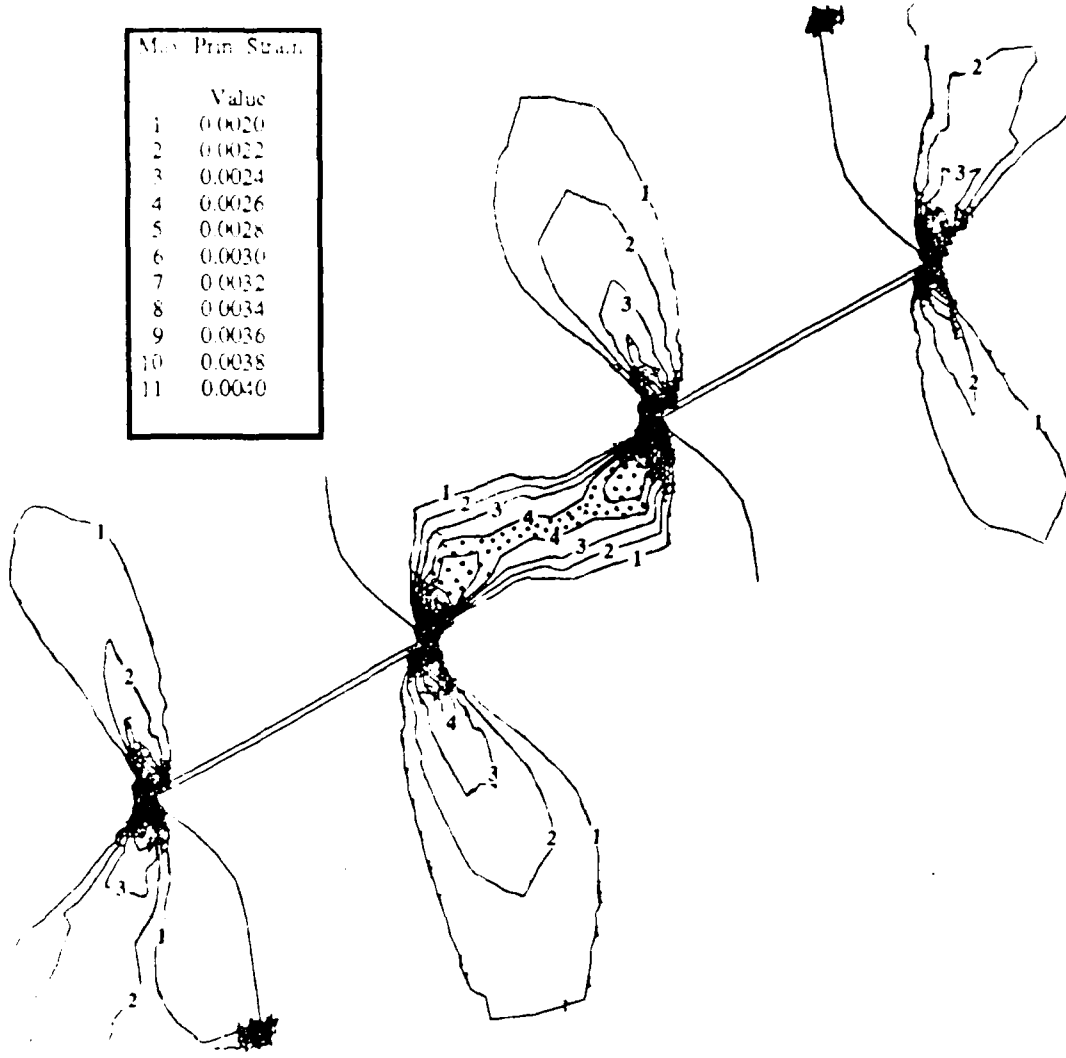
Figure 4.11(b) Expanded contour plot of maximum principal strains around 30°-45° flaws with wing cracks under far-field compression. Highest maximum principal strains exist within dotted regions.
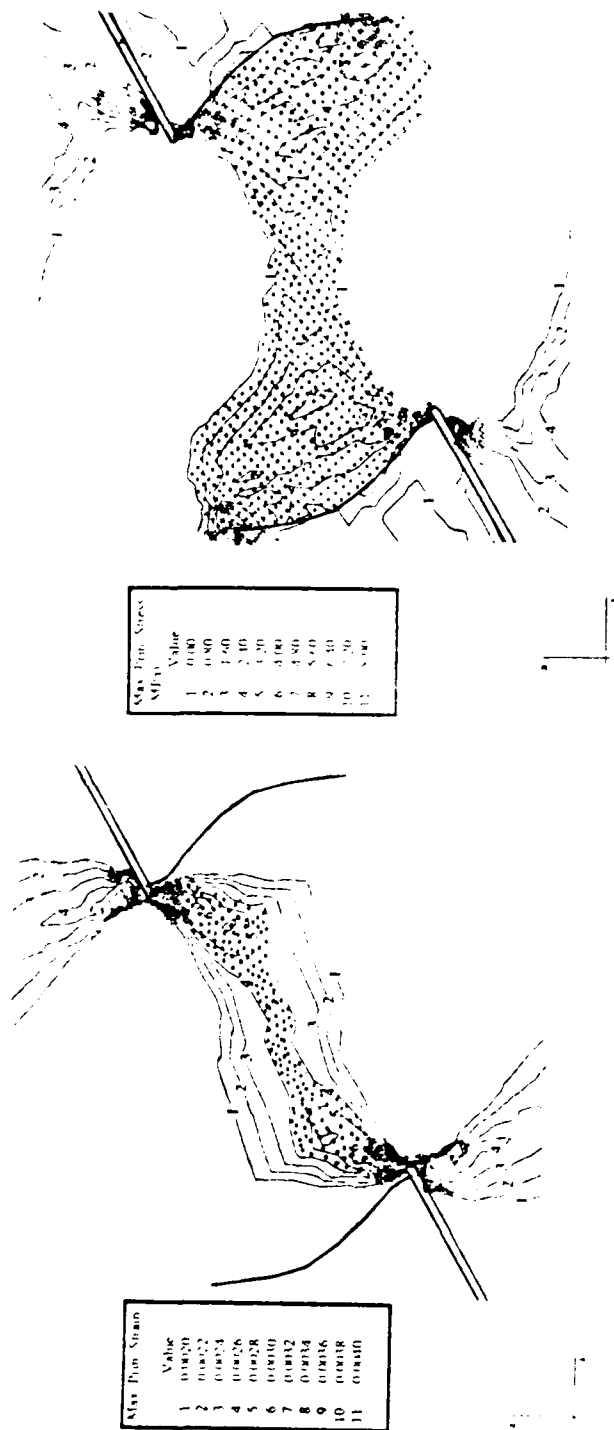
Figure 4.12   Approximate regions of smeared cracking between 30°-45° flaws with wing cracks obtained using (a) maximum principal strain and (b) maximum principal stress criteria.
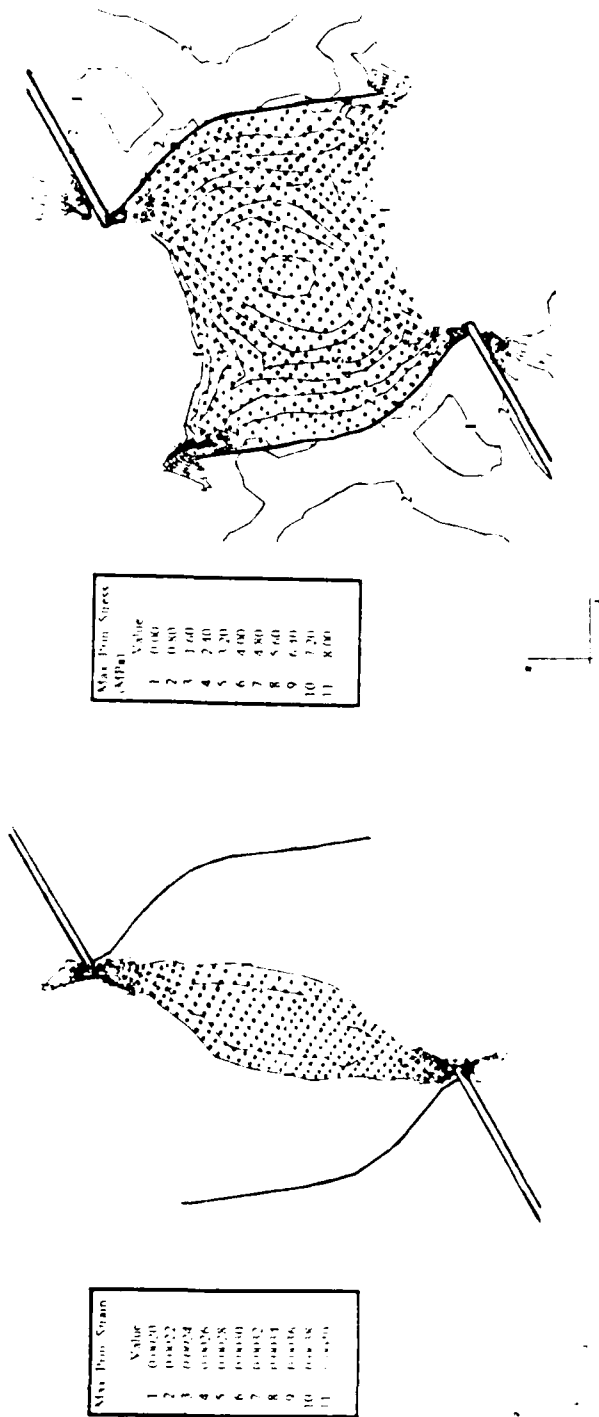
Figure 4.13   Approximate regions of smeared cracking between 30°-75° flaws with wing cracks obtained using (a) maximum principal strain and (b) maximum principal stress criteria.

143
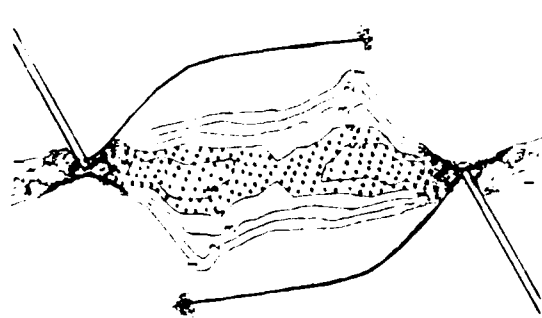
Figure 4.14   Approximate regions of smeared cracking between 30°-90° flaws with wing cracks obtained using (a) maximum principal strain and (b) maximum principal stress criteria.

144
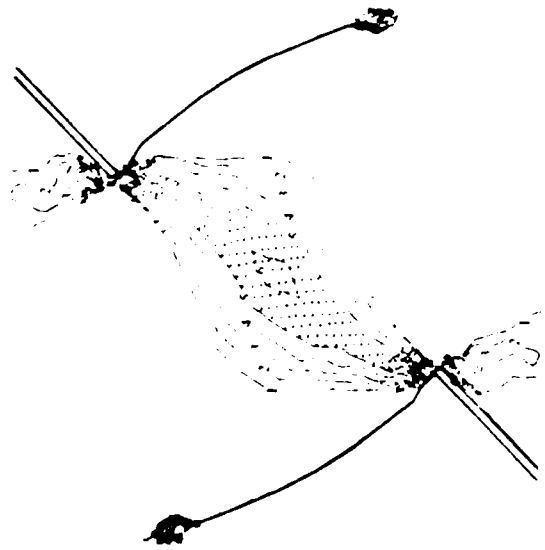
Figure 4.15   Approximate regions of smeared cracking between 45°-60° flaws with wing cracks obtained using (a) maximum principal strain and (b) maximum principal stress criteria.
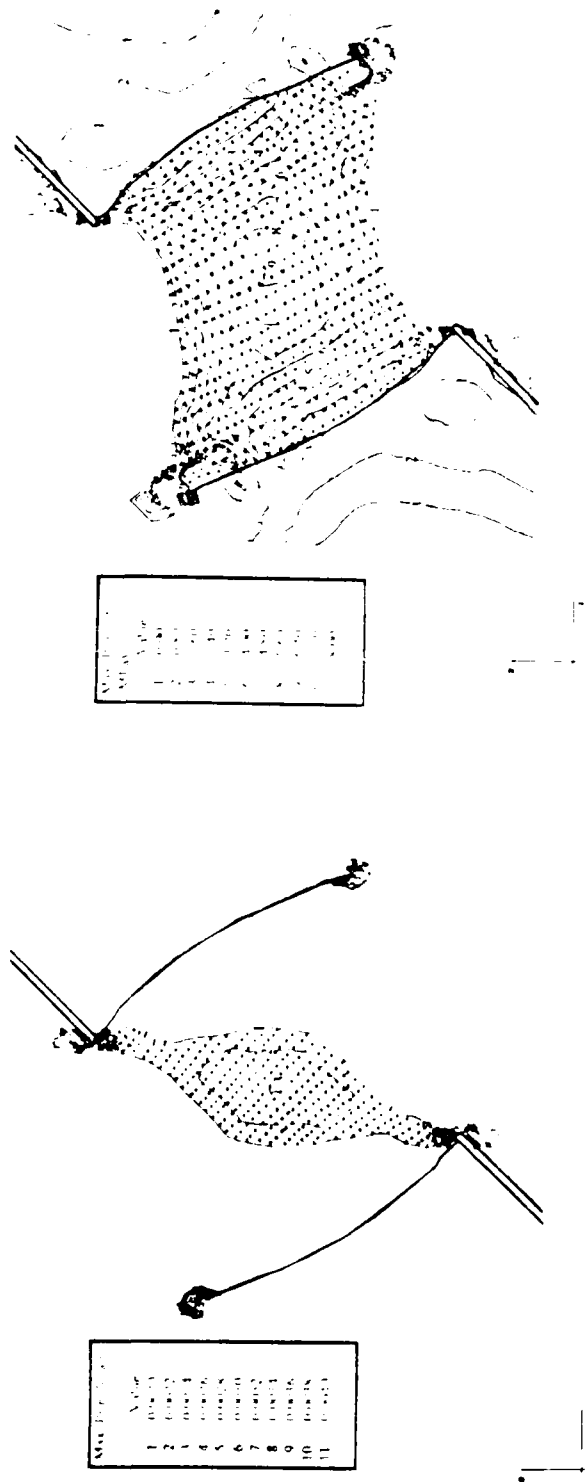
Figure 4.16   Approximate regions of smeared cracking between 45°-75° flaws with wing cracks obtained using (a) maximum principal strain and (b) maximum principal stress criteria.

146
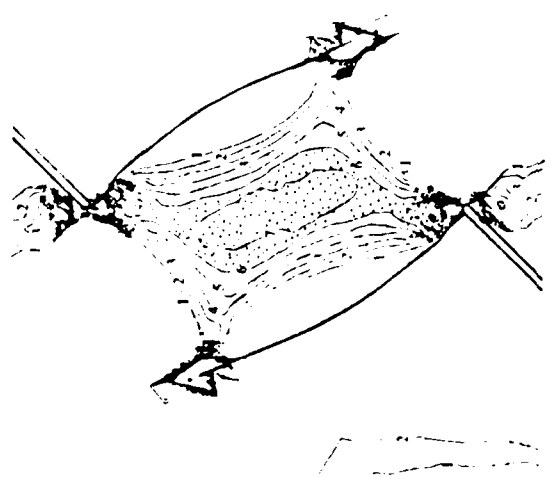
Figure 4.17   Approximate regions of smeared cracking between 45°-90° flaws with wing
cracks obtained using (a) maximum principal strain and (b) maximum
principal stress criteria.

147

4.3.3 A Comparison Between Stress and Strain-Based Failure Criteria

One interesting implication of using strains rather than stresses is the "automatic" incorporation of the biaxial strength effect which, in the case of combined tensile/compressive stress states, refers to a decrease in the tensile stress at failure due to a compressive stress that is applied normal to the direction of tension. According to the MTPS fracture criterion, fracturing occurs at a point where the maximum principal stress reaches a critical value, say σ_t. On the other hand, the MTPSN fracture criterion assumes that fracturing occurs at a point where the maximum principal strain reaches a critical value, say ε_t. Both of these values can be obtained from a uniaxial tensile test such that, if the material is elastic prior to fracture, the critical strain and stress are simply related by $\sigma_t = E\varepsilon_t$ where E is the modulus of elasticity.

Consider now the biaxial stress condition:

$$\sigma_3 = -k\sigma_1$$

where k is a positive number. According to MTPS, fracturing will occur when $\sigma_1 = \sigma_t$, regardless of the value of σ_3. However, a different result will be obtained with MTPSN since both σ_1 and σ_3 will be contributing to the maximum principal strain as follows:

$$\varepsilon_1 = \frac{1}{E}(\sigma_1 - \nu\sigma_3) = \frac{1}{E}(1 + \nu k)\sigma_1 \tag{4.3}$$

but since $\sigma_t = E\varepsilon_t$, MTPSN will predict fracturing at

$$\sigma_1 = \frac{\sigma_t}{1 + \nu k} \tag{4.4}$$

Since k is a positive number, then the fracture stress according to MTPSN is lower than the fracture stress according to MTPS. Furthermore, Eqn. (4.4) implies that the fracture stress

is reduced when k is not equal to zero. Thus, the biaxial strength effect follows from using the maximum principal strain as a failure criterion.

If both stresses are tensile, i.e., k is a negative number, then σ_1 would be greater than σ_t in Eqn. (4.4). Thus, the use of MTPSN for biaxial stress conditions where both stresses are tensile would result in a fracture stress that is higher than the uniaxial fracture stress. However, no experimental data on the biaxial tensile strength of rocks exist to support or refute this result. Fortunately, in this study, there are virtually no such biaxial tensile stress conditions around the flaws, except possibly around the wing crack tips where the stresses are singular. Within the ligament areas of the non-overlapping flaws, the stress conditions are such that always one of the principal stresses is compressive.

Another interesting consequence of using MTPSN is the possibility of tensile fracture in completely compressive fields. Consider an axisymmetric stress state given by:

$$\begin{aligned} \sigma_3 &= -p \\ \sigma_1 &= \sigma_2 = -q \end{aligned}$$
(4.5)

where p and q are positive values. Assuming that the material is elastic, the maximum principal strain is:

$$\varepsilon_1 = \varepsilon_2 = \frac{1}{E}\left(\sigma_1 - v\sigma_2 - v\sigma_3\right) = \frac{1}{E}\left[q(v-1) + vp\right].$$
(4.6)

Thus, the principal strain ε_1 is tensile if:

$$\frac{p}{q} \geq \frac{1-v}{v}.$$
(4.7)

Table 4.1 shows values of minimum p/q ratios for which tensile fracturing could occur in a completely compressive stress field according to MTPSN.

Table 4.1 Minimum $\frac{p}{q}$ values to cause tensile strain failure

v	$\frac{p}{q}$
0.1	9.0
0.2	4.0
0.3	2.33

Substituting $\varepsilon_1 = \varepsilon_t$ in Eqn. (4.6) and rearranging, an expression for the failure envelope in (p - q) vs q space is obtained:

$$p - q = \frac{E\varepsilon_t}{v} + \frac{q}{v}(1 - 2v) \tag{4.8}$$

If q = 0 in Eqn. (4.2), then p = uniaxial compressive strength = σ_c:

$$p = \sigma_c = \frac{E\varepsilon_t}{v} \tag{4.9}$$

Using Eqn. (4.9), a normalized failure envelope can be obtained from Eqn. (4.8):

$$\frac{p - q}{\sigma_c} = 1 + \frac{q}{\sigma_c}\frac{(1 - 2v)}{v} \tag{4.10}$$

The above failure envelope, with $v = 0.15$ and $v = 0.28$, is compared to the Griffith and Modified Griffith criteria, as well as experimental data summarized by McClintock and Walsh (1962) in Fig. 4.18. It is rather striking that the failure envelope constructed using the MTPSN fracture hypothesis fits the data as well as the Modified Griffith criterion.
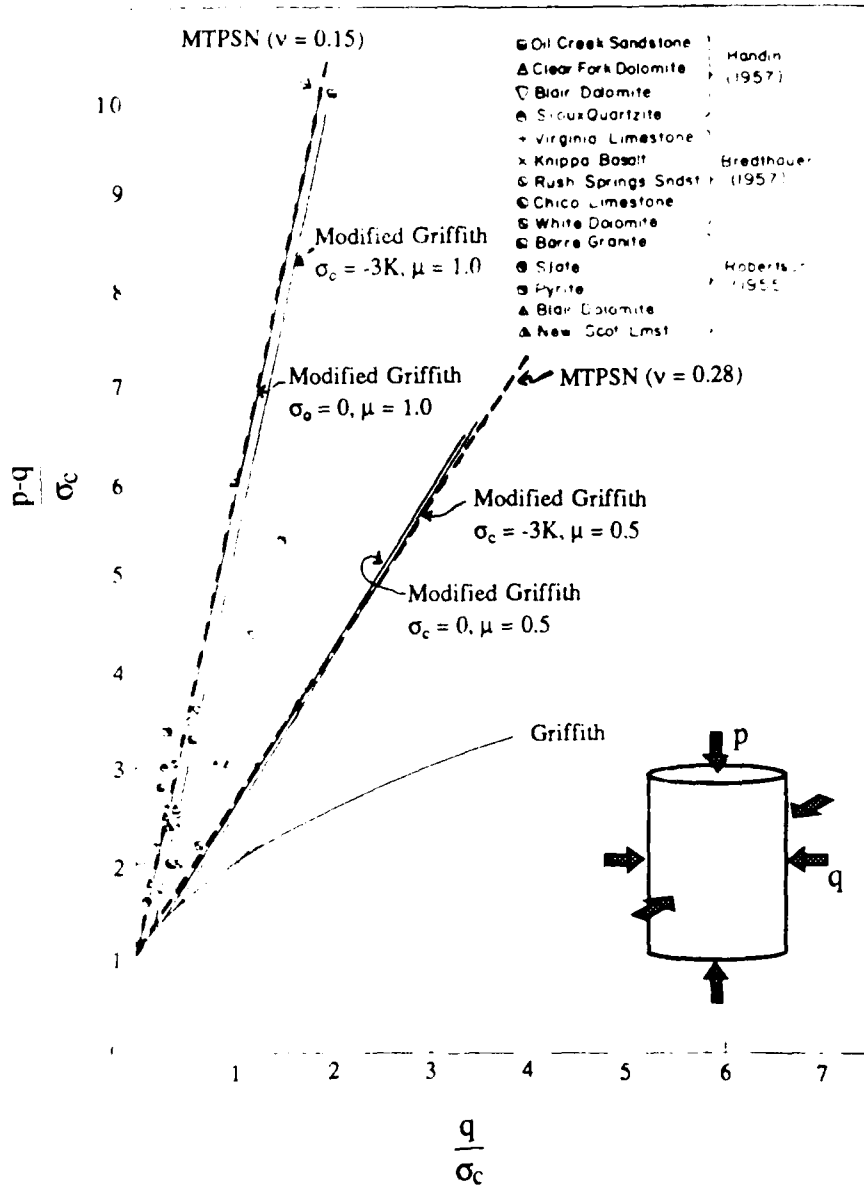
Figure 4.18   Comparison of Maximum Tensile Principal Strain, Modified Griffith and Griffith failure criteria with data from literature (from McClintock and Walsh, 1962). Note: σ_0, K and μ are material parameters required by the Modified Griffith criterion, σ_c is the uniaxial compressive strength.

151

4.4 A Tensile Strain-Based Damage Model for Coalescence

It has been shown in previous sections that the smeared crack approach coupled with the maximum tensile principal strain criterion (MTPSN) seemed to provide a good framework for modelling coalescence. The development, implementation and application of a strain-based smeared crack/damage model for coalescence is described below.

4.4.1 Model Formulation and Implementation

The underlying assumption of damage mechanics is that material damage causes a degradation of the material stiffness. For uniaxial conditions, it is assumed that the stiffness degrades according to the following rule [Kachanov, 1958; Lemaitre, 1986]:

$$\sigma = (1 - D)E\varepsilon \tag{4.11}$$

where σ = uniaxial tensile stress, ε = uniaxial tensile strain, E = elastic modulus of the undamaged material, and D = a scalar internal state variable which measures damage. The values of D can range from 0 through 1, corresponding to "no damage" through "completely damaged" states. For a strain-based damage model, the variable D is assumed to be a direct function of strain and, in this study, the following functional form for D was used:

$$D = \begin{cases} 0 & \text{for } \varepsilon < \varepsilon_o \\ H(\varepsilon) & \text{for } \varepsilon \geq \varepsilon_o \end{cases} \tag{4.12}$$

where $H(\varepsilon)$ is defined as follows:

$$H(\varepsilon) = 1 - \frac{1}{\exp\left[A\left(\dfrac{\varepsilon}{\varepsilon_o} - 1\right)\right]}. \tag{4.13}$$

152

This function has the following mathematical characteristics: (1) when $\varepsilon \leq \varepsilon_0$, $D = 0$, and (2) as $\varepsilon \to \infty$ $D \to 1$. The parameter ε_0 is a damage threshold value while the parameter A, determines the rate at which D approaches 1 as strain increases. The parameter A is limited to values greater than 0 and less than or equal to 1[2]. Plots of D vs ε for A = 0.5, 0.75 and 1.0 are shown in Fig. 4.19 for $\varepsilon_0 = 0.003$. Note that larger A values cause a more rapid increase in damage with increasing strain.

Substituting Eqn. (4.12) into Eqn. (4.13), an expression for the variation of stress versus strain is obtained:

$$\sigma = \begin{cases} E\varepsilon & \text{for } \varepsilon < \varepsilon_o \\[2ex] \dfrac{E\varepsilon}{\exp\left[A\left(\dfrac{\varepsilon}{\varepsilon_o} - 1\right)\right]} & \text{for } \varepsilon \geq \varepsilon_o \end{cases} \qquad (4.14)$$

This stress-strain relation is plotted in Fig. 4.20 for $\varepsilon_0 = 0.003$, and A = 0.5, 0.75, 1.0. As expected, higher A values give rise to more pronounced strain-softening behavior.

The damage model defined above had to be revised in order to account for the fact that damage is irreversible, i.e., damage does not decrease with material "unloading". The simplest possible model that accounts for damage irreversibility is to assume that the material unloads along a linear elastic line defined by the damage state prior to unloading. To illustrate this loading-unloading concept, consider the stress-strain curve in Fig. 4.21 on

---

[2] Justification for this limitation in A-values will be given later.

which the strain state at time t [3], $\varepsilon(t)$, denoted by ε^* is marked. Since $\varepsilon^* > \varepsilon_0$, the corresponding damage, $D(\varepsilon^*)$ can be found from Eqns. (4.12) and (4.13). If the strain decreases after time t, then the material will follow the linear curve given by $\sigma = [1-D(\varepsilon^*)]E\varepsilon$ (see Fig. 4.21). If the strain increases again after unloading (reloading), then the material will still follow the curve defined by $\sigma = [1-D(\varepsilon^*)]E\varepsilon$ until ε becomes greater than ε^*. This implies that damage is irreversible during unloading and that while $\varepsilon < \varepsilon^*$, no additional damage occurs during reloading. Therefore, ε^*, the strain prior to unloading which can also be defined as the maximum strain in the loading history of the material, is like a "moving" damage threshold. Once $\varepsilon > \varepsilon^*$, damage starts to increase again and the material follows the non-linear curve as shown in Fig. 4.21.

The damage model which accounts for these loading/unloading conditions is defined below [following Simo and Ju, 1987]:

1)   Define $\varepsilon^*(t)$ = a damage threshold that varies with time t. Its initial value is ε_0.

2)   Define a damage surface, analogous to the yield surface in plasticity, such that strain states must always be within this surface:

$$\varepsilon(t) - \varepsilon^*(t) \leq 0 \qquad\qquad (4.15)$$

This implies that once $\varepsilon(t)$ exceeds ε_0, $\varepsilon(t) \to \varepsilon^*(t)$, i.e., the damage threshold is set to the maximum strain in the loading history of the material.

---

[3]The variable t refers to "pseudo-time" in the loading history [Bathe, 1982]. It has nothing to do with viscous effects.

154

3)   Damage evolution is determined by the following rule:

$$\dot{D} = \begin{cases} \varepsilon \dfrac{\partial H(\varepsilon)}{\partial \varepsilon} & \text{if } \varepsilon(t) = \varepsilon*(t) \\ \\ 0 & \text{if } \varepsilon(t) < \varepsilon*(t) \end{cases} \qquad (4.16)$$

where $H(\varepsilon)$ is defined by Eqn. (4.13). Eqn. (4.16) is equivalent to specifying that damage increases (i.e., $\dot{D} > 0$) only when the strain exceeds the current damage threshold $\varepsilon*(t)$. Eqn. (4.12) still holds but is stated in differentiated form in Eqn. (4.16).

The uniaxial constitutive law defined by Eqn. (4.11) can be generalized to multiaxial stress/strain conditions by replacing the scalars by their tensorial representations:

$$\sigma_{ij} = (1 - D) C_{ijkl} \varepsilon_{kl} \qquad (4.17)$$

Here, C_{ijkl} are the components of the elastic constitutive tensor. Note that the damage variable, D, is still a scalar. Thus, the model used in this study assumes isotropic damage, as opposed to anisotropic models in the literature which assume that damage can be represented by higher order tensors [e.g., Krajcinovic, 1986; Valanis, 1990]. The damage evolution equations also need to be generalized for multiaxial conditions. This can be done by replacing ε in Eqn. (4.16) with ε_{eq}, a scalar function of the strain components sometimes referred to as an equivalent strain [Simo and Ju, 1987]. Thus, for multiaxial stress/strain states, the damage evolution equations are:

$$
\dot{D} = \begin{cases} \dot{\varepsilon}_{\alpha_i} \dfrac{\partial H(\varepsilon_{\alpha})}{\partial \varepsilon_{\alpha_i}} & \varepsilon_{eq} = \varepsilon^*(t) \\[20pt] 0 & \varepsilon_{eq} < \varepsilon^*(t) \end{cases} \tag{4.18}
$$

$$
\text{where } H(\varepsilon_{\alpha}) = 1 - \frac{1}{\exp\left[A\left(\dfrac{\varepsilon_{\alpha_i}}{\varepsilon_o} - 1 \right) \right]}
$$

In this study, the equivalent strain was defined as follows:

$$
\varepsilon_{eq} = \begin{cases} \varepsilon_1 & \text{for } \varepsilon_1 > 0 \\[15pt] 0 & \text{for } \varepsilon_1 \leq 0 \end{cases} \tag{4.19}
$$

where ε_1 = major principal strain. Eqn. (4.19) implies that only tensile strains cause material damage in accordance with the MTPSN fracture hypothesis.

The preceding damage model was implemented as a material subroutine of the finite element program ABAQUS [ABAQUS User's Manual, 1990]. The latter program uses a Newton-Raphson scheme to solve non-linear problems. Therefore, the material subroutine must return an incremental material stiffness matrix to the main program. By differentiating Eqn. (4.17), an expression for the material Jacobian, $\dfrac{\partial \sigma_{ij}}{\partial \varepsilon_{kl}}$, may be obtained:

$$
\dot{\sigma}_{ij} = (1 - D)C_{ijkl} \, \dot{\varepsilon}_{kl} - \dot{D}C_{ijkl} \, \varepsilon_{kl} \tag{4.20}
$$

By using Eqn. (4.18) and letting

$$
\sigma_{ij}^0 = C_{ijkl} \, \varepsilon_{kl}
$$

which is the stress corresponding to an undamaged material, Eqn. (4.20) becomes:

156

$$\dot{\sigma}_{ij} = (1-D)C_{ijkl}\dot{\varepsilon}_{kl} - \frac{\partial H(\varepsilon_{eq})}{\partial \varepsilon_{eq}}\sigma_{ij}^{o}\dot{\varepsilon}_{eq} \tag{4.21}$$

But since

$$\dot{\varepsilon}_{eq} = \frac{\partial \varepsilon_{eq}}{\partial \varepsilon_{kl}}\dot{\varepsilon}_{kl} \tag{4.22}$$

Eqn. (4.21) can be written as

$$\dot{\sigma}_{ij} = (1-D)C_{ijkl}\dot{\varepsilon}_{kl} - \frac{\partial H(\varepsilon_{eq})}{\partial \varepsilon_{eq}}\sigma_{ij}^{o}\frac{\partial \varepsilon_{eq}}{\partial \varepsilon_{kl}}\dot{\varepsilon}_{kl} \tag{4.23}$$

so that the material Jacobian is:

$$\frac{\partial \sigma_{ij}}{\partial \varepsilon_{kl}} = (1-D)C_{ijkl} - \frac{\partial H(\varepsilon_{eq})}{\partial \varepsilon_{eq}}\sigma_{ij}^{o}\frac{\partial \varepsilon_{eq}}{\partial \varepsilon_{kl}} \tag{4.24}$$

Note that this Jacobian is not symmetric due to the presence of the second term. Consequently, there would be a significant increase in computational effort to solve the resulting unsymmetric system of equations. On the other hand, using an approximate but symmetric Jacobian:

$$\frac{\partial \sigma_{ij}}{\partial \varepsilon_{kl}} \approx (1-D)C_{ijkl} \tag{4.25}$$

which neglects the unsymmetric part of Eqn. (4.24) would lead to a solution that would require more iterations to achieve convergence. However, the increase in number of iterations could be offset by the reduced amount of time required to solve a symmetric system of equations. Thus, the approximate Jacobian in Eqn. (4.25) was used in the implementation of the damage model. Furthermore, Eqn. (4.25) essentially gives a secant material stiffness, as opposed to a tangential material stiffness given in Eqn. (4.24).

During initial attempts to use the above material model coupled with the approximate Jacobian, difficulties in convergence were encountered whenever a material point started to strain-soften, i.e., unreasonably small load steps were required to achieve convergence. It is possible that the approximate Jacobian in Eqn. (4.25) is not suitable for solving strain-softening problems. However, it is also likely that the numerical schemes programmed into ABAQUS do not include a method that is appropriate for material softening [e.g. indirect displacement control proposed by de Borst, 1986].

In order to avoid the numerical problems associated with strain-softening materials, the following simplification was made. Rather than letting $D \to 1$, a saturation value of D was assumed to exist and correspond to the damage at the peak of the stress-strain curve. By maximizing the second part of Eqn. (4.14), one finds that the peak stress occurs at $\varepsilon = \varepsilon_{sat} = \varepsilon_o/A$ which is given by the following expression:

$$\sigma_{sat} = \frac{E\varepsilon_o}{A} \frac{1}{\exp(1-A)} \qquad (4.26)$$

where the subscript "sat" has been used because this also corresponds to the stress at which the saturation damage is reached. The reasons behind the previously stated constraints set on possible values of A are now evident. The parameter A must be less than 1 so that $\varepsilon_{sat} > \varepsilon_0$. Otherwise, if A were greater than 1, a physically nonsensical situation will arise wherein damage saturation will occur at a strain that is lower that the strain at which damage initiates. Also one can infer from Eqn. (4.26) that A cannot be zero since this will produce a singular σ_{sat}, and that A must be a positive number so that positive strains will correspond to positive stresses. By substituting $\varepsilon = \varepsilon_{sat} = \varepsilon_0/A$ in Eqns. (4.12) and (4.13), the saturation damage D_{sat} is obtained:

158

$$D_{sat} = 1 - \frac{1}{\exp(1-A)} \qquad (4.27)$$

Therefore, with this assumption, no further damage occurs when $\varepsilon_{eq} > \varepsilon_o/A$ (i.e., ε_{eq} is greater than the strain at damage saturation) and the material behavior remains linearly elastic with a reduced modulus:

$$\sigma_{ij} = (1 - D_{sat})C_{ijkl}\, \varepsilon_{kl}. \qquad (4.28)$$

The uniaxial stress-strain curve for this revised, non-softening model is shown in Fig. 4.22. Other authors have also proposed a saturation value for damage for microcracking materials, with D_{sat} corresponding to a saturation microcrack density [Charalambides et al., 1987; Brockenbrough et al., 1987, Ortiz, 1987].

Computational and uniqueness problems associated with strain-softening materials were avoided in this study through the use of a non-softening damage model. Simulations of the coalescence processes observed in the experiments are presented in the following section.

159
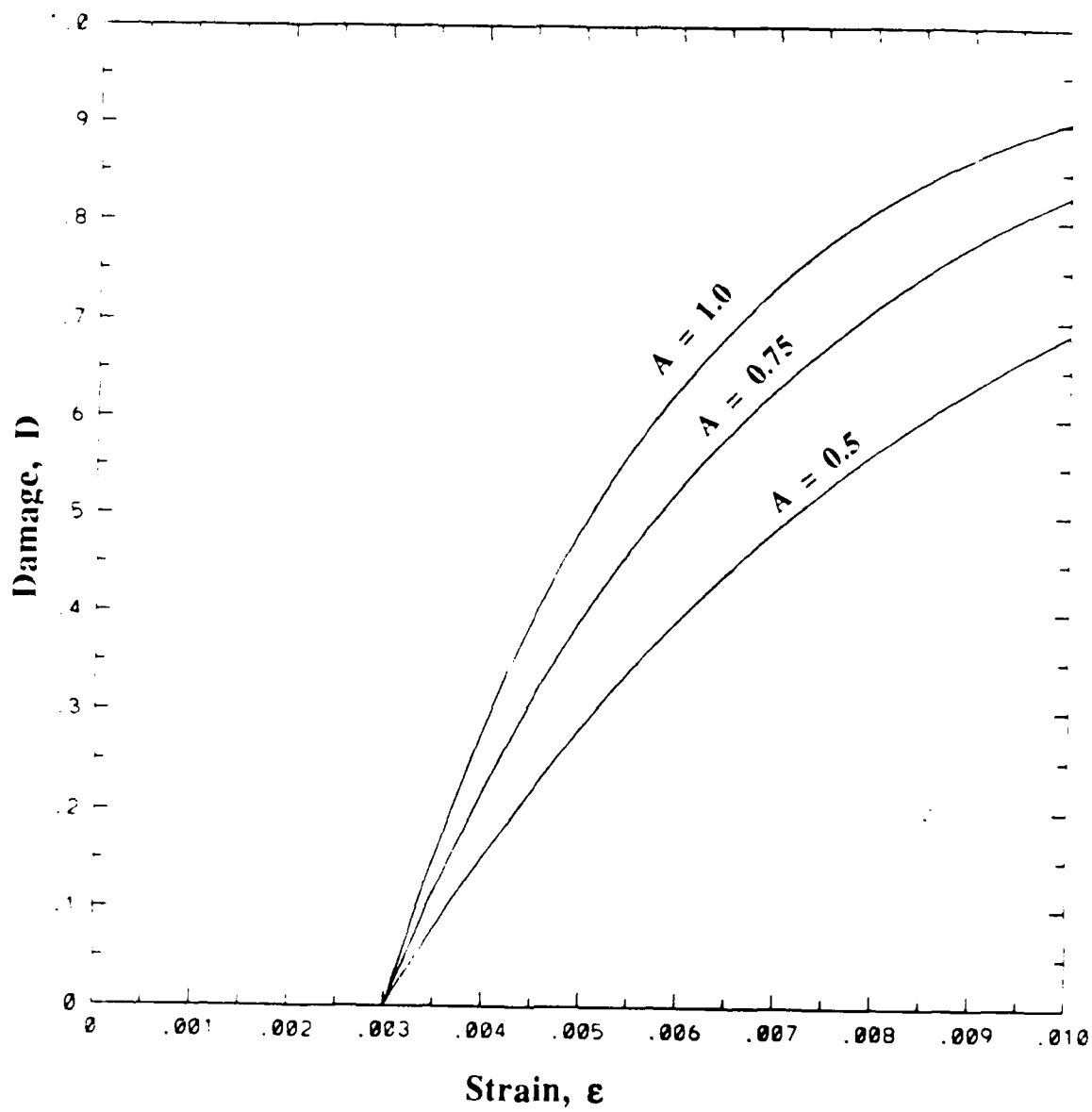
Figure 4.19   Damage as a function of strain for various values of A, $\varepsilon_0 = 0.003$.
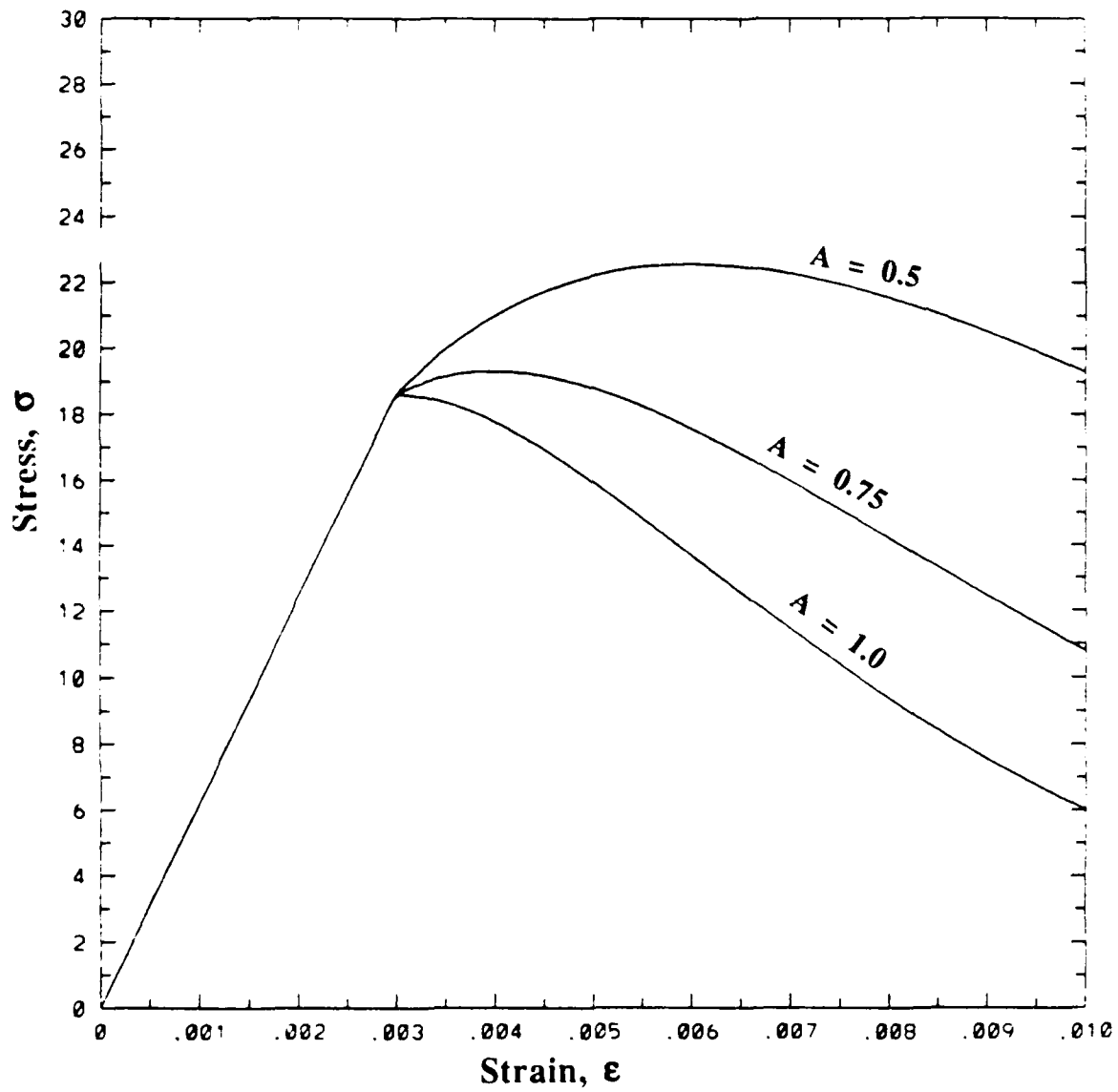
Figure 4.20   Stress-strain curve for various values of A, $\varepsilon_0 = 0.003$.
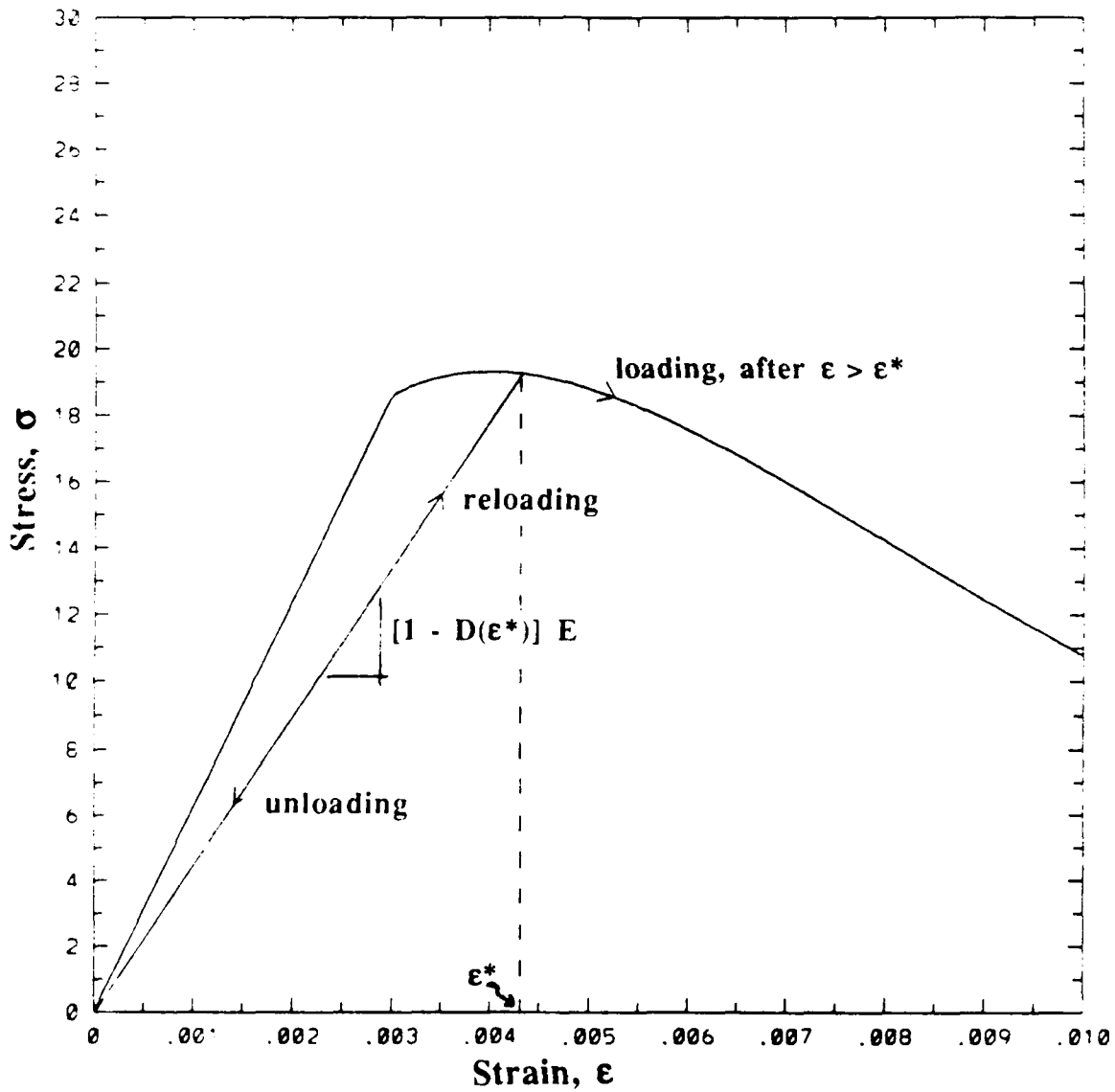
Figure 4.21   Illustration of irreversible damage during loading and unloading cycle (refer to text for explanation of symbols).

162
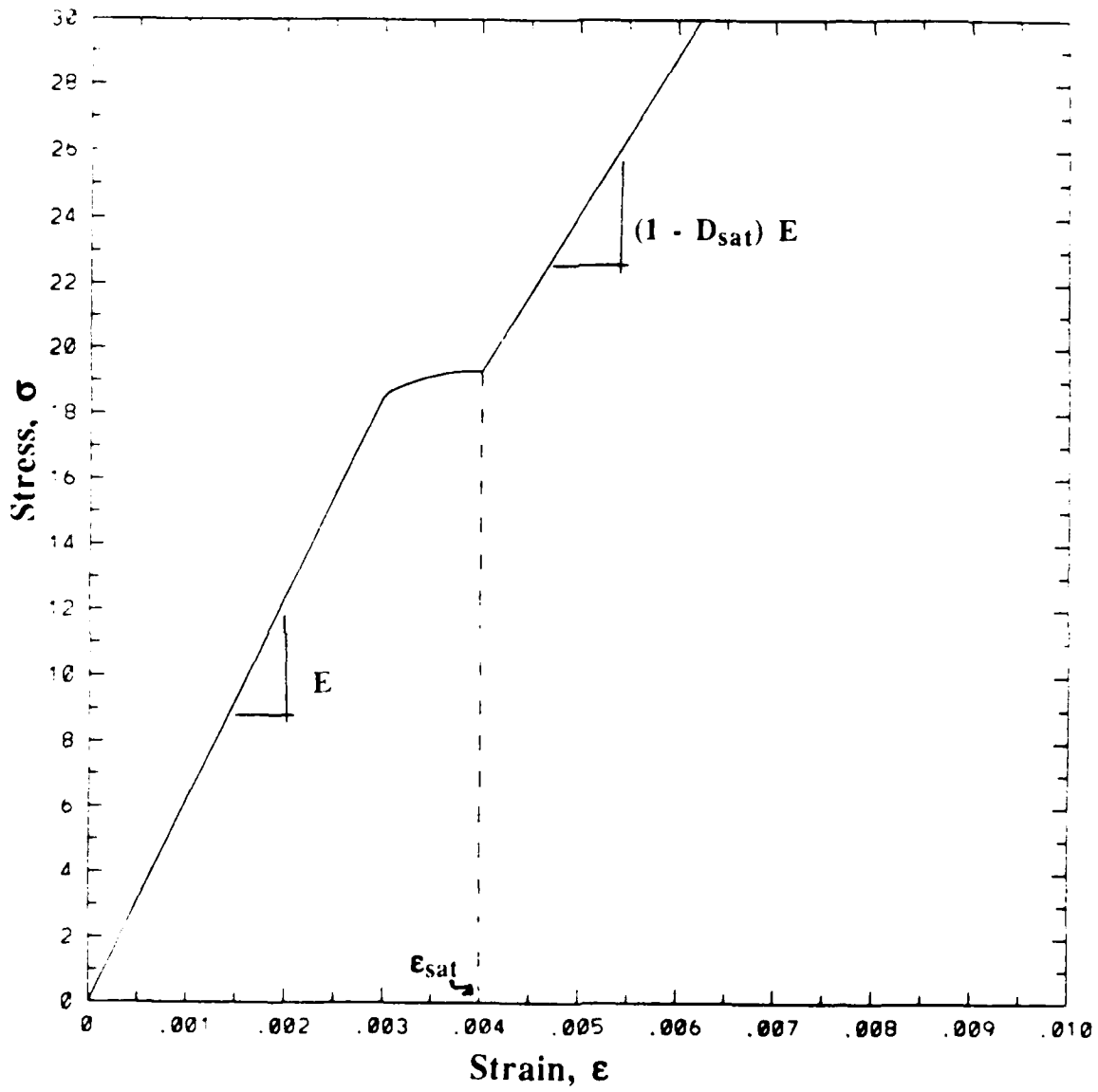
Figure 4.22   Non-softening stress-strain curve with damage saturation D_{sat}.

163

4.4.2 Coalescence Simulations Using a Strain-based Damage Model

The objective of the following simulations is to verify whether or not the strain-based damage model presented in section 4.4.1 can successfuly reproduce the observed coalescence in the experiments and the corresponding loads at which coalescence occured. The approach taken in these simulation studies was as follows: (1) parameters ε_0 and A were estimated and modified until the simulated coalescence load was close to the observed value for one flaw geometry, in particular, for 30°-75° flaws, (2) these parameters were then used to predict coalescence loads for the other flaw geometries and, (3) the predicted coalescence loads were then compared to the observed values. Satisfactory predictions of secondary crack growth/coalescence and coalescence loads as functions of flaw geometry were achieved.

The "Edge" Finite Element Model

Because of limited computer resources and the expected iterative nature of finite element analyses involving material non-linearity, a simplified block geometry was used in applying the damage model . "Edge" models, where the edge flaws had lengths equal to half the flaw lengths in the full model, were thought to be adequate for investigating coalescence crack growth in the ligaments (see Figs. 4.23 and 4.24 for a comparison of "edge" and "full" models of 30°-45° and 30°-75° flaw geometries, respectively). At the same time, the "edge" models required a smaller number of finite elements than the full models. A comparison between the strain fields using the "edge" and full models are presented in Figs. 4.25 and 4.26 for 30°-45° and 30°-75° flaws respectively. Note that the strain fields for the 30°-45° flaws compare quite well whereas the strain levels for the 30°-75° flaws are higher in the "edge" model than in the full model. It was generally observed

164

that edge models overestimated the strain levels in the ligaments when the resulting "edge" blocks were too thin, as in the case of the 30°-75° flaws. Intuitively, this is not surprising since the edges were probably having a dominant effect on the strain distribution in the ligament areas of thinner edge models.

Coalescence Criterion

A simulation of an edge model using a strain-softening damage model would most likely result in a load-displacement curve that exhibits a "peak" when the load-carrying capacity of the ligament has been reached. This "peak" load could then be taken as the coalescence load for the edge model. However, no such peaks are expected from the load-displacement curves when a non-strain-softening damage model, such as the one proposed in this study (see Fig. 4.22), is used. Therefore, the coalescence criterion adopted for the simulations was as follows: the coalescence load is the load at which a region of damage with $D \approx D_{sat}$ connects the flaw tips. The application of this criterion will be made clearer in the subsequent discussion of simulation results.

Parameter Selection

In selecting the damage threshold value, ε_0, some guidance was obtained from the linear elastic analysis results in Section 4.3. As mentioned in 4.3.1, strain fields in Figs. 4.12(a) through 4.17(a) were induced by applying uniformly distributed loads which were approximately equal to the observed coalescence loads. Thus, neglecting any effects of damage, these figures show the approximate strain fields just prior to coalescence. It was observed that the computed strains within the ligament areas were within the range of 0.0022 to 0.0032 from the analysis results shown in Figs. 4.12(a) through 4.17(a).

165

Therefore, for the first simulation, ε_0 was set to 0.003. A value of 0.25 was arbitrarily chosen for A. The same modulus of 6200 MPa and Poisson's ratio of 0.28 used in the linear elastic analyses were adopted for the non-linear analyses. Damage saturation occurs at a strain of $\varepsilon_{sat} = \varepsilon_0/A - 0.012$ so that, from Eqns. 4.27 and 4.28, $D_{sat} = 0.53$ and $\sigma_{sat} = 35$ MPa. The resulting stress-strain curve is shown in Fig. 4.27.

Figs. 4.28(a)-(d) show the contours of the damage variable D for increasing applied loads in the 30°-75° edge model using the preceding parameters. Damage values corresponding to the contour levels are also tabulated in these figures. At an applied load of 26.4 MPa [Fig. 4.28(d)], the damage within the ligament area was still ~0.25 which is less than the saturation value of 0.53. Since the observed coalescence loads for the 30°-75° flaws were 15.7/17.8 MPa (see Section 3.3.3), it was apparent that the initial choice of parameters was quite inappropriate. Specifically, the saturation stress, σ_{sat} of 35 MPa was probably too high and should be lowered by decreasing both A and ε_0 [see Eqn. (4.26)]. This was achieved in the succeeding choice of parameters.

In the second run, rather than setting ε_0 to 0.003, the strain at damage saturation ε_{sat} was set to 0.003, an assumption which effectively lowered the value of ε_0. A second condition was required to uniquely define the two unknown parameters. Since in the initial run it was observed that σ_{sat} was too high, in the second run this was prescribed as a factor of $E\varepsilon_0$ as follows:

$$\sigma_{sat} = 1.1 E\varepsilon_o \tag{4.29}$$

This implies that damage saturation is reached at a stress which is only 10% above the stress at which the damage initiates, i.e., $E\varepsilon_0$. By combining Eqn. (4.26) and (4.29), and since $\varepsilon_{sat} = \varepsilon_0/A$, ε_0 and A were found from the following equations:

$$\sigma_{sat} = \frac{E\varepsilon_o}{A} \frac{1}{\exp(1-A)} = 1.1 E\varepsilon_o$$

166

$$\varepsilon_{sat} = \frac{\varepsilon_o}{A} = 0.003$$

The parameters which satisfy the above equations are: $\varepsilon_o = 0.00175$ and $A = 0.583$, with $D_{sat} = 0.34$. The resulting stress-strain curve is shown in Fig. 4.29. Note that σ_{sat} is ~13 MPa, less than half of the value for the initial run.

The damage evolution with increasing load for $\varepsilon_o = 0.00175$ and $A = 0.583$ is shown in Figs. 4.30(a)-(d). At an applied load of 11 MPa (Fig. 4.33(d)), the region of damage with $D \approx D_{sat}$ has connected the flaw tips. Therefore, according the aforementioned coalescence criterion, the coalescence load predicted by $\varepsilon_o = 0.00175$ and $A = 0.583$ is ~11 MPa. The fact that the coalescence load for this set of parameters is lower than the value computed from the initial run is not surprising given the smaller value of σ_{sat} in the second run. However, 11 MPa is lower than the observed coalescence loads of 15.7 and 17.8 MPa. The assumed σ_{sat} was probably too low; consequently, a higher σ_{sat} was prescribed for the succeeding run.

For the third simulation, ε_{sat} was still set to 0.003 as in the previous run. However, σ_{sat} was set to a value of 15 MPa, a value which is slightly higher than 13 MPa for the previous run. Thus, the parameters for the third simulation were found from the following equations:

$$\sigma_{sat} = \frac{E\varepsilon_o}{A} \frac{1}{\exp(1-A)} = 15\,\text{MPa}$$

$$\varepsilon_{sat} = \frac{\varepsilon_o}{A} = 0.003$$

The parameters which satisfy the above equations are: $\varepsilon_o = 0.0024$ and $A = 0.785$, and the resulting stress-strain curve is shown in Fig. 4.31. Due to a slightly higher prescribed

167

σ_{sat}, this new choice of parameters was expected to predict higher coalescence loads which could be closer to the observed values.

Figs. 4.32(a)-(d) show the damage evolution for $\varepsilon_0 = 0.0024$ and $A = 0.785$, with $D_{sat} = 0.19$. In Fig. 4.32(d) where the applied load is 13.6 MPa, there is an entire region between the flaw tips where the damage is approximately equal to D_{sat}. Thus, the predicted coalescence load is ~13.6 MPa and was thought to be sufficiently close to the observed values of 15.7/17.8 MPa. Subsequent analyses on other flaw geometries were performed using $\varepsilon_0 = 0.0024$ and $A = 0.785$.

Model Validation

Three other flaw geometries, namely 30°-45°, 45°-60° and 60°-45° flaws, for which coalescence was observed in the experiments were analyzed using the strain-based damage model with $\varepsilon_0 = 0.0024$ and $A = 0.785$ with $D_{sat} = 0.19$. The simulated damage evolution for each geometry are shown in Fig. 4.33(a)-(d), 4.34(a)-(c) and 4.35(a)-(d). In all three sets of figures, the last figure shows a region between the flaw tips where $D \approx D_{sat}$ such that the loads associated with these contour plots were chosen as the coalescence loads (e.g. Fig. 4.33(d) for 30°-45°, Fig. 4.34(c) for 45°-60° and Fig. 4.35(d) for 60°-45°). The predicted and observed coalescence loads for all four geometries which were analyzed are listed in Table 4.2. These are also plotted against ligament orientation angle in Fig. 4.36, where the hollow symbols represent observed coalescence loads and the filled symbols represent predicted coalescence loads. There is a satisfactory agreement between the experimental and computed values with discrepancies that are roughly the same for all geometries. An additional calibration cycle would have resulted in an even better agreement between experimental and computed coalescence loads. However, the current results already show that the trends in coalescence loads as a function of flaw geometry were very

168

captured by the smeared-crack/strain-based damage criterion proposed in this study. Any additional parameter refinement would just be an exercise in curve fitting.

Table 4.2 Comparison between Experimental and Computed Coalescence Loads

Flaw Geometry	Coalescence Loads (MPa)	
	Experimental	Computed
30°-75°	15.7 / 17.8	13.6
30°-45°	24.2 / 24.1	21.4
45°-60°	22.4 / 23.3	18.0
60°-45°	29.6 / 30.3	24.5

One final simulation was performed on 30°-30° flaws for which no coalescence was observed. Figs. 4.37(a)-(c) show the damage evolution for the edge model of the 30°-30° flaws. At an applied load of 23.4 MPa, damage zones extending away from the ligament had substantially grown but, in contrast to the previous simulations, damaged regions did not "connect" within the ligament zone. This is in agreement with the fracturing that was observed for the 30°-30° flaws. As mentioned in Section 3.3.1, one of the blocks "failed" at an applied load of 30 MPa through secondary crack growth but these secondary cracks did not form a coalescence crack (see Fig. 3.32). Thus, the strain-based damage model was also successfully used to predict the non-occurence of coalescence between 30°-30° flaws.

169
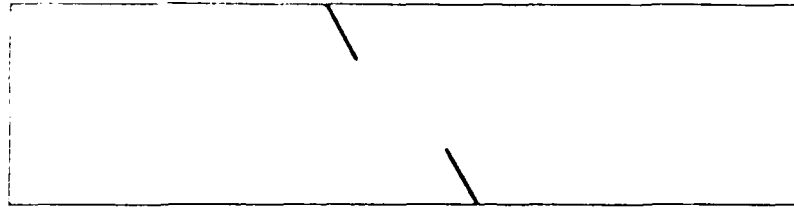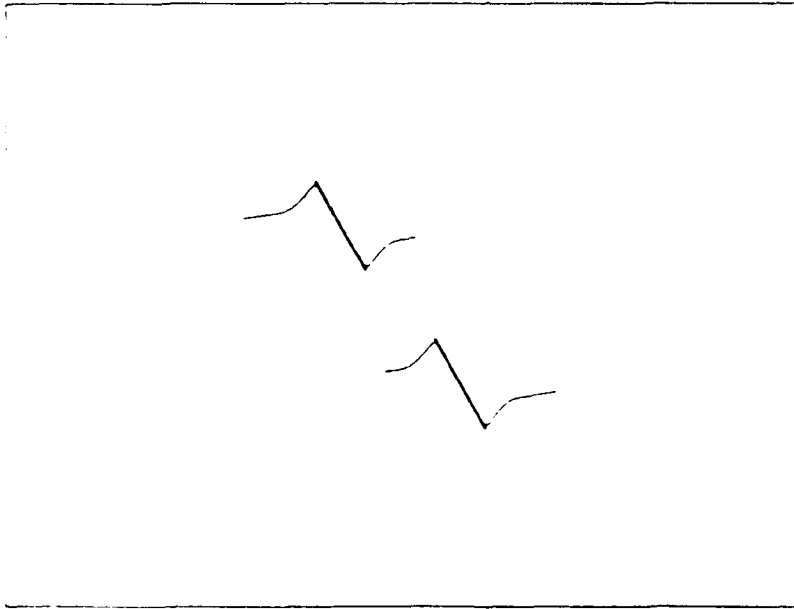
"Edge"

"Full"

Figure 4.23   "Full" and "edge" models for specimen with 30°-45° flaws.

170
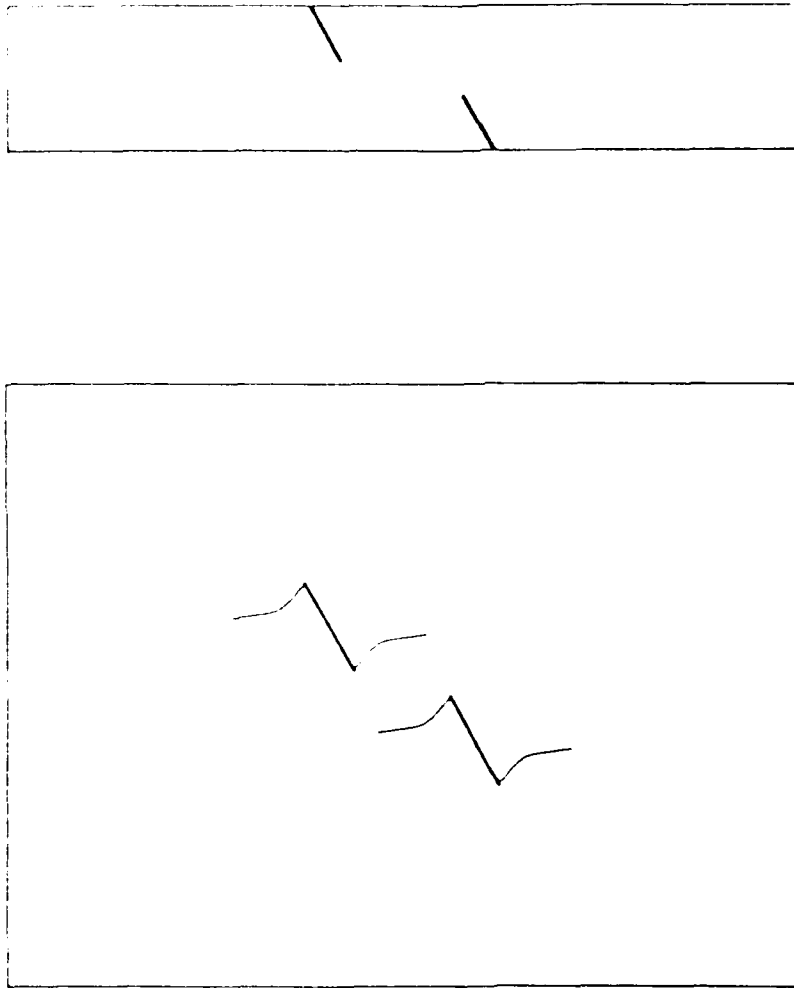
Figure 4.24   "Full" and "edge" models for specimen with 30°-75° flaws.
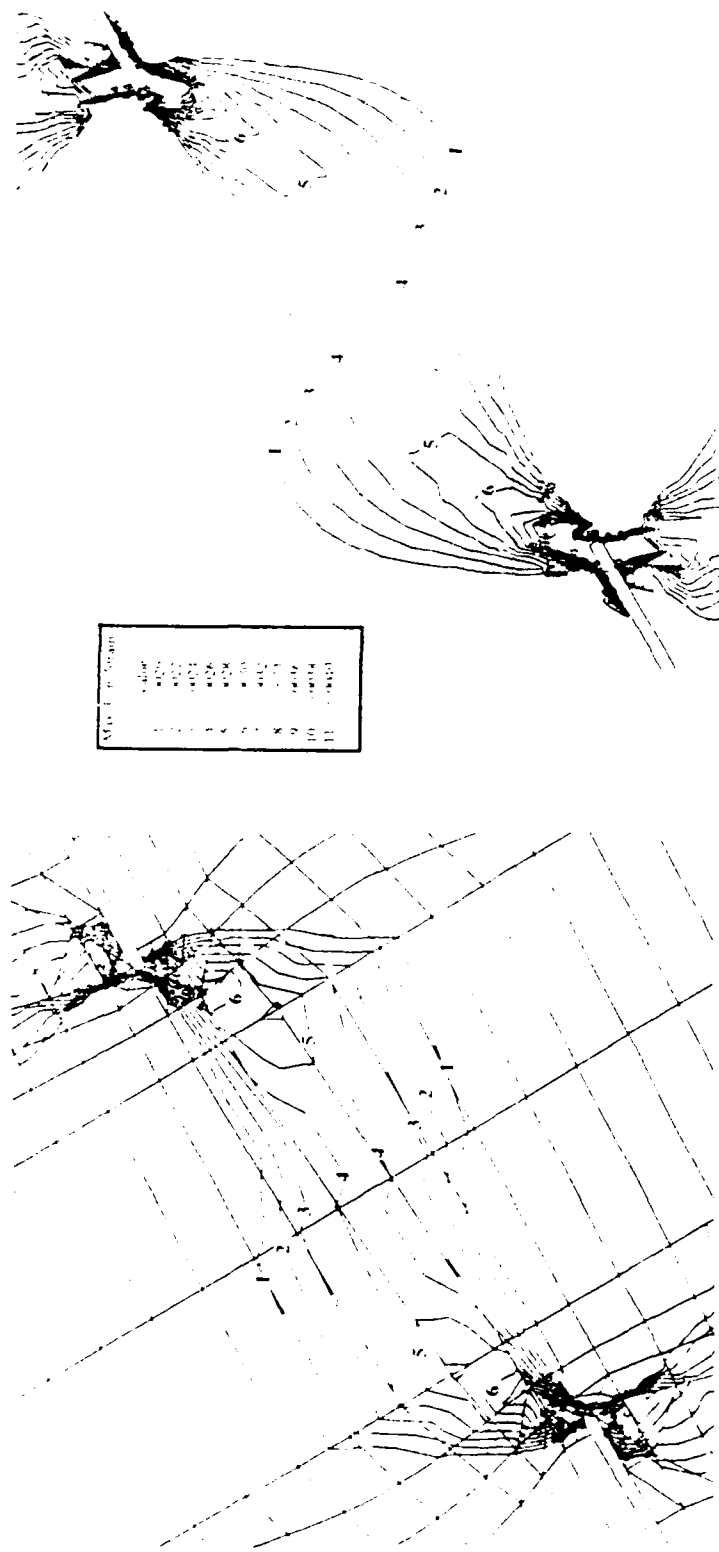
Figure 4.25 Contour plot of maximum principal strain within the ligament area in (a) "full" and (b) "edge" models for specimen with 30°-45° flaws.

172
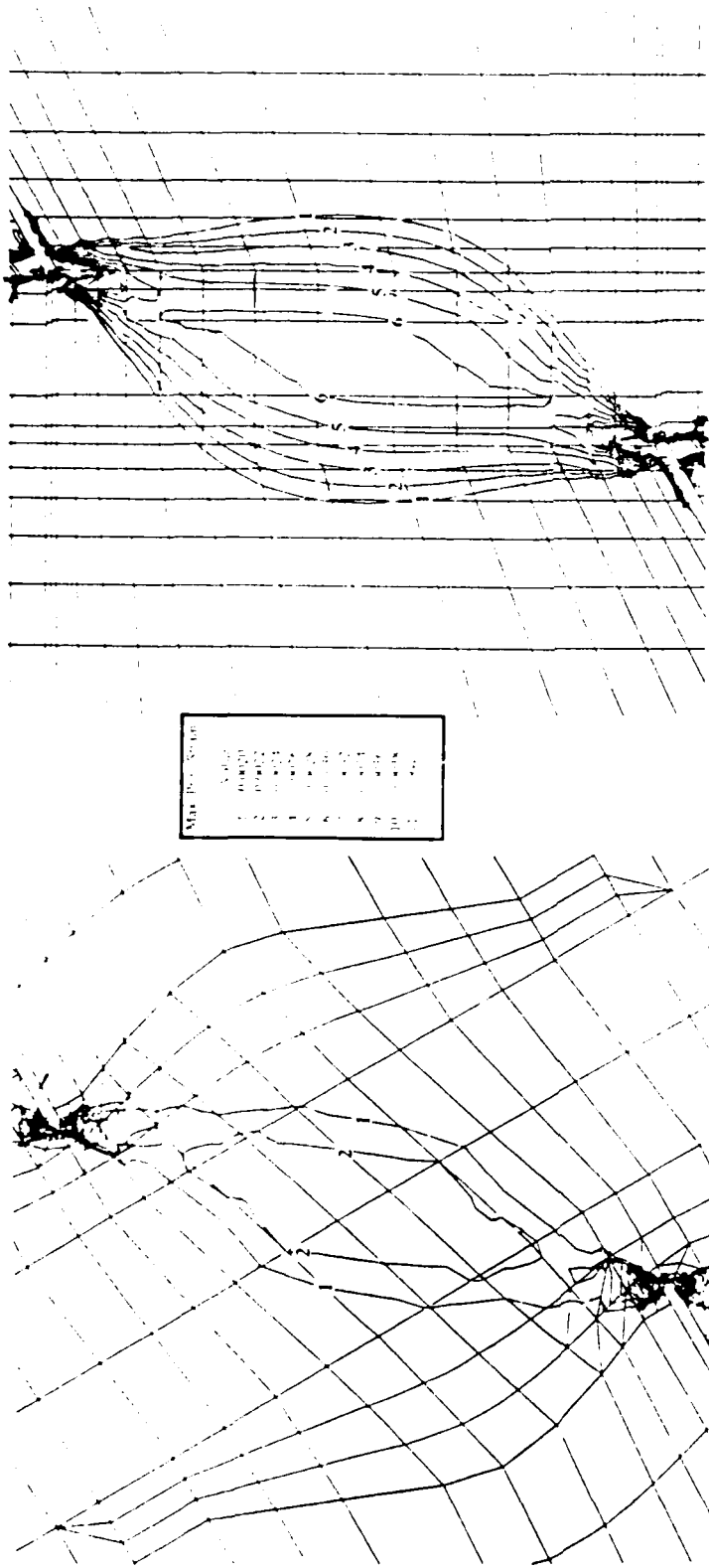
Figure 4.26   Contour plot of maximum principal strain within the ligament area in (a) "full" and (b) "edge" models for specimen with 30°-75° flaws.
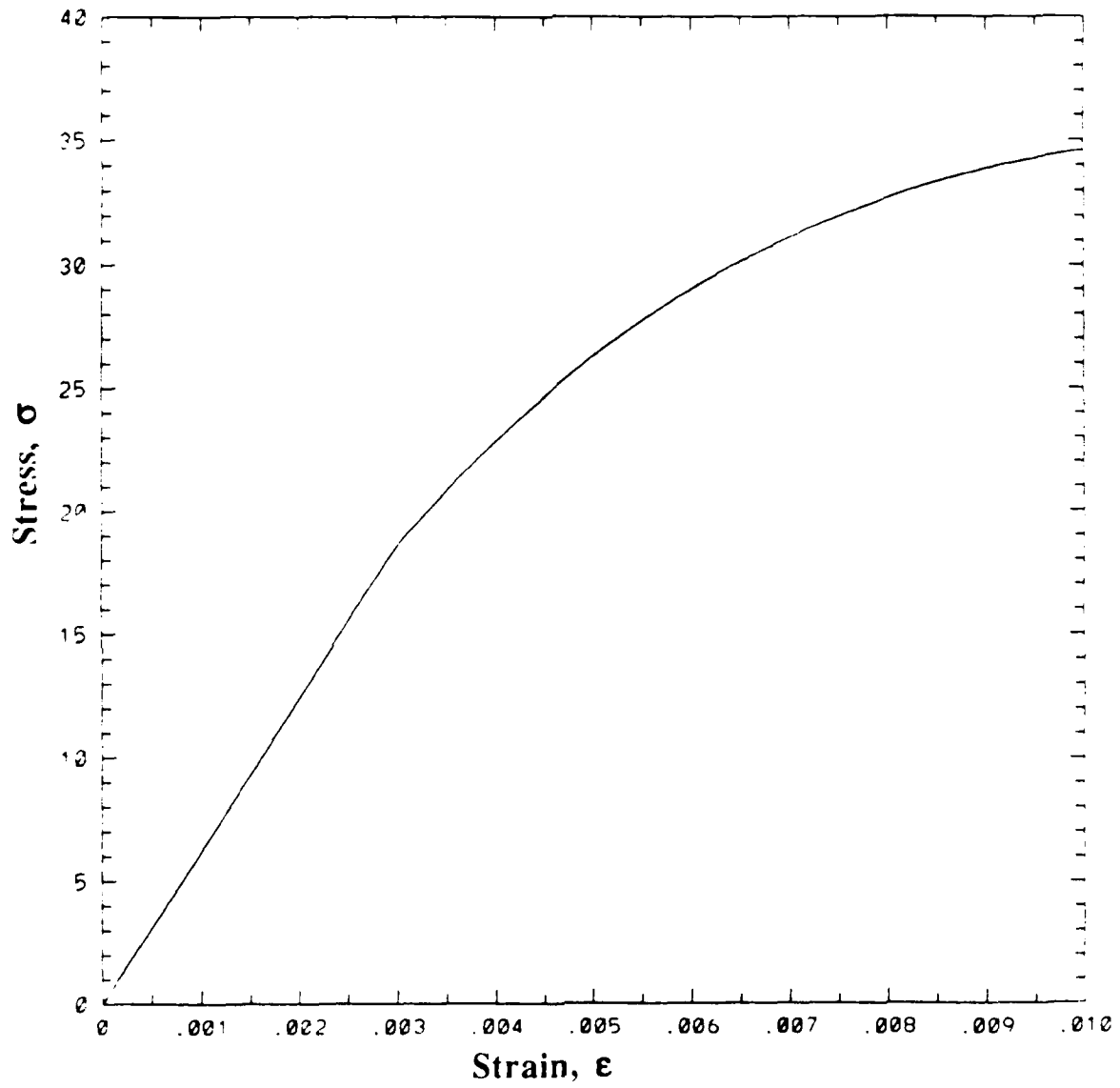
Figure 4.27   Stress-strain curve for initial choice of parameters to simulate coalescence, $\varepsilon_0 = 0.003$ and $A = 0.25$.

174

Figure 4.28(a) Damage contours in 30°-75° edge model, $\varepsilon_0 = 0.003$ and $A = 0.25$
Applied Load = 22.7 MPa.

Damage	
	Value
1	0.10
2	0.15
3	0.20
4	0.25
5	0.30
6	0.35
7	0.40
8	0.45
9	0.50

175

Figure 4.28(b) Damage contours in 30°-75° edge model, $\varepsilon_0 = 0.003$ and $\Lambda = 0.25$
Applied Load = 23.7 MPa.

Damage	
	Value
1	0.10
2	0.15
3	0.20
4	0.25
5	0.30
6	0.35
7	0.40
8	0.45
9	0.50

176
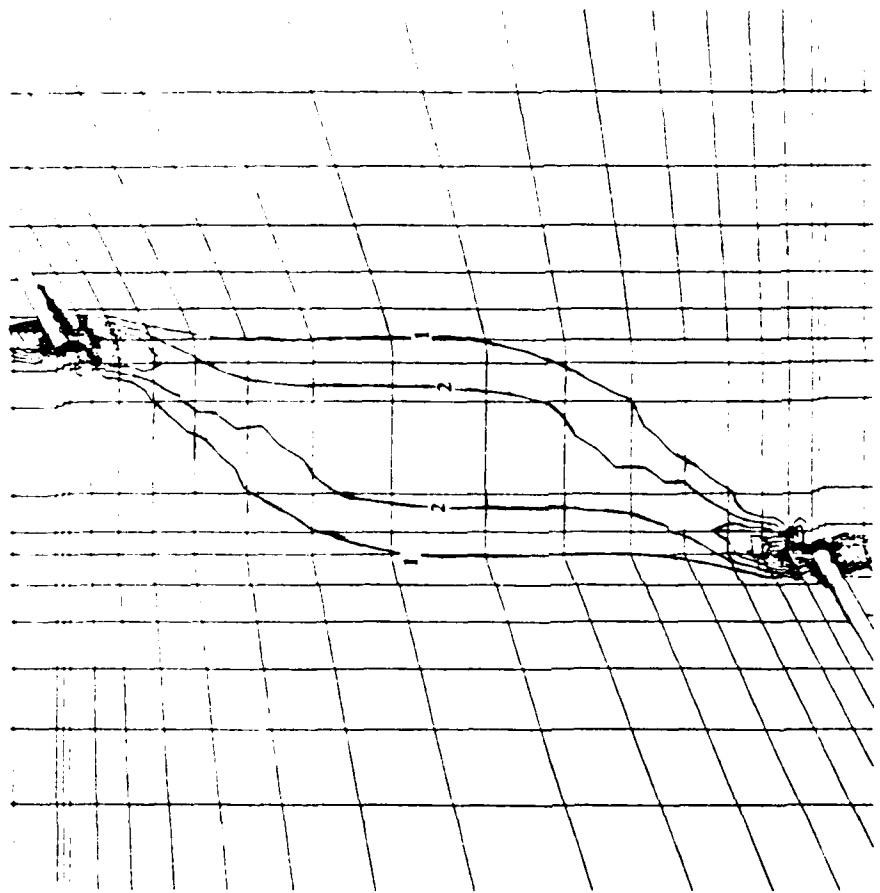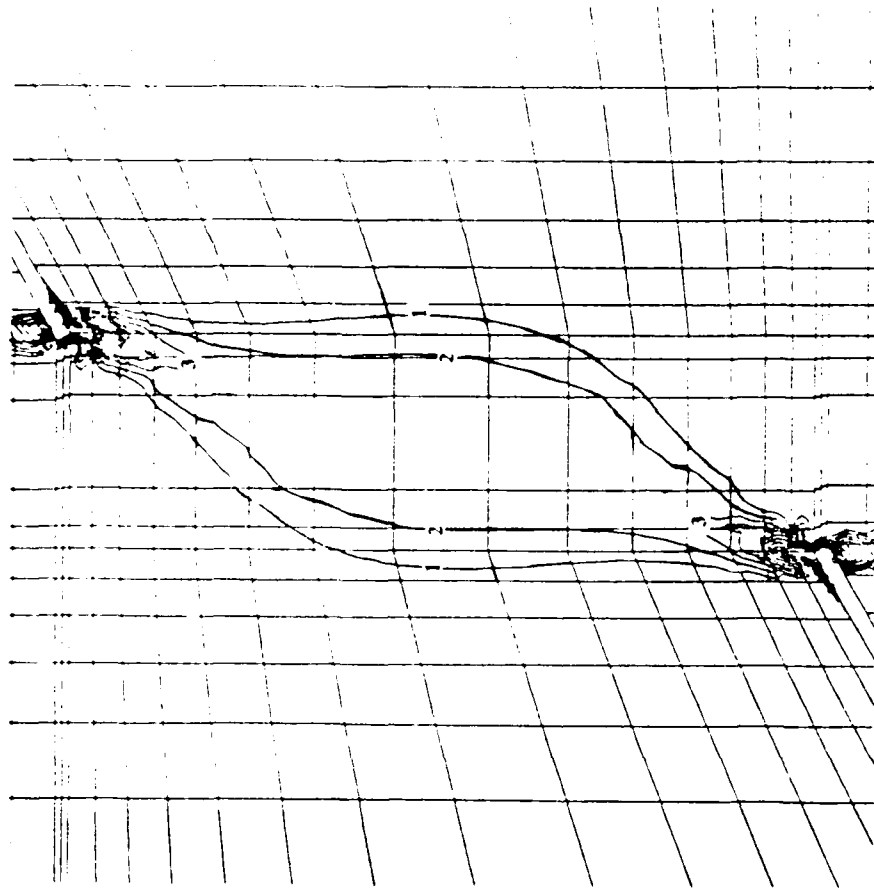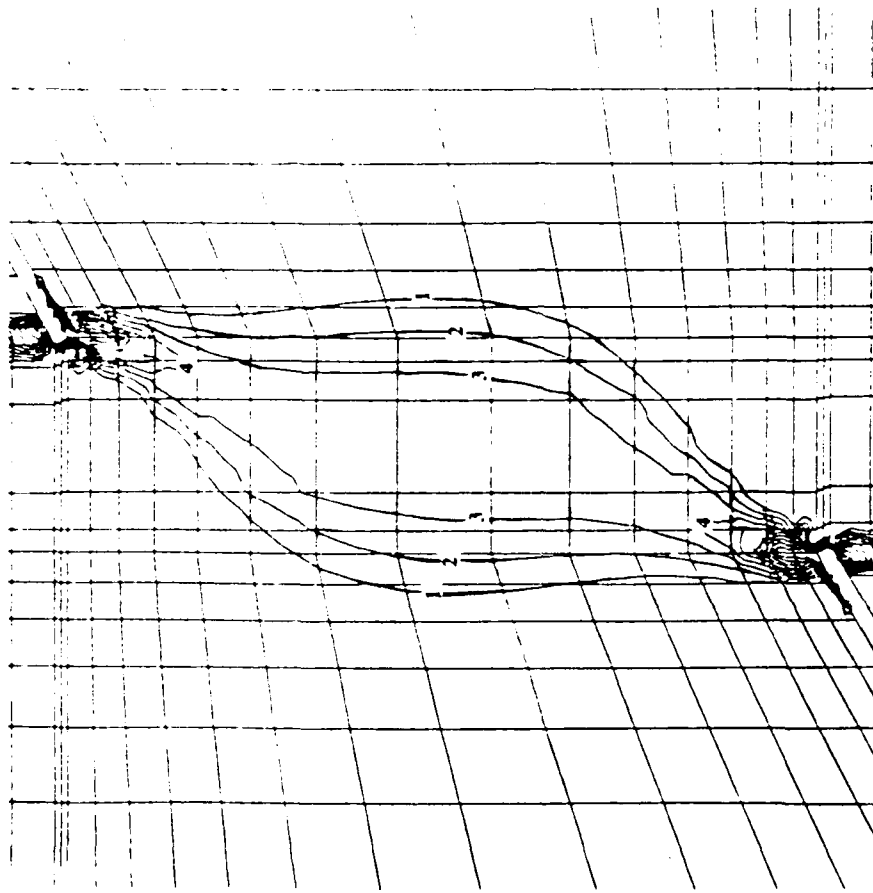
Damage	
	Value
1	0.10
2	0.15
3	0.20
4	0.25
5	0.30
6	0.35
7	0.40
8	0.45
9	0.50

Figure 4.28(c) Damage contours in 30°-75° edge model, $\varepsilon_0 = 0.003$ and $A = 0.25$ Applied Load = 25.0 MPa.

Figure 4.28(d) Damage contours in $30°$-$75°$ edge model, $\varepsilon_o = 0.003$ and $\Lambda = 0.25$
Applied Load = 26.4 MPa.

Damage	Value
1	0.10
2	0.15
3	0.20
4	0.25
5	0.30
6	0.35
7	0.40
8	0.45
9	0.50

178
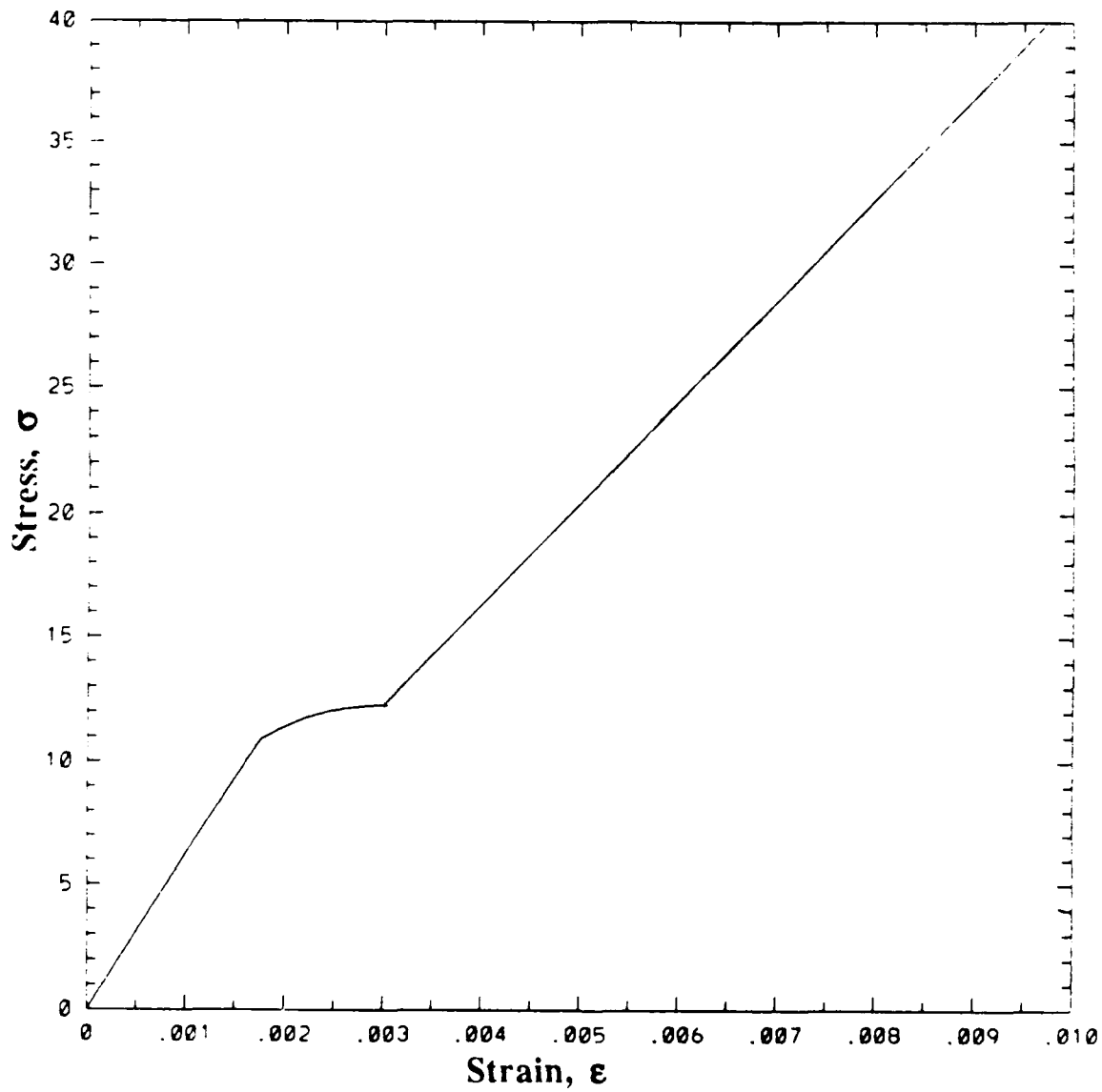
Figure 4.29   Stress-strain curve for second choice of parameters to simulate coalescence.
$\varepsilon_0 = 0.00175$ and A = 0.583.
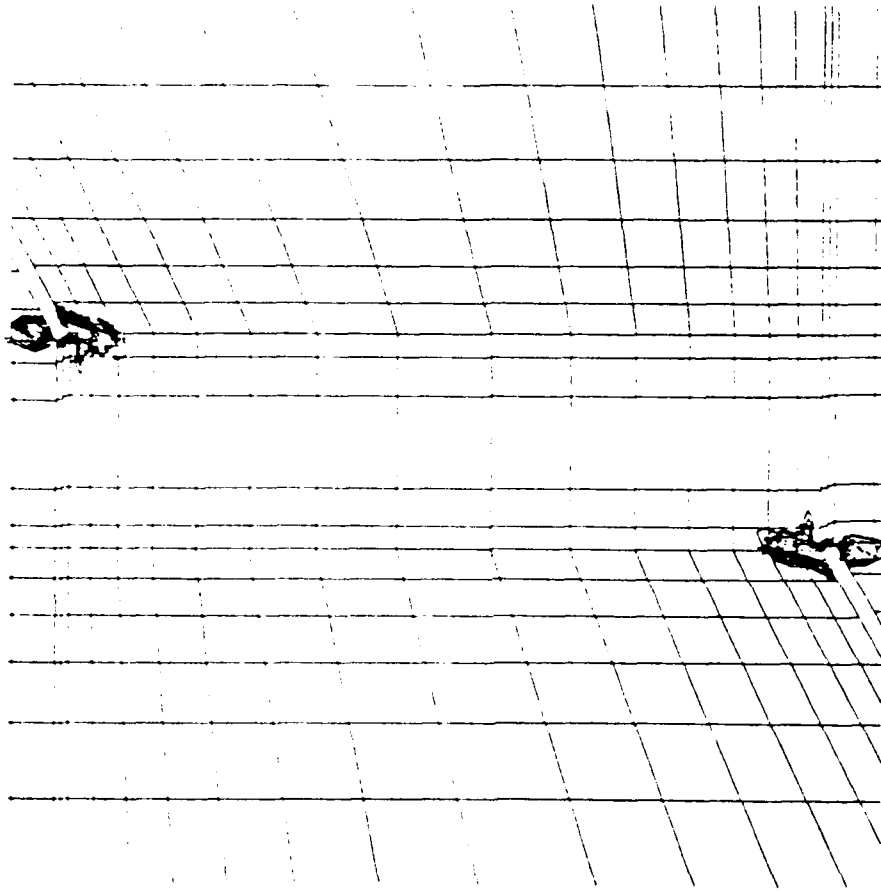
Damage	
	Value
1	0.100
2	0.134
3	0.168
4	0.202
5	0.237
6	0.271
7	0.305
8	0.340

Figure 4.30(a) Damage contours in 30°-75° edge model, $\varepsilon_0 = 0.00175$ and $A = 0.583$. Applied Load = 8.77 MPa.
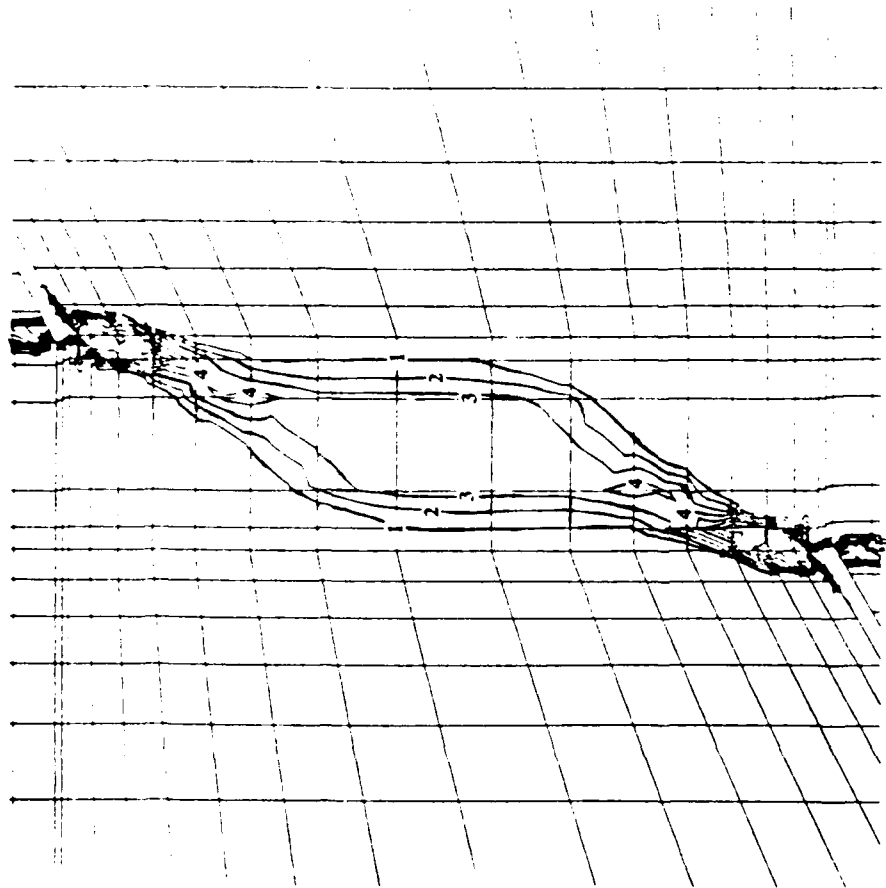
Damage	
	Value
1	0.100
2	0.134
3	0.168
4	0.202
5	0.237
6	0.271
7	0.305
8	0.340

Figure 4.30(b) Damage contours in 30°-75° edge model, $\varepsilon_0 = 0.00175$ and $\Lambda = 0.583$. Applied Load = 10.4 MPa.

181
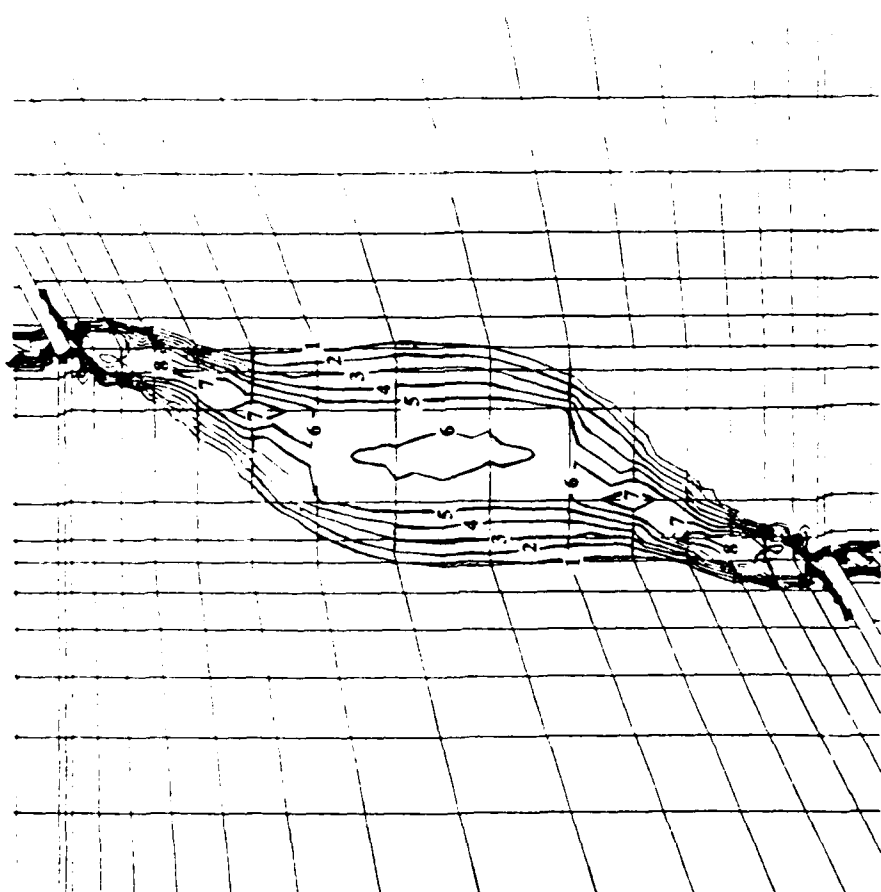
Damage	Value
1	0.100
2	0.134
3	0.168
4	0.202
5	0.237
6	0.271
7	0.305
8	0.340

Figure 4.30(c) Damage contours in 30°-75° edge model, $\varepsilon_o = 0.00175$ and $A = 0.583$
Applied Load = 10.8 MPa.
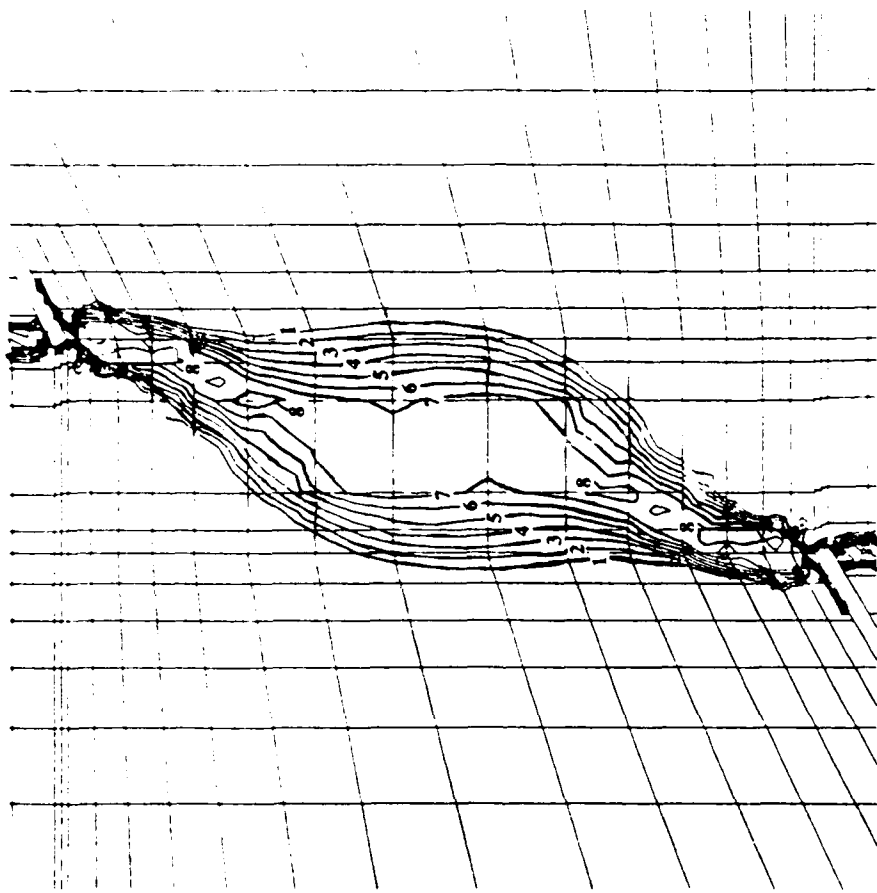
Figure 4.30(d) Damage contours in 30°-75° edge model, $\varepsilon_o = 0.00175$ and $A = 0.583$
Applied Load = 11.0 MPa.

Damage	Value
1	0.100
2	0.134
3	0.168
4	0.202
5	0.237
6	0.271
7	0.305
8	0.340

183
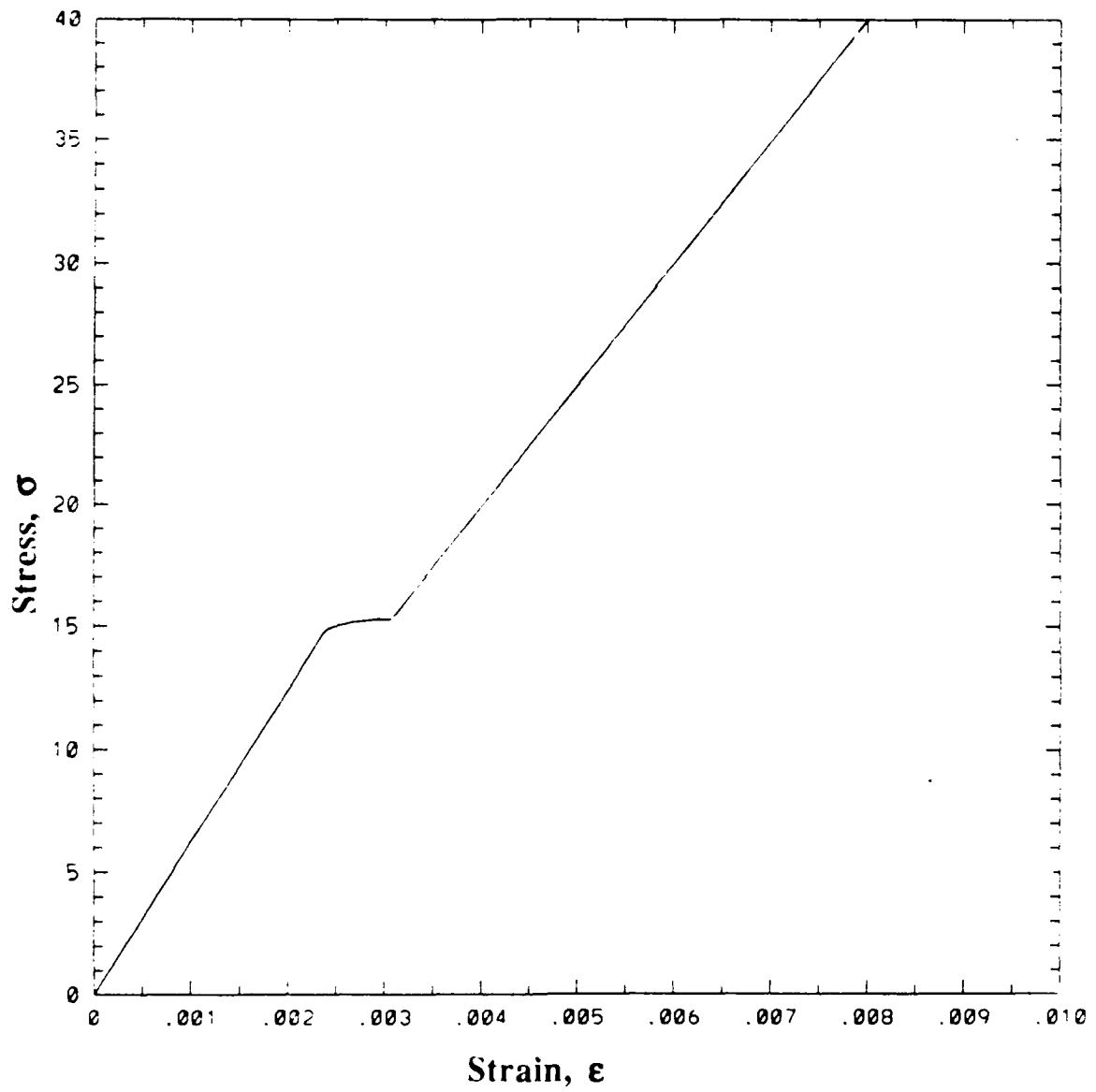
Figure 4.31   Stress-strain curve for third and final choice of parameters to simulate
coalescence, $\varepsilon_O = 0.0024$ and A = 0.785.
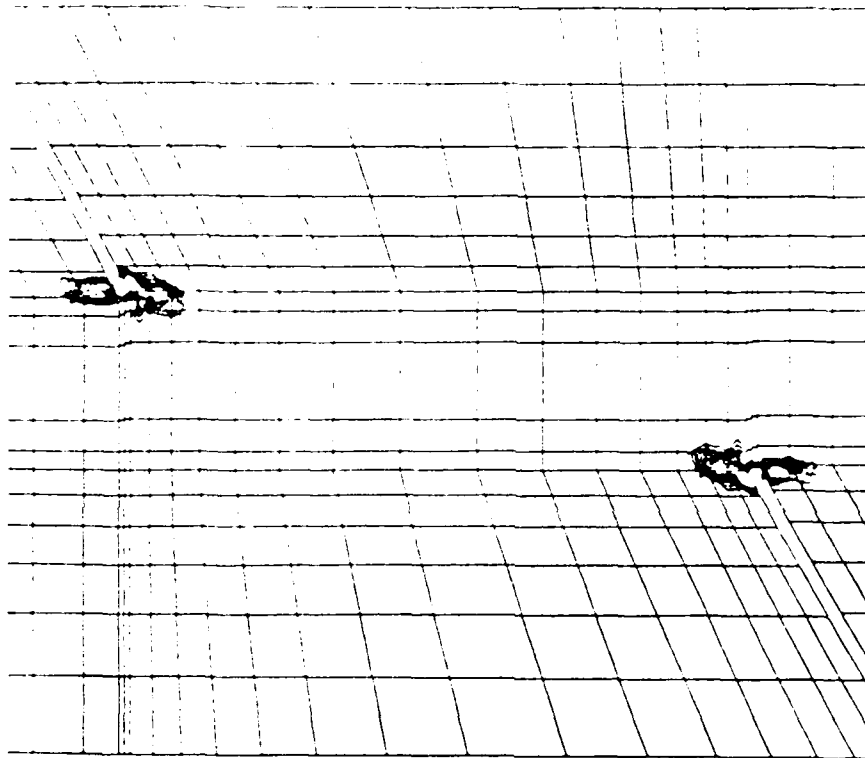
Figure 4.32(a) Damage contours in 30°-75° edge model. $\varepsilon_0 = 0.0024$ and $A = 0.785$ Applied Load = 11.7 MPa.

Damage	Value
1	0.050
2	0.070
3	0.090
4	0.110
5	0.130
6	0.150
7	0.170
8	0.190

185
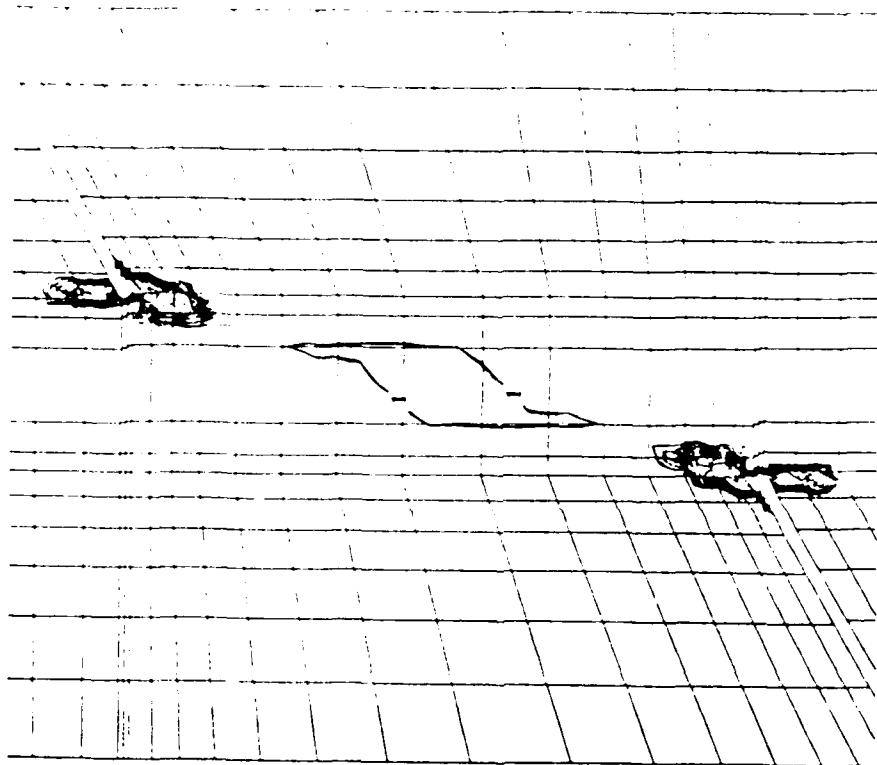
Figure 4.32(b) Damage contours in 30°-75° edge model, $\varepsilon_0 = 0.0024$ and $\Lambda = 0.785$. Applied Load = 12.9 MPa.

Damage

	Value
1	0.050
2	0.070
3	0.090
4	0.110
5	0.130
6	0.150
7	0.170
8	0.190

186
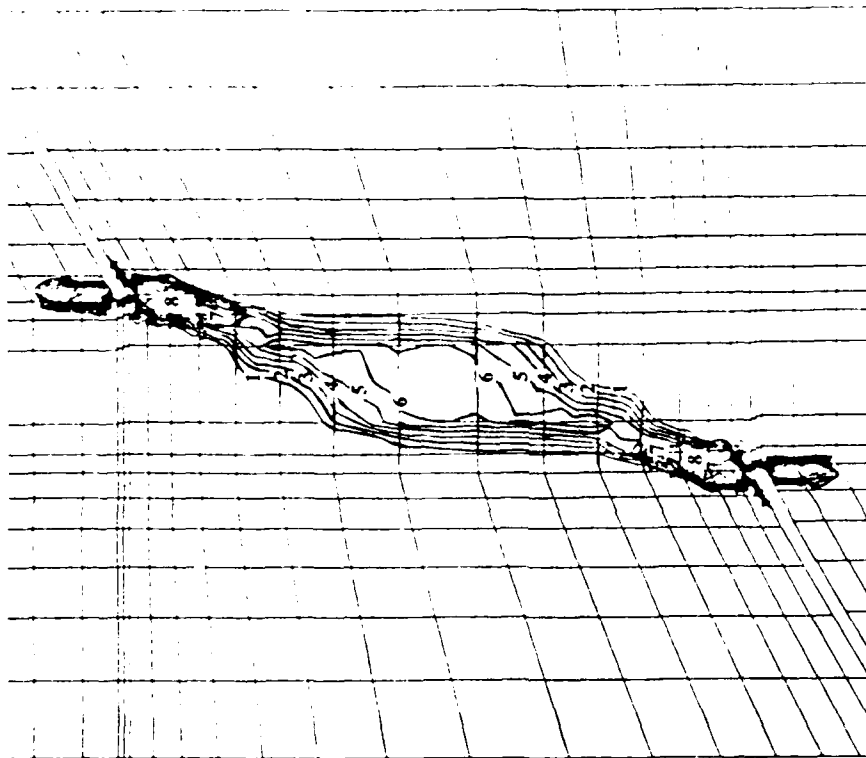
Figure 4.32(c) Damage contours in 30°-75° edge model. $\varepsilon_o = 0.0024$ and $A = 0.785$ Applied Load = 13.3 MPa.
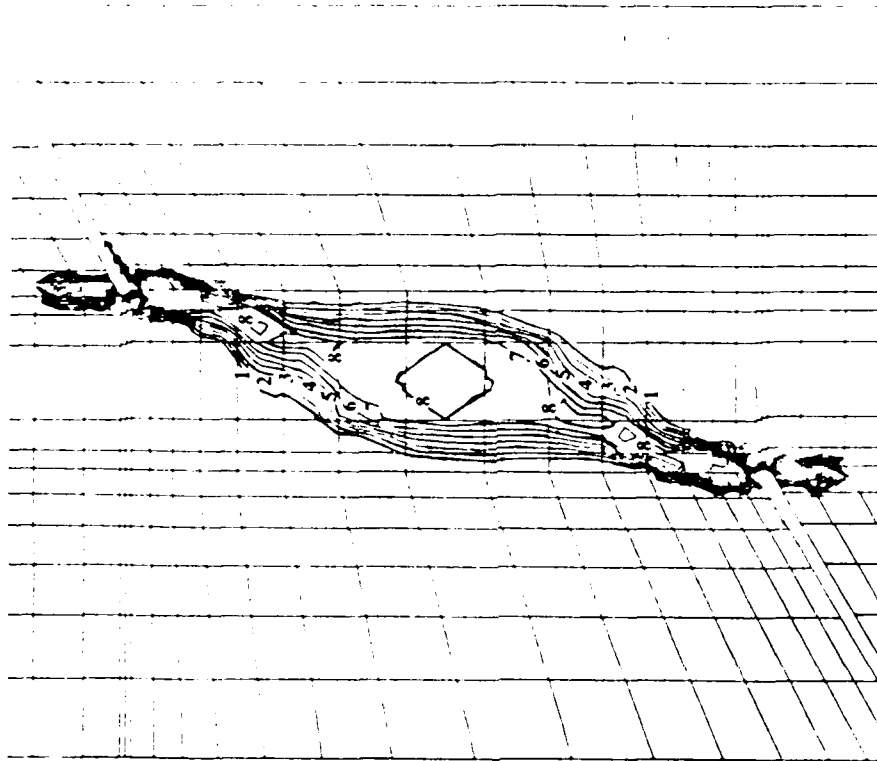
Damage	Value
1	0.050
2	0.070
3	0.090
4	0.110
5	0.130
6	0.150
7	0.170
8	0.190

Figure 4.32(d) Damage contours in 30°-75° edge model, $\varepsilon_0 = 0.0024$ and $\Lambda = 0.785$. Applied Load = 13.58 MPa.
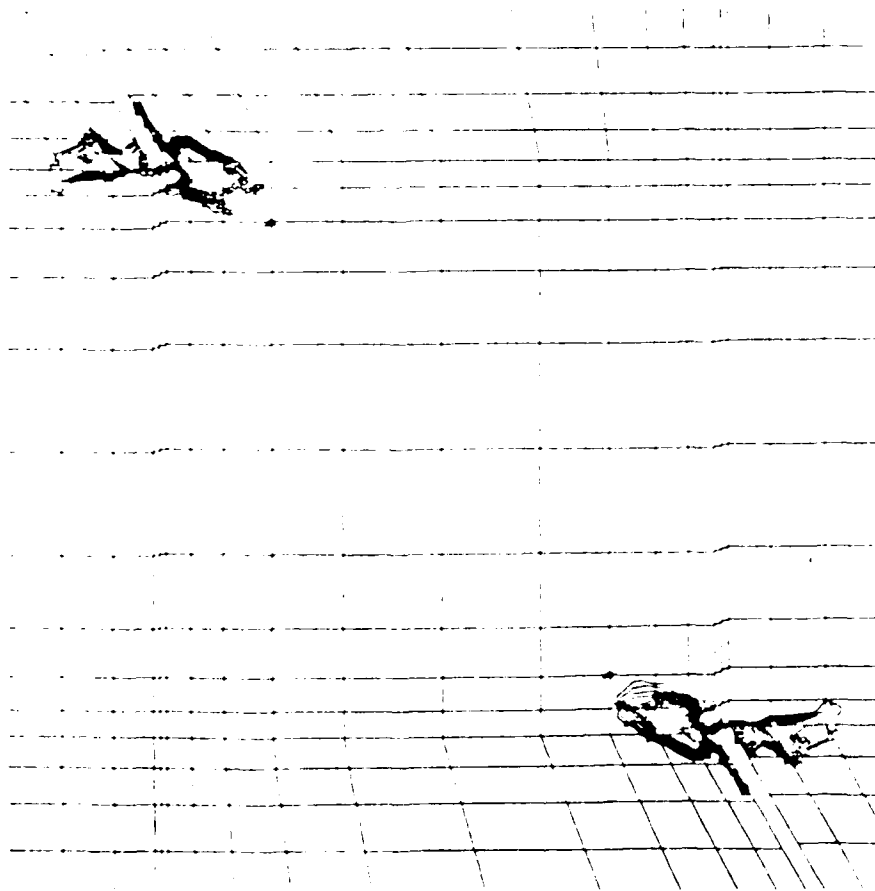
Damage	Value
1	0.050
2	0.070
3	0.090
4	0.110
5	0.130
6	0.150
7	0.170
8	0.190

Figure 4.33(a) Damage contours in 30°-45° edge model, $\varepsilon_0 = 0.0024$ and $A = 0.785$ Applied Load = 18.4 MPa.
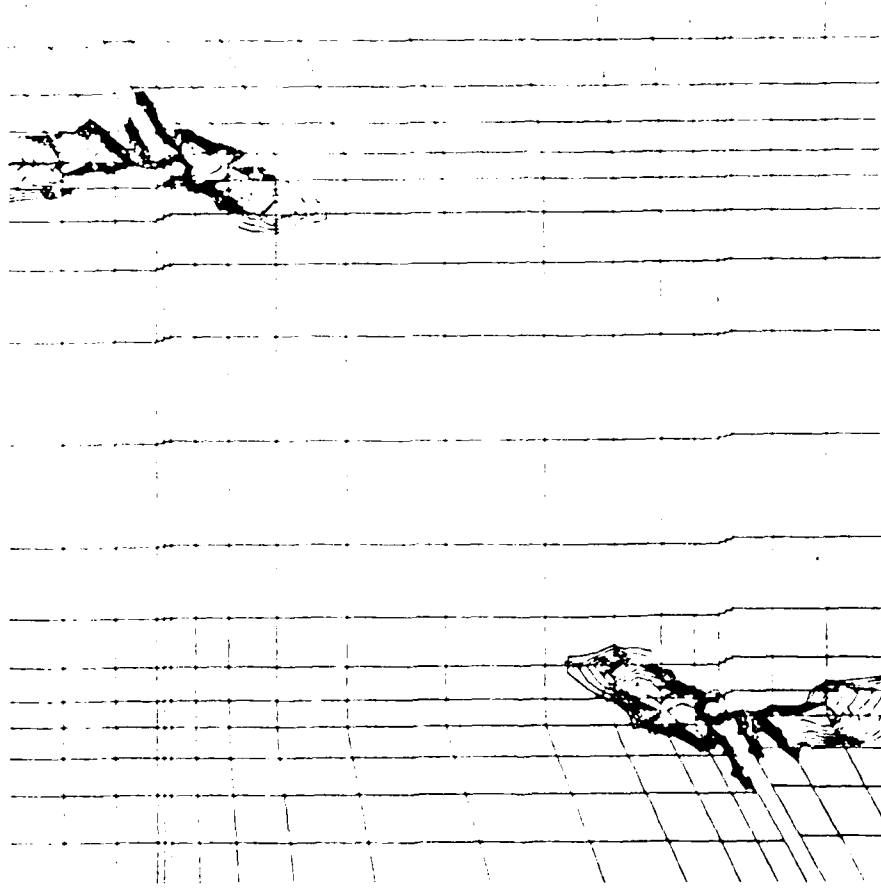
Figure 4.33(b) Damage contours in 30°-45° edge model, $\varepsilon_0 = 0.0024$ and $\Lambda = 0.785$
Applied Load = 19.6 MPa.
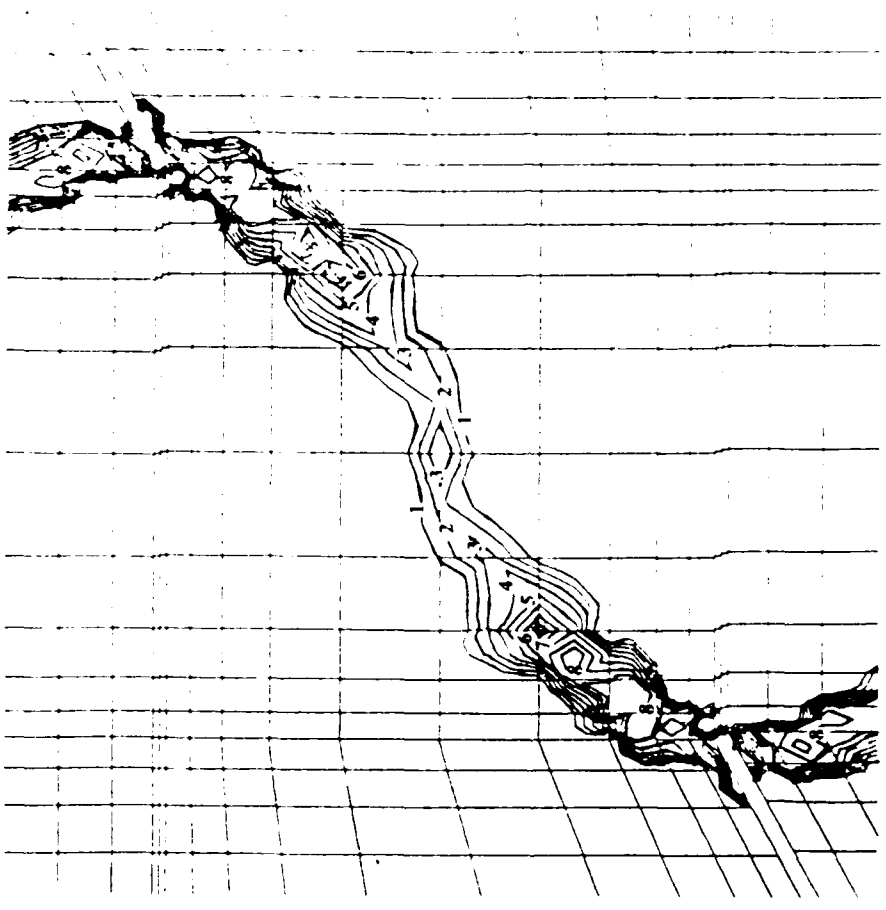
Damage	
	Value
1	0.050
2	0.070
3	0.090
4	0.110
5	0.130
6	0.150
7	0.170
8	0.190

Figure 4.33(c) Damage contours in 30°-45° edge model, $\epsilon_0 = 0.0024$ and $\Lambda = 0.785$. Applied Load = 20.8 MPa.
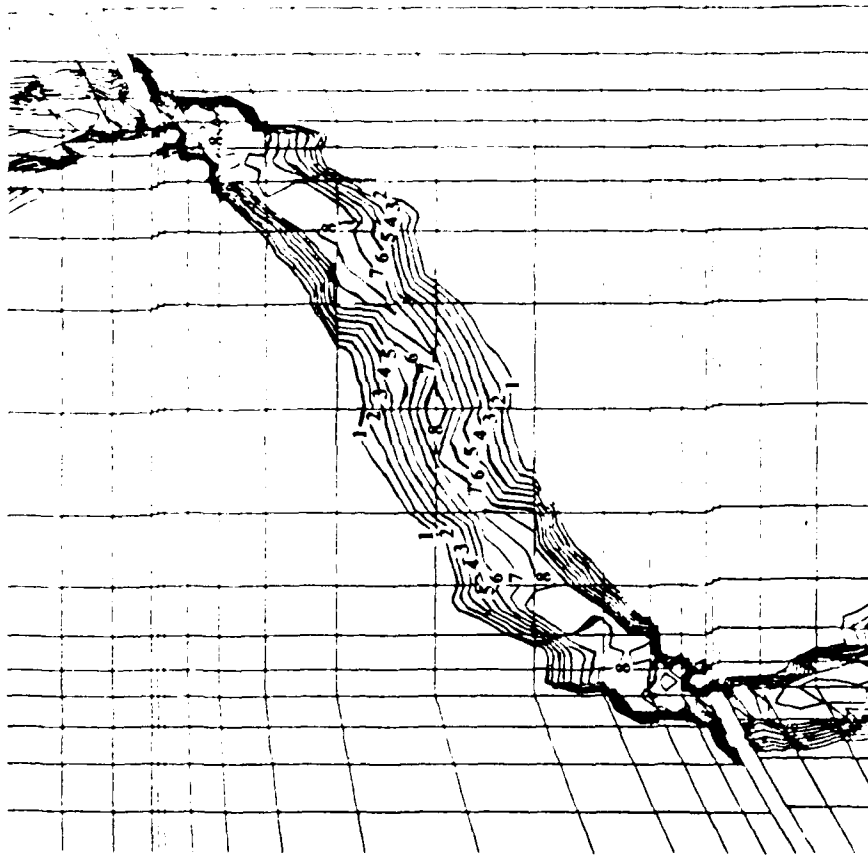
Damage	
	Value
1	0.050
2	0.070
3	0.090
4	0.110
5	0.130
6	0.150
7	0.170
x	0.190

Figure 4.33(d) Damage contours in 30°-45° edge model, $\varepsilon_0 = 0.0024$ and A = 0.785. Applied Load = 21.4 MPa.

Damage	Value
1	0.050
2	0.070
3	0.090
4	0.110
5	0.130
6	0.150
7	0.170
8	0.190
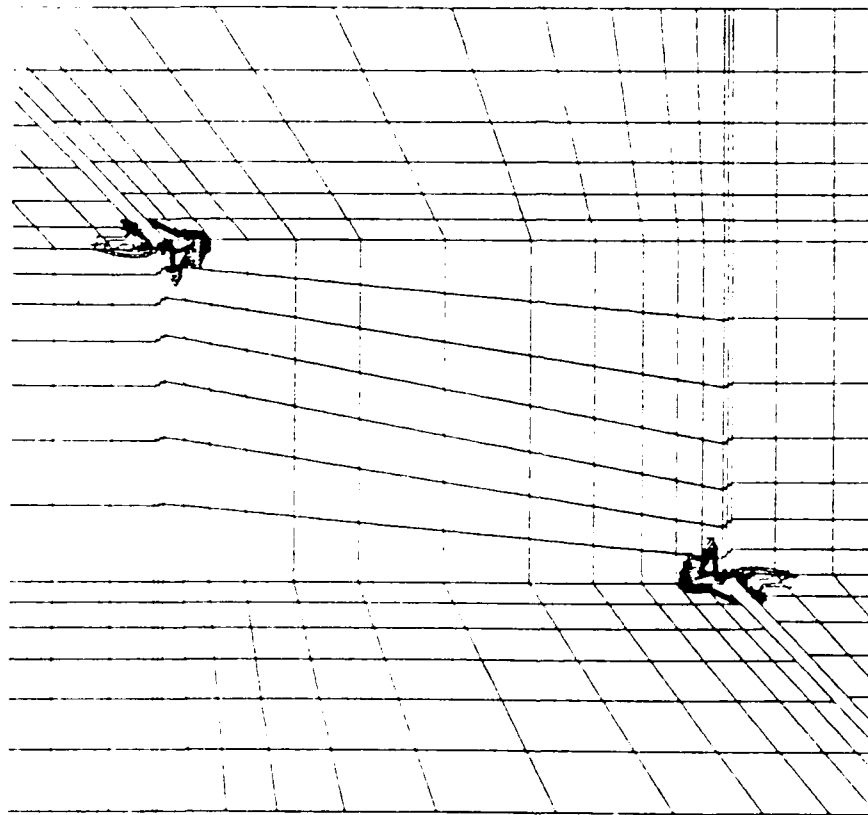
Damage	
	Value
1	0.050
2	0.070
3	0.090
4	0.110
5	0.130
6	0.150
7	0.170
8	0.190

Figure 4.34(a) Damage contours in 45°-60° edge model, $\varepsilon_0 = 0.0024$ and $\Lambda = 0.785$ Applied Load = 15.7 MPa.
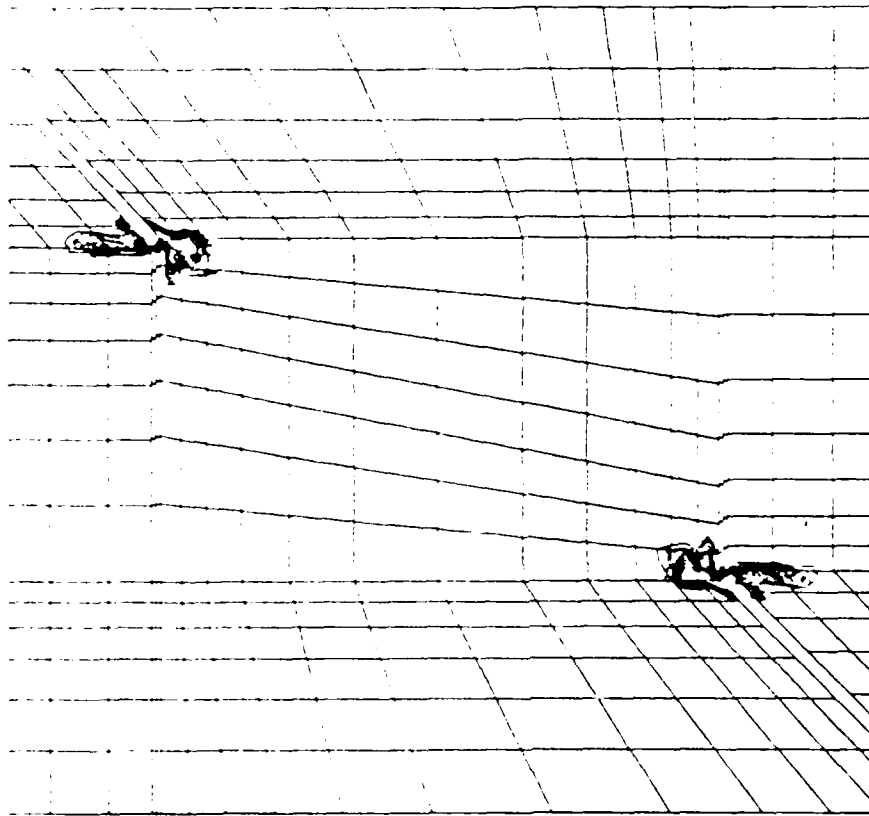
Figure 4.34(b) Damage contours in 45°-60° edge model, $\varepsilon_0 = 0.0024$ and $A = 0.785$. Applied Load = 16.6 MPa.

Damage		
	Value	
1	0.050	
2	0.070	
3	0.090	
4	0.110	
5	0.130	
6	0.150	
7	0.170	
8	0.190	

194
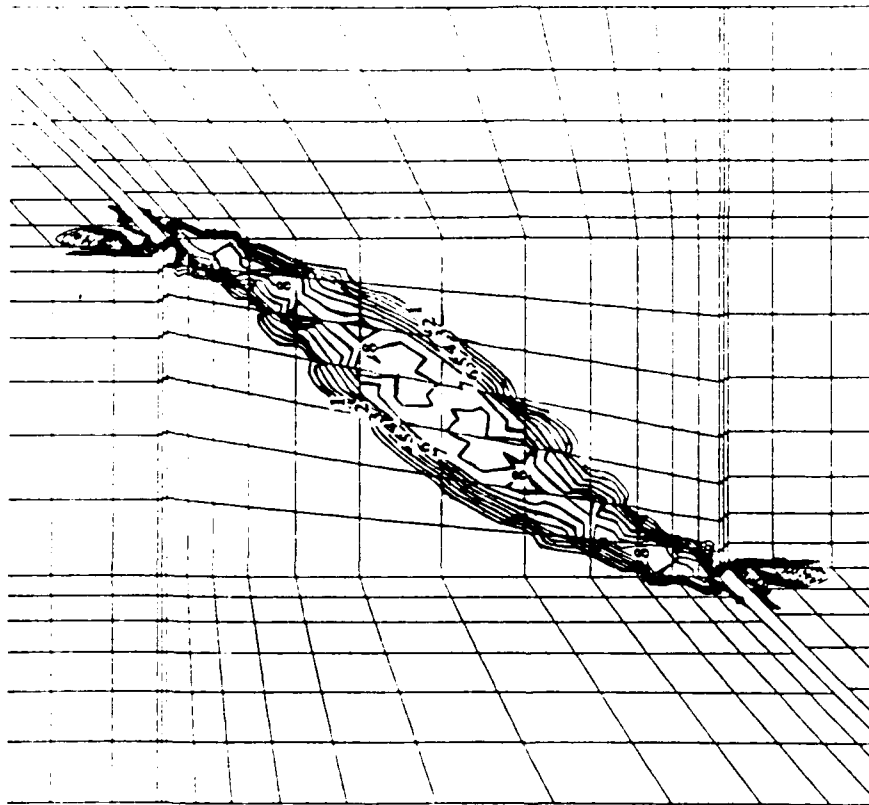
Damage	
	Value
1	0.050
2	0.070
3	0.090
4	0.110
5	0.130
6	0.150
7	0.170
8	0.190

Figure 4.34(c) Damage contours in 45°-60° edge model, $\varepsilon_0 = 0.0024$ and $A = 0.785$ Applied Load = 18.0 MPa.
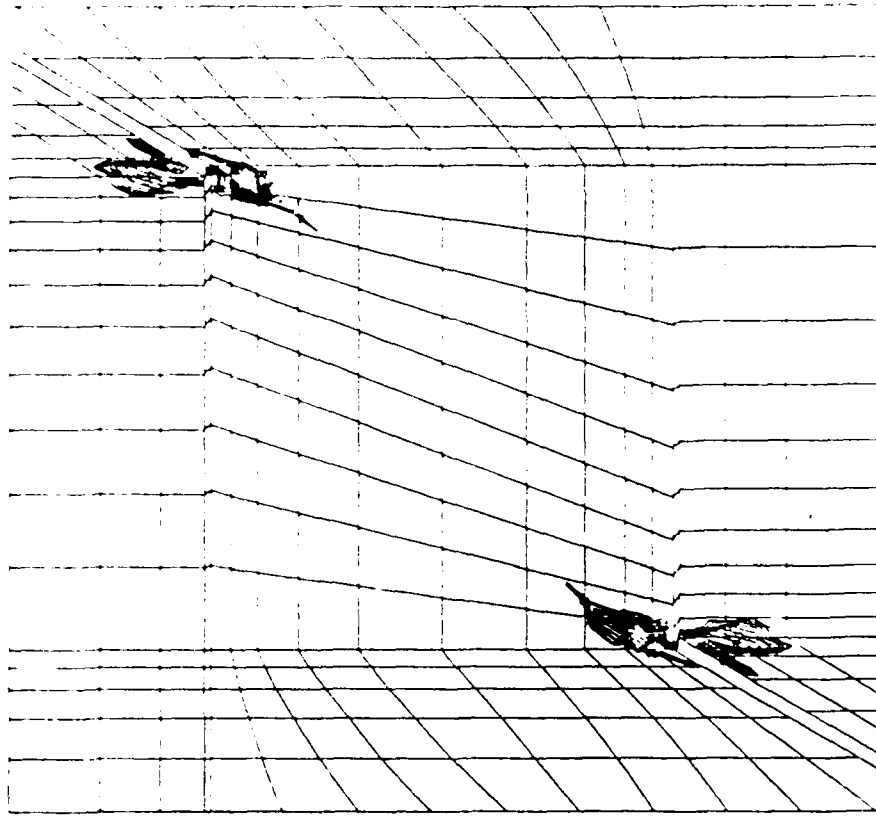
Damage		
	Value	
1	0.050	
2	0.070	
3	0.090	
4	0.110	
5	0.130	
6	0.150	
7	0.170	
8	0.190	

Figure 4.35(a) Damage contours in 60°-45° edge model, $\varepsilon_0 = 0.0024$ and $\Lambda = 0.785$. Applied Load = 18.4 MPa.
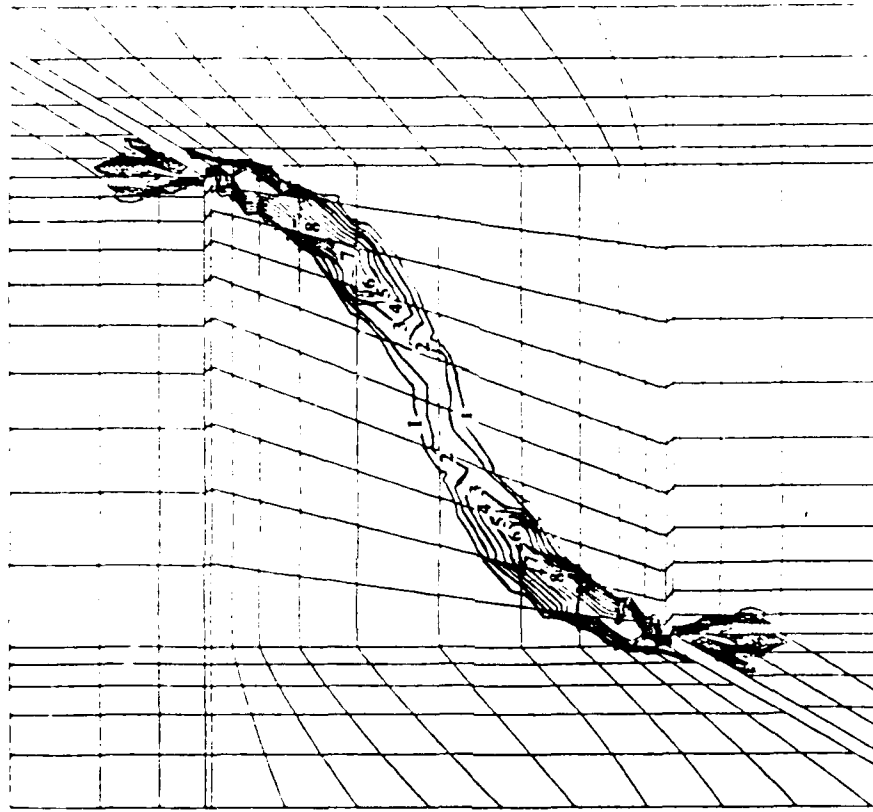
Damage	
	Value
1	0.050
2	0.070
3	0.090
4	0.110
5	0.130
6	0.150
7	0.170
8	0.190

Figure 4.35(b) Damage contours in 60°-45° edge model, $\varepsilon_0 = 0.0024$ and $A = 0.785$. Applied Load = 23.1 MPa.
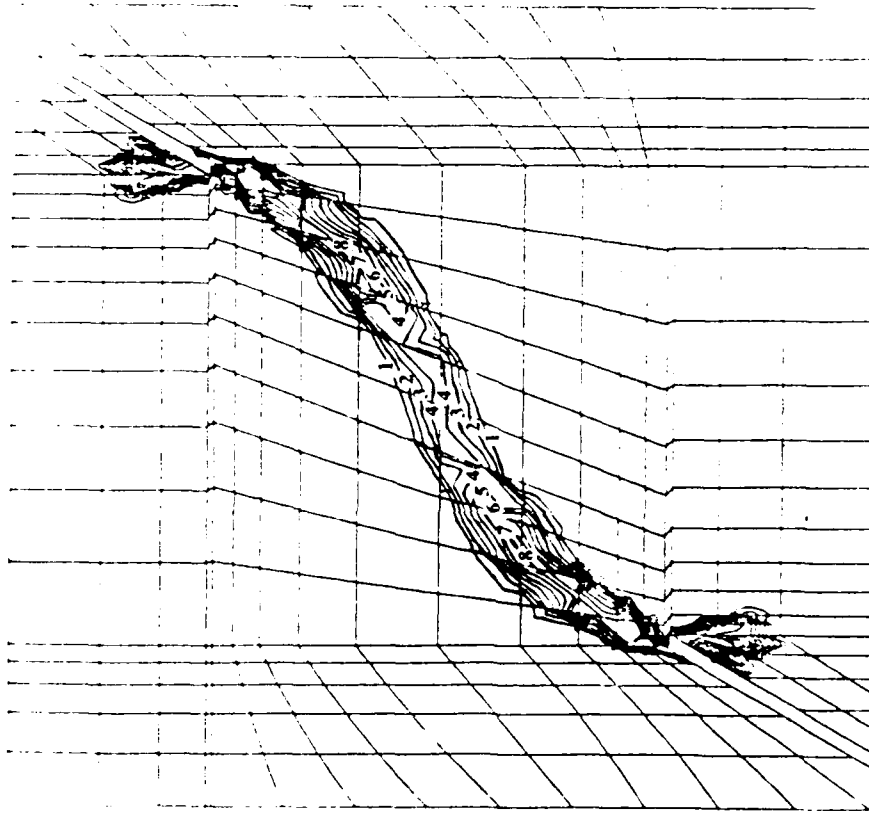
Damage	
	Value
1	0.050
2	0.070
3	0.090
4	0.110
5	0.130
6	0.150
7	0.170
8	0.190

Figure 4.35(c) Damage contours in 60°-45° edge model, $\varepsilon_o = 0.0024$ and A $= 0.785$ Applied Load $= 24.0$ MPa.
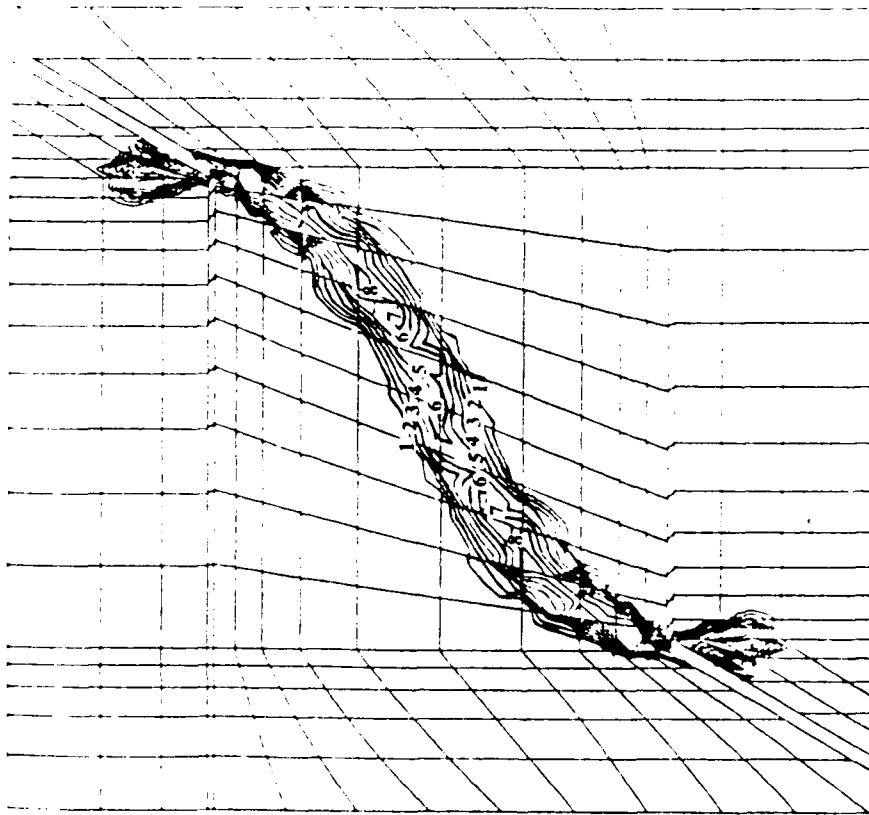
Figure 4.35(d) Damage contours in $60°-45°$ edge model, $\varepsilon_0 = 0.0024$ and $\Lambda = 0.785$. Applied Load = 24.4 MPa.

Damage	
	Value
1	0.050
2	0.070
3	0.090
4	0.110
5	0.130
6	0.150
7	0.170
8	0.190
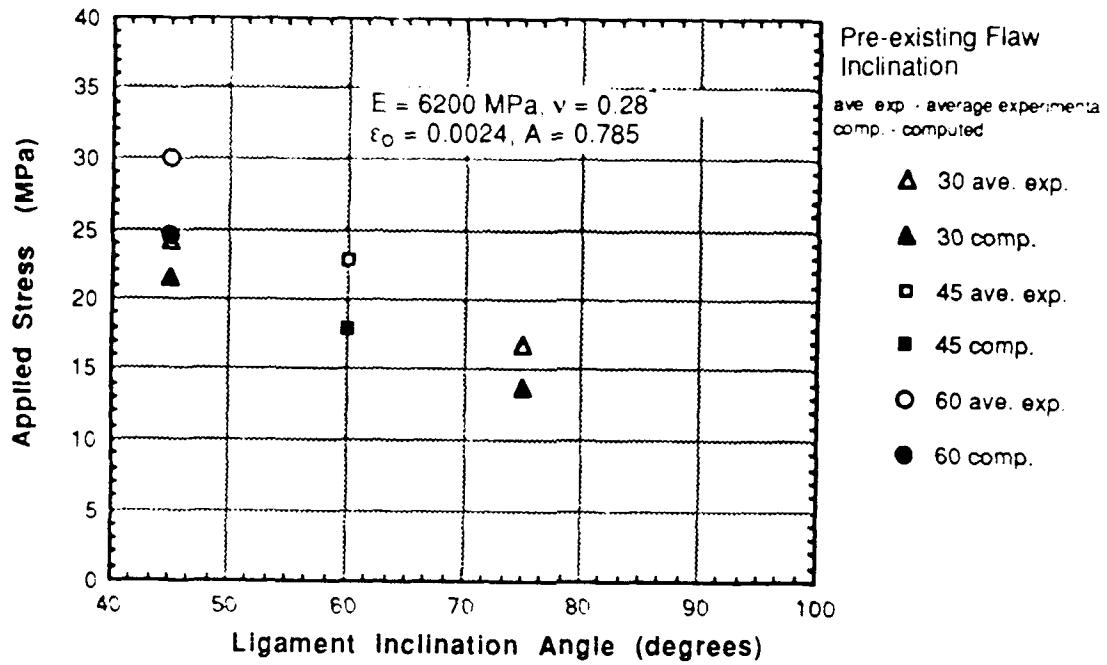
Figure 4.36   Comparison of experimental and computed coalescence loads for non-overlapping flaws.
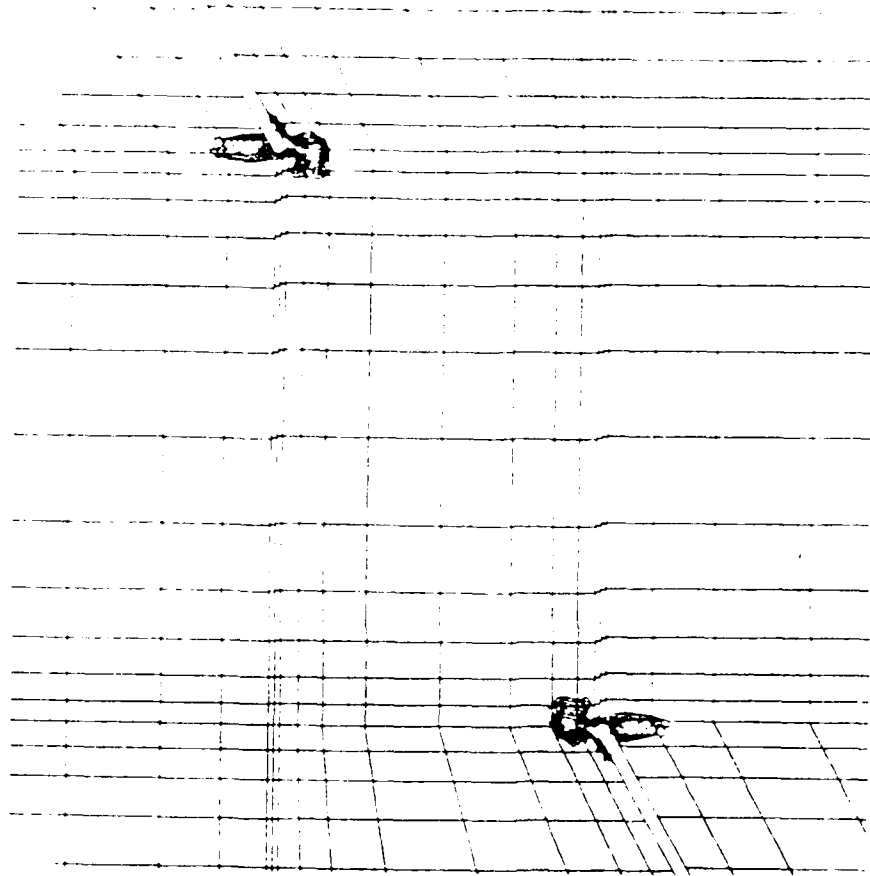
Damage	
	Value
1	0.050
2	0.070
3	0.090
4	0.110
5	0.130
6	0.150
7	0.170
x	0.160

Figure 4.37(a) Damage contours in 30°-30° edge model, $\varepsilon_o = 0.0024$ and A = 0.785 Applied Load = 18.1 MPa.
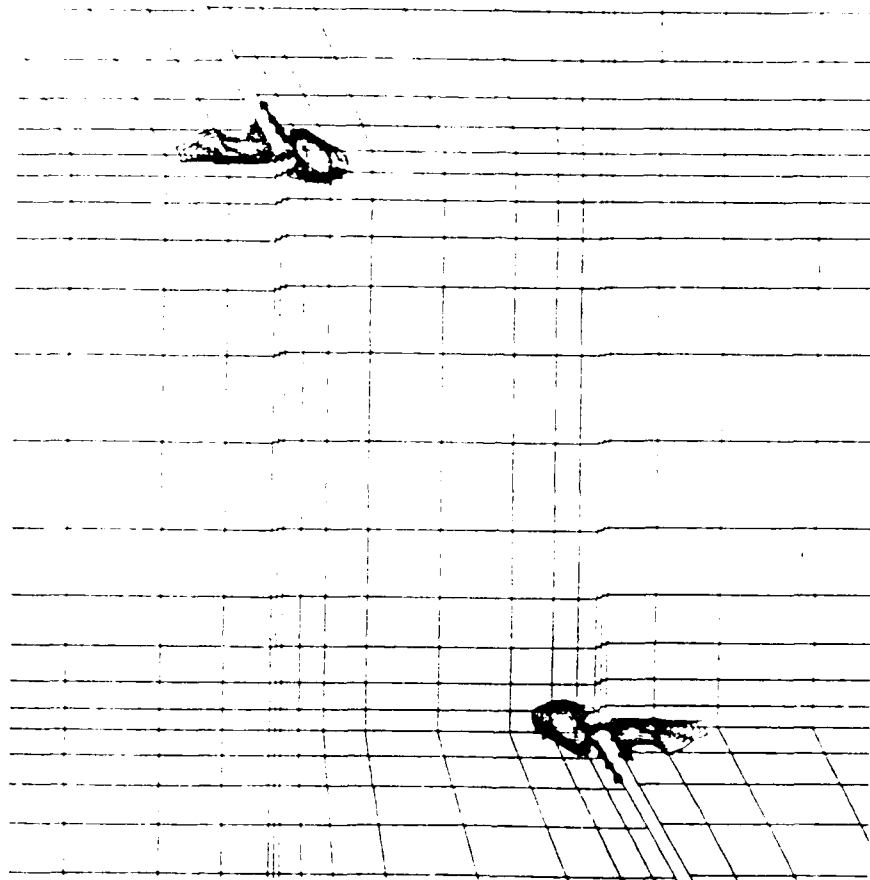
Damage		
	Value	
1	0.050	
2	0.070	
3	0.090	
4	0.110	
5	0.130	
6	0.150	
7	0.170	
8	0.190	

Figure 4.37(b) Damage contours in 30°-30° edge model, $\varepsilon_0 = 0.0024$ and $\Lambda = 0.785$. Applied Load = 19.9 MPa.
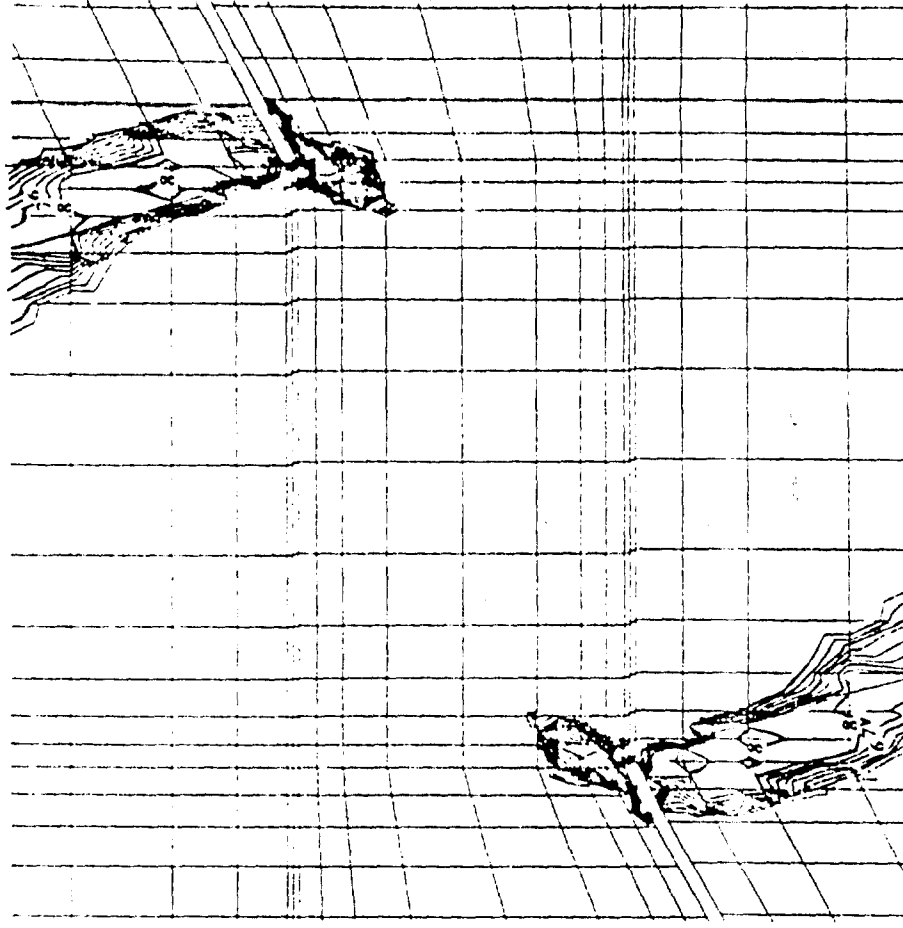
Figure 4.37(c) Damage contours in 30°-30° edge model, $\varepsilon_0 = 0.0024$ and $A = 0.785$ Applied Load = 23.4 MPa.

Damage	Value
1	0.050
2	0.070
3	0.090
4	0.110
5	0.130
6	0.150
7	0.170
8	0.190

Chapter 5
Conclusions and
Recommendations for Future Study

An extensive series of crack growth experiments using gypsum as a model material for rock showed fracturing that was quite different from that observed by others in polymer materials. In particular, only wing cracks grew from pre-existing flaws in polymer specimens while in gypsum, wing cracks grew first and were followed by secondary crack growth. More importantly, secondary crack growth led to coalescence between non-overlapping flaws in gypsum specimens whereas such coalescence has never been observed in previous experiments on polymers. On the other hand, coalescence between overlapping flaws in gypsum occured through wing crack growth and at loads that were higher than the coalescence loads measured for non-overlapping flaws. Thus, analytical modeling in this study was focused on representing secondary crack growth and the associated coalescence between pre-existing, non-overlapping flaws.

In the analytical phase, linear elastic stress and strain fields after wing crack growth were determined for various interacting flaw geometries. Principal stress and strain plots from these analyses revealed that secondary crack growth can be best modelled by a smeared crack/damage approach coupled with a tensile strain-based failure criterion. A non-softening, tensile strain-based damage model was then developed and implemented as a material subroutine in a finite element program (ABAQUS). Material parameters were chosen such that the simulated coalescence load for one of the flaw geometries was close to the experimental value. To validate the model, the same set of parameters was used to simulate coalescence between flaws with other arrangements. Very satisfactory agreement was achieved between experimental and simulated coalescence loads.

Although the damage model presented in this study was derived from tests on several different flaw arrangements, it would be interesting to validate this model on other flaw geometries which may be obtained by varying the flaw inclination angle, ligament (rock bridge) inclination angle, flaw length and ligament length. Other variations of specimen geometry are specimens with: (1) more than two flaws, (2) sub-parallel or even non-parallel flaws, and (3) closed flaws. The results of these additional fracture tests could then be compared to results of numerical simulations. It would also be interesting to see whether the fracturing of double-edge notched concrete beams described in Chapter 1 of this report could be simulated using the tensile strain-based damage model. In fact, since the model is based on stresses and strains, it could be applied to any geometry as long as the material remains elastic prior to fracture, and the fracturing of the material is adequately characterized by a strain-based failure criterion.

Another obvious extension of this work would be to perform the crack growth/coalescence experiments on other types of rock and, eventually, different brittle materials. Since secondary crack growth was seen in other rocks as reported in the literature, it is highly possible that coalescence would also occur in these other rock types as it did in gypsum. Different rock types have different microstructures, and it would be interesting to see how the coalescence behavior is affected by these differences.

In this study, the stress-strain distribution around the flaws in the test specimens was only established through numerical simulation of the experiments. The non-homogeneity and strong gradients of the strain field around the flaws made point-strain measurement techniques such as using strain gages infeasible. However, techniques are currently being developed for measuring "whole strain fields" in non-photoelastic materials such as rock. Examples of these are holographic and speckle interferometry. The application of these methods to the crack growth/coalescence experiments described in this

205

report would not only verify the numerically derived stress and strain fields but would also confirm or refute the hypothesis that fracturing occurs in regions with highest tensile strains.

References

ABAQUS User's Manual, Hibbit, Karlsson and Sorensen, Inc., 1990.

M. Adams and G. Sines, "Crack extension from flaws in a brittle material subjected to compression," Tectonophysics, 49, pp. 97-118, 1978.

B. Annigeri, Surface Integral Finite Element Hybrid Method for Localized Problems in Continuum Mechanics, Ph.D. Thesis, MIT, 1984.

K. J. Bathe, Finite Element Procedures in Engineering Analysis, Prentice-Hall, Inc., New Jersey, 1982.

Z. P. Bazant and B. H. Oh, "Crack band theory for fracture of concrete," Materials and Structures, RILEM, 16 (94), pp. 155-177, 1983.

Z. P. Bazant and P. A. Pfeiffer, "Shear fracture tests of concrete," Materials and Structures, 19, pp. 111-121, 1986.

E. Bombolakis, "Photoelastic investigation of brittle crack growth within a field of uniaxial compression," Tectonophysics, 1 (4), pp. 343-351, 1964.

E. Bombolakis, "Photoelastic study of initial stages of brittle fracture in compression," Tectonophysics, 6 (6), pp. 461-473, 1968.

E. Bombolakis, "Study of the brittle fracture process under uniaxial compression," Tectonophysics, 18, pp. 231-248, 1973.

R. de Borst, Non-linear Analysis of Frictional Materials, Ph.D. thesis, 1986.

R. Bourcier and D. Koss, "Ductile fracture under multiaxial stress states between pairs of holes" in Proceedings, 5th International Conference on Fracture, D. Francois (ed), 1, pp. 187-194, 1981.

W. Brace and E. Bombolakis, "A note on brittle crack growth in compression," Journal of Geophysical Research, 68 (12), pp. 3709-3713, 1963.

W. Brace and J. Byerlee, "Recent experimental studies of brittle fracture of rocks," in Failure and Breakage of Rock, AIME, pp. 57-81, 1967.

J.R. Brockenbrough and S. Suresh, "Constitutive behavior of a microcracking brittle solid in cyclic compression," Journal of Mechanics and Physics of Solids, 35 (6), pp. 721-742, 1987.

B. Budiansky and R. O'Connell, "Elastic moduli of a cracked solid," International Journal of Solids and Structures, 12, pp. 81-97, 1976.

H. C. Chan, Automatic Two-dimensional Multi-Fracture Propagation Modelling of Brittle Solids with Particular Application to Rock, Ph.D. Thesis, MIT, 1986.

K. Chang, "On the maximum strain criterion - a new approach to the angled crack problem," Engineering Fracture Mechanics, 14, pp. 107-124, 1981.

P.G. Charalambides and R.M. McMeeking, "Finite element simulation of crack propagation in a brittle microcracking solid," Mechanics of Materials, 6, pp. 71-87, 1987.

E. Chen, "Dynamic brittle fracture analysis based on continuum damage mechanics" in Fracture Mechanics: Perspectives and Directions (Twentieth Symposium), ASTM STP 1020, R. Wei and R. Gangloff, eds., American Society for Testing and Materials, pp. 447-458, 1989.

E. Chen and D. Tzou, "A continuum damage model for the quasi-static response of brittle materials" in Micromechanics of Failure of Quasi-Brittle Materials, S. Shah, S. Swartz and M. Wang, eds., pp. 620-626, 1990.

W. Chen and D. Han, Plasticity for Structural Engineers, Springer-Verlag, 1988. Z. Chen and H. Schreyer, "Failure-controlled solution strategies for damage softening with localization" in Micromechanics of Failure of Quasi-Brittle Materials, S. Shah, S. Swartz and W. Wang, eds., pp. 135-145, 1990.

L. Costin and D. Holcomb, "A continuum model of inelastically deformed brittle rock based on the mechanics of microcracks" in Proceedings, International Conference on Constitutive Laws for Engineering Materials: Theory and Applications, C. Desai ar J R. Gallagher, eds., pp. 185-195, 1983.

L. Costin and C. Stone, "Implementation of a finite element damage model for rock" in Constitutive Laws for Engineering Materials: Theory and Applications, C. Desai, E. Krempl, P. Kiousis and T. Kundu, eds., pp. 829-840, 1987.

B. Cotterell, "Brittle fracture in compression," International Journal of Fracture Mechanics, 8, 2, pp. 195-207, 1972.

F. Erdogan and G. C. Sih, "On the crack extension in plates under plane loading and transverse shear," Journal of Basic Engineering, December 1963, pp. 519-527.

E. Gdoutos, Problems of Mixed Mode Crack Propagation, Martinus Nijhoff Publishers, 1984.

K. Hellan, Introduction to Fracture Mechanics, McGraw-Hill Book Company, 1984.

E. Hoek and Z. Bieniawski, "Brittle fracture propagation in rock under compression," International Journal of Fracture, 1, pp. 137-155, 1965.

D. Holcomb, C. Stone and L. Costin, "Combining acoustic emission locations and a microcrack damage model to study development of damage in brittle materials" in Rock Mechanics Contributions and Challenges, Justrulid and Johnston (eds), pp. 645-651, 1990.

H. Horii and S. Nemat-Nasser, "Compression-induced microcrack growth in brittle solids: axial splitting and shear failure," Journal of Geophysical Research, 90 (B4), pp. 3105-3125, 1985.

208

H. Horii and S. Nemat-Nasser, "Brittle failure in compression: splitting, faulting and brittle-ductile transition," Philosophical Transactions of the Royal Society of London, Vol. 319 (1549), pp. 337-374, 1986.

H. Horii and S. Nemat-Nasser, "Elastic fields of interacting inhomogeneities," International Journal of Solids and Structures," 21, pp. 731-745, 1985.

M. A. Hussain, S. L. Pu and J. H. Underwood, "Strain energy release rate for a crack under combined Mode I and Mode II," in Fracture Analysis, ASTM STP 560, 1974.

A. Ingraffea and F. Heuze, "Finite element models for rock fracture mechanics," International Journal for Numerical and Analytical Methods in Geomechanics, 4, pp. 24-43, 1980.

A. Ingraffea and N. Panthaki, "Analysis of shear fracture tests of concrete beams," in Finite Element Analysis of Reinforced Concrete Structures, C. Meyer and H. Okamura, eds., May 21-24, 1985.

P. Jacquot, "Interferometry in scattered coherent light applied to the analysis of cracking in concrete," in Fracture Mechanics of Concrete, A. Carpinteri and A. Ingraffea, eds., 1984.

J. Jaeger and N. Cook, Fundamentals of Rock Mechanics, Chapman and Hall, 1976.

L. M. Kachanov, "Time of the rupture process under creep conditions," Izv. Akad. Nauk SSR Otd. Tech. Nauk, 8, pp. 26-31, 1958.

M. E. Kipp and G. C. Sih, "The strain energy density failure criterion applied to notched elastic solids," Int. Journal of Solids and Structures, 11, pp. 153-173, 1975.

D. Krajcinovic and D. Fanella, "A micromechanical damage model for concrete," Engineering Fracture Mechanics, 25 (5/6), 1986, pp. 585-596.

D. Krajcinovic and G. Fonseka, "The continuous damage theory of brittle materials, Part I: General theory," Journal of Applied Mechanics, 48, pp. 809-815, 1981.

R. Kranz, "Crack-crack and crack-pore interactions in stressed granite," International Journal of Rock Mechanics and Mining Sciences, 16, pp. 37-47, 1979.

E. Lajtai, "A theoretical and experimental evaluation of the Griffith theory of brittle fracture," Techtonophysics, 11, pp. 129-156, 1971.

E. Lajtai and V. Lajtai, "The evolution of brittle fracture in rocks," Journal of Geology, 130, pp. 1-18, 1974.

E. Lajtai, "Brittle fracture in compression," International Journal of Fracture, 10 (4), pp. 525-536, 1974.

E. Lajtai and V. Lajtai, "The collapse of cavities," International Journal of Rock Mechanics and Mining Sciences, 12, pp. 81-86, 1975.

J. Lemaitre, "Local Approach of Fracture," Engineering Fracture Mechanics, 25 (5/6), 1986, pp. 523-537.

S. Maiti and R. Smith, "Comparison of the criteria for mixed mode brittle fracture based on the preinstability stress-strain field, Part II: Pure shear and uniaxial compressive loading." International Journal of Fracture. 24, pp. 5-22, 1984.

J. Mazars, "A description of micro- and macroscale damage of concrete structures," Engineering Fracture Mechanics. 25 (5/6), pp. 729-737, 1986.

F. A. McClintock and J. B. Walsh, "Friction on Griffith cracks in rocks under pressure," in Proc. 4th U.S. Nat. Congr. Appl. Mech. Vol. 2, pp. 1015-1021, 1962.

S. Melin, "Why are crack paths in concrete and mortar different form those in PMMA?" Materials and Structures. 22, pp. 23-27. 1989.

S. Melin, "When does a crack grow under mode II conditions?" International Journal of Fracture. 30, pp. 103-114, 1986.

R. Nelson, Modeling a Jointed Rock Mass. S.M. Thesis, MIT, 1968.

V. Nesetova and E. Lajtai, "Fracture from compressive stress concentrations around elastic flaws." International Journal of Rock Mechanics and Mining Sciences, 10, pp. 265-284, 1973.

M. Ortiz. "An analytical study of the localized failure modes of concrete," Mechanics of Materials. 6, pp. 159-174, 1987.

M. Ortiz. "A continuum theory of crack shielding in ceramics," Journal of Applied Mechanics. 54, pp. 54-58, 1987.

J.-P. Petit, "Normal stress dependent rupture morphology in direct shear tests on sandstone with applications to some natural fault surface features," International Journal of Rock Mechanics and Mining Sciences, 25 (6), pp. 411-419, 1988.

J.-P. Petit and M. Barquins, "Can natural faults propagate under mode II conditions?" Tectonics. 7 (6), pp. 1243-1256, 1988.

L. Resende and J. Martin, "Parameter identification in a damage model for rock mechanics." International Journal for Numerical and Analytical Methods in Geomechanics. 12, pp. 79-97, 1988.

O. Reyes, H. H. Einstein and V. C. Li, Stochastic and Centrifuge Modelling of Jointed Rock. Part I - Fracturing of Jointed Rock. Annual Report submitted to the Air Force Office of Scientific Research, 1989.

J. G. Rots, P. Nauta, G. Kusters, J. Blaauwendraad, "Smeared crack approach and fracture localization in concrete," HERON, 30 (1), pp. 1-48, 1985.

G. Sih, "Strain-energy-density factor applied to mixed mode crack problems," International Journal of Fracture. 10 (3), pp. 305-321, 1974.

G. Sih and P. Theocaris, eds., Mixed Mode Crack Propagation, Sijthoff and Noordhoff, 1981.

J. C. Simo and J. W. Ju, "Strain- and stress-based continuum damage models - I. Formulation," International Journal of Solids and Structure, 23 (7), pp. 821-840, 1987.

B. Stimpson, "Modelling materials for engineering rock mechanics," International Journal for Rock Mechanics and Mining Sciences, 7, pp. 77-121, 1970.

S. Swartz and N. Taha, "Mixed mode crack propagation and fracture in concrete," Engineering Fracture Mechanics, Vol. 35, No. 1/2/3, pp. 137-144, 1990.

S. Timoshenko and J. Goodier, Theory of Elasticity, McGraw-Hill International Book Company, 1982.

J. Tirosh and E. Catz, "Mixed-mode fracture angle and fracture locus of materials subjected to compressive loading," Engineering Fracture Mechanics, 14, pp. 27-38, 1981.

V. Tvergaard, "Ductile fracture by cavity nucleation between larger voids," Journal of Mechanics and Physics of Solids, 30 (4), pp. 265-286, 1982.

K. C. Valanis, "A theory of damage in brittle materials," Engineering Fracture Mechanics, 36 (3), pp. 403-416, 1990.

L. Vallejo, "The influence of fissures in a stiff clay subjected to direct shear," Geotechnique, 37 (1), pp. 69-82, 1987.

R. Wang, Y. Zhao, Y. Chen, H. Yan, Y. Yin, C. Yao and H. Zhang, "Experiment and finite element simulation of X-type shear fractures from a crack in marble," Tectonophysics, 144, pp. 141-150, 1987.

H. Wu and K. Chang, "Angled elliptic notch problems in compression and tension," Journal of Applied Mechanics, 45, pp. 258-262, 1978.

S. Yarema and G. Ivanitskaya, "Limiting equilibrium and the development angled cracks, review of criteria," Translated from Fiziko-Khimicheskaya Mekhanika Materialov, 22 (1), pp. 45-57, January-February, 1986.